DEVELOPMENT OF SOLID PROPELLANT MICROTHRUSTERS

ZHANG KAILI

NATIONAL UNIVERSITY OF SINGAPORE

2005

DEVELOPMENT OF SOLID PROPELLANT MICROTHRUSTERS

ZHANG KAILI

(*B. Eng, M. Eng*)

A THESIS SUBMITTED FOR

THE DEGREE OF DOCTOR OF PHILOSOPHY

DEPARTMENT OF MECHANICAL ENGINEERING

NATIONAL UNIVERSITY OF SINGAPORE

2005

Acknowledgements

I would like to thank Professor Chou Siaw Kiang from the National University of Singapore, my supervisor, for his valuable guidance throughout this research project and for being a great teacher and mentor. I am also thankful to Professor Simon S. Ang from the University of Arkansas, my co-supervisor, for his many suggestions and constant support during this research.

I would also like to express my gratitude to the National University of Singapore for providing the research funding and scholarship for this research. I wish to acknowledge the support of National University of Singapore Micro Systems Technology Initiative (MSTI) Lab, Thermo Lab, Supercomputing-Visualisation Center, Materials Lab, Advanced Manufacture Lab, Impact Mechanics Lab, and PCB Fabrication Center for their contributions to the solid propellant preparation, the microthruster fabrication, simulation, and testing.

I am also grateful to Dr. Fred Barlow and Dr. Victor Wang of CEPAL at the University of Arkansas for their technical assistance in the LTCC microthruster fabrication.

I am especially thankful to the Institute of Materials Research and Engineering (IMRE) and the Institute of Microelectronics (IME) for their assistance in the fabrication of the solid propellant microthrusters.

Finally, I wish to thank my family - my mom and dad for their encouragement; my mother-in-law and father-in-law, who give me more love than I could ever hope for; and my lovely wife - *Gao Shan*, to whom I will always owe every bit of my success and happiness.

Zhang Kaili

February 16, 2005

Contents

Summary

Various trends in the spacecraft industry are driving the development of micropropulsion systems. Solid propellant microthruster is suitable for micropropulsion applications because of its interesting advantages, such as ability to deliver precise thrust and impulse, no moving parts, very low fuel leakage possibility, and large manoeuvrability and flexibility. This thesis presents the new designs, fabrication, packaging, and testing of the silicon-based solid propellant microthrusters. They can be used in micropropulsion field, such as station keeping, attitude control, drag compensation, and orbit adjust for microspacecraft. Moreover, they can have the potential for terrestrial, security, and biomedical applications. The new designs offer interesting advantages over previous approaches, such as more design freedom of nozzle and chamber, more effective and efficient fabrication process, better bonding quality, more freedom of igniter position selection, and a higher degree of flexibility, maneuverability and integration. Computational fluid dynamics (CFD) modeling is performed to establish a benchmark for the experimental microthrusters before the fabrication. Electro-thermal multi-physics modeling is also carried out to find an optimal ignition system by modeling the electro-thermal ignition process. Single microthruster, microthruster layers, and arrays are successfully fabricated using microelectromechanical systems (MEMS) technology. To document the feasibility of the novel designs and obtain the characteristics of the new solid propellant microthrusters, a specially designed experimental setup is constructed. The experimental microcombustion, thrust and impulse measurements have proven the feasibility of the novel designs, validated the CFD modeling, and characterized the performance of the silicon-based solid propellant microthrusters.

In addition to the development of the silicon-based solid propellant microthrusters, this thesis presents the development of the ceramic-based solid propellant microthruster using low temperature co-fired ceramic (LTCC) technology. The ceramic-based solid propellant microthruster has some merits over silicon-based solid propel-

lant microthruster, such as simple and inexpensive fabrication, improved thermal properties, and more design freedom. The design, fabrication, and packaging of the LTCC solid propellant microthruster are described. Interesting results are obtained by experimental microcombustion, thrust, and impulse measurements. The LTCC solid propellant microthruster demonstrates desirable merits over the silicon-based solid propellant microthruster by actual fabrication, packaging, and testing.

Moreover, the development of a wireless addressing circuitry is also described in this thesis. The circuitry is used for the solid propellant microthruster systems to realize addressing for microthruser array, to trigger and control the ignition process. Operation principle, design, fabrication, and testing of the circuitry are presented and testing results using the circuitry both for the thin film Au/Ti micro-heater and the solid propellant microthruster with Au/Ti igniter are also included in this thesis. The electro-thermal multi-physics modeling is validated by the experimental measurements using the circuitry.

This thesis is submitted to the Department of Mechanical Engineering, National University of Singapore in partial fulfillment of the requirements for the degree of Doctor of Philosophy.

Thesis Supervisors:

Professor Chou Siaw Kiang, the National University of Singapore

Professor Simon S. Ang, the University of Arkansas, USA

List of Tables

List of Figures

Nomenclature

Roman

A	Area (m^2)
a	Temperature coefficient $(kg^{-n}m^{n+1}s^{2n-1})$
c_e	Nozzle exit velocity (m/s)
E	Total energy (J)
F	Force (N)
h	Convective heat transfer coefficient (W/m^2K)
h	Specific enthalpy (J/kg)
J	Diffusion flux (kg/m^2s)
K_n	Knudsen number
k	Thermal conductivity (W/mK)
Ma	Mach number
n	Combustion index
p	Pressure (P_a)
Re	Reynolds number
S	Source term
T	Thrust (N), Temperature (K)
t	Time (s)
u	x velocity in Cartesian coordinates (m/s)
v	y velocity in Cartesian coordinates (m/s)
W	Width (m)

Greek

α	Half divergence angle (degree)
γ	Thermal capacity ratio
λ	Mean free path (m)

μ	Viscosity (kg/ms)
ρ	Density (kg/m^3)
δ	Surface tension (kg/m)
δ_v	Accommodation coefficient
τ	Stress tensor (N/m^2)
υ	Specific volume (m^3/kg)

Subscripts

a	Ambient
c	Chamber
e	Nozzle exit
t	Nozzle throat

Full quantities

C_p	Specific heat capacity (J/kgK)
I_t	Total impulse (Ns)
$\dot{m}$	Mass flow rate (kg/s)
r	Combustion rate (m/s)

Acronyms

CFD	Computational Fluid Dynamics
DRIE	Deep Reactive Ion Etching
IR	Infra-red
LTCC	Low Temperature Co-fired Ceramic
MEMS	Micro Electro Mechanical Systems
SEM	Scanning Electron Microscope/Micrograph
TCR	Temperature Coefficient of Resistance

Chapter 1

Introduction

1.1 Background

Microelectromechanical systems (MEMS) are a collection of microsensors and microactuators that can sense the environment and have the ability to react to changes in the environment with a microcircuit control. They include microelectronics packaging, integrating antenna structures to deliver control signals into microelectromechanical structures for desired sensing and actuating functions. The system may also need micropower supply, microrelay, and microsignal processing units. Micro-components make the system faster, more reliable, cheaper, and capable of incorporating more complex functions. MEMS emerged with the aid of the development of integrated circuit (IC) fabrication processes, in which sensors, actuators and control functions are co-fabricated in silicon at the beginning of 1990s. MEMS technologies take advantage of all previous microelectronics developments and deal with the new challenges of packaging, media interfacing, and interfacing with microscale devices and three-dimensional structures implementation. Remarkable research progresses have been achieved in MEMS under strong capital promotions from both governments and industries. MEMS are destined to become a hallmark 21st-century manufacturing technology with diverse applications. It will have a dramatic impact on many fields such as microfluidics, aerospace, bio-

medical, chemical analysis, wireless communications, data storage, display, optics, etc. MEMS are forecasted to have a commercial market growth similar to its parent IC technology [Menz et al 2001, Senturia 2001].

1.2 Microspacecraft and Micropropulsion

One application of MEMS technology is in the aerospace field. The focus of NASA, and the aerospace industry at large, is to reduce spacecraft life-cycle costs while still delivering a spacecraft with the capability of performing useful science or commercial service. One of the objectives is the development of microspacecraft [Collins et al l996]. Such a microspacecraft may contain only one instrument, but the reduction in complexity will lower costs, by facilitating systems integration. In addition, the small sizes allow the selection of a smaller, less expensive launch vehicle, or the integration of multiple microspacecrafts per vehicle. Future microspacecraft missions may be composed of many microspacecrafts flying in formation rather than a single larger spacecraft. Clusters of microspacecrafts may be employed to increase the reliability of the system, form a large sparse aperture, or simply to provide greater coverage of an area, such as those illustrated in Figure 1.1 [Lewis et al 2000]. In each case, the micropropulsion system will be required in microspacecraft for station keeping, attitude control, gravitation compensation, and orbit adjust [Bayt and Breuer 2001].

The ongoing trend in space system designs is clearly focused on decreasing mass, dimensions, and overall complexity so as to generate low mission cost. The microspacecraft concept has supported a new approach in which micropropulsion systems move towards accurate, reliable, and low-cost systems. Thus, several space missions currently under investigation require finely predicted microthrust to compensate for the aerodynamic drag, solar pressure disturbances, and counteract gravity-well distortions due to the oblateness of the Earth. In this context, studies and developments in micropropulsion systems based on MEMS fabrication

methods can yield valuable solutions.

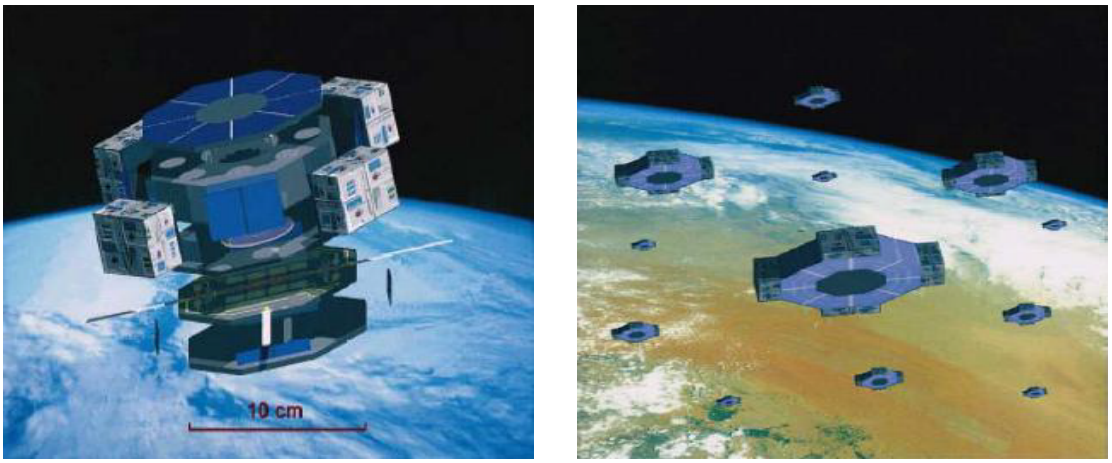

(a) (b)

Figure 1.1. (a) Microspacecraft. (b) Microspacecraft array.

1.3 Motivation for Solid Propellant Microthrusters

With the utility of micropropulsion established, the ideal architecture for meeting the requirements should be assessed. There are many kinds of micropropulsion systems being investigated, such as micro pulsed plasma thruster (MicroPPT), colloid microthruster, field emission electric propulsion microthruster (FEEP), hall microthruster, cold gas microthruster, vaporizing microthruster, field ionization microthruster, digital microthruster, etc. As for the propellant, there are several fuels available for microthruster. Liquid or gaseous fuels can be used in microthruster. They will present a few major benefits. Liquid or gaseous fuels can flow for arbitrarily long times, and the devices can be refueled. The disadvantages of liquid or gaseous fuels are leakages, high pressure storage, technical complication, and contamination problems. Generally, solid fuel microthruster is a single-use device. However, the disadvantage can be partially compensated by microthruster arrays. Even if some of the individual microthrusters fail to work, the array with some redundant microthrusters can still deliver the designed thrust and impulse. Furthermore, solid propellant microthruster might be easier and cheaper to fabricate.

It requires no elaborate system of pumps, fuel lines, and valves. Therefore, there are no moving parts and the leakage possibility of the propellant is very low. High level of integration can be possibly achieved due to the minimization of the total system volume and complexity. Integrated with MEMS technology, the solid propellant microthruster is specifically suitable for microspacecraft. It will have the following main advantages:

- It delivers precise thrust and impulse for microspacecraft applications for station keeping, attitude control, gravitation compensation, and orbit adjust.
- This kind of microthruster has no moving parts.
- The fuel leakage possibility is very low.
- It has a large manoeuvrability and flexibility depending on the design: variable chambers, adjustable nozzles, and varied solid propellants. Based on MEMS technology, it achieves high level of integration and miniaturization and is adaptable to many kinds of applications.

1.4 Review of Previous Research

Studies and developments in micropropulsion systems based on MEMS technologies have provided valuable solutions in past few years. Janson et al [Janson et al 1999, Janson and Helavijian 1996] discussed microfabricated cold gas thrusters, digital thruster arrays, resistojets, and field ion engines. These thrust-producing devices had been fabricated through various micromachining processes with thrust up to 1 mN for cold gas thrusters, and impulses in the 0.09 mN·s range for the digital thrusters. The digital thrusters fabricated in this study used resistive heaters to ignite a solid explosive, which exited the combustion cavity primarily unburned. JPL reported prototypes of micro-resistojets fabricated using MEMS technology in 1997 [Mueller 1997]. E. Y. Choueiri [Choueiri 1999] presented an overview of recent electric propulsion research activities carried out by twelve research groups

at US academic institutions. Bayt [Bayt 1999] reported a cold gas expansion microthruster fabricated in a process that allowed arbitrary nozzle geometry within two dimensions. Bayt's gas expansion thrusters produced thrust in the 0-12 mN range for chamber pressures up to 100 psia. [Hoskins et al 1999, Kohler et al 2002, Kakamia et al 2004, Kang et al 2002, London et al 2001, Mukerjee et al 2000] present some of the latest development on bipropellant microthruster, PPT microthruster, vaporizing liquid microthruster, vaporizing water microthruster, hall effect microthruster, and digital microthruster using low boiling temperature liquid propellant.

The solid propellant microthruster is a relatively new class of microthruster. It is becoming a world-wide active field of research in recent years. A solid propellant microthruster on silicon was proposed in Europe under an EC funded project (IST-99047). Its principle is based on the integration of energetic material within a silicon micromachined system. The operational concept is based on the combustion of an energetic propellant stored in a micromachined chamber. Each microthruster contains three main parts (a heater, a chamber, and a nozzle). Partners in this research are LAAS (CNRS laboratory-France), IMT (University of Neuchatel-Switzerland), IMTEK (University of Freiburg-Germany), SIC (University of Barcelona-Spain), ASTC (University of Uppsala-Sweden), and LACROIX (France) [Rossi et al 2000, Rossi et al 2001, Rossi et al 2002, Orieux et al 2002, Rossi et al 2004]. The University of California at Berkeley detailed the design, fabrication, and testing of millimeter scale solid propellant rockets for use as one-time deployment platforms carrying communication-equipped MEMS sensor systems, known as Smart Dust. Each rocket assembly was an integrated system, incorporating a combustion chamber, composite propellant grain, nozzle, igniter, and thermoelectric power converter [Teasdale et al 2001]. TRW Space and Electronics group, California Institute of Technology and Aerospace Corp carried out research work on MEMS microthruster digital propulsion system. They fabricated and tested arrays of "Digital Propulsion" microthruster. According to their design, a three-layer sandwich mi-

crothruster was fabricated containing microresistors, thrust chambers, and rupture diaphragms. Propellant was loaded into each individually sealed chamber. When energizing the resistor, the propellant was ignited, raising the pressure in the chamber and rupturing the diaphragm. An impulse was imparted as the high-pressure fluid was expelled from the chamber. A total of 106 thrusters were fabricated on a single wafer. Their initial tests, using lead styphnate as the propellant, produced 10^{-4} N·s of impulse and about 100 W of power [Lewis et al 2000]. A MEMS mega-pixel microthruster array designed for station keeping of small satellites was proposed in [Youngner et al 2000]. Modeling, design and layout, processing and testing facilities were described in this paper. But no further results were reported then. A solid propellant microrocket was introduced for simple attitude control of a 10 kg class microspacecraft in [Tanaka et al 2003]. The microrocket was expected to have some possible applications for "Penetrator", a simple spacecraft, which would travel to the lunar surface from a mother ship, "Lunar-A". Generally speaking, the basic design concepts of previous approaches are the three-layer sandwich configurations, which normally contain three parts consisting of a propellant combustion chamber, a micronozzle (or burst diaphragm), and an igniter.

1.5 Development Approach

This section describes the author's approaches that are adopted for the development of solid propellant microthrusters.

- The final objective of this research is to develop solid propellant microthrusters, which can be used in micropropulsion field, such as station keeping, attitude control, drag compensation, and orbit adjust for microspacecraft. Moreover, these devices can also have terrestrial, security, and biomedical applications. To meet this goal, different approaches in computational fluid dynamics (CFD) modeling, electro-thermal multi-physics simulation, microfabrication, low temperature co-fired ceramic (LTCC) technology, wireless

addressing circuitry, and experimental measurements are employed in this thesis.

- The CFD modeling approach is to perform numerical simulations to establish a benchmark for the experimental microthrusters. The key to the development of micropropulsion systems lies in the generation of extremely accurate thrust and impulse levels. This is made possible by simulation tools that can predict the processes inside the microthruster during the microcombustion and compute the theoretical performance of the microthruster system. The model enables the determination of several fundamental design parameters, such as microchamber size, micronozzle shape and dimension, for given performance requirements.

- The electro-thermal multi-physics simulation approach is to locate an optimal ignition system enabling minimization of ignition energy by modeling the electro-thermal ignition process. The transient electro-thermal simulation can predict and optimize the ignition energy for specific igniter and solid propellant, thus improving the ignition efficiency.

- The microfabrication approaches are established to support the primary micropropulsion objectives. First, the novel solid propellant microthruster with wire igniter is designed and fabricated using MEMS technologies. The new design has several advantages over the approaches proposed by former research groups, such as more design freedom of nozzle and chamber, more effective and efficient fabrication process, better bonding quality, and more freedom of igniter position slection. Second, the solid propellant microthruster with thin film igniter is developed. The new design not only inherits all the important advantages of the design for solid propellant microthruster with wire igniter, but also has several other advantages, such as more suitable for batch fabrication, improved ignition efficiency and reliability, and higher level integration.

- The LTCC technology is employed to design and fabricate solid propellant microthruster. The LTCC solid propellant microthruster has some merits over the silicon-based solid propellant microthrusters, such as simple and inexpensive fabrication, improved thermal properties, and more design freedom.

- A wireless addressing circuitry is developed for solid propellant microthrusters proposed in this research. The electronic circuitry is indispensable for the microthruster system to realize addressing for microthruser array, to trigger and control the ignition process.

- The experimental testing approach is essential to prove the feasibility of the new designs, to validate the models, and to characterize the performances of the proposed solid propellant microthrusters.

- The experimental and numerical results are also synthesized to empirically identify the key drivers of combustion and propulsion phenomena at the microscale, and to propose design guidelines for future solid propellant microthruster development.

1.6 Contributions of the Research

The contributions of this thesis are as follows:

1. New designs for silicon-based solid propellant microthrusters.

2. Development of ceramic-based solid propellant microthruster using LTCC technology.

3. Development of modeling methods for:

    - Performance characterization of the new designed solid propellant microthrusters in terms of thrust and impulse.

- Identification of the electro-thermal transient ignition process of the solid propellant.

4. Development of the wireless addressing circuitry for the new designed silicon-based solid propellant microthrusters and ceramic-based LTCC solid propellant microthruster.

5. Experimental verification of the new designed silicon-based solid propellant microthrusters and ceramic-based LTCC solid propellant microthruster.

1.7 Organization of the Thesis

This chapter introduces the background and motivation for the solid propellant microthrusters, reviews previous research on micropropulsion, and summarizes the key approaches and contributions of this thesis.

Chapter 2 details the design and CFD modeling of the solid propellant microthruster with wire igniter. A new design concept of solid propellant microthruster is proposed for micropropulsion applications. CFD modeling and simulation that are performed to establish a benchmark for the microthruster fabrication are described amply in this chapter.

Chapter 3 introduces the microfabrication using MEMS technologies of the new designed microthruster with wire igniter. The experimental measurements are also performed to prove the feasibility of the new design, to characterize the performance of the novel solid propellant microthruster, and to validate the CFD modeling.

Chapter 4 presents the development of the solid propellant microthruster with Au/Ti igniter. Several improvements are added to the new design described in Chapters 2 and 3. The improvements bring more interesting advantages, which has been proven by the microfabrication, packaging, and experimental measurements of the improved solid propellant microthruster with Au/Ti igniter.

Chapter 5 details the electro-thermal multi-physics simulation for the ignition

process of the solid propellant microthruster with Au/Ti igniter. A method is presented to estimate the temperature variations of resistivity and thermal conductivity for the thin film gold and titanium samples that is based on a room-temperature measurement and trends of the variations reported in the literature. Finite-element modeling is introduced and used to simulate the entire three-dimensional device structure both for the Au/Ti micro-heater and the solid propellant microthruster with Au/Ti igniter.

Chapter 6 focuses on the development of the LTCC solid propellant microthruster. The design, fabrication, and experimental testing of the LTCC solid propellant micorthruster are detailed in this chapter. LTCC technology is successfully utilized for the realization of solid propellant microthruster with desirable results. The LTCC microthruster offers more merits over the silicon-based microthrusters described in Chapters 2-5. The experimental results of the three kinds of solid propellant microthrusters developed in this thesis are compared in this chapter.

Chapter 7 describes the development of the wireless addressing circuitry for the new solid propellant microthrusters proposed in this thesis. It presents the operation principle, design, fabrication, and testing of the circuitry. Both RF wireless and RS232 communications are available in the circuitry. The comparison between the transient electro-thermal simulation results and those of the experimental measurements is also described in this chapter.

Chapter 8 outlines the conclusions of this thesis along with recommendations for future work.

Chapter 2

Design and CFD Modeling of the Solid Propellant Microthruster with Wire Igniter

Main Publication:

K. L. Zhang, S. K. Chou, and S. S. Ang, "Performance Prediction of a Novel Solid-Propellant Microthruster", AIAA Journal of Propulsion and Power. (Accepted for publication, will appear in Vol. 22, No. 1, 2006)

2.1 Introduction

As described in Chapter 1, MEMS-based smart microspacecraft is an active research field. The low-cost, reliable, and versatile clusters of microspacecraft have more advantages than a conventional spacecraft in fabrication, launch, and operation. A micropropulsion system is required in microspacecraft for high-accuracy station keeping, attitude control, drag compensation, and orbit adjust. With the utility of micropropulsion established, the ideal architecture for meeting the requirements should be assessed. There are some micropropulsion systems being investigated, such as MicroPPT, colloid microthruster, FEEP, hall microthruster,

cold gas microthruster, and vaporizing microthruster [Mueller 1997, Choueiri 1999, Bayt 1999, Kohler et al 2002]. The solid propellant microthruster is a relatively new class of micropropulsion system. It requires no elaborate system of pumps and valves. Therefore, the total system complexity can be minimized. Integrated with MEMS technology, the solid propellant microthruster has a great potential for application in microspacecraft. Several groups are performing research and development on solid propellant microthrusters [Orieux et al 2002, Rossi et al 2002, Teasdale et al 2001, Lewis et al 2000, Youngner et al 2000, Tanaka et al 2003]. Their main design concepts are the three-layer sandwich configurations, which normally contain three parts consisting of a propellant combustion chamber, a micronozzle (or burst diaphragm), and an igniter. In this chapter, a new solid propellant microthruster design is advanced and a computational fluid dynamics (CFD) based model is proposed to predict the microthruster performance, and establish a benchmark for the optimum design.

2.2 Design of the Solid Propellant Microthruster with Wire Igniter

The new designed solid propellant microthruster configuration has no pumps, fuel lines, and valves. Therefore, there are no moving parts and the leakage possibility of the propellant is low. In the design, a silicon layer is fabricated to contain a combustion chamber, a convergent-divergent nozzle, and an ignition slot. A specific glass layer is diced with the same dimensions as the silicon layer and is bonded together with the silicon layer to form a three-dimensional microthruster. The chamber is then loaded with the solid propellant. Once ignited, the resultant gas expands through the convergent-divergent nozzle as its velocity increases drastically, thus producing the desired thrust and impulse. A special ignition wire is installed in the ignition slot for ignition of the propellant. The schematic view of

a single microthruster is shown in Figure 2.1.

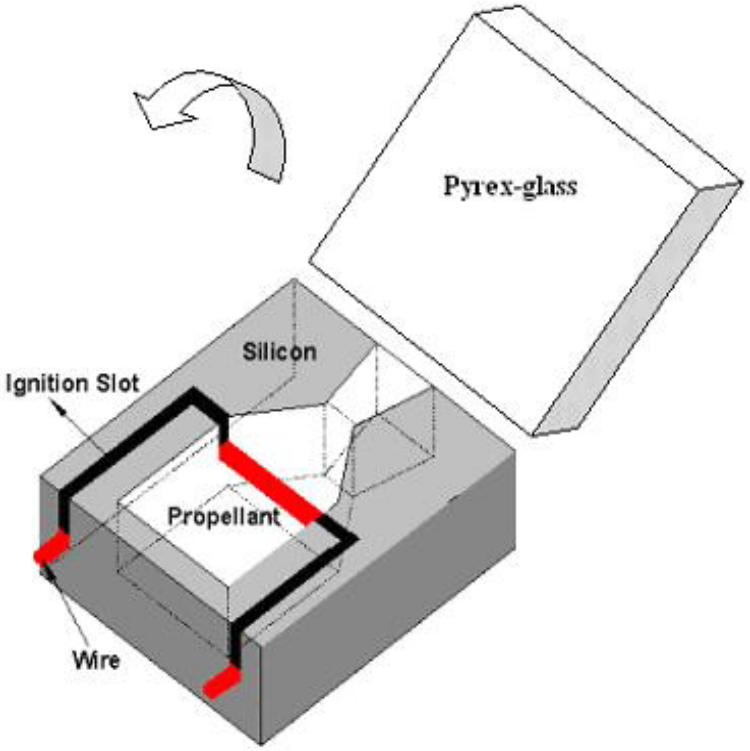

Figure 2.1. Schematic of a single microthruster.

The novel design has some advantages over the former sandwich-based solid propellant microthruster designs. First, the chamber, convergent-divergent nozzle, and ignition slot are fabricated simultaneously. This makes the fabrication process effective and efficient. Second, for the former solid propellant microthruster designs, the chambers are etched vertically from the wafer surface. Therefore, longer chamber length is difficult to fabricate due to the depth limitation of microfabrication technology. Moreover, the nozzle divergence angle, length and throat dimension have a great impact on the performance of the microthruster. It is very difficult for the former designs to fulfill arbitrary nozzle divergence angle, length and throat dimension. Especially, some design employs anisotropic KOH etching to fabricate the nozzle. KOH etches silicon selectively along the $< 100 >$ planes, while almost stopping on the $< 111 >$ planes, resulting in a fixed 35 degree angle between the

nozzle edge and the centerline. However, for the new design, the chamber and convergent-divergent nozzle can be etched horizontally along the wafer surface. Consequently, longer chambers and arbitrary nozzle dimensions can be fabricated according to the applications. Third, anodic bonding is employed here to bond the glass and silicon wafers together, whose bonding quality is better than that of the bonding methods (cyanoacrylate adhesive and thermal epoxy) adopted before. Fourth, for the new design, there are many possible positions for igniters, such as the throat of the nozzle, the front and the back of the combustion chamber. Igniter position will affect the microthruster performance, which will be validated by the experimental measurements in Chapter 3. Propellant sublimation is a concern for the use of the new designed microthruster for deep-space applications since the solid propellant is exposed to space through the open nozzle. However, the propellant exposure to space has been found to have no impact on performance after 10-15 months of in-space storage [Mcgrath 1995].

2.3 Simulation and Modeling of the Thrust and Impulse both at Sea Level and in Space

2.3.1 Foreword

One of challenges in developing the solid propellant microthruster lies in finding the proper modeling approach to understand and describe the propellant combustion and gas expansion processes inside the microthruster and then derive the microthruster performance. Once the microthruster performance is predicted, the optimal design parameters can be determined. Some modeling techniques for microthrusters have been presented before [Mirels 1999, Gatsonis et al 2000, Bayt and Breuer 2001, Rossi et al 2001, Orieux et al 2002]. All the approaches have their own advantages, especially for their specified microthruster designs. However, the convergent-divergent micronozzle jet flow is seldom discussed in de-

tail, which is essential to our novel microthruster. Moreover, the produced impulse and the expected performance in space are sometimes missing, which are usually important to spacecraft designers. Furthermore, some interesting phenomena appearing in microscale devices are sometimes ignored. First, the microcombustion in small volume microthruster is somewhat different from normal combustion in conventional thruster. One key difference is the flame quenching problem. The increased surface area-to-volume ratio that comes with the small size of the microthruster can cause heat loss through the combustor wall to outweigh the heat generated by combustion process. The flame can be extinguished because there is insufficient energy to sustain combustion in the face of heat loss through the microthruster wall. Second, the wall boundary layer growth can impact the subsonic/supersonic flow in the diverging section of the nozzle. Especially for microscale nozzle flow, the rarefaction effects are suspected to play an important role. Therefore, the microthruster performance variation caused by the micronozzle wall boundary layer effects should be evaluated.

In this chapter, a CFD-based model is proposed to simulate the propellant microcombustion inside the chamber, calculate the gas flow characteristics through the convergent-divergent micronozzle, predict the thrust and impulse, and establish a benchmark for the optimum design. The propellant microcombustion, convergent-divergent micronozzle jet flow, heat loss through the wall, slip wall boundary condition, thrust and impulse both at sea level and in space, different propellants and diverse microthruster geometries are all addressed in the model. The CFD modeling results are compared with the one-dimensional thermodynamic modeling results and experimental testing data.

2.3.2 One-dimensional Thermodynamic Computation

Thermodynamic descriptions of the processes inside the microthruster chamber and convergent-divergent nozzle furnish the mathematical tools needed to calculate the

performance and determine the key design parameters of the microthruster system. With proper assumptions and simplifications, the one-dimensional thermodynamic model is adequate for obtaining useful solutions to the microthruster system. The main assumptions and simplifications are as follows: the chemical reaction products are homogeneous, gaseous and obey the perfect gas law; the flow is adiabatic and friction and boundary layer effects are neglected; the flow is steady and there are no shock waves or discontinuities in the nozzle flow; the gas velocity, pressure, temperature, and density are all uniform across any section normal to the nozzle axis. The one-dimensional thermodynamic descriptions are usually used to emphasize the importance of exit-to-throat area ratio and exit-to-chamber pressure ratio in determining some important parameters, such as exit Mach number and thrust.

The exit-to-chamber pressure ratio p_e/p_c is an important parameter to identify the gas expansion through the microthruster nozzle, which can be obtained from Eq. (2.1) developed by the 1-D thermodynamic model [Sutton and Biblarz 2001].

$$\frac{A_t}{A_e} = \left(\frac{\gamma+1}{2}\right)^{\frac{1}{\gamma-1}} \left(\frac{p_e}{p_c}\right)^{\frac{1}{\gamma}} \sqrt{\frac{\gamma+1}{\gamma-1}\left[1-\left(\frac{p_e}{p_c}\right)^{\frac{\gamma-1}{\gamma}}\right]} \tag{2.1}$$

The thrust is a key parameter to describe the propulsion performance, which is calculated by Eq. (2.2) in the 1-D thermodynamic model [Sutton and Biblarz 2001].

$$T = A_t p_c \sqrt{\frac{2\gamma^2}{\gamma-1}\left(\frac{2}{\gamma+1}\right)^{\frac{\gamma+1}{\gamma-1}}\left[1-\left(\frac{p_e}{p_c}\right)^{\frac{\gamma-1}{\gamma}}\right]} + (p_e - p_a)A_e \tag{2.2}$$

The one-dimensional thermodynamic computation is performed using MATLAB 7.0 and the obtained results are compared with those of the following two-dimensional CFD modeling to verify the accuracy and advantages of the two-dimensional CFD modeling.

2.3.3 Two-dimensional CFD Modeling

Propellant Characteristics

Propellant characteristics affect the microthruster performance in terms of thrust and impulse. To achieve the smallest overall structure while preserving relatively

Table 2.1. Characteristics of the solid propellants

Solid propellant	a $(kg^{-n} \cdot m^{n+1} \cdot s^{2n-1})$	n	ρ_p $(kg \cdot m^{-3})$	Combustion temperature (K)
HTPB/AP/AL	6.73×10^{-5}	0.40	1854.6	2000
AN/Polymer	1.51×10^{-6}	0.60	1467.0	900
PU/AP/AL	9.02×10^{-4}	1.05	1771.5	2000
DB	4.00×10^{-5}	0.30	1605.4	1480
DB/AP/AL	5.05×10^{-5}	0.40	1800.0	2250

high specific impulse, the propellant must be selected carefully. Some representative operational solid propellants are chosen for the microthruster modeling. Their characteristics are listed in Table 2.1, (HTPB, hydroxyl-terminated polybutadiene; AP, ammonium perchlorate; AL, aluminum; AN, ammonium perchlorate; PU, polyurethane; DB, double-base) and the γ value of combustion gas for all listed propellants is assumed to be 1.3 (Ref. [Sutton and Biblarz 2001]).

The empirical law or "Saint Robert's" law (2.3) is used to determine the burning rate for the noncorrosive combustion of the propellant [Sutton and Biblarz 2001].

$$r = ap_c^n \tag{2.3}$$

where r is the burning rate that is defined as the spatial rate of change of the burning surface normal to the propellant surface and a (temperature coefficient) is an empirical constant influenced by the initial propellant grain temperature. The rate exponent n, called the combustion index, is independent of the initial propellant grain temperature and describes the effect of chamber pressure on the burning rate.

Microthruster Geometry

The dimensions of the simulated microthruster are shown in Figure 2.2. The thickness of the wafer processed here is 650 μm. The silicon in the defined area of

the wafer is etched away slowly from the wafer surface. Finally, a deep trench is formed in the wafer with the desired top-view shape and desired depth of 350 μm (see Figures. 2.1 and 2.2). The 100-μm plane in the nozzle throat is to avoid sharp edges and facilitate the fabrication. Furthermore, the microthruster has different half divergence angle a, divergence length L, and widths for the combustion chamber W_c, micronozzle throat W_t, and micronozzle exit W_e. Thus different chamber-to-throat (A_c/A_t) and exit-to-throat (A_e/A_t) area ratios are available for evaluation. In the design, the chamber and nozzle are made by deep reactive ion etching (DRIE). Because the DRIE process creates the common etch depth for various features [Menz et al 2001], the chamber and nozzle have the same depth of 350 μm. Consequently, A_c/A_t equals W_c/W_t and A_e/A_t equals W_e/W_t.

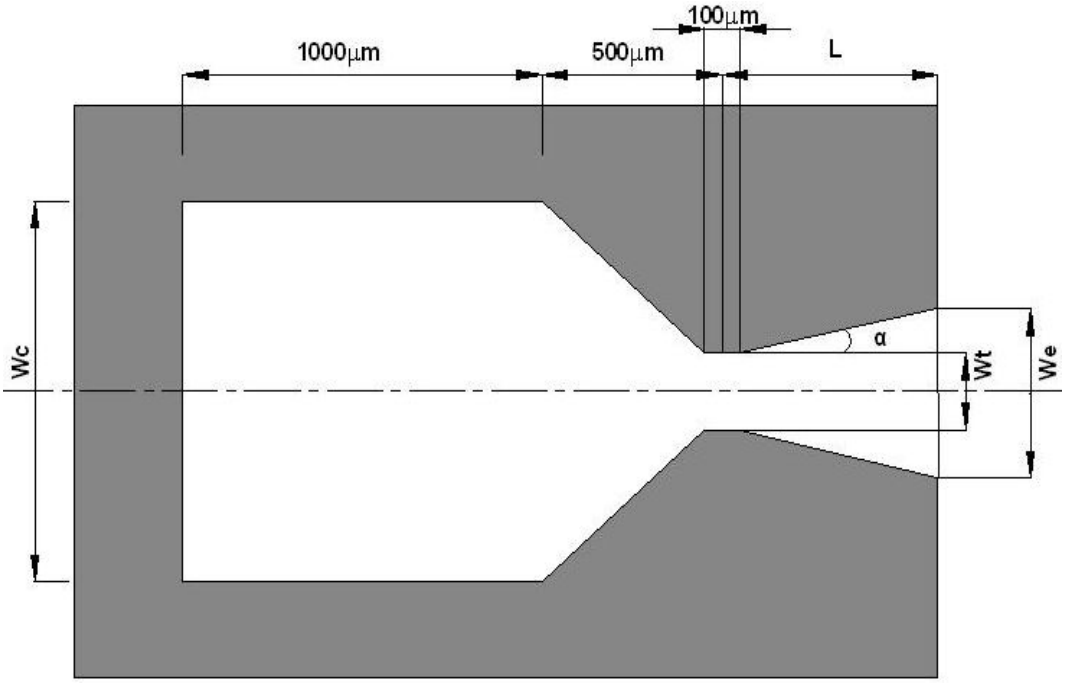

Figure 2.2. Geometry of the solid propellant microthruster with wire igniter.

Governing Equations

The mass conservation equation in Cartesian coordinates can be expressed as

$$\frac{\partial \rho}{\partial t} + \frac{\partial}{\partial x}(\rho u) + \frac{\partial}{\partial y}(\rho v) = S_m \tag{2.4}$$

where the source term S_m denotes the mass added to the control volume.

The momentum conservation equations can be written as

$$\frac{\partial}{\partial t}(\rho u) + \frac{\partial}{\partial x}(\rho u u) + \frac{\partial}{\partial y}(\rho u v) = -\frac{\partial p}{\partial x} + \frac{\partial \tau_{xx}}{\partial x} + \frac{\partial \tau_{yx}}{\partial y} + F_x \tag{2.5}$$

$$\frac{\partial}{\partial t}(\rho v) + \frac{\partial}{\partial x}(\rho v u) + \frac{\partial}{\partial y}(\rho v v) = -\frac{\partial p}{\partial y} + \frac{\partial \tau_{xy}}{\partial x} + \frac{\partial \tau_{yy}}{\partial y} + F_y \tag{2.6}$$

where p is the pressure, τ_{ij} are components of the stress tensor, and F_i are the gravity and body forces in the component directions. The stree tensor τ_{ij} is defined as

$$\tau_{ij} = \left[\mu\left(\frac{\partial u_i}{\partial x_j} + \frac{\partial u_j}{\partial x_i}\right)\right] - \frac{2}{3}\mu\frac{\partial u_l}{\partial x_l}\delta_{ij} \tag{2.7}$$

Finally, the energy conservation equation is written as

$$\frac{\partial}{\partial t}(\rho E) + \frac{\partial}{\partial x_i}\left[u_i(\rho E + p)\right] = \frac{\partial}{\partial x_i}(k\frac{\partial T}{\partial x_i} - \sum_j h_j J_j + u_j \tau_{ij}) + S_h \tag{2.8}$$

where J_j is the diffusion flux of species j and x_i denotes summation over $i = 1, 2$. The source term S_h denotes heat of chemical reaction and any other volumetric heat sources.

Boundary Conditions

The computational domain should extend well beyond the microthruster itself, so that the domain boundary will not influence the problem unrealistically. Figure 2.3 shows the computational domain and the boundary conditions for the microthruster model. The computational domain is 15 times larger than the microthruster itself.

- Inlet Condition

  The combustion of the propellant is combined into the model as the inlet

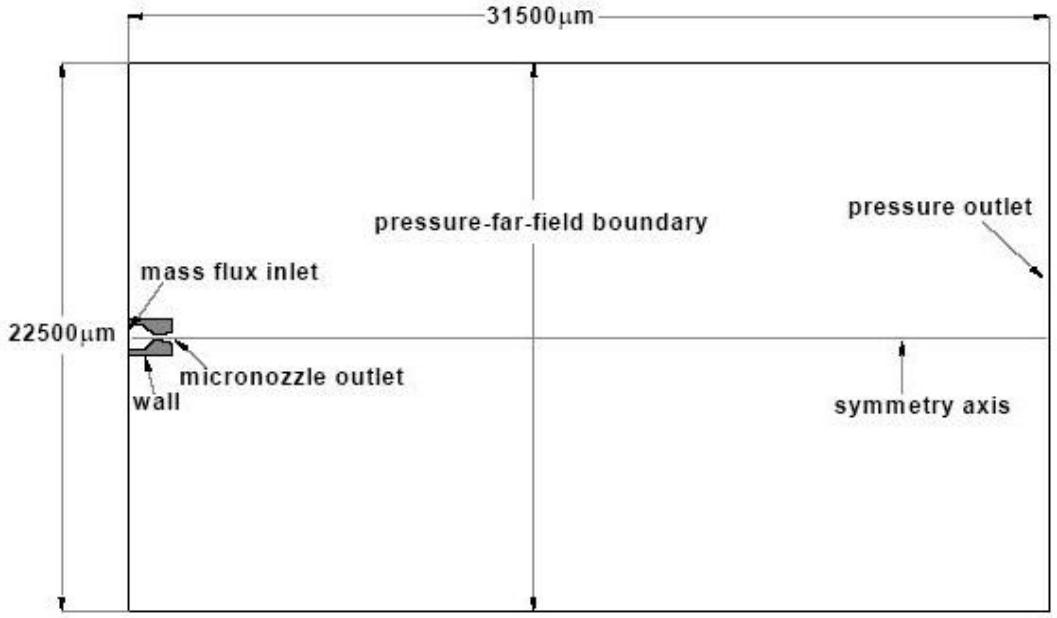

Figure 2.3. Control volume and boundary conditions.

boundary condition. It is assumed that the species created from propellant combustion are all gaseous and homogenous. The chamber temperatures for different propellants in the steady state are shown in Table 2.1. Because the chamber temperatures are high, all the combustion gases are well above their respective saturation conditions and follow the perfect-gas law very closely. The micronozzle entrance (base) consists of the burning solid propellant with a surface burning rate per unit area given by

$$\dot{m}/A_c = \rho_p r = \rho_p a p_c^n \tag{2.9}$$

and,

$$\frac{\partial x}{\partial t} = r = a p_c^n \tag{2.10}$$

where x is the combustion front ordinate.

- Wall Conditions

  The wall is made of silicon. The silicon properties are as follows: thermal conductivity = 141.2 W/mK; density = 2330 kg/m^3; and heat capacity = 700 J/kgK. Heat flux through the wall at the inlet is assumed to be zero. All other walls are set to be two-sided walls, so that fluid regions exist on one

Table 2.2. Air characteristics at different altitudes

Altitude	Temperature (K)	Pressure (atm)	Density (kg/m^3)
sea level	300	1	1.2250
50 km	270.65	7.8735×10^{-4}	1.0269×10^{-3}
100 km	195.08	3.1593×10^{-7}	5.6040×10^{-7}

side and solid regions exist on the other side of these walls. The two-sided walls have coupled thermal and slip boundary conditions.

- Outlet, Far-field, and Initial Conditions

  The outlet, far-field, and initial conditions are as follows: static air; $\mu = 1.7894\, kg/ms$; $k = 0.0242\, W/mK$. The air temperature, pressure, density are different at varied altitudes as shown in Table 2.2 [Sutton and Biblarz 2001]. For reasons described next, most of our simulations are performed for the 50-km condition.

Thrust and Total Impulse Determination

Subsequent to combustion of the propellant, the expansion of the gas through the nozzle produces a thrust T and a total impulse I_t. The expression for thrust T is given as

$$T = \dot{m}c_e + (p_e - p_a)A_e \tag{2.11}$$

The values of c_e and p_e are obtained by averaging the integration of velocity and pressure along the nozzle exit. Total impulse I_t is another key parameter to describe the propulsion performance. I_t is the thrust T integrated over the burn time t.

$$I_t = \int_0^t T dt \tag{2.12}$$

For steady state, thrust T is constant. The burning time is a function of chamber length and burning rate. The chamber length is 1 mm for the designed mi-

crothrusters. The burning rate r is calculated from $r = ap_c^n$, where chamber pressure p_c is obtained from the simulation.

2.3.4 Computation

Across the defined computational domain, the Navier-Stokes (N-S) equations are solved using a finite volume software-FLUENT [Fluent 2003]. For the case of normal shock wave, the pressure, density, and temperature ratios across the shock can be expressed by the following equations:

$$\frac{p_2}{p_1} = 1 + 2\frac{\gamma}{\gamma+1}(M_1^2 - 1) \tag{2.13}$$

$$\frac{\rho_2}{\rho_1} = \frac{(\gamma+1)M_1^2}{2+(\gamma-1)M_1^2} \tag{2.14}$$

$$\frac{T_2}{T_1} = \frac{p_2}{p_1}\frac{\rho_2}{\rho_1} = \frac{[2\gamma M_1^2 - (\gamma-1)][2+(\gamma-1)M_1^2]}{(\gamma+1)^2 M_1^2} \tag{2.15}$$

where the subscripts 1 and 2 denote the positions just in front of and after the shock, respectively.

For the case of oblique shock wave, the pressure, density, and temperature ratios across the shock can be expressed by the following equations:

$$\frac{p_2}{p_1} = 1 + 2\frac{\gamma}{\gamma+1}(M_1^2 sin^2\theta - 1) \tag{2.16}$$

$$\frac{\rho_2}{\rho_1} = \frac{(\gamma+1)M_1^2 sin^2\theta}{2+(\gamma-1)M_1^2 sin^2\theta} \tag{2.17}$$

$$\frac{T_2}{T_1} = \frac{[2\gamma M_1^2 sin^2\theta - (\gamma-1)][2+(\gamma-1)M_1^2 sin^2\theta]}{(\gamma+1)^2 M_1^2 sin^2\theta} \tag{2.18}$$

where θ is the shock wave angle. The FLUENT software would solve the N-S and the shock equations (2.13 to 2.18) in a coupled manner.

FLUENT allows users to apply boundary conditions as user defined functions. Both the inlet boundary and the slip-flow wall boundary conditions are programmed in C language and inserted into FLUENT as user defined functions. The computational grids used for the numerical simulations are determined by performing grid

independent study to minimize the modeling error. When the change in the solution between subsequent stages of grid refinement is considered to be negligible, the lower, but still sufficient, grid resolution is kept. The domain is meshed using 7995 nodes. A high grid density is used near the nozzle walls, throat, and exit to resolve the boundary layers and capture the possible shocks and expansion waves. Figure 2.4 (a) shows the typical computational grid for the domain illustrated in Figure 2.3. The enlarged view of the grid in the nozzle is shown in Figure 2.4 (b).

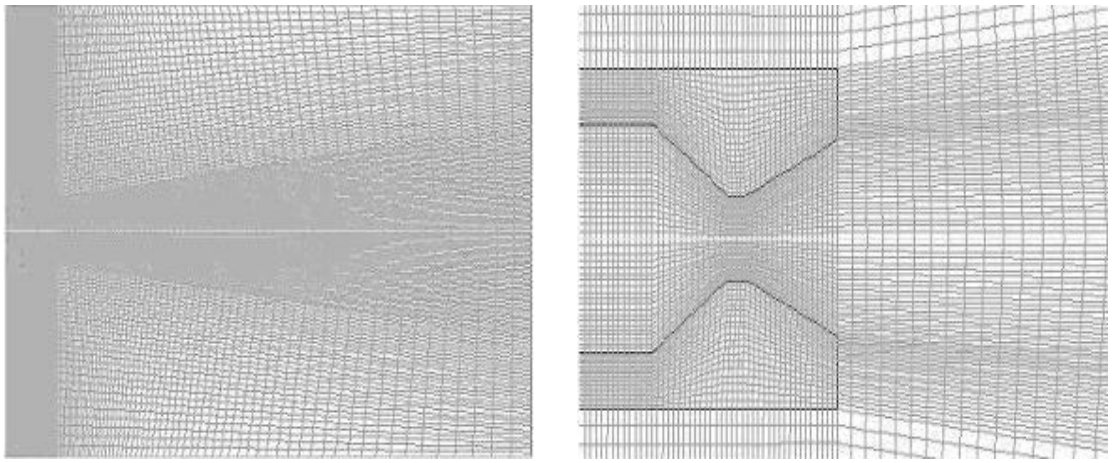

(a) (b)

Figure 2.4. (a) Computational grid of the domain. (b) Enlarged view of the grid in nozzle part.

For the initial simulations, both laminar and turbulent flow modeling are performed for the microthruster. The resulting flow Reynolds number is below 1500. Therefore, the laminar flow modeling is safely employed for the following simulations. A three-dimensional simulation would provide a complete picture of the flow and an accurate performance prediction. However, this will come at a high computational price. A two-dimensional simulation will provide an accurate performance prediction for our cases in which the endwall boundary layers are thin with respect to the trench depth. The endwalls are the upper and bottom walls of the microthruster. The results for steady-state are shown in following sections.

Effect of Propellant Characteristics on Microthruster Performance

Figure 2.5 shows the variation of the thrust in space (50 km) with different propellants for the microthrusters with different A_c/A_t ratios with $W_c = 1000\ \mu m$, a half divergence angle $a = 12$ degree, and a divergence length $L = 600\ \mu m$. The wall heat loss and slip flow are considered in the simulation. It can be clearly seen from Figure 2.5 that the influence of the propellant characteristics on the microthruster performance is of great importance. The performance difference of different propellants is mainly caused by the temperature coefficient, combustion index, and combustion temperature variance. Therefore, the propellant should be selected carefully according to the requirements and applications. HTPB/AP/Al is the most common composite propellant today. It has many advantages, such as widest ambient temperature, good burning rate control, usually stable combustion, good storage stability, good physical properties, and good experience. Therefore, HTPB/AP/Al is selected as the representative for the following simulations.

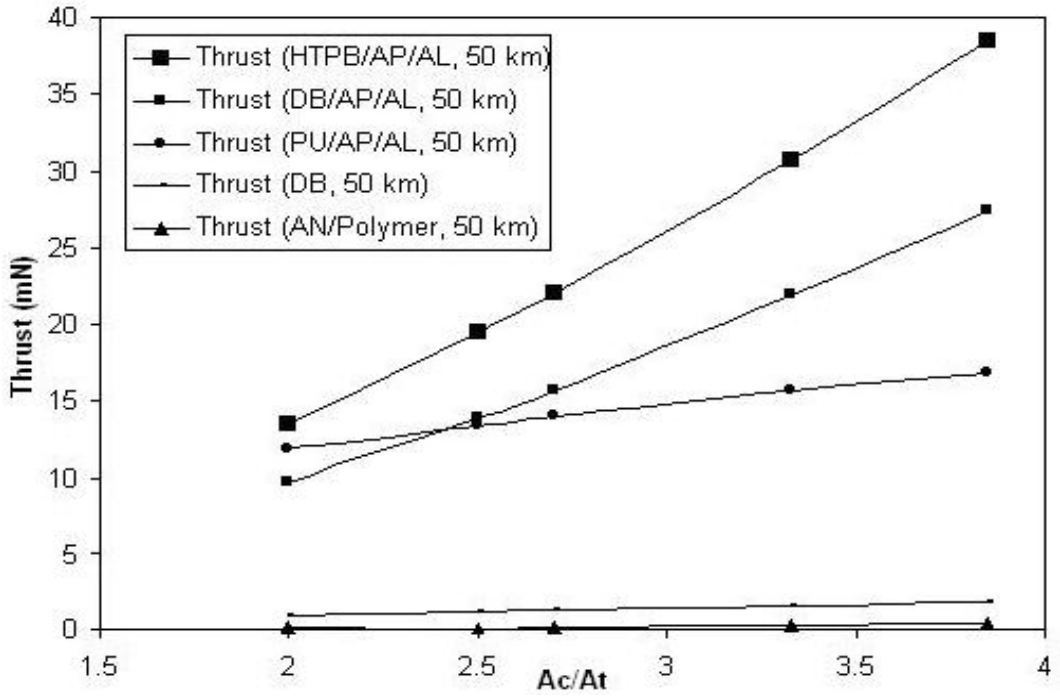

Figure 2.5. Thrust variation with propellants and A_c/A_t ratio.

Effect of the Altitude on Microthruster Performance

Microthruster performance is evaluated at sea level, 50 km, and 100 km. Figure 2.6 shows the thrust and total impulse at different altitudes for microthrusters with different A_c/A_t ratios with $W_c = 1000\ \mu m$, a half divergence angle $a = 12$ degree, and a divergence length $L = 600\ \mu m$. It can be seen that the thrust and total impulse increase with altitude, though the difference between 50 km and 100 km is quite small compared to that with sea level. At sea level, the jet is subsonic, whereas at both 50 km and 100 km it is supersonic and nearly identical. Thus, we can use results from 50 km to simulate microthruster performance in space. This approach facilitates comparison of numerical and experimental results because the pressure at 50 km (80 Pa) is much easier to achieve in the laboratory than the pressure at 100 km (0.032 Pa).

Effect of Wall Heat Loss on Microthruster Performance

Unlike conventional rockets, the increased surface-area-to-volume ratio that comes with the small size of the microscale thruster can cause the heat loss through the plenum wall to outweigh the heat generated by combustion process, thus resulting in flame quenching. Therefore, the viability of the microthruster should be proven with regard to wall heat loss. To characterize the effect of wall heat loss on microthruster performance, the performance for zero thermal resistance wall, silicon wall, and adiabatic wall are compared. Figure 2.7 shows the effect of wall conditions on the thrust and total impulse at sea level for the microthrusters with different A_c/A_t ratios with $W_c = 1000\ \mu m$, a half divergence angle $a = 12$ degree, and a divergence length $L = 600\ \mu m$. It can be seen that the thrust and total impulse for an adiabatic wall are higher than those of zero thermal resistance wall and silicon wall. The reason is that the thermal loss through the wall is neglected if the microthruster wall is assumed to be adiabatic. However, the thrust for zero

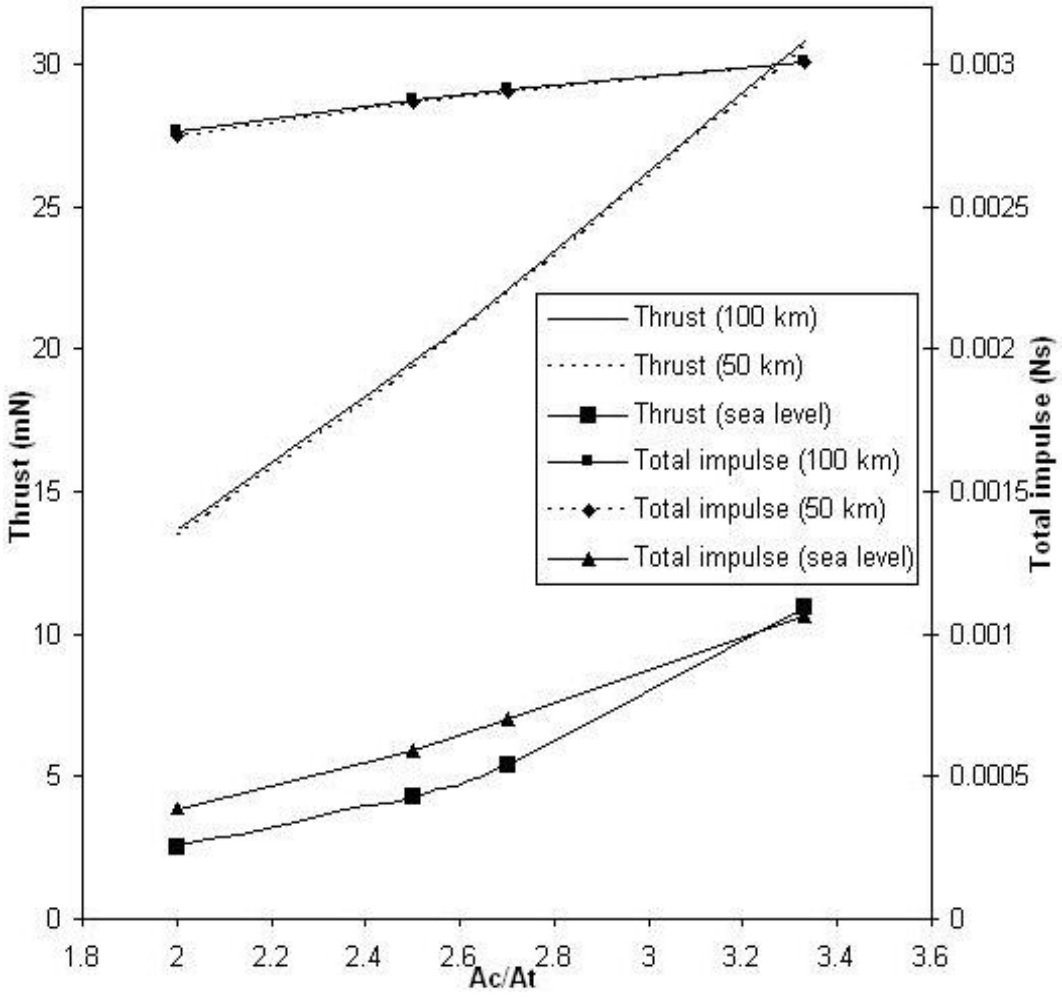

Figure 2.6. Thrust and total impulse variations with altitude and A_c/A_t.

thermal resistance wall and silicon wall are almost the same. This is because of the high thermal conductivity of silicon compared to the combustion gas and ambient air. The performance losses caused by wall heat loss are 7∼9 % and 5∼7 % in terms of thrust and total impulse, respectively. The results agree with the previous research performed by Mirels [Mirels 1999]. In that study, the impulse losses were about 10 % or less for millimeter-scale thrusters that used high flame speed propellants. The microthruster appears to viable with regard to wall heat loss. Nevertheless, the heat loss through the wall should be considered in the simulation for accurate performance prediction.

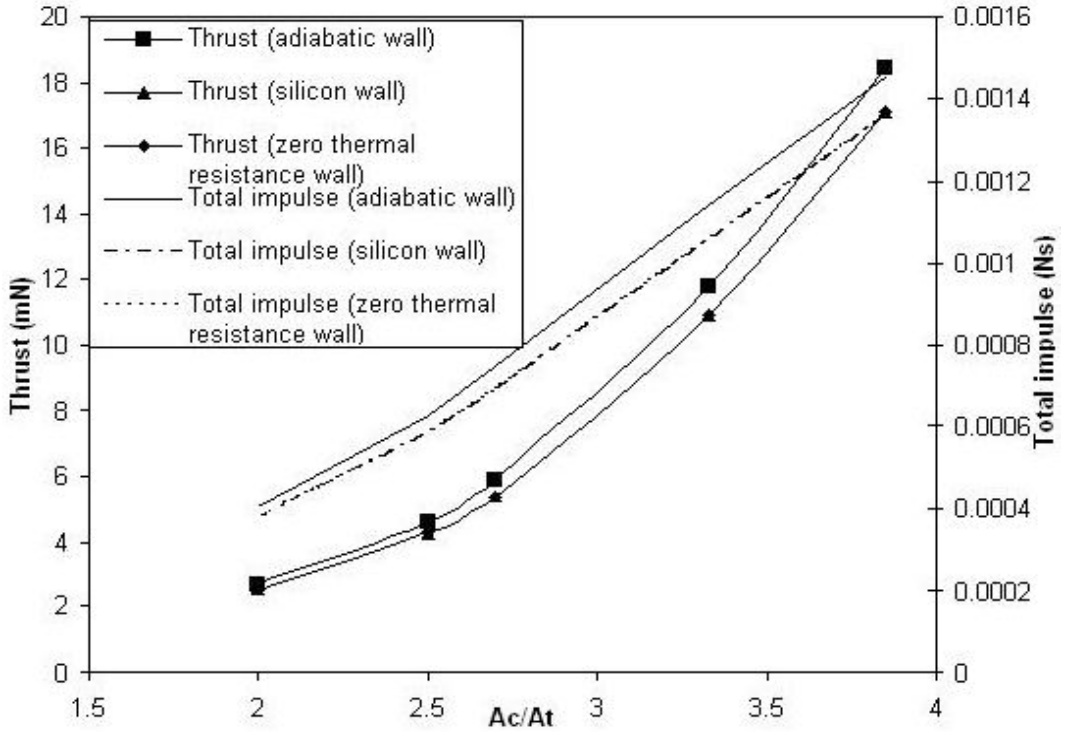

Figure 2.7. Effect of wall heat loss on microthruster performance.

Effect of Slip Wall Boundary Layer on Microthruster Performance

One key difference between gas flow at microscale and in the macrodomain is the rarefaction effect. When the gas rarefaction effect becomes important, the continuum hypothesis in the macrodomain can be unreasonable. Because the fabricated microthruster dimensions are small with a minimum nozzle feature of 100 μm, the gas rarefaction effect for the device should be tested. Knudsen number (Kn), the ratio of mean free path (λ) to a characteristic length scale of the system, is used to describe various flow regimes. Knudsen number can be written in terms of Mach number (the ratio of the gas velocity to the sound speed) and Reynolds number as [Karniadakis and Beskok 2002]

$$Kn = \sqrt{\frac{\pi\gamma}{2}}\frac{Ma}{Re} \tag{2.19}$$

By computing the values of Kn throughout the flow field at the normal wall boundary condition of noslip, it is found that Kn is between 0.001 and 0.1. For example, the throat Kn is 0.0102 to 0.0155 at sea level and 0.0028 in space (50 km) for the

microthruster with $W_c = 1000\ \mu m$, $W_t = 370\ \mu m$, a half divergence angle $a = 12$ degree, and a divergence length $L = 600\ \mu m$. This suggests that the gas flow is in the slip regime. In the slip regime the flow is governed by the N-S equations, and rarefaction effect is modeled through the partial slip at the wall using Maxwell's velocity slip condition. Therefore, the wall velocity, which is previously assumed to be zero in the state vector, can be replaced by the term $[(2 - \delta_v)/(\delta_v)]\, K_n(du/dy)_w$, where δ_v is the accommodation coefficient, defined as the fraction of molecules undergoing diffuse reflection, which is assumed to be 1 due to higher microthruster wall roughness [Karniadakis and Beskok 2002].

To demonstrate and qualify the impact of the slip wall boundary layer on microthruster performance, the simulation is performed for the microthrusters with different divergence lengths with $W_c = 1000\ \mu m$, $W_t = 370\ \mu m$, and a half divergence angle $a = 12$ degree. Figure 2.8 shows the thrust and total impulse differences for nonslip and slip wall conditions in space (50 km). In the former simulations performed by other researchers, the gas rarefaction effect is normally ignored in the divergent part. This assumption is reasonable for short divergence length. However, the rarefaction effect or wall slip velocity must be considered for long divergence length. It can be clearly seen from Figure 2.8 that the differences are small when the divergence length is shorter than 500 μm in our design. When the divergence length is longer than 500 μm, the differences become large and up to 7.2 % and 11.3 % for thrust and total impulse, respectively. Therefore, the wall slip flow cannot be neglected for microscale thrusters. Accordingly, the wall slip flow will be considered in the following simulations.

Effect of Exit-to-Throat Area Ratio on Microthruster Performance

The exit-to-throat area ratio (A_e/A_t) of the nozzle is a major driver of microthruster performance. To illustrate and qualify the impact of A_e/A_t on the thrust and

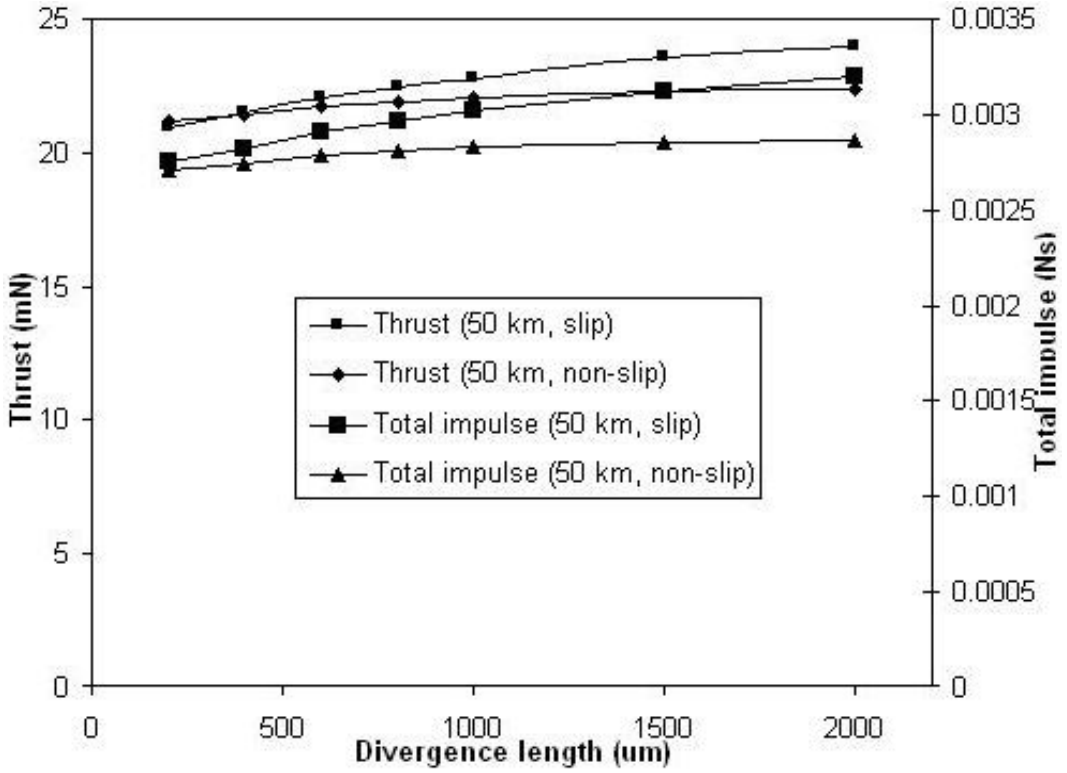

Figure 2.8. Effect of slip wall boundary layer on microthruster performance.

impulse, the gas flow is computed for the microthrusters with different A_e/A_t and $W_c = 1000\ \mu m$, $W_t = 370\ \mu m$, and a divergence length $L = 600\ \mu m$. Figure 2.9 shows the thrust and total impulse variations with A_e/A_t. At sea level, when A_e/A_t increases, the thrust and total impulse decrease slowly and tend to become stable around 2.45 mN and $3.13 \times 10^{-4}\ N \cdot s$, respectively, for $A_e/A_t > 3.0$. All of the designed nozzles are overexpanded because of the higher ambient pressure at sea level. When $A_e/A_t > 1.85$, separation of the flow takes place inside the divergent portion of the nozzle as shown in Figure 2.10 (a). In space (50 km), both the thrust and total impulse increase slightly with the increase of A_e/A_t. When A_e/A_t is too small (for $A_e/A_t < 1.63$ in our design), the nozzle is underexpanded. However, when A_e/A_t is too big (for $A_e/A_t > 2.08$ in our design), the nozzle is overexpanded as shown in Figure 2.10 (b).

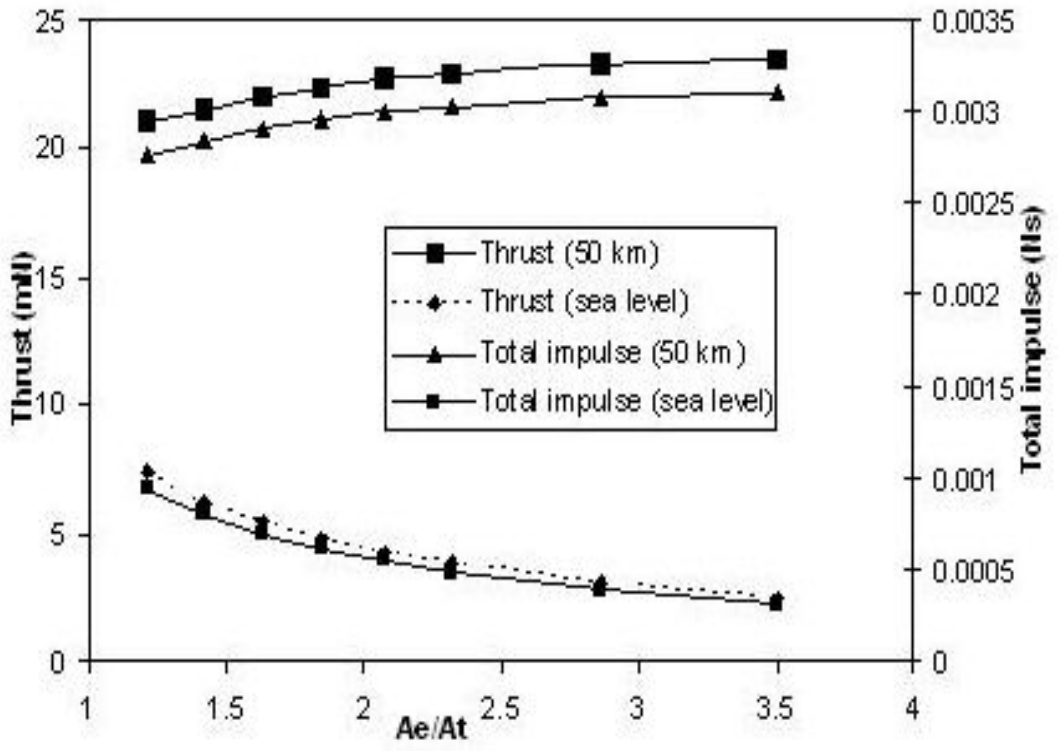

Figure 2.9. Thrust and total impulse variations with A_e/A_t ratio.

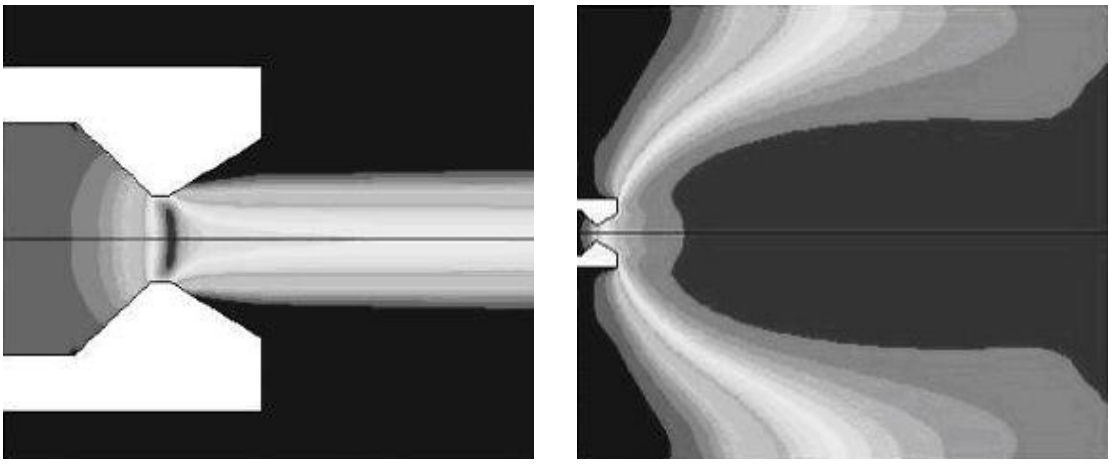

(a) (b)

Figure 2.10. (a) Flow separation at sea level. (b) Overexpanded flow in space.

Effect of Chamber-to-Throat Area Ratio on Microthruster Performance

The "Saint Robert's" law (2.3) expresses the fact that the burning rate is dependent on the propellant composition and the chamber pressure. The chamber pressure, however, is determined by the equilibrium that should exist between the gas generation rate and the nozzle exhaust flow rate. Thus, the stable pressure level that

is achieved is determined by the propellant composition and the ratio between the propellant burning area A_c and the nozzle throat area A_t. Consequently, the A_c/A_t ratio is an important parameter that impacts the microthruster performance.

- Effect of Chamber-to-Throat Area Ratio on Flow Pattern

  Figure 2.11 shows the Mach-number profiles along the axis at different A_c/A_t ratios for the microthrusters with $W_c = 1000\ \mu m$, a half divergence angle $a = 12$ degree, and a divergence length $L = 600\ \mu m$. In the abscissa, 0 corresponds to the position inside the chamber 500 μm away from the end of the chamber; 0.001 corresponds to the center of the nozzle throat plane; and 0.0016 corresponds to the nozzle exit. At sea level, when $A_c/A_t = 2.50$ ($W_t = 400\ \mu m$), the flow through the nozzle is completely subsonic. The flow accelerates out of the chamber through the convergent section, reaching its maximum (subsonic) velocity at the throat. The flow then decelerates through the divergent section and exhausts into the ambient as a subsonic jet. When $A_c/A_t = 2.70$ ($W_t = 370\ \mu m$), the flow pattern is exactly the same as in subsonic flow, except that the flow velocity at the throat has just reached Mach 1. Flow through the nozzle is just choked. When $A_c/A_t = 2.78$ ($W_t = 360\ \mu m$), the Mach number at the throat is still one. But a region of supersonic flow forms just downstream of the throat. Unlike a subsonic flow, the supersonic flow accelerates as the area gets bigger. This region of supersonic acceleration is terminated by a normal shock wave. The shock wave produces a near-instantaneous deceleration of the flow to subsonic velocity. This subsonic flow then decelerates through the remainder of the divergent section and exhausts as a subsonic jet. When $A_c/A_t = 3.33$ ($W_t = 300\ \mu m$) and $A_c/A_t = 3.85$ ($W_t = 260\ \mu m$), the shock bends out into the jet, the jet becomes a supersonic jet. Because the shock is no longer perpendicular to the flow near the nozzle walls, it deflects inward as it leaves the exit producing an initially contracting jet. We refer to this as over-

expanded flow because in this case the pressure at the nozzle exit is lower than that in the ambient. The flow has been expanded by the nozzle too much. In space, the flow patterns for different A_c/A_t ratios are similar. The flow in the chamber and convergent section is subsonic. Then it reaches sonic flow at the throat (Mach number = 1). In the divergent part, the supersonic flow accelerates when the area gets bigger and exhausts as a supersonic jet.

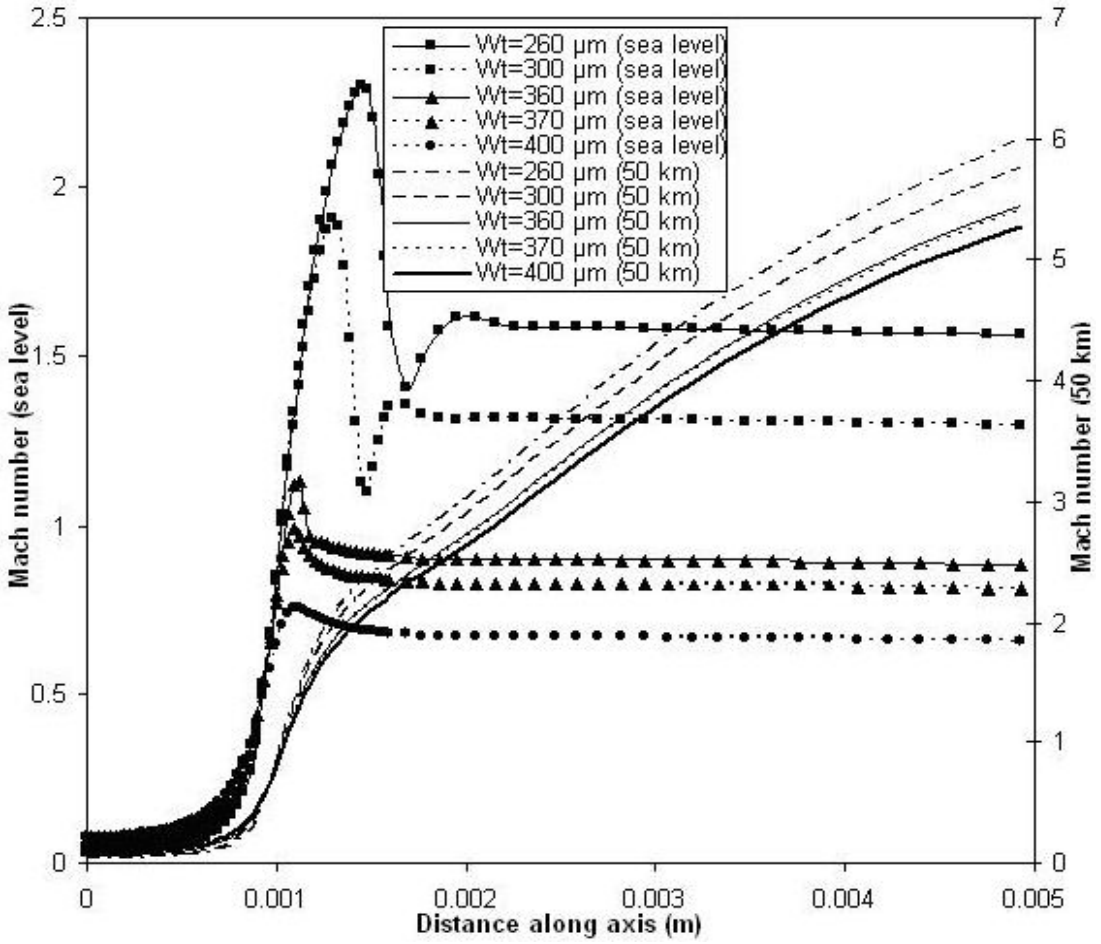

Figure 2.11. Mach number profiles along the axis at different throat widths.

- Effect of Chamber-to-Throat Area Ratio on Thrust and Total Impulse

  By increasing the A_c/A_t ratio, the chamber pressure is greatly increased and the gas can be accelerated to a higher velocity, resulting in a greater thrust level. Figure 2.12 shows the variations of the thrust and total impulse as a

function of A_c/A_t ratio for the microthrusters with $W_c = 1000\ \mu m$, a half divergence angle $a = 12$ degree, and a divergence length $L = 600\ \mu m$. Both at sea level and in space, the thrust increases when the A_c/A_t ratio increases. The total impulse increases with the increase of A_c/A_t ratio when A_c/A_t ratio is lower than five. However, when A_c/A_t ratio is higher than five, the total impulse changes very slowly although A_c/A_t ratio increases from 5 to 10. The reason is that not only the thrust increases but also the chamber pressure increases when the A_c/A_t ratio increases. The chamber pressure increase causes burning rate to rise, thus resulting in the decrease in burn time. Consequently, as the integration of thrust and burning time, the total impulse changes very slowly. One key to designing an efficient subsonic nozzle lies in adjusting the nozzle throat area in order to have a fluid throat velocity close to the sound speed. For the designed microthrusters, this is achieved for $A_c/A_t = 2.70$ at sea level. In space, the jet is uniformly supersonic for the Ac/At ratios in our design.

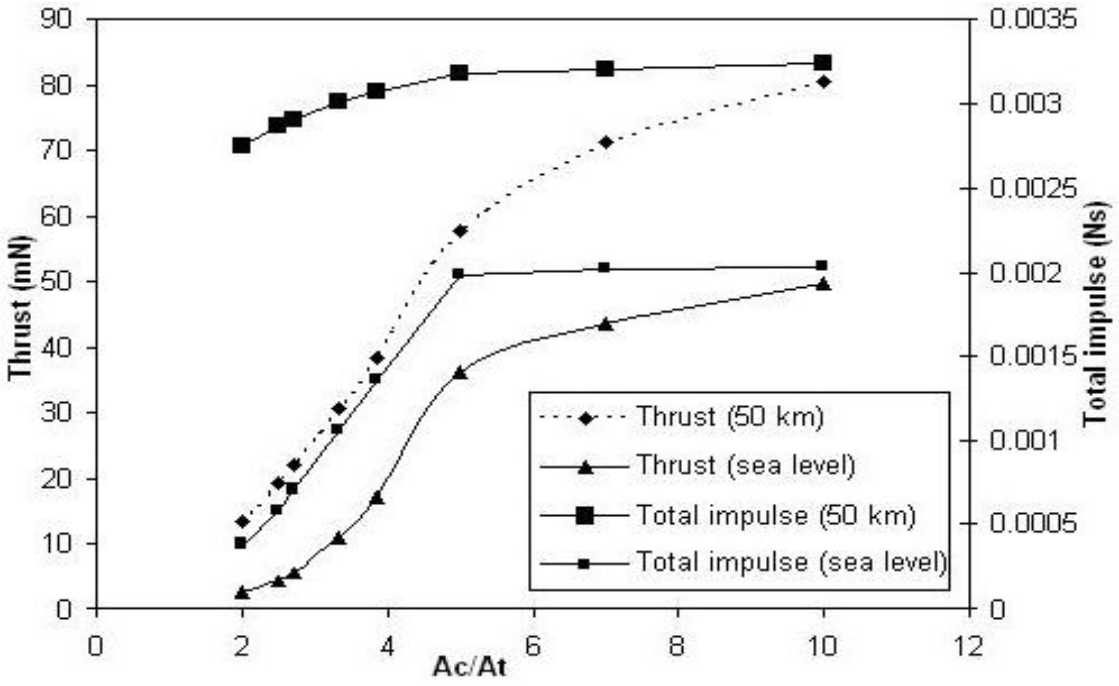

Figure 2.12. Thrust and total impulse variations with A_c/A_t ratio.

2.3.5 Comparison with One-dimensional Thermodynamic Modeling

Figure 2.13 shows the P_e/P_c ratios and thrusts obtained from the one-dimensional thermodynamic modeling and two-dimensional CFD modeling, respectively. The simulations are performed for the microthrusters with different A_e/A_t with $W_c = 1000\ \mu m$, a half divergence angle $a = 12$ degree, and $W_t = 370\ \mu m$. Both the P_e/P_c ratio and thrust from the one-dimensional modeling are higher than those from the two-dimensional modeling. The differences are mainly caused by some of the assumptions and simplifications of the one-dimensional modeling that are somewhat different from actual situations. First, the heat transfer across the walls is ignored in one-dimensional modeling, whereas the decrement in thrust due to wall heat loss is about 7∼9 % for microthruster according to two-dimensional modeling. Second, the boundary layer effects are neglected in one-dimensional modeling, whereas slip wall boundary layer effect is important for microthruster nozzle flow. It can impact the thrust at about 7.2 % in accordance with the two-dimensional modeling. Third, the possible discontinuity in the nozzle flow is ignored in one-dimensional modeling, whereas the two-dimensional model shows that flow separation or discontinuity does exist in the nozzle flow. The flow separation decreases the microthruster performance because of the overexpanded nozzle flow. Fourth, the gas velocity, pressure, and temperature are all supposed to be uniform across any section normal to the nozzle axis in one-dimensional modeling, which is obviously not suitable for accurate microthruster performance prediction compared to two-dimensional modeling.

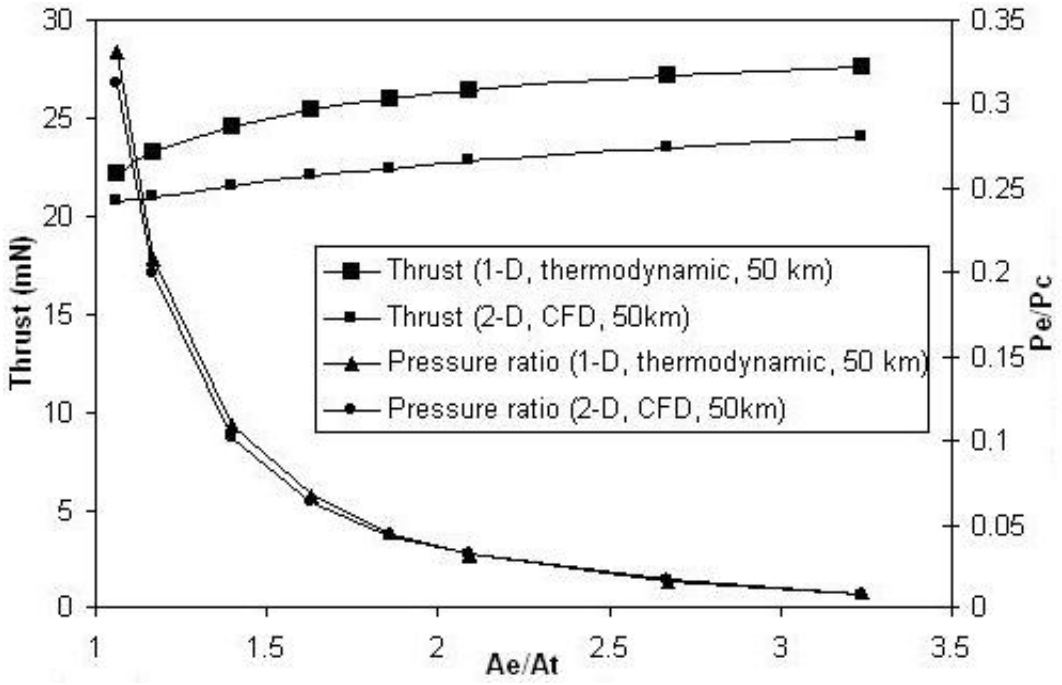

Figure 2.13. P_e/P_c ratio and thrust comparisons.

2.3.6 Chamber Pressure and Thrust Variations with Burning Time

After ignition, the combustion gas flow operates in an unsteady state for short time and then reaches steady state characterized by a steady combustion chamber pressure and a steady thrust level. Figures 2.14 and 2.15 show chamber pressure and thrust variations at sea level, respectively, for the microthrusters with $W_c = 1000\ \mu m$, $a = 12$ degree, $L = 600\ \mu m$, and different throat widths W_t. Ignition of propellant occurs at time t = 0 ms. After ignition, chamber pressure and thrust increase rapidly and reach a static regime at about 45 ms. The slight decrease of chamber pressure and thrust in the static regime is caused by the thermal heat loss through the chamber wall.

Figures 2.16 and 2.17 show the chamber pressure and thrust variations in vacuum, respectively, for the microthrusters with $W_c = 1000\ \mu m$, $a = 12$ degree, $L =$

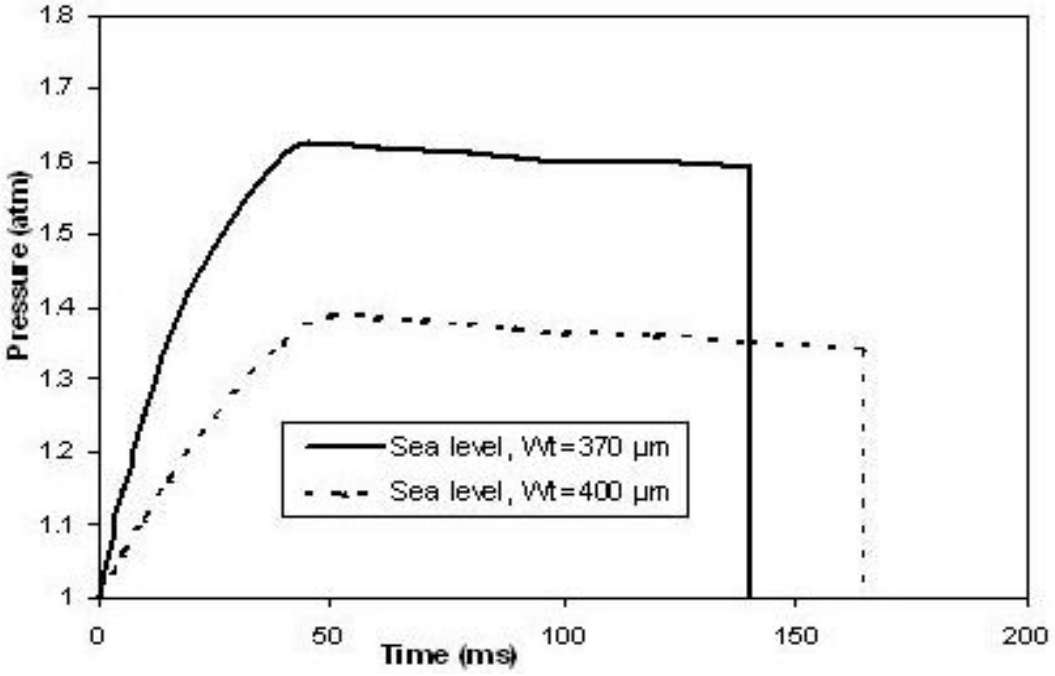

Figure 2.14. Chamber pressure variation with burning time at sea level.

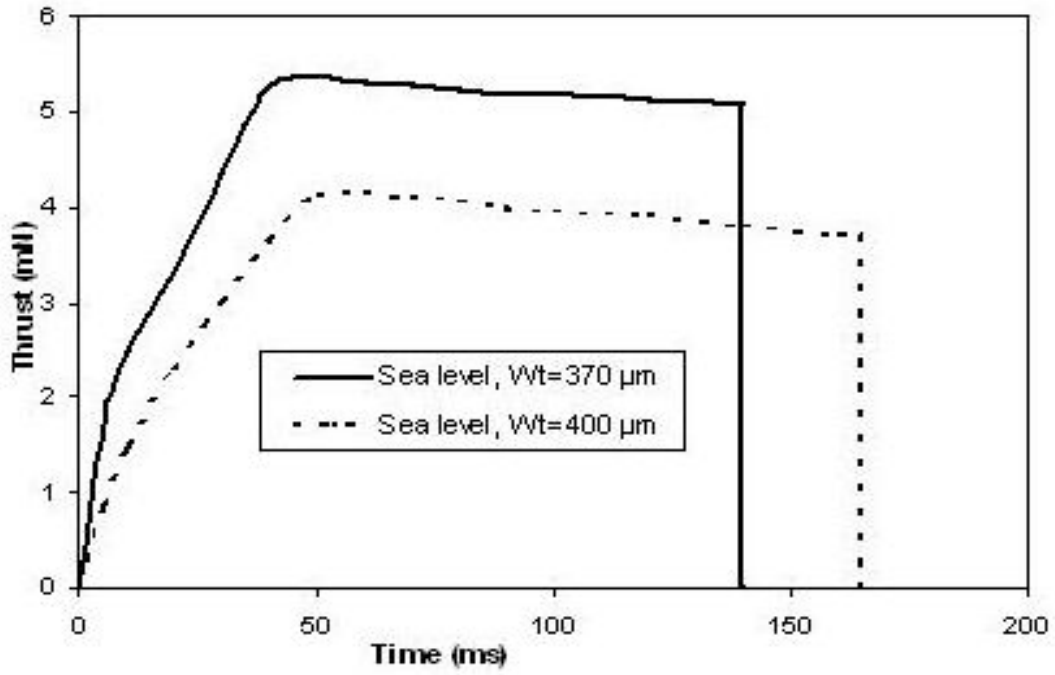

Figure 2.15. Thrust variation with burning time at sea level.

600 μm, and different W_t. The chamber pressure and thrust trends are similar to those at sea level except that they reach static regime at about 70 ms.

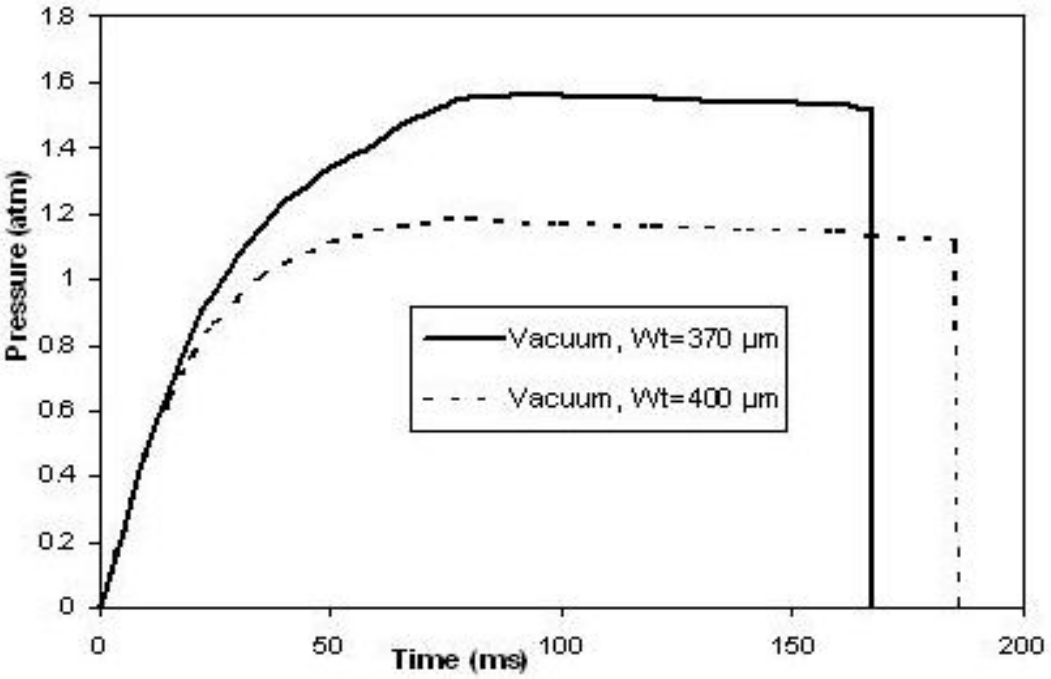

Figure 2.16. Chamber pressure variation with burning time in vacuum.

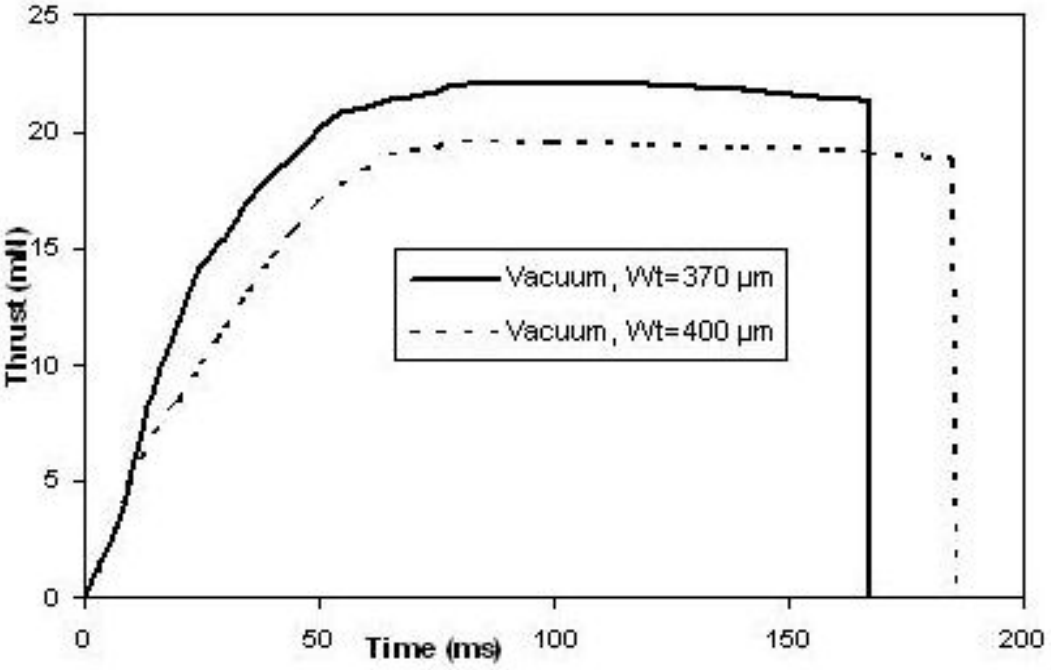

Figure 2.17. Thrust variation with burning time in vacuum.

2.3.7 Comparison with Experimental Testing Results

The comparison between the CFD modeling results and those from experimental testing is detailed in Section 3.5, Chapter 3.

2.4 Chapter Summary

A novel MEMS-based solid propellant microthruster with wire igniter has been discussed in this chapter for meeting the micropropulsion requirements of the microspacecraft. The new design has high fabrication efficiency, much design flexibility, and good bonding quality. Computational-fluid-dynamics (CFD)-based simulation is performed for the solid propellant microthruster. The simulation is carried out to obtain the optimal microthruster configuration and to predict the performance. The convergent-divergent nozzle jet flow is discussed in detail for microscale thruster. The simulation indicates that chamber-to-throat area ratio and exit-to-throat area ratio have great impact on the jet flow patterns. Wall heat loss effect is important for the viability of microthruster. The simulation shows that wall heat loss can change the microthruster performance by 5$\sim$7 % in terms of total impulse. Slip wall boundary layer effect is significant because rarefaction effects play an important role in microthruster. According to the simulation, microthruster total impulse can vary up to 11.3 % as a result of slip wall boundary layer effect. The propellants also have crucial impact on microthruster performance. They must be selected carefully according to the requirements.

The employment of the burning-rate law in the microscale thruster has limitations, and needs to be validated for microthrusters. The combustion gases are assumed to follow the perfect-gas law, which should be studied further owing to the aluminum contained in the propellant. Other assumptions made, for example, the assumption of axisymmetric, steady flow must also be questioned to address the difference among two-dimensional CFD simulation, one-dimensional thermodynamic computation, and experimental testing.

Chapter 3

Fabrication and Testing of the Solid Propellant Microthruster with Wire Igniter

Main Publication:

K. L. Zhang, S. K. Chou, and Simon S. Ang, "MEMS-based Solid Propellant Microthruster Design, Simulation, Fabrication and Testing", IEEE/ASME Journal of Microelectromechanical Systems, Vol. 13, No. 2, pp. 165-175, 2004.

3.1 Introduction

A new solid propellant microthruster with wire igniter has been discussed in Chapter 2 for meeting the micropropulsion requirements of the microspacecraft such as high-accuracy station keeping, attitude control, drag compensation, and orbit adjust. The microthruster has higher fabrication efficiency, much more design flexibility, and better bonding quality over fomer solid propellant microthrusters. CFD-based simulation is also performed for the new designed solid propellant microthruster in Chapter 2. The simulation is carried out to obtain the optimal microthruster configuration and to predict the performance. In this chapter, the

fabrication and assembly of the new designed microthruster are presented; experiments to evaluate the feasibility of the new design and to characterize the characteristics of the microthruster are described; and the comparison between the experimental testing results and those from the CFD modeling is detailed.

3.2 Fabrication of the Solid Propellant Microthruster with Wire Igniter

3.2.1 Two-dimensional Microthruster Fabrication

A double-polished 6-inch (100) oriented silicon wafer is cleaned. A 10-μm-thick positive photoresist is deposited by spin coating at 1000 rpm. Then the photoresist is patterned by exposure to ultraviolet (UV) light through a designed mask. The exposed photoresist is developed. With the pattern transferred through lithography, the deep reactive ion etching (DRIE) is performed on the wafer. The DRIE process is a succession of SF_6 etch cycles and C_4F_8 passivation cycles performed in a STS etcher. When the photoresist is stripped and the wafer is cleaned, a thermal oxidation process is performed. The entire wafer is covered by the silicon dioxide with a thickness of 218 nm after the thermal oxidation. The purpose of the thermal oxidation is to improve the insulation performance of the silicon wafer, which will improve the ignition efficiency by minimizing the current leakage. The resultant silicon trench depth is 350 μm as shown in Figure 3.1(a). It can be seen that the sidewalls are vertical during and after the etching. Lastly, the individual microthrusters are separated using a dicing machine. Figure 3.1 shows the scanned electron micrograph (SEM) of a two-dimensional microthruster.

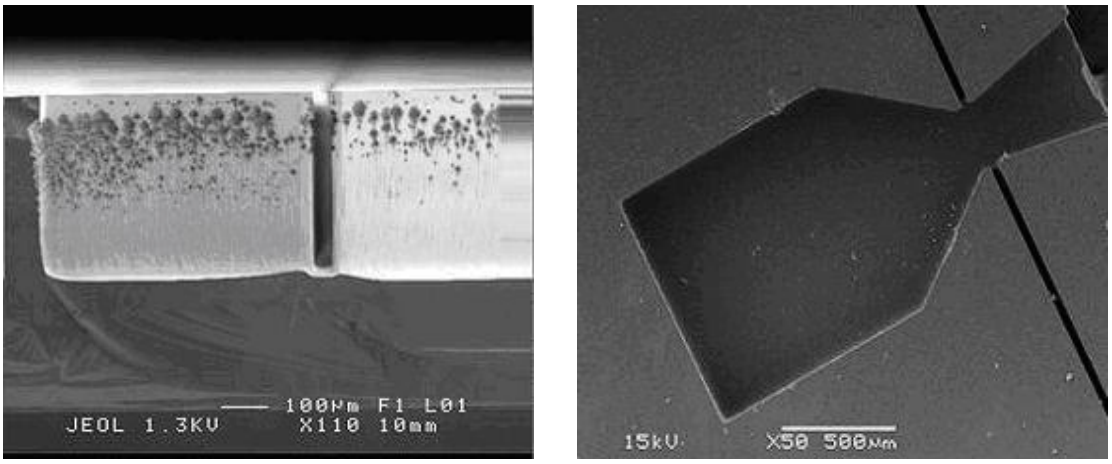

(a) (b)

Figure 3.1. (a) SEM of the cross-section of the microthruster. (b) SEM of the front-side of the microthruster.

3.2.2 Igniter Installation, Propellant Injection, and Three-dimensional Microthruster Formation

The wafer is diced into separate microthruster chips by a dicing machine. A Pyrex-7740 glass is diced with the same dimensions as the microthruster to form the seal. The reasons to employ Pyrex-7740 are as follows: its thermal expansion matches that of silicon; it has well characterized and understood methods of anodic bonding to silicon; and it has high electrical resistivity. A nickel chromium aluminum copper wire with a diameter of 25 μm is employed as the igniter, which is installed in the 30-μm slot of the microthruster under a microscope. In our design, the igniter can be placed in the throat, the middle, or the back of the combustion chamber. The disadvantage of placing the igniter on the back of the chamber is that portion of the propellant will expel before combustion. When the igniter is placed at the throat, the igniter will affect the gas flow in the throat. Therefore the igniter should be placed at the middle of the chamber as a compromise. The optimal position can be evaluated by experiments. The microthruster with the igniter is cleaned using ultrasonic agitation, rinsed in DI water, and blown dry with a nitrogen gas. This is followed by an anodic bonding process at 400 ^{o}C and a voltage of 1100 V. A reliable

bond between the silicon layer and glass layer is then formed although there is a 218 nm silicon dioxide layer between the silicon and the glass. Finally, the solid propellant powder is loaded slowly into the microthruster in order to expel the trapped air inside the chamber. The fabricated three-dimensional microthruster with igniter and solid propellant is shown in Figure 3.2. The main fabrication process is illustrated in Figure 3.3.

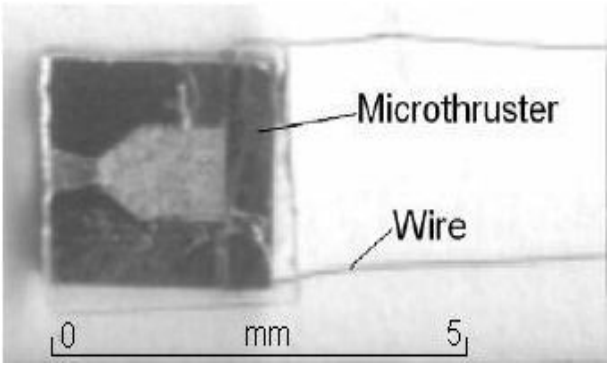

Figure 3.2. Three-dimensional microthruster with igniter and solid propellant.

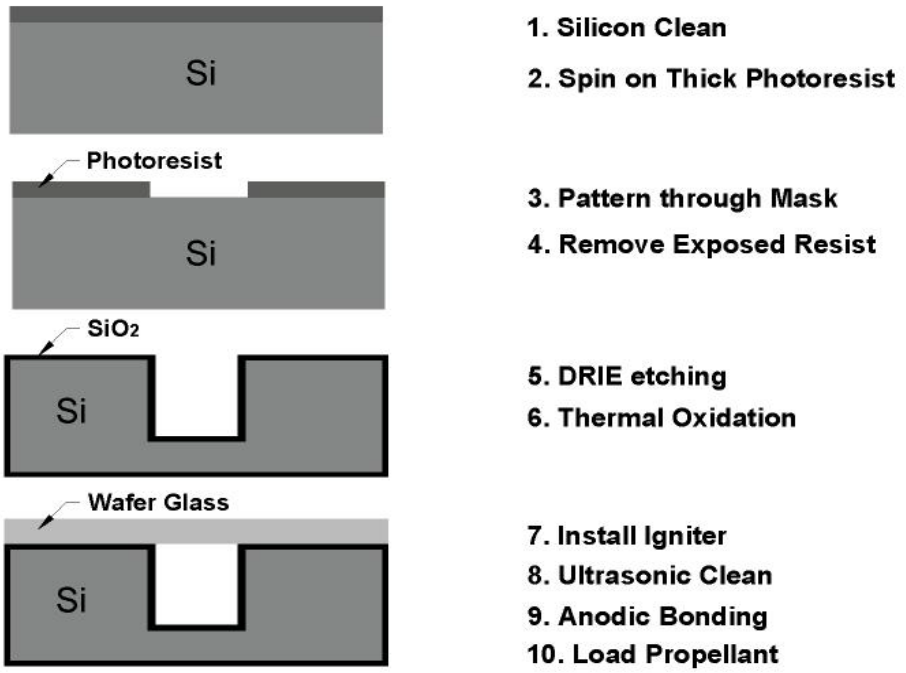

Figure 3.3. Fabrication process flow.

One disadvantage of the solid propellant microthruster is that it is generally not restartable, and therefore, does not allow for orbit trimming. However, the disadvantage can be partially redeemed by microthruster arrays. Even if some of the individual microthrusters fail to work, the array with some redundant microthrusters can still deliver the designed thrust and impulse. Furthermore, the microthrusters in the array can be fired individually, several together, or in controlled sequences, so as to produce controlled, vectored thrust according to the requirements. In the current design, the microthruster array can be fabricated by bonding single microthruster and/or microthruster layer together. The bonding can be realized simply as building blocks for diverse ways to suit the application. One of the fabricated microthruster arrays is shown in Figure 3.4 (a). Adding addressing capability is one key part of developing the microthruster array. A schematic of one way to address and ignite microthrusters individually in the microthruster array to produce the controlled, vectored thrust and impulse is shown in Figure 3.4 (b).

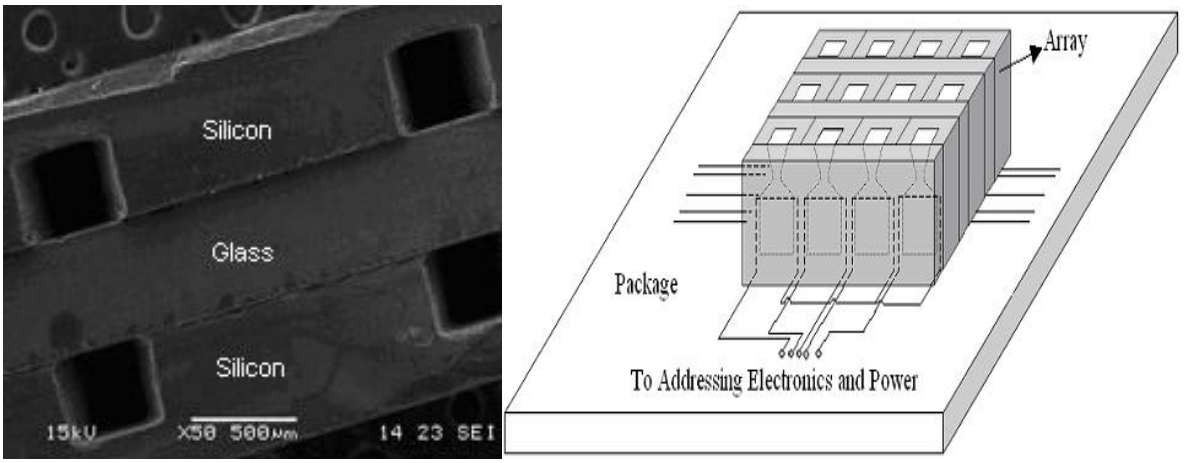

(a) (b)

Figure 3.4. (a) SEM of a microthruster array. (b) Schematic of addressing single microthrusters in an array.

3.3 Experimental Testing with Gunpowder-based Propellant

To document the feasibility of the novel design and obtain the characteristics of the new solid propellant microthruster both at sea level and in vacuum, a specially designed experimental facility is constructed. The setup consists of a high-speed digital video camera to capture the microcombustion of the solid propellant; a piezoelectric force sensor with high sensitivity, a charge amplifier, a data acquisition system, and a digital DC power supply to measure the thrust precisely; and a vacuum system to simulate the microthruster performance in space.

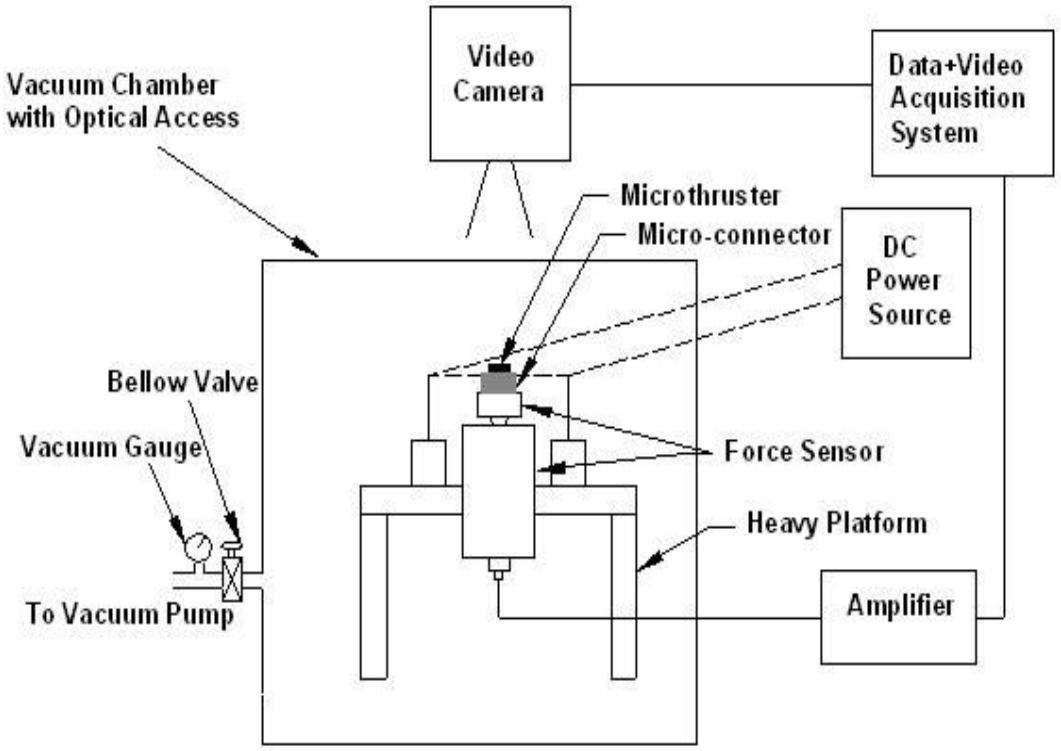

Figure 3.5. Schematic of the measurement setup.

A schematic diagram of the setup is shown in Figure 3.5 (see also Figure 3.6). One key part of the setup is the Kistler quartz force sensor. The sensor is a piezoelectric sensor, which produces an electric charge proportional to the applied force

with the unit [pC]. High sensitivity, high rigidity, and very small transverse sensitivity are outstanding features of this sensor. Moreover, the sensor possesses a highly sensitive, transversal quartz element, which is mounted without preload. Therefore, the sensor is largely insensitive to thermal influences [Kail and Mahr 1999]. This feature of the sensor is very important to the experiment because the microthruster temperature will increase because of the propellant combustion. The force sensor is calibrated with a sensitivity of -118.8 pC/N and a threshold of 0.5 mN.

A charge amplifier is employed to convert the very small electric charge generated by the force sensor into a proportionate voltage, which is connected to the force sensor with a low noise cable and is calibrated using an integral potentiometer. The Dewetron DEWE-ViDEO system is selected as the acquisition system. One interesting feature of the system is that it combines video and data acquisitions in a MIL-STD package with a built-in computer and display, which is very useful for testing the microcombustion and thrust synchronously [Dewe 2002]. The force sensor is installed tightly into a specially designed heavy platform to minimize the possible vibration caused by the thrust, and to allow a convenient power supply. The performance of the microthruster in a vacuum environment is very important because the microspacecraft will operate in space eventually. Therefore, a specially designed vacuum chamber with optical access, a Bellow valve, a vacuum gauge, and a vacuum pump are combined into the testing system to simulate the microthruster performance in space.

3.3.1 Microcombustion Experiment with Gunpowder-based Propellant

Microcombustion experiment is performed to visually validate the feasibility of the novel solid propellant microthruster design with gunpowder-based propellant.

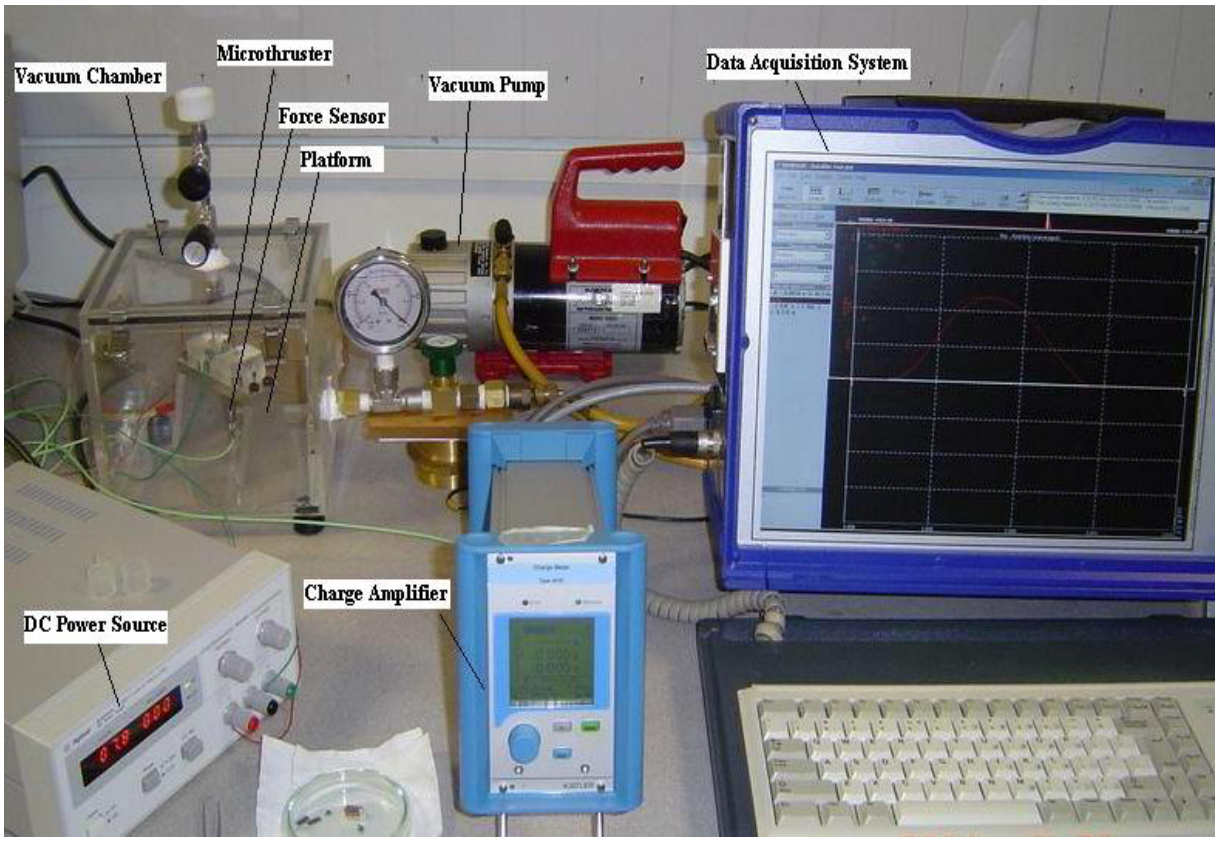

Figure 3.6. Picture of the experimental setup.

The increased surface area-to-volume ratio that comes with the small size of the microthruster may cause chemical and thermal quenching. The quenching may cease the microcombustion [Lee and Kwon 2002], which is needed to be addressed. Continuous combustion is observed successfully after igniting the gunpowder-based solid propellant with the special wire igniter. The combustion lasts for about 0.7 ms for a typical single microthruster. A series of frames from a high-speed digital video camera of the combustion are shown in Figure 3.7. The images are acquired at 30,000 frames/s. The combustion process of the propellant can be visually observed in the novel design because of the transparent property of the Pyrex-7740 glass. It can be seen that the propellant is ignited initially at some point near the igniter. The combustion occurs and propagates to all the surface and then progresses rapidly. The ejected plume from the convergent-divergent nozzle exit can also be visually observed from Figure 3.7.

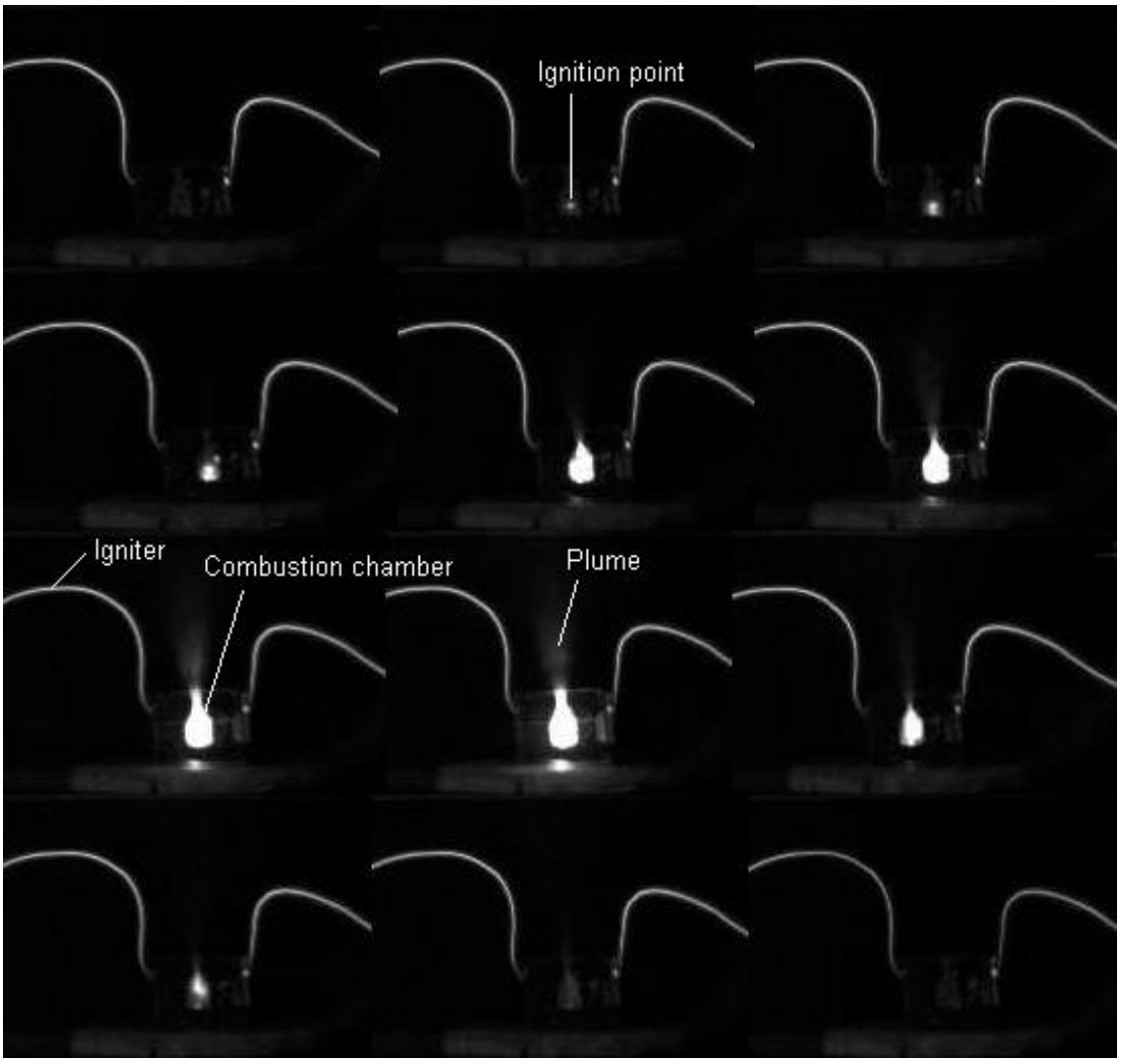

Figure 3.7. Microthruster firing (Images are acquired at 30,000 frames/s).

3.3.2 Thrust and Impulse Testing with Gunpowder-based Propellant

The solid gunpowder-based propellant is the mixture of gunpowder (75 % potassium nitrate, 15 % charcoal, and 10 % sulfur), potassium perchlorate, and the powders of Al and Fe_2O_3. Adding Al is to increase the burning rate, flame temperature, and specific impulse of the propellant. Fe_2O_3 is used as the combustion catalyst. The mass fractions of Al and Fe_2O_3 in the propellant are about 3 % and 1 %, respectively. The loaded solid propellant mass affects the solid propellant mi-

Table 3.1. Masses of the microthruster and gunpowder-based propellant

Single microthruster	Empty vehicle mass (mg)	Loaded mass (mg)	Propellant mass (mg)	Propellant mass fraction (%)
$W_c = 1000\ \mu m$	20.3	21.4	1.1	5.14
$W_c = 1500\ \mu m$	17.5	18.8	1.3	6.91

crothruster performance in terms of specific impulse, which is defined as the ratio of total impulse to propellant weight. Therefore, the propellant mass should be controlled and measured carefully before the ignition. Table 3.1 shows the masses of the microthruster and propellant. The empty vehicle mass is the microthruster mass before loading, the loaded mass is the microthruster mass with the propellant loaded, and the propellant mass fraction is equal to the ratio of the propellant mass to the mass of the loaded microthruster before firing.

All the tests are performed at sea level and the surrounding temperature is approximately 300 K. To more efficiently capture the signals, the dynamic acquisition rate of the acquisition system is set as 100,000 samples per second. Figure 3.8 shows the typical original test signal for the microthruster with $W_c = 1000\ \mu m$, $W_t = 260\ \mu m$, $W_e = 493.81\ \mu m$, and the microthruster chip contains one single microthruster. It can be seen that the combustion and the thrust lasts for about 1 ms and the peak value is about 0.34 N. A vibration wave can be found after the propellant combustion, which is because of the test stage vibration as a result of thrust impact. Although the range of the wave is negligible compared to the thrust, a damping system is recommended to add in the testing system to reduce the vibration and improve the accuracy. Ignition occurs with input voltage of 12 V DC. Although current is not measured directly, the DC power supply current output of 71 mA is observed at the time of ignition. The power supplied during ignition is then estimated to be 0.85 W. Figure 3.9 is an enlarged plot of the com-

bustion region shown in Figure 3.8. It can be seen that the duration of combustion and thrust produced is about 0.73 ms and the peak value of thrust is about 0.34 N. The combustion process and the thrust production process can be found in Figure 3.9. At $t = 0$ ms, the igniter is energized and the combustion of the propellant begins, producing the thrust. The thrust increases rapidly and reaches its peak value at $t = 0.21$ ms. The high value thrust sustains for a short time and reduces gradually. By $t = 0.73$ ms, the combustion is complete, and the impulse of thrust has been delivered. Total impulse I_t is an important parameter to describe the propulsion performance. For this microthruster, $I_t = 1.22 \times 10^{-4}\ N \cdot s$. Because the burning rate of the selected solid propellant is somewhat large, the chemical energy of the propellant is released within a very short time, resulting in a high value thrust. Lewis Jr. et al [Lewis et al 2000] showed some results for their digital microthruster, which have the same magnitude of the total impulse as the author's results, although the design and propellant are different. According to Teasdale's results [Teasdale et al 2001], the thrust of their solid propellant microrocket can last for several seconds, but the magnitude of the thrust is in the range of mN.

An interesting phenomenon, a oscillatory decrease in thrust, can be seen in Figure 3.9. The main cause is the combustion instability of the solid propellant in the microthruster. When instability occurs, the heat transfer to the burning surfaces, the nozzle, and the walls is greatly increased. As a result, the propellant burning rate, chamber pressure, and thrust usually increase. However, the burning duration is normally decreased. Three periods of instability can be seen in the thrust-time history, with enlargements of three sections of the curve. There are many possible causes of this instability, such as a change in pressure due to unburnt propellant flowing through the nozzle and temporarily blocking the nozzle; the dynamic response of the combustion to a flow disturbance (igniter and ignition slot); and the oscillations in the burning rate. The instability is harmful to the microthruster performance and the hardware. Optimization of the microthruster geometry or changing the propellant composition may mitigate this instability.

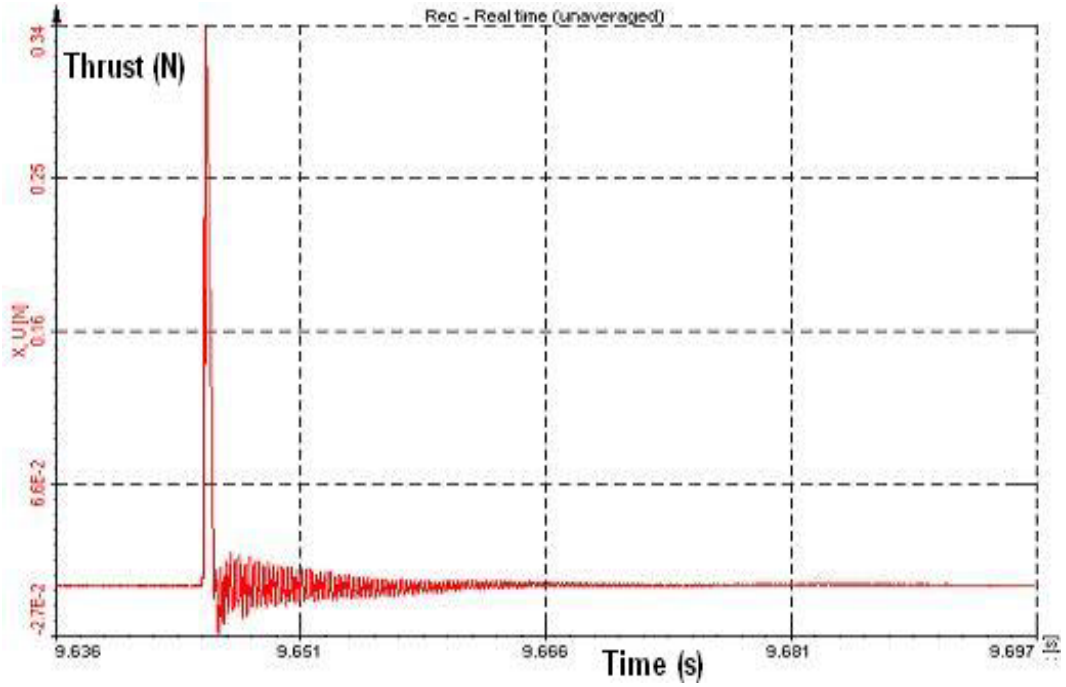

Figure 3.8. Original signal of the microthruster testing.

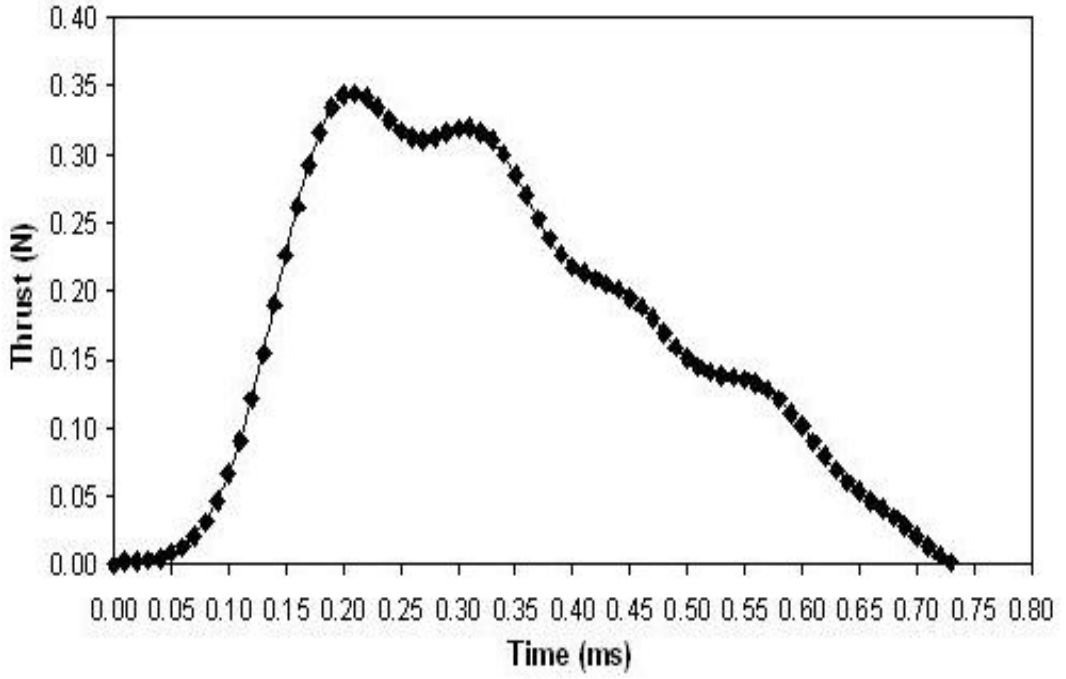

Figure 3.9. Variation of the thrust with the combustion time.

As far as the nozzle design is concerned, the nozzle throat width (W_t) is an important parameter that impacts the thrust and impulse levels while the nozzle throat depth is constant (350 μm). By decreasing the W_t of the throat, the chamber pressure is greatly increased and the gas can be accelerated to a higher velocity, thus resulting in a greater thrust level. Figure 3.10 shows the variation of the thrust as a function of W_t. The four single microthrusters have the similar chamber width of 1000 μm. The results show that the peak thrust and total impulse are multiplied by about 1.98 and 2.04, respectively, when W_t decreases 1.50 times. The nozzle exit-to-throat width ratio (W_e/W_t) plays an important role in the gas expansion process. As a result, it impacts the microthruster performance. It can be seen in Figure 3.10 that when W_e/W_t decreases from 2.17 to 1.78, the peak thrust and total impulse are multiplied by about 0.51 and 0.49, respectively. The ignition powers in Figure 3.10 for W_t = 300 μm, W_t = 280 μm, W_t = 260 μm, and W_t = 200 μm are 0.91 W, 1.03 W, 0.85 W, and 0.95 W, respectively. The difference of ignition power is mainly caused by the nonuniformities of the propellant and the small variation of the contact area between the propellant and the igniter.

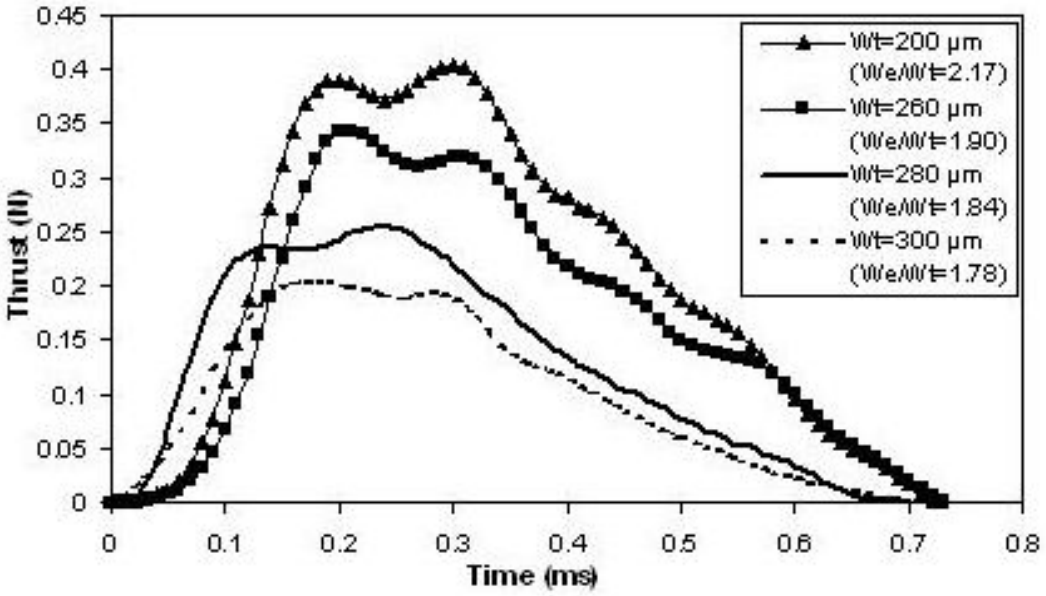

Figure 3.10. Thrust profiles of the microthruster at different nozzle throat widths.

In the author's design, several choices are available to position the igniter. The igniter can be located at the throat of the nozzle (position 1), the front (position 2) or back (position 3) of the combustion chamber as can be seen in Figure 3.11. The disadvantage of placing the igniter on the back of the chamber is that portion of the solid propellant will be expelled before combustion. If the igniter is placed at the throat of the nozzle, the igniter itself will affect the gas flow in the nozzle. Consequently, the igniter is placed at the front of the chamber as a compromise. Figure 3.12 shows the experimental results of the three ignition positions for the microthrusters with the same dimensions ($W_c = 1000\ \mu m$, $W_t = 200\ \mu m$, and $W_e = 493.81\ \mu m$). It can be seen that the combustion duration of position 3 is less than that of position 2 and the combustion duration of position 2 is less than that of position 1. Evidently, this is caused by much propellant ejection before combustion when igniting from the back of the chamber. Only some propellant is ejected before combustion when igniting from the front the chamber. However, there is nearly no propellant ejection while igniting from the nozzle throat. It can be known that the peak thrust and total impulse of position 3 are less than those of position 1 and 2. Although the combustion duration of position 2 (0.71 ms) is less than that of position 1 (0.97 ms), the total impulse of position 2 ($1.52 \times 10^{-4} N \cdot s$) is more than that of position 1 ($1.36 \times 10^{-4} N \cdot s$) due to the higher average thrust produced. It is proven that ignition in the front of the chamber (position 2) is the optimum choice. The ignition powers in Figure 3.12 for position 1, position 2, and position 3 are 1.12 W, 0.86 W, and 0.80 W, respectively. According to the experiments, the success rate of ignition is high (about 90 %) if the igniter is in position 2 or position 3. This is mainly due to the stable contact and large contact area between the propellant and the igniter. However, if the igniter is in position 1, the success rate of ignition is relatively low (about 40 %). This is mainly because of the unstable contact and small contact area between the propellant and the igniter.

Specific impulse, defined as the ratio of total impulse to propellant weight, is another metric for evaluating the microthruster performance. According to the

experiment results, the specific impulse is on the order of 10 s (similar to Teasdale's result: 15 s [Teasdale et al 2001]), which is much less than those of traditional solid rockets. This is mainly caused by the gunpowder's relatively low specific impulse, incomplete combustion of the propellant, and thermal heat loss through the silicon wall.

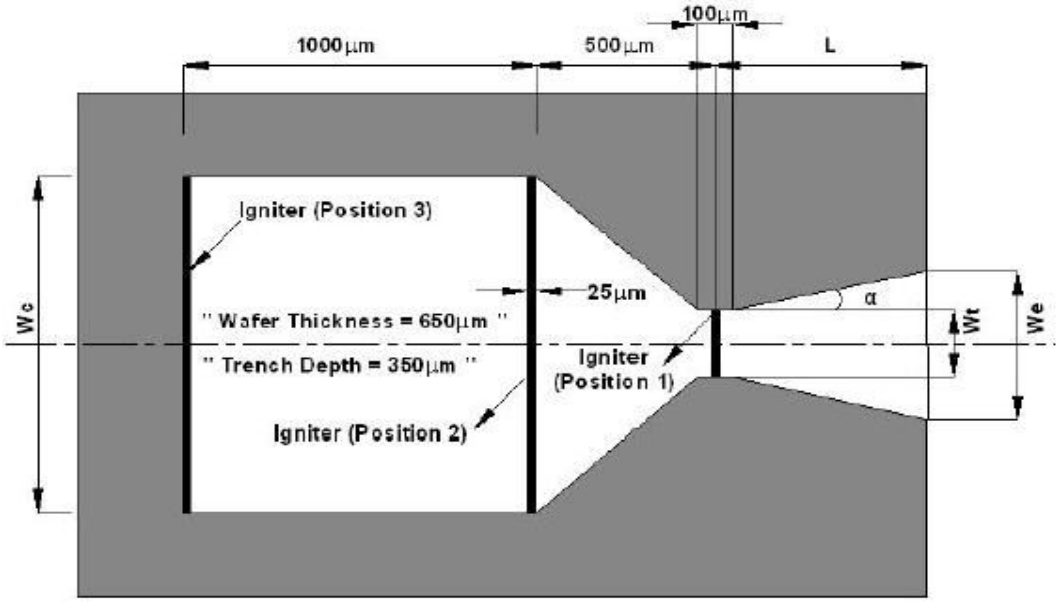

Figure 3.11. Geometry of the solid propellant microthruster with wire igniter.

3.4 Experimental Testing with HTPB/AP/Al-based Propellant

The propellant selection is critical to the microthruster design. To realize the smallest overall structure while preserving design simplicity and relatively good performance, the HTPB/AP/Al-based composite solid propellant is chosen for the microthruster application. Unlike gunpowder-based propellant, the HTPB/AP/Al-based composite propellant does not require high pressure to form the propellant

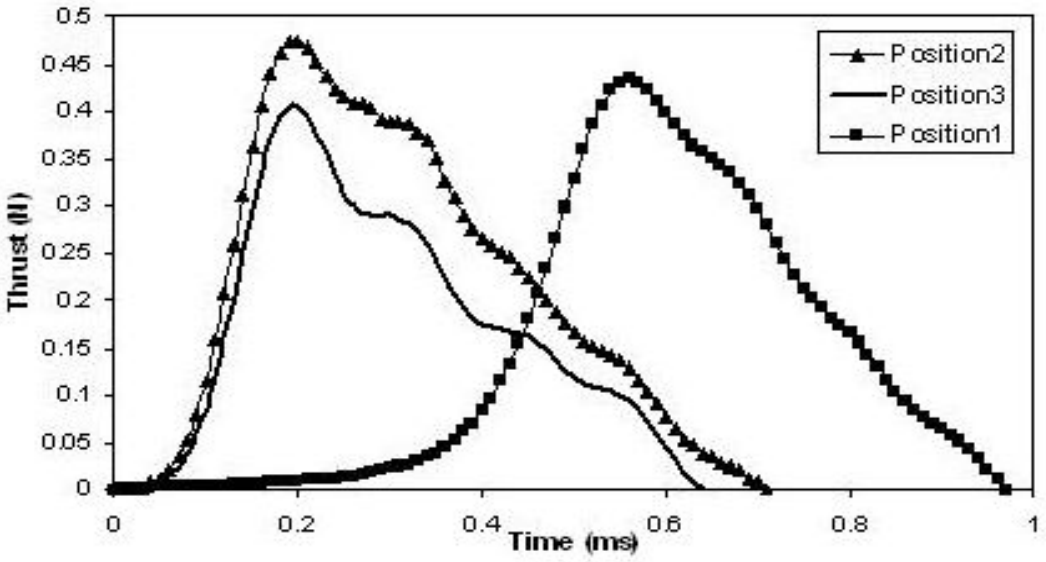

Figure 3.12. Thrust profiles of the microthruster at different ignition positions.

grain. HTPB/AP/Al-based composite propellant has other advantages, such as widest ambient temperature, good burning rate control, usually stable combustion, good physical properties, and good experience [Sutton and Biblarz 2001].

3.4.1 Propellant Formation and Loading

The ingredients of the solid propellant include ammonium perchlorate (AP) oxidizer (mass fraction: 73 %), hydroxyl-terminated polybutadiene (HTPB) binder (14 %), 2-ethylhexyl acrylate (EHA) plasticizer (6 %), isophorone diisocyanate (IPDI) curing agent (3 %), tepanol (TBA) bonding agent (0.8 %), ferric oxide (Fe_2O_3) combustion catalyst (1 %), and aluminum (Al) fuel (2.2 %). These components are processed carefully to form the composite solid propellant according to the Refs [Purrington 1999, McCreary 2000, Sutton and Biblarz 2001]. 50 g propellant is first formulated for experiment. A plastic container is placed on a precision balance with readabilities of 0.0001 g for weighing the mass of the ingredients. First, 7 g HTPB is weighed out and put into a plastic mixing bowl. Then, 3 g EHA and 0.4 g TBA are added into the mixing bowl subsequently. The three ingredients are mixed thoroughly by hand at room temperature. 1.1 g fine mesh Al powder is gently

added into the polymer mix being careful not to cause airborne dust particles. Hand mixing is performed carefully until Al powder is well coated and dispersed in the polymer mix. Adding Al is to increase the specific impulse of the propellant by increasing the combustion temperature. AP (36.5 g) powder and Fe_2O_3 (0.5 g) powder are then added into and mixed thoroughly with the liquids. The AP particle size is selected as 200 μm to achieve slightly lower ignition point, higher combustion rate, more complete combustion, and more suitable application for microthruster. Subsequently, 1.5 g curing agent IPDI is added and the propellant is hand mixed thoroughly. The mixing bowl is then put into a specially designed vacuum chamber with temperature control and optical access to remove the "whipped" gases during mixing cycles and trapped curing gasses. The vacuum degassing time is supposed to be adequate until the bubbles stop rising to the surface of the propellant. This is why the vacuum chamber with optical access is needed. Then, the viscous propellant is put into the vacuum chamber for curing. The curing temperature is 55 ^{o}C and the curing time is 36 hours. The heating stage with temperature control in the vacuum chamber is to provide the temperature required for curing the propellant. The propellant curing system is shown in Figure 3.13.

The propellant before curing is shown in Figure 3.14 (a). It can be seen that the propellant before curing has a viscosity between molasses and play-dough. The propellant in the vacuum chamber for degassing and curing is shown in Figure 3.14 (b). The propellant after curing is shown in Figure 3.15 (a). The viscous propellant premix is cured into hardened rubbery matrix through cure agent by forming longer chains of molecular weight in the polymer and interlocking them between chains. Finally, the elastic propellant is made into tiny configuration as shown in Figure 3.15 (b) and loaded into the microthruster for testing.

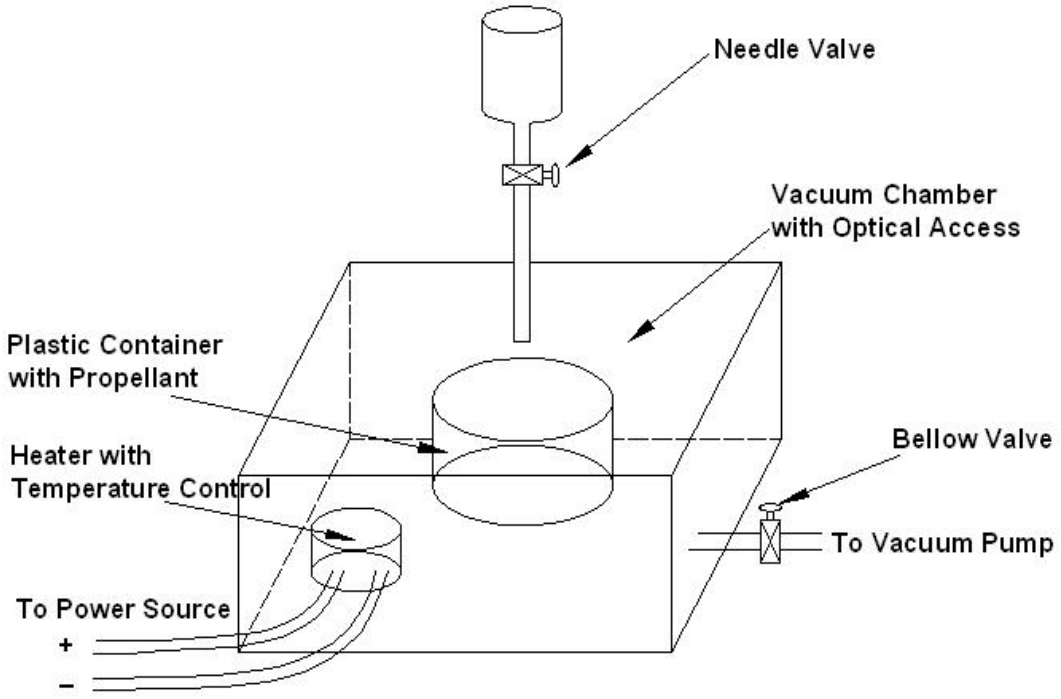

Figure 3.13. Propellant curing system.

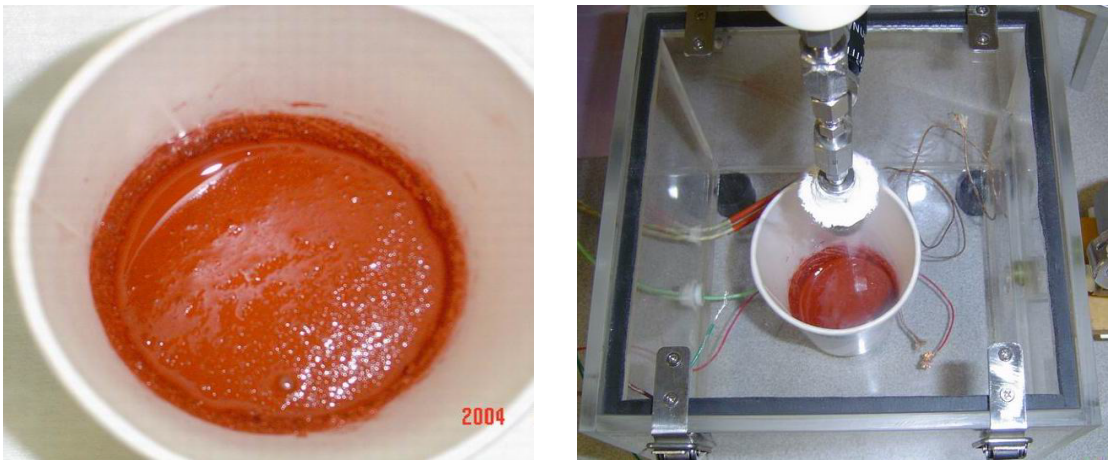

(a) (b)

Figure 3.14. (a) Propellant before curing. (b) Propellant in vacuum chamber for degassing and curing.

3.4.2 Microcombustion Experiment with HTPB/AP/Al-based propellant

Continuous combustion is observed after igniting the solid propellant using the igniter for the microthruster with $W_c = 1000\ \mu m$, $W_t = 260\ \mu m$, and a half divergence angle $a = 12$ degree. Successful production of thrust is verified by the

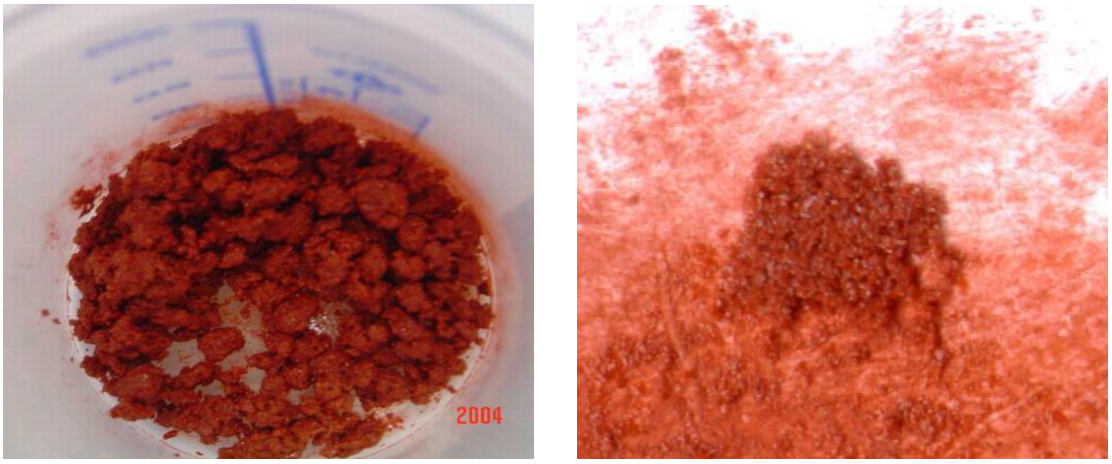

(a) (b)

Figure 3.15. (a) Propellant after curing. (b) Propellant before loading.

microthruster displacement. A series of frames from a high-speed digital video camera of the microthruster experiment are shown in Figure 3.16. The images shown in Figure 3.16 are acquired at 500 frames/s. The ejected plume can be clearly seen from the series of images. The microthruster is placed between a fixed plate and a movable cover to stabilize the microthruster. The schematic diagram of the geometry in Figure 3.16 is shown in Figure 3.17. However, the cover is not heavy enough to prevent the microthruster from rotating caused by the produced thrust. The microthruster rotation is indicated by the variation of ejected plume direction. The thrust production can be proven by the microthruster rotation. Accurate measurement of the produced thrust and impulse will be performed next. The images shown in Figure 3.18 are acquired at 5000 frames/s, and they are taken in a different direction from those shown in Figure 3.16. Two microthrusters are fired. The combustion occurs at different times after ignition.

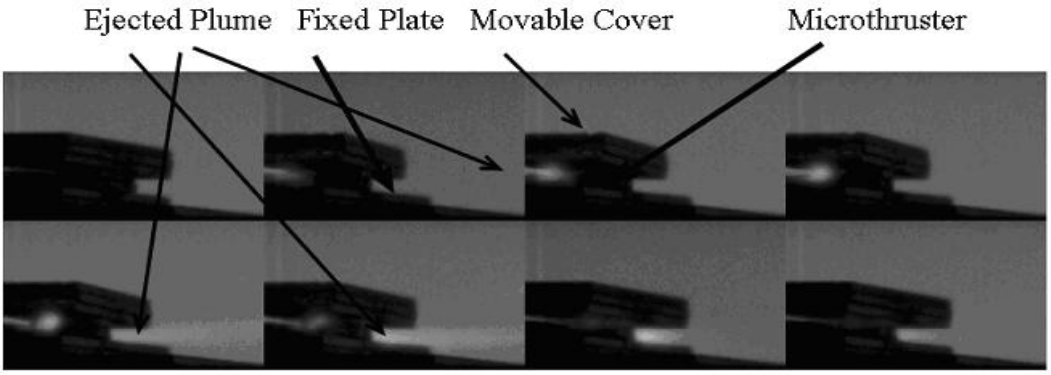

Figure 3.16. Microthruster firing (Images are acquired at 5000 frames/s).

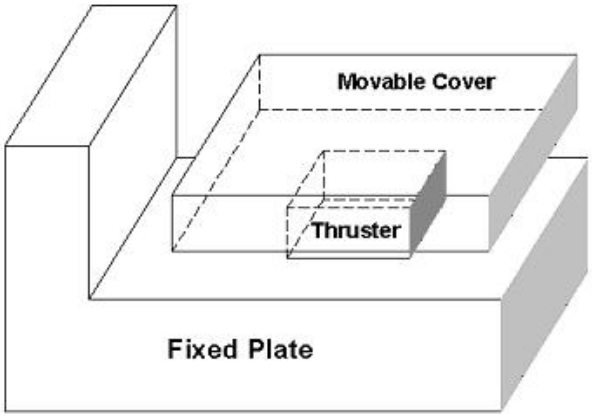

Figure 3.17. Schematic of the geometry in Figure 3.16.

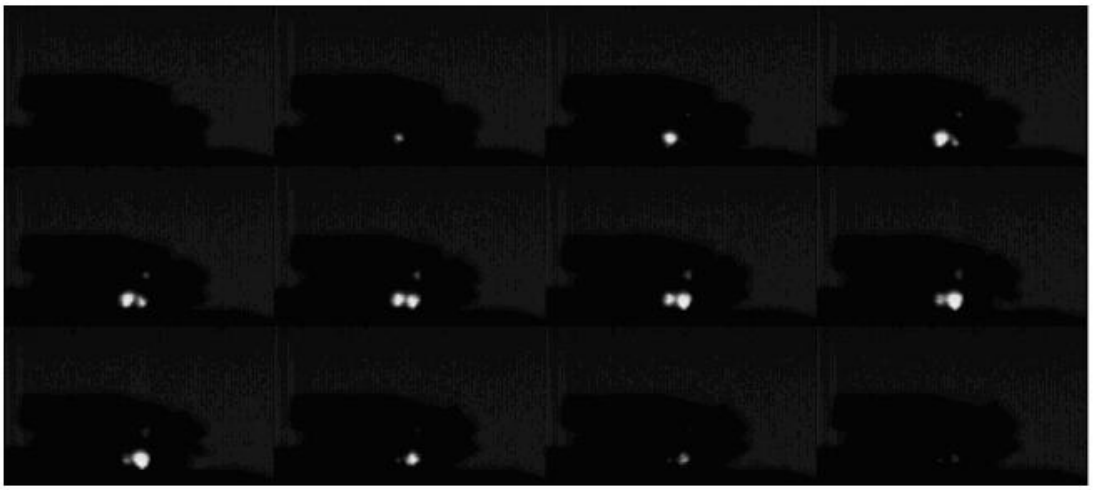

Figure 3.18. Microthruster firing (Images are acquired at 5000 frames/s).

3.4.3 Performance Testing with HTPB/AP/Al-based Propellant

The thrust and impulse measurements are performed both at sea level with the ambient temperature of approximately 300 K and in vacuum with the back pres-

Table 3.2. Masses of the microthruster and HTPB/AP/Al-based propellant

Single microthruster	Empty vehicle mass (mg)	Loaded mass (mg)	Propellant mass (mg)	Propellant mass fraction (%)
$W_c = 1000\ \mu m$	20.3	21.0	0.7	3.33

sure of 80 Pa. The dimensions of the single solid propellant microthruster are shown in Figure 3.11. Table 3.2 shows the masses of the microthruster and the HTPB/AP/Al-based propellant.

Figure 3.19 shows a typical experimental thrust curve using HTPB/AP/Al-based solid propellant. The testing is performed at sea level. In the thrust curve, a small peak is followed by a steady burn, which is commensurate with what might be expected for an end burning geometry [Purrington 1999]. The generated thrust peak value, total impulse, and specific impulse are 5.37 mN, $6.95 \times 10^{-4} N \cdot s$, and 101.21 s, respectively. Although the thrust, total impulse, and specific impulse generated are not high enough for most flight applications on the earth's surface, they may be well-suited to applications for microspacecraft in space. Only small thrust and impulse are needed for station keeping, attitude control, gravitation compensation and orbit adjust of microspacecraft in space due to the tiny air resistance.

Effect of Nozzle Throat Width on Microthruster Performance

As stated before, the nozzle throat width (W_t) is an important parameter that impacts the microthruster performance when the nozzle throat depth is constant. By decreasing W_t, the chamber pressure is greatly increased and the gas can be accelerated to a higher velocity, thus resulting in a greater thrust level and impulse. Figures 3.20 and 3.21 show the variations of the thrust as a function of W_t at

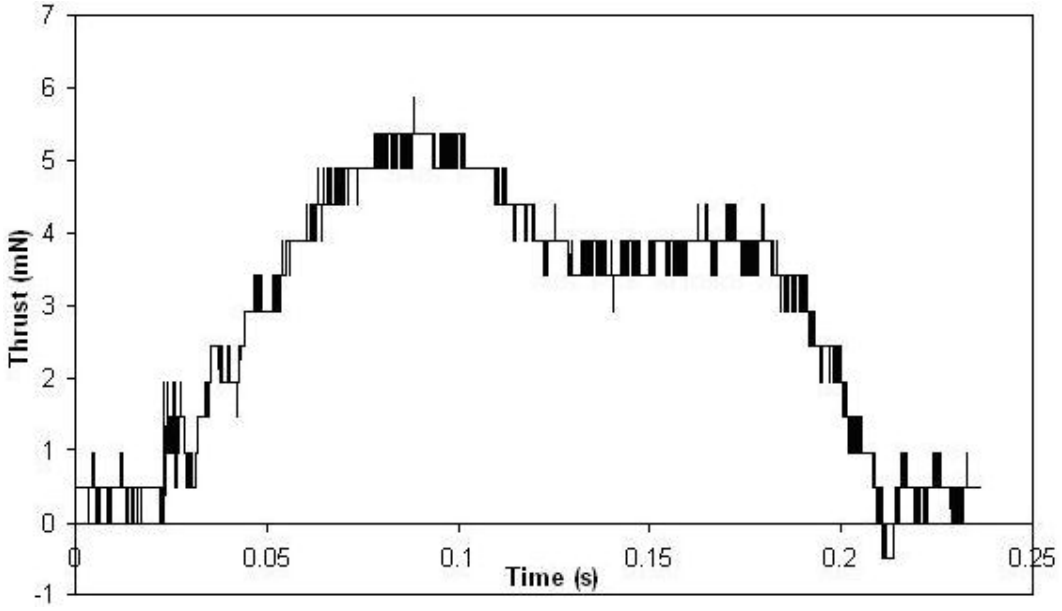

Figure 3.19. Typical microthruster thrust curve from experimental testing.

sea level and in vacuum, respectively. The tested microthrusters have a similar chamber width of 1000 μm, a similar divergence length of 600 μm, and a similar half divergence angle of 12 degree. At sea level, the peak thrust increases from 5.37 mN to 7.81 mN, the total impulse is changed from 6.95×10^{-4} $N\cdot s$ to 8.19×10^{-4} $N\cdot s$, and the specific impulse is increased from 101.21 s to 119.27 s when W_t decreases from 400 μm to 370 μm. In vacuum, the peak thrust increases from 10.75 mN to 23.44 mN, the total impulse changes from 30.91×10^{-4} $N \cdot s$ to 32.50×10^{-4} $N \cdot s$, and the specific impulse is increased from 327.65 s to 448.52 s when W_t varies from 500 μm to 370 μm.

Microthruster Performance Comparison at Sea Level and in Vacuum

The microthruster performance is tested both at sea level and in vacuum (80 Pa). Figure 3.22 shows the performance comparison at sea level and in vacuum for the microthrusters with identical dimensions (divergence length = 600 μm, half divergence angle = 12 degree, chamber width = 1000 μm, and nozzle throat width

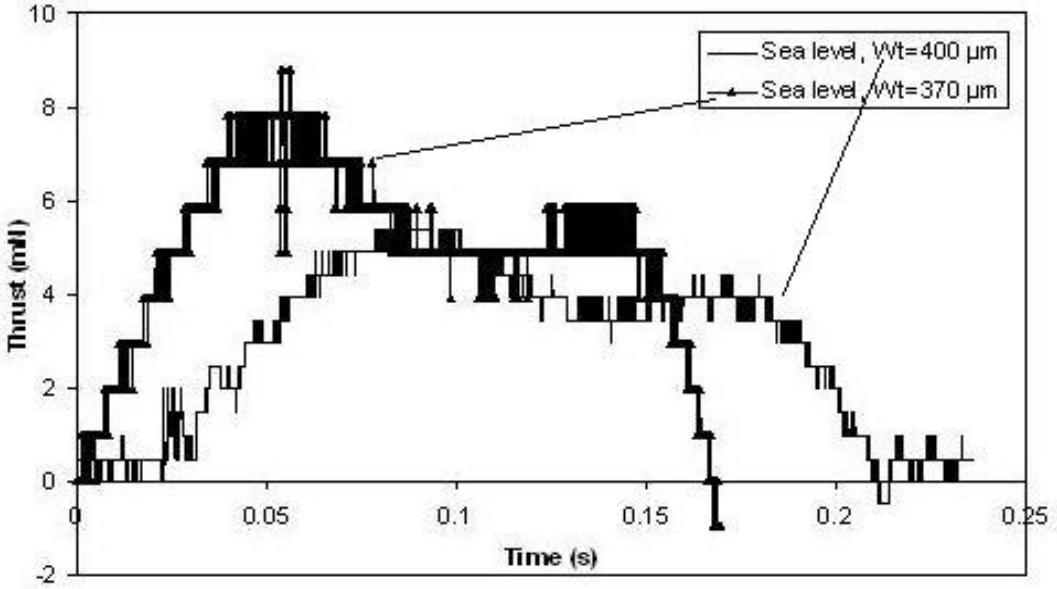

Figure 3.20. Thrust variation with W_t at sea level.

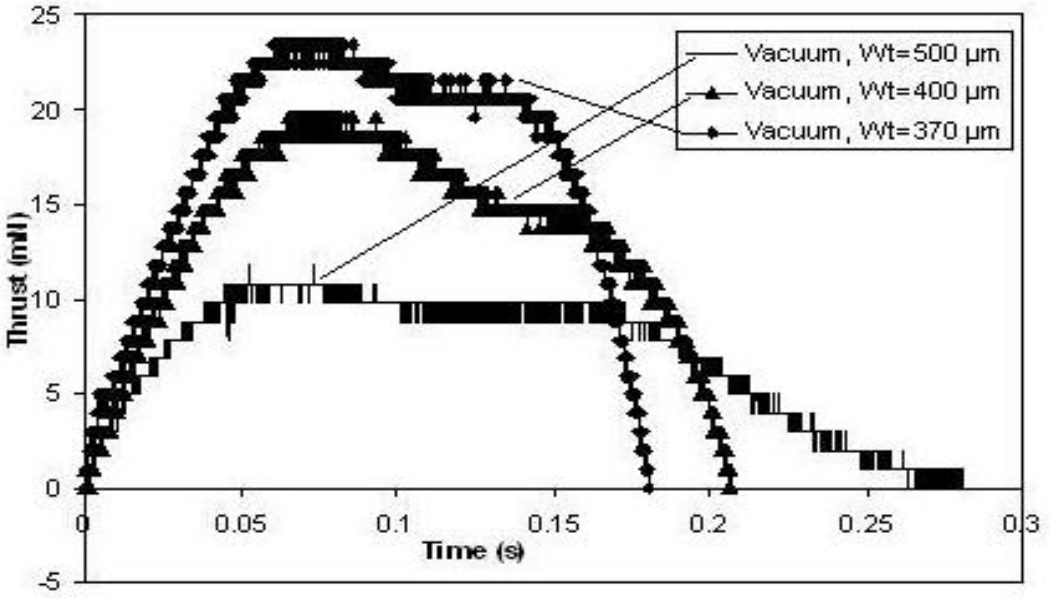

Figure 3.21. Thrust variation with W_t in vacuum.

$= 400\ \mu m$). The thrust peak value is increased from 5.37 mN to 19.54 mN, the total impulse is changed from $6.95 \times 10^{-4}\ N \cdot s$ to $31.59 \times 10^{-4}\ N \cdot s$, and the specific impulse is increased from 101.21 s to 399.01 s when the back pressure is changed from sea level to vacuum. The microthruster performance is greatly improved in vacuum. One cause for the improvement is the increase of the exit-ambient pressure difference in vacuum. The other reason is due to the flow pattern

difference of the microthruster jet. At sea level, the jet flow is subsonic caused by the high back pressure. Whereas in vacuum, the jet flow is supersonic due to the low back pressure. The supersonic jet produces higher thrust and impulse than the subsonic jet.

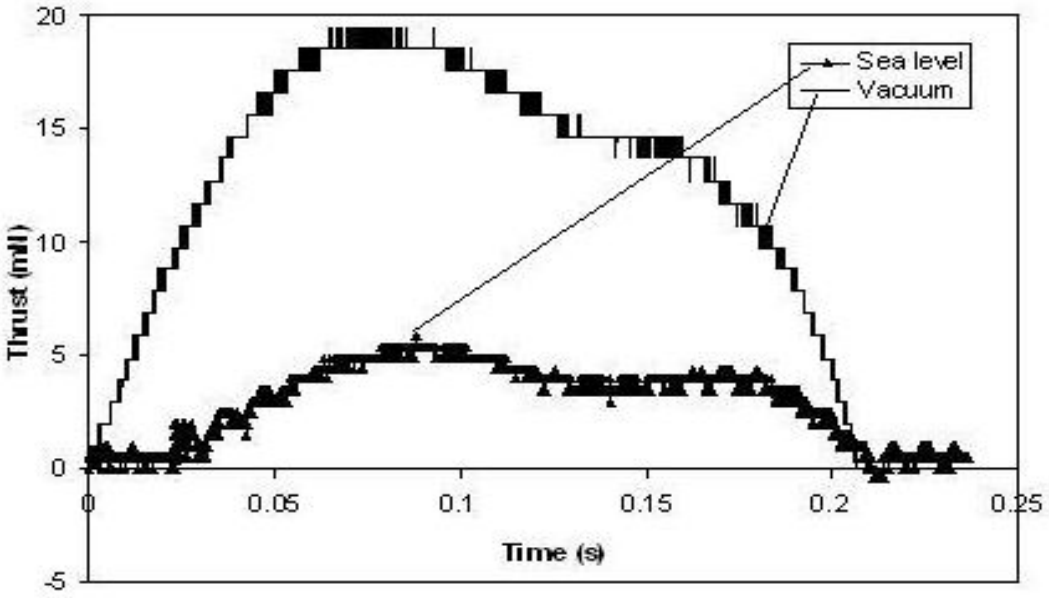

Figure 3.22. Microthruster performance comparison at sea level and in vacuum.

Comparison with "Explosive Propulsion"

Figure 3.23 shows the performance comparison at sea level for the microthrusters with identical dimensions using gunpowder-based and HTPB/AP/Al-based propellants. The thrust curve using HTPB/AP/Al-based propellant is very much different from that of using gunpowder-based propellant. This is mainly caused by the difference of the propellant characteristics. For the gunpowder-based propellant, because the burning rate is very large, the chemical energy is released within a very short time, resulting in a high thrust peak value. This propulsion mechanism may aptly be called "explosive propulsion". Explosively generated thrust can reach over several orders of magnitude greater than the thrust produced by the microthruster using HTPB/AP/Al-based propellant. However, the total impulse

and specific impulse are not necessarily enhanced. For the microthrusters tested in Figure 3.23, the total impulse and specific impulse are $7.21 \times 10^{-5}\ N \cdot s$ and 10.50 s for gunpowder-based propellant, and $8.19 \times 10^{-4}\ N \cdot s$ and 119.27 s for HTPB/AP/Al-based propellant. The main reason is that the high thrust value for gunpowder-based propellant is sustained for only several milliseconds during the "explosion".

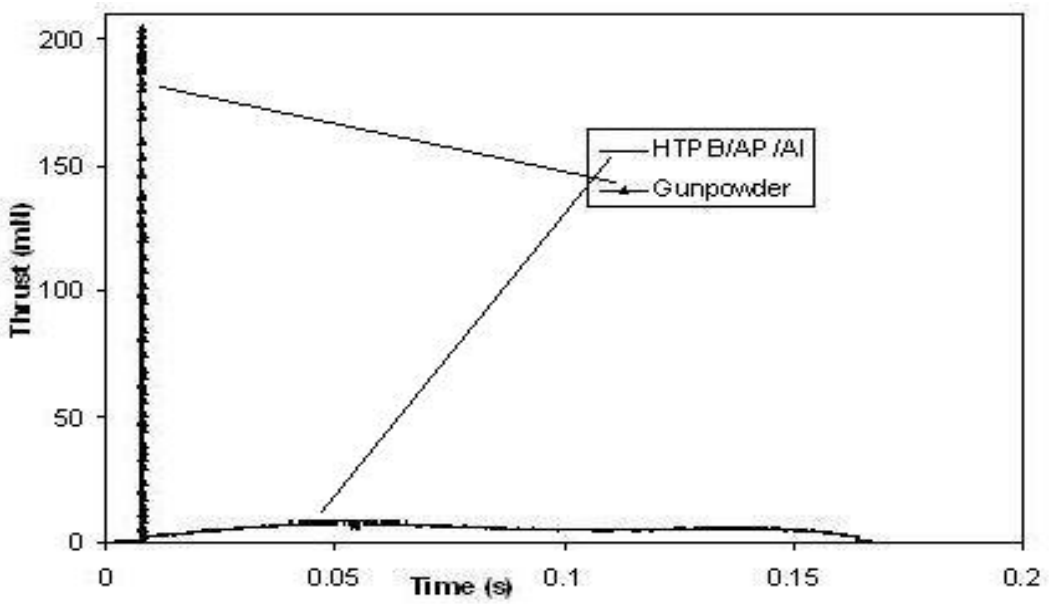

Figure 3.23. Microthruster performance comparison with different propellants.

3.5 Experimental Testing and CFD Modeling Results Comparison

Figures 3.24 and 3.25 show the performance comparison both at sea level and in vacuum between two-dimensional CFD modeling described in Chapter 2 and experimental testing for the microthruster with a chamber width $W_c = 1000\ \mu m$, a throat width $W_t = 370\ \mu m$, a half divergence angle $a = 12$ degree, and a divergence length $L = 600\ \mu m$. Basically, the CFD modeling can simulate the thrust variation

with time. However, the small thrust peak at the early stage of combustion can not be simulated. More improvements are needed in the CFD modeling. One improvement is to include the detailed combustion process of the solid propellant in the model. The other improvement is to carry out three-dimensional modeling instead of the two-dimensional modeling currently employed in this thesis.

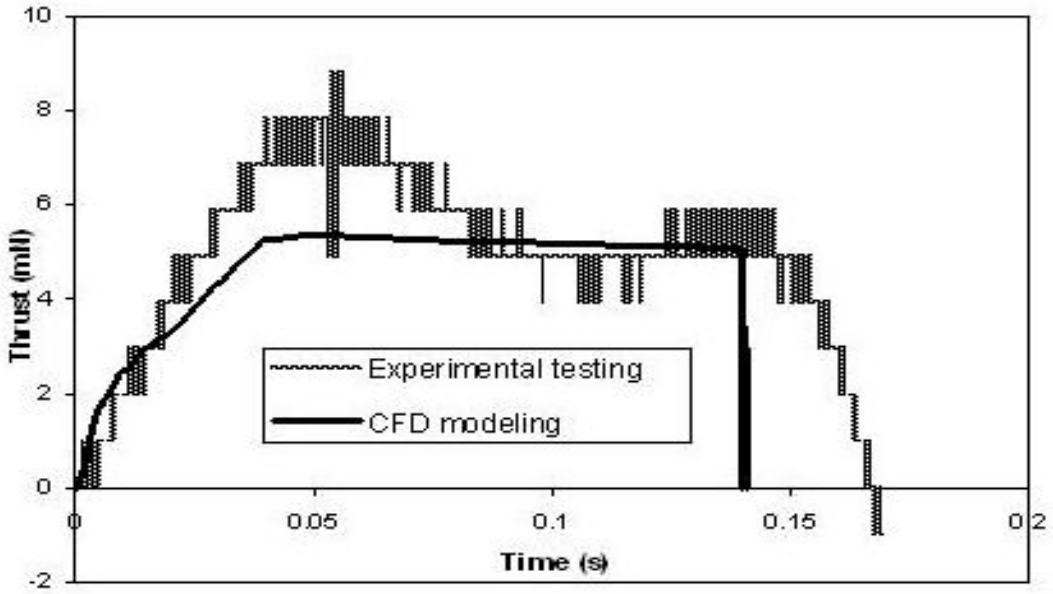

Figure 3.24. Thrust comparison between experiment and modeling at sea level.

Table 3.3 shows the performance difference between modeling and testing. The thrust from testing is the average value within the steady burning period in the thrust curve. The experimental thrust levels are lower than those from simulation. But the total impulses from testing are higher than those from simulation. This is mainly caused by the burning time difference between testing and simulation. The main reason for the difference is that the modeling can not simulate the thrust peak at the combustion early stage. Another reason is the characteristics variation between the HTPB/AP/Al-based propellant employed here and that from

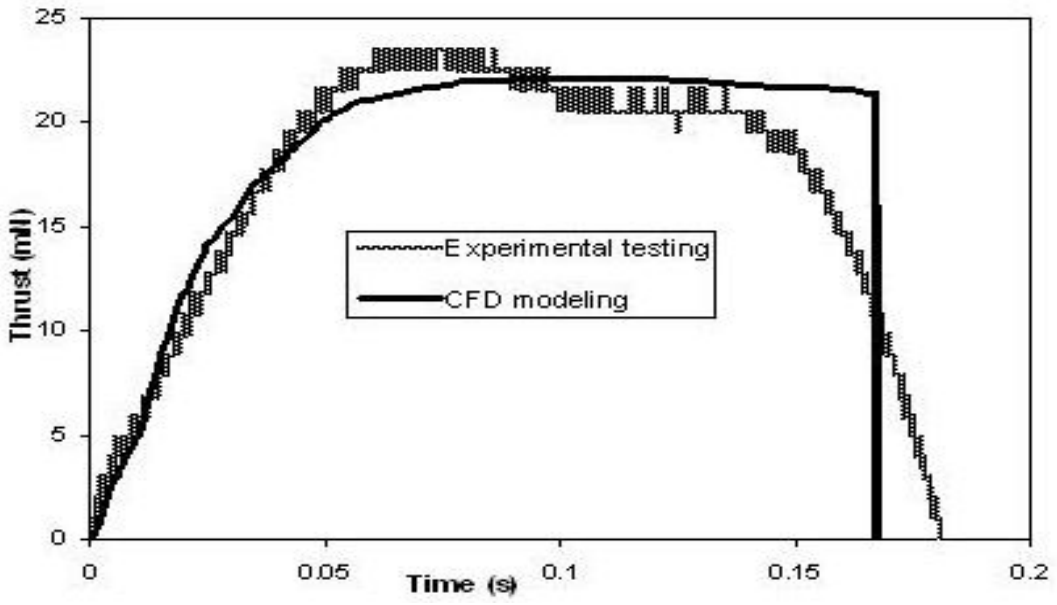

Figure 3.25. Thrust comparison between experiment and modeling in vacuum.

Ref. [Sutton and Biblarz 2001] because the HTPB/AP/Al-based propellant characteristics in the CFD simulation are obtained from Ref. [Sutton and Biblarz 2001]. There are some other possible causes for the performance difference, such as the testing uncertainty, the nozzle wall roughness, and the heat loss.

3.6 Chapter Summary

A novel MEMS-based solid propellant microthruster with wire igniter is successfully developed in this chapter for meeting the propulsion requirements of the microspacecraft. The feasibility of the new microthruster is proven by microcombustion experiment, thrust and impulse measurements both employing HTPB/AP/Al-based propellant and gunpowder-based propellant. Propellant combustion in the microchamber is visually observed through the transparent glass layer of the microthruster and the ejected plume. The measurements employing gunpowder-based solid propellant, have produced 205.08 mN to 405.37 mN of thrust peak value, $7.21 \times 10^{-5}\ N \cdot s$ to $1.49 \times 10^{-4}\ N \cdot s$ of total impulse, and 10.50 s to 21.70 s of specific impulse at sea level. The measurements employing HTPB/AP/Al-based solid

Table 3.3. Performance comparison between modeling and testing

	Thrust (CFD)	Thrust (testing)	Burning time (CFD)	Burning time (testing)	Total impulse (CFD)	Total impulse (testing)
W_t=400μm Sea level	4.273 mN	3.698 mN	165 ms	180 ms	0.577 mN·s	0.665 mN·s
Difference	13.457 %		8.333 %		13.233 %	
W_t=370μm Sea level	5.402 mN	4.631 mN	140 ms	169 ms	0.651 mN·s	0.792 mN·s
Difference	14.273 %		17.160 %		17.803 %	
W_t=400μm Vacuum	19.453 mN	15.652 mN	185 ms	206 ms	3.074 mN·s	3.159 mN·s
Difference	19.539 %		10.194 %		2.691 %	
W_t=370μm Vacuum	22.030 mN	20.513 mN	167 ms	181 ms	3.149 mN·s	3.250 mN·s
Difference	6.886 %		7.735 %		3.108 %	

propellant, have produced 5.37 mN to 7.81 mN of thrust peak value, $6.95 \times 10^{-4}\ N \cdot s$ to $8.19 \times 10^{-4}\ N \cdot s$ of total impulse, and 101.21 s to 119.27 s of specific impulse at sea level, and 10.75 mN to 23.44 mN of thrust peak value, $30.91 \times 10^{-4}\ N \cdot s$ to $32.50 \times 10^{-4}\ N \cdot s$ of total impulse, and 327.65 s to 448.52 s of specific impulse in vacuum. The thrust peak values of gunpowder-based propellant are much higher than those of the HTPB/AP/Al-based propellant. However, the total impulse and specific impulse of gunpowder-based propellant are much smaller than those of the HTPB/AP/Al-based propellant because of the much longer burning time of HTPB/AP/Al-based propellant compared with that of gunpowder-based proepellant. Lastly, the results from CFD modeling are compared with those from experimental testing.

Chapter 4

Design, Fabrication, and Testing of the Solid Propellant Microthruster with Au/Ti Igniter

Main Publication:

K. L. Zhang, S. K. Chou, S. S. Ang, and X. S. Tang, "A MEMS-based Solid Propellant Microthruster with Au/Ti Igniter", Sensors and Actuators A: Physical, Vol. 122, No. 1, pp. 113-123, 2005.

4.1 Introduction

The application of MEMS technologies to space field initiates the state-of-the-art microspacecraft. The motivations behind the development of microspacecraft are to reduce mission costs and increase launch rates by reducing launch masses, to reduce mission risk and increase mission flexibility by launching a cluster of microspacecrafts rather than a single large conventional spacecraft, and to open up new application areas of space technology. Building microspacecraft necessitates the development of every subsystem to maintain a high degree onboard capability. Micropropulsion is an important subsystem that should be significantly addressed.

Recently, several kinds of micropropulsion systems are being investigated, such as bi/mono-propellant microthruster, cold/hot-gas microthruster, field emission microthruster, colloid microthruster, and pulsed plasma microthruster. The solid propellant microthruster is a relatively new class of micropropulsion system. Its concept is based on the combustion of the energetic propellant stored in the microchamber. The solid propellant microthruster presents many advantages, such as minimized system complexity, no moving parts, and very low propellant leakage possibility. Consequently, the solid propellant microthruster is being studied extensively in the past years [Orieux et al 2002, Rossi et al 2002, Teasdale et al 2001, Lewis et al 2000, Youngner et al 2000, Tanaka et al 2003]. Their main design concepts are based on the three-layer sandwich configurations, which normally comprise three parts, namely, a combustion chamber, a micronozzle (or burst diaphragm), and an igniter. A building block design different from sandwich configuration is proposed in Chapters 2 and 3. This design has several advantages over the former solid propellant microthruster designs, such as higher fabrication efficiency, more design flexibility, and better bonding quality. However, this design employs a special wire as the igniter, which is not optimum for high level integration and batch fabrication. In this chapter, a new solid propellant microthruster with Au/Ti igniter design is presented, which not only inherits the advantages of the building block design presented in Chapters 2 and 3, but also is more suitable for high level integration and batch fabrication. The design, fabrication process, and assembly of the novel solid propellant microthruster are detailed. Facilities developed to characterize the characteristics of the solid propellant microthruster are described. Lastly, the experimental results of the microcombustion, thrust, and impulse testing are presented. The performance of the solid propellant microthruster with Au/Ti igniter is also compared with that of the solid propellant microthruster with wire igniter presented in Chapters 2 and 3.

4.2 Design and Fabrication of the Solid Propellant Microthruster with Au/Ti Igniter

Figure 4.1 shows the schematic of a proposed single microthruster in the author's system. In the new design, a metal igniter is deposited by lift-off method on a sodium-rich glass wafer. A silicon wafer is fabricated using MEMS technologies to contain a combustion chamber and a convergent-divergent nozzle. The glass layer and the silicon layer are bonded together to form a three-dimensional microthruster. The chamber is then loaded with the solid propellant. Once ignited, the resultant gas expands through the convergent-divergent nozzle as its velocity increases drastically, thus producing the desired thrust and impulse. A larger piece of glass wafer is used and connection is made to the end of the glass protruding out from the silicon part of the microthruster. The protruding glass part of the microthruster is installed into a micro-connector to realize the connection with the motherboard which contains the power source, addressing electronics, and communication ports.

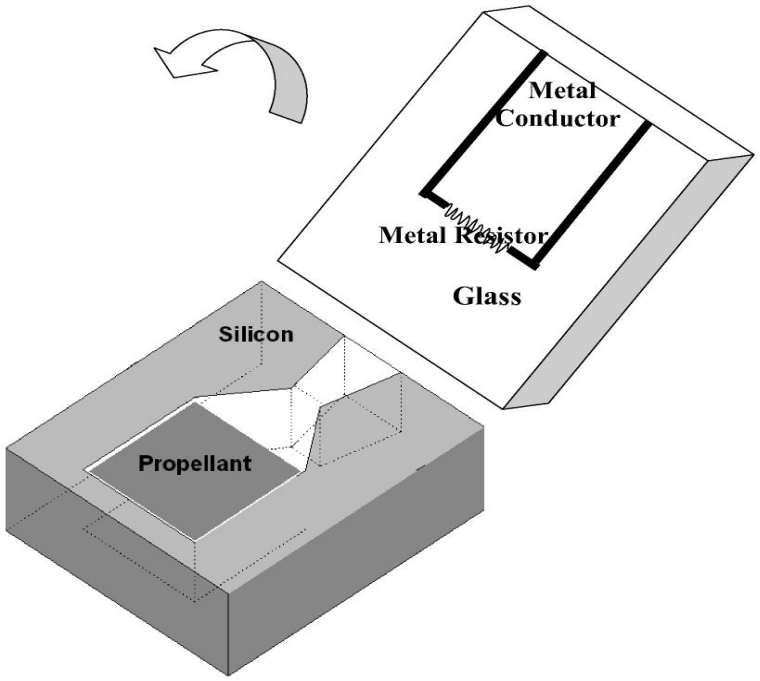

Figure 4.1. Schematic of a single microthruster with Au/Ti igniter.

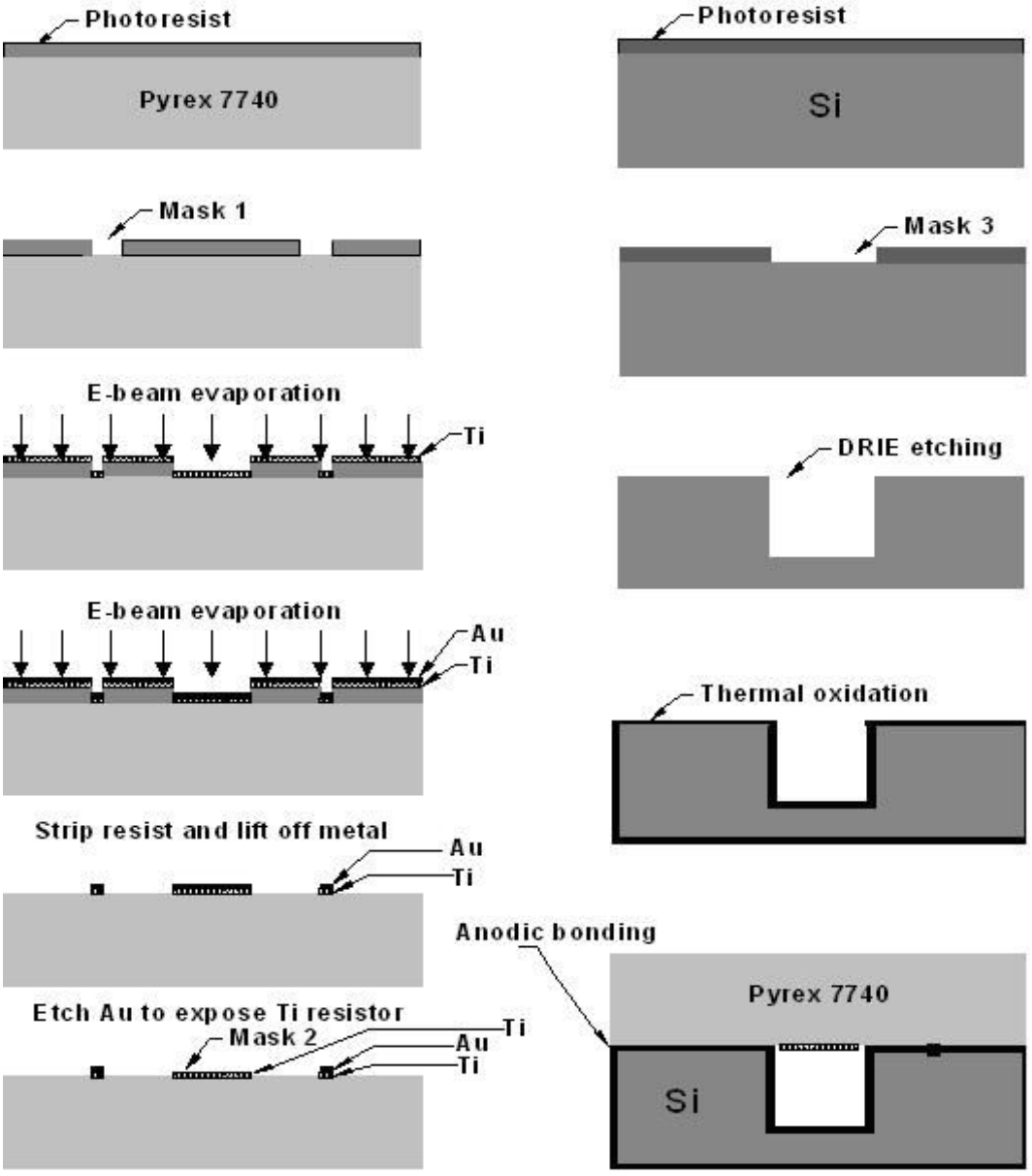

Figure 4.2. Microthruster fabrication process flow.

The fabrication is performed using standard MEMS fabrication tools at the Institute of Materials Research and Engineering (IMRE). The simplified fabrication process is shown in Figure 4.2. The process starts with a 550 μm thick double polished Pyrex 7740 glass substrate. Positive photoresist is spin-coated onto the Pyrex glass and patterned using photolithography through a designed mask-1. A

metal layer of Ti with the thickness of 206 nm is deposited by e-beam evaporation. The Ti layer acts as both the resistor and the adhesion layer. Then a metal layer of Au with the thickness of 77 nm is deposited onto the Ti layer through e-beam evaporation. The Au layer acts as both the conductor and contact pad. Metal Ti and Au lift-off is performed in acetone with ultrasonic for 20 minutes. After solvent and DI-water clean, the Pyrex substrate with Ti and Au metals is spin-coated and patterned using photolithography by a designed mask-2. After the exposed photoresist is removed, the substrate is put into Au etchant. The Au in the designed area is removed and the Ti is exposed as the igniter. The Pyrex substrate is diced into separate chips along the designed dice lines using a dicing machine. The SEM of a fabricated single igniter with Ti as the resistor and Au as the conductor is shown in Figure 4.3. The optic photo and SEM of the enlarged part of Ti resistor are shown in Figure 4.4.

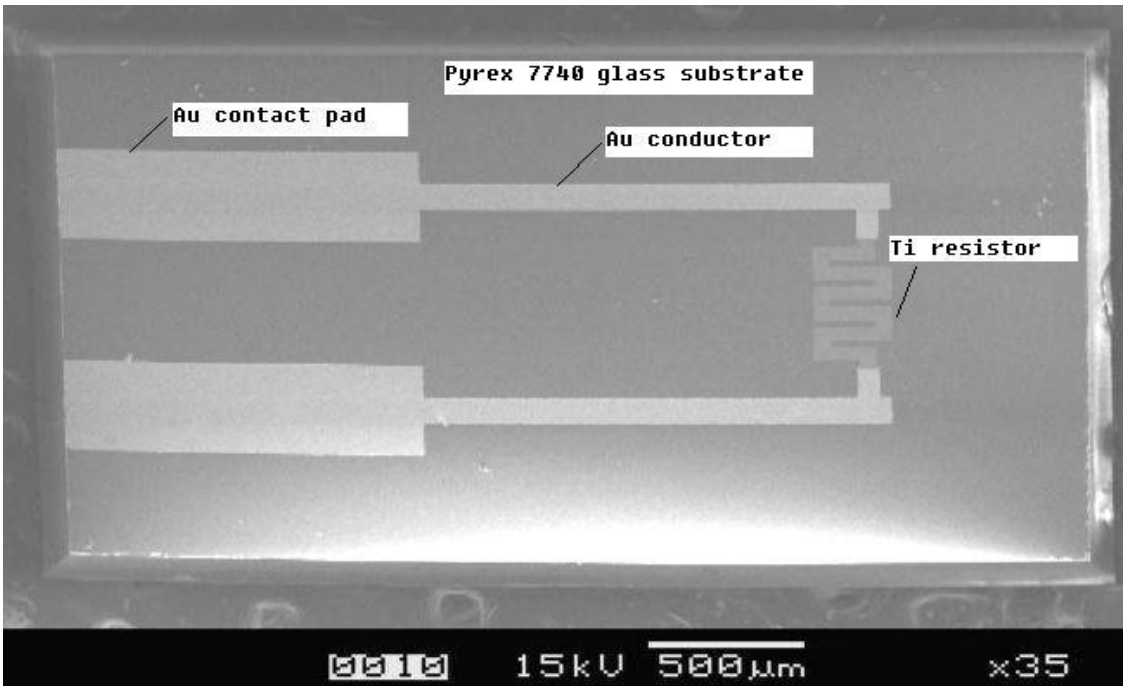

Figure 4.3. SEM of Au/Ti igniter on the glass chip.

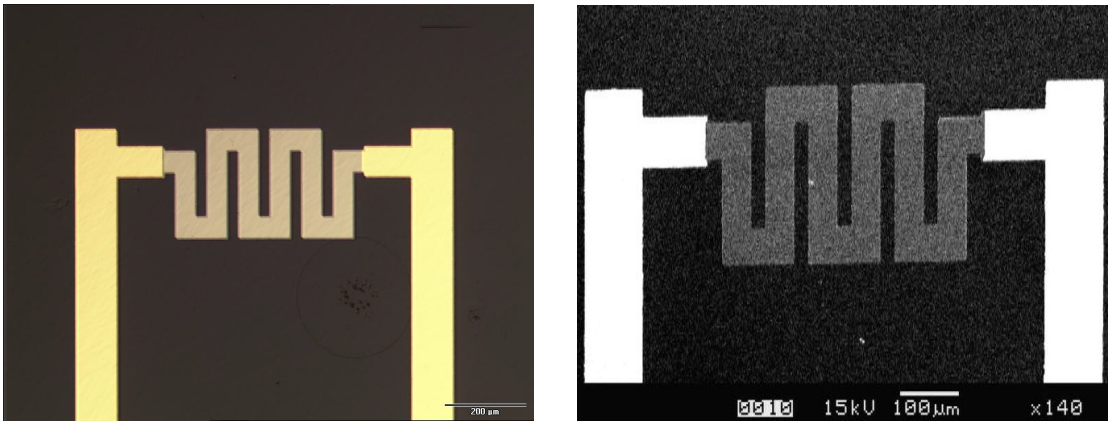

(a) (b)

Figure 4.4. (a) Optical picture of Au/Ti igniter. (b) SEM of Au/Ti igniter.

A double-polished 4-inch (100) oriented silicon wafer with the thickness of 750 μm is cleaned and deposited by spin coating at 1000 rpm to a photoresist thickness of 12 μm. After the photoresist is patterned by exposure to UV light through mask-3, the exposed photoresist is developed. With the pattern transferred through photolithography, a deep reactive ion etching (DRIE) is carried out on the silicon wafer. When the photoresist is stripped and the wafer is cleaned, a thermal oxidation process is performed. After thermal oxidation, the entire silicon wafer is covered by the silicon dioxide with a thickness of 246 nm. The insulation performance of the silicon wafer is improved by the thermal oxidation process. Consequently, the ignition efficiency is increased due to the minimization of the possible current leakage. The resulting silicon wafer trench depth is 400 μm after DRIE. The silicon wafer is diced into separate chips along the designed dice lines using a dicing machine. Figure 4.5 shows the front-side and cross-section views of the microthruster. It can be seen that the sidewalls are vertical during and after the DRIE. The micronozzle is shown in Figure 4.6. It shows that a well defined nozzle structure with smooth sidewalls can be obtained to a depth of 400 μm.

The glass wafer with the Au/Ti igniter and the silicon wafer with the trench are cleaned using ultrasonic agitation, rinsed in DI water and blown dry with a nitrogen gas. This is followed by an anodic bonding process at 400 ^{o}C and a voltage of 1100

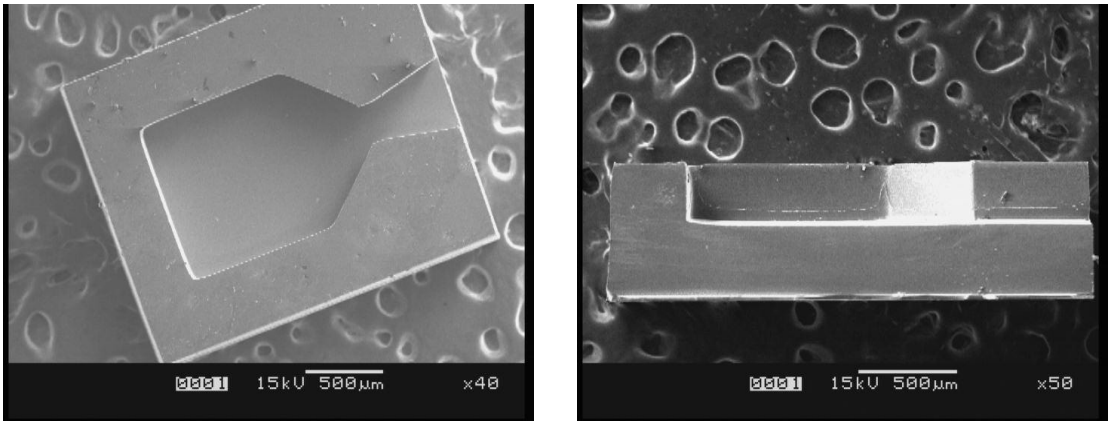

(a) (b)

Figure 4.5. (a) SEM of the front-side. (b) SEM of the cross-section.

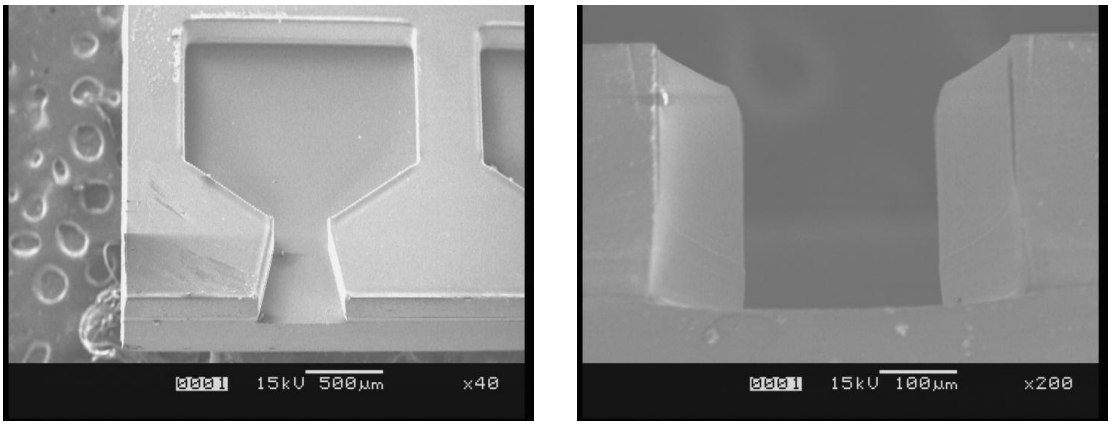

(a) (b)

Figure 4.6. (a) SEM of the micronozzle. (b) SEM of the micronozzle exit.

V. A reliable bond between the silicon layer and glass layer is then formed although there is a 246 nm silicon dioxide layer between the silicon and the glass. The protruding glass part of the microthruster is installed into a special micro-connector to realize the connection with the power source. The fabricated three-dimensional microthruster with igniter and solid propellant is shown in Figure 4.7.

One disadvantage of the solid propellant microthruster is that it is generally not restartable. Therefore, it can not fulfill some of the functions required by microspacecraft, for example, orbit trimming. However, this disadvantage can be partially mitigated by developing the microthruster arrays. The array is more

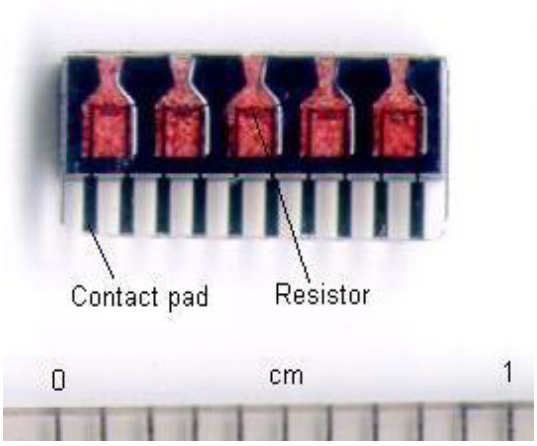

Figure 4.7. Three-dimensional microthruster with Au/Ti igniter.

robust than a single microthruster and can produce controlled, vectored thrust according to the applications. One of the fabricated microthruster layers is shown in Figure 4.7. The protruding glass part of the microthruster array is then installed into a micro-connector to realize the connection with the motherboard which contains the power source, addressing electronics, and communication ports. The microthruster layer and the micro-connector have the same pitch of 0.8 mm. The gold on the protruding glass part of the microthruster is held tightly with plated contact area (gold) of the micro-connector to realize a good ohmic contact as shown in Figure 4.8. A schematic of the way to address and ignite single microthrusters individually in the microthruster array is shown in Figure 4.9.

The new design not only inherits all the advantages of the design in Chapters 2 and 3, such as higher fabrication efficiency, more design flexibility, and better bonding quality, but also has several other advantages. First, the new design employs the Au/Ti igniter instead of the wire igniter, which is more suitable for batch fabrication and the ignition efficiency and reliability are improved. Second, adding addressing capability is one key part of developing the microthruster array. The new design makes the realization of addressing capability easier by employing the special micro-connector. In addition, a higher level of integration can be possibly

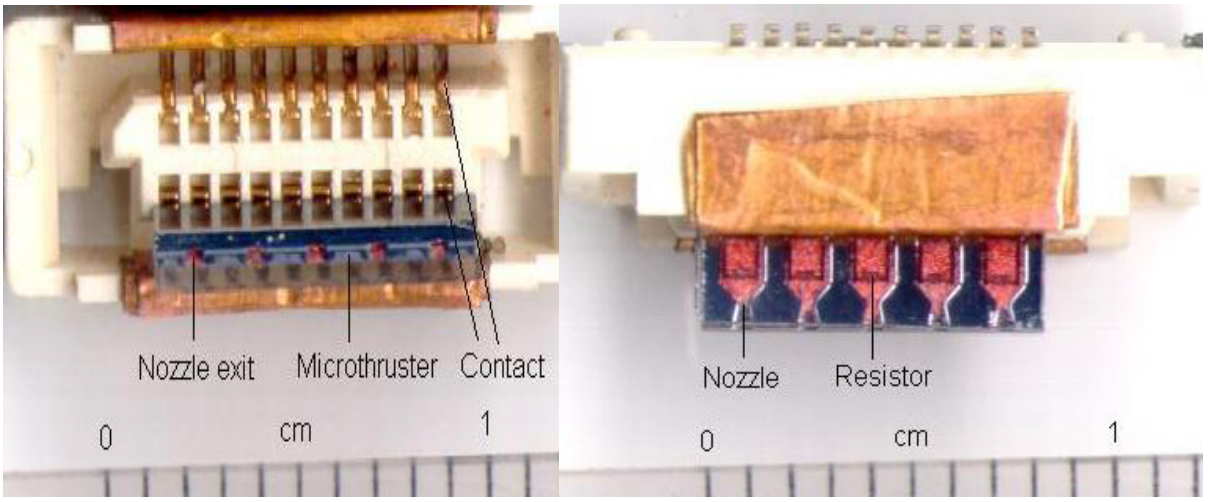

(a) (b)

Figure 4.8. (a) Front view of the microthrusters installed a micro-connector. (b) Side view of the microthrusters installed a micro-connector.

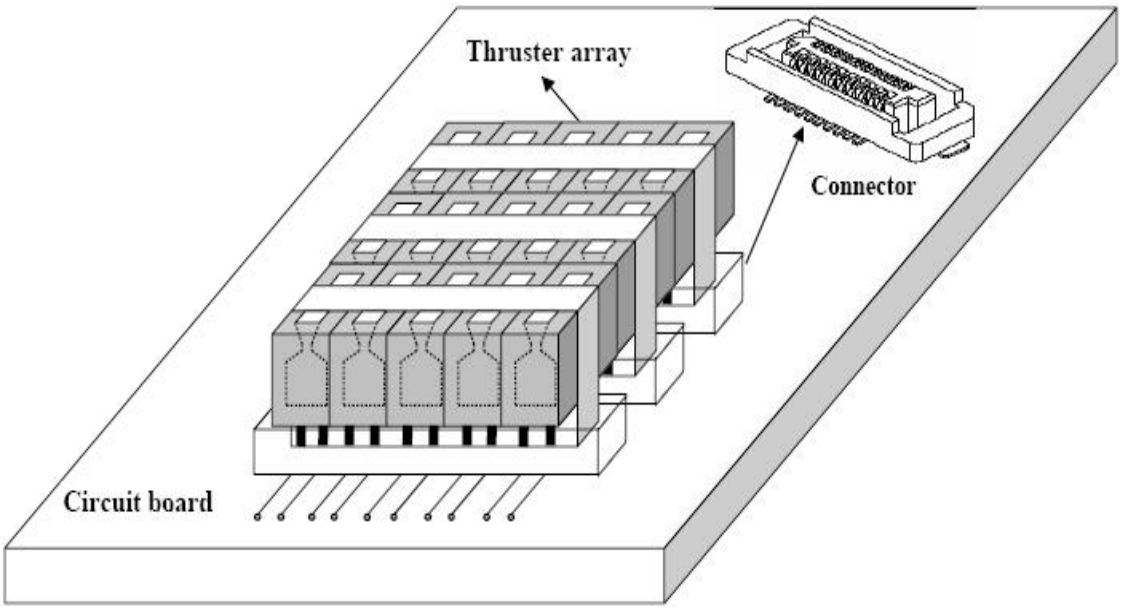

Figure 4.9. Schematic of addressing single microthrusters in an array.

achieved. Third, the new design creates an end-burning of the solid propellant by igniting the propellant from the end of the microchamber. The end-burning delivers a constant thrust level for considerably longer burn durations which is supplied by a consistent burn surface area. Lastly, the novel design makes it more convenient to observe the propellant combustion process visually inside the microscale device.

4.3 Experimental Testing

The specially designed experimental setup developed in Chapter 3 as shown in Figure 3.5 (see also Figure 3.6) is used to address the viability of the new design and acquire the characteristics of the solid propellant microthruster with Au/Ti igniter both at sea level and in vacuum.

4.3.1 Propellant Compositions and Microthruster Dimensions

Gunpowder-based solid propellant is employed here for the experimental testing because of its lower ignition temperature compared to HTPB/AP/Al-based solid propellant. The solid propellant consists of 90 % (mass fraction) gunpowder (75 % potassium nitrate, 15 % charcoal, and 10 % sulfur), 6 % ammonium perchlorate, 3 % aluminum, and 1 % Fe_2O_3. Adding ammonium perchlorate is to lower the ignition temperature and to improve the specific impulse of the propellant. Aluminum is used to increase flame temperature and specific impulse. Fe_2O_3 is utilized as the combustion catalyst. Testing the single microthruster enables us to furnish a more precise performance measurement than the microthruster array and is more beneficial for optimizing the microthruster geometry. Therefore, the single microthruster is tested. The dimensions of the single microthruster are similar to those in Figure 2.2.

The microthruster has different nozzle divergence lengths (L), half divergence angles (a), combustion chamber widths (W_c), microthruster throat widths (W_t), and microthruster exit widths (W_e). As a result, different chamber-to-throat section ratios (A_c/A_t) and exit-throat section ratios (A_e/A_t) are available for evaluation. Because the DRIE process creates the common etch depth for various features, the chamber and nozzle have the same depth of 400 μm. Consequently, A_c/A_t is equal to W_c/W_t and A_e/A_t is equal to W_e/W_t.

The loaded propellant mass affects the microthruster performance in terms of

Table 4.1. Masses of the microthruster with Au/Ti igniter and propellant

Single microthruster	Empty vehicle mass (mg)	Loaded mass (mg)	Propellant mass (mg)	Propellant mass fraction (%)
$W_c = 1000\ \mu m$	14.9	15.7	0.8	5.10

specific impulse that is defined as the ratio of total impulse to propellant weight. Therefore, the propellant mass should be measured precisely before the firing. Table 4.1 shows the masses of the microthruster and propellant. The empty vehicle mass is the microthruster mass before loading, the loaded mass is the microthruster mass with the propellant loaded, and the propellant mass fraction is equal to the ratio of the propellant mass to the mass of the loaded microthruster before firing. The propellant mass fraction (5.1 %) of the current design is much lower than that (16 %) of previous study by Teasdale et al [Teasdale et al 2001]. An improved design is expected to increase the propellant mass fraction and to increase the specific impulse of the microthruster.

4.3.2 Microcombustion Experiment

Microcombustion experiment is performed to visually validate the feasibility of the novel solid propellant microthruster design. The increased surface area-to-volume ratio that comes with the small size of the microthruster may cause chemical and thermal quenching. The quenching may cease the microcombustion [Lee and Kwon 2002], which is needed to be addressed. Continuous combustion is observed successfully after igniting the gunpowder-based solid propellant with the Au/Ti igniter. The combustion lasts for about 0.7 ms for a typical single microthruster. A series of frames from a high-speed digital video camera of the combustion are shown in Figure 4.10. A microthruster layer is installed into a micro-connector during the experiment as shown in Figure 4.8. The images are acquired at 30,000 frames/s.

The combustion process of the propellant can be visually observed in the design because of the transparent property of the Pyrex-7740 glass. It can be seen that the propellant is ignited initially at some point near the igniter. The combustion occurs and propagates to all the surface and then progresses rapidly. The ejected plume from the convergent-divergent nozzle exit can also be visually observed from Figure 4.10. The propellant explosion in one microthruster cavity may shatter the walls of that cavity caused by the mechanical shock, or cause the fuel in neighboring cavities to ignite unexpectedly due to the thermal shock because of the high thermal conductivity of silicon [Youngner et al 2000]. For our design, the walls are not broken after combustion. The propellant in the neighboring cavity is not ignited during combustion despites the spacing among the single microthrusters in the layer is only 600 μm.

4.3.3 Thrust and Impulse Testing

The thrust and impulse measurements are performed both at sea level with the ambient temperature of approximately 300 K and in vacuum with the back pressure of 80 Pa. To more efficiently capture the thrust and impulse signals, the dynamic acquisition rate of the acquisition system is selected as 100,000 samples per second.

Figure 4.11 shows a typical measurement signal in vacuum for the single microthruster with Wc = 1000 μm, Wt = 500 μm, L = 600 μm, and a half divergence angle a = 12 degree. When the gunpowder-based propellant is ignited, its combustion is extremely rapid. Consequently, the energy of the propellant is released within a very short time, producing a high peak value of thrust. The peak value is approximately 0.13 N. Ignition occurs with an input voltage of 8 V. Although current is not measured directly, a DC current output of 20 mA as indicted on the power supply is observed at the time of ignition. The ignition power is estimated to be 0.16 W. The data acquisition and the power supply are set to begin simulta-

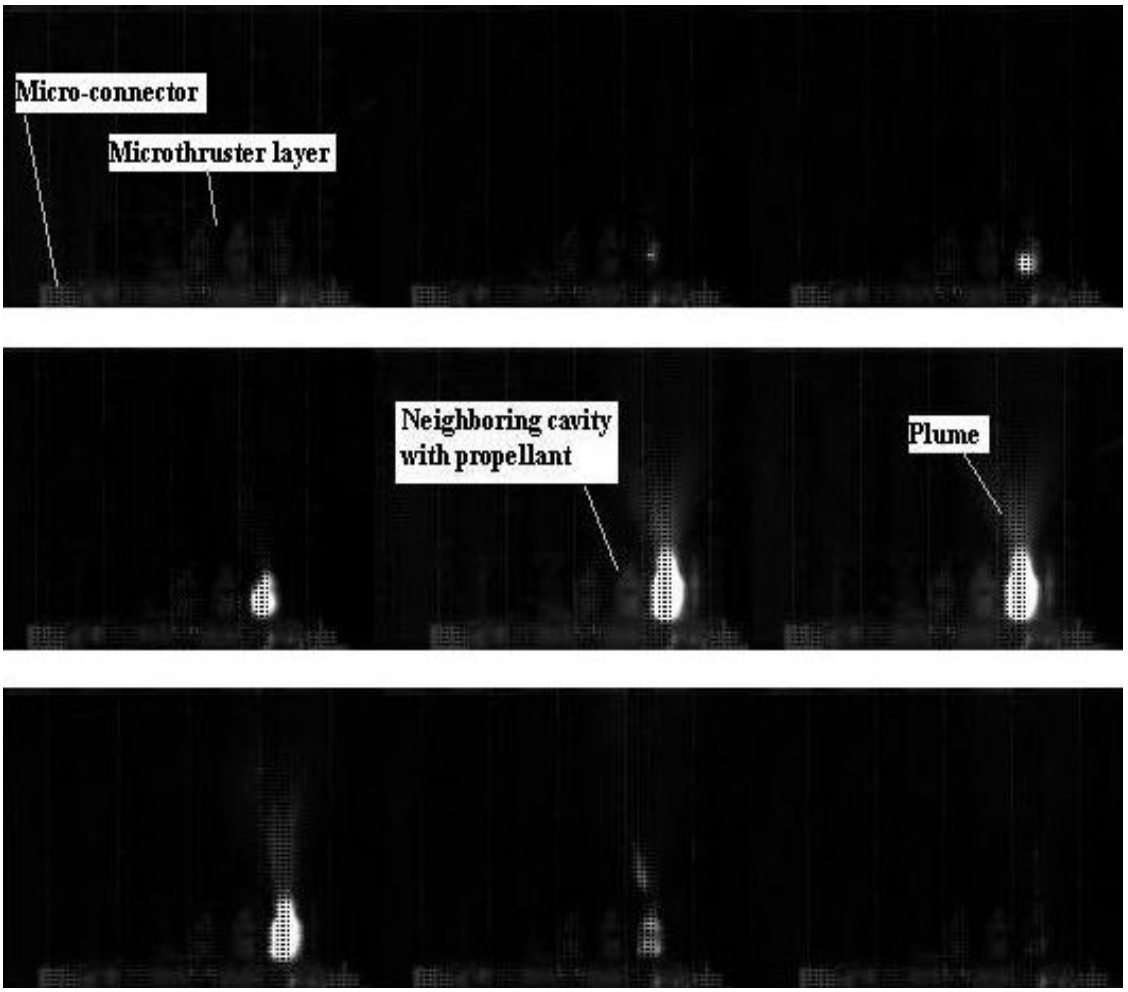

Figure 4.10. Microthruster firing (Images are acquired at 30,000 frames/s).

neously. Accordingly, the ignition delay can be acquired through the measurement signal as shown in Figure 4.11. The ignition delay is found to be 12.940 s and the ignition energy is then estimated to be 2.070 J. The large ignition energy is mainly caused by the large heat loss because the thin film ignition heater is directly deposited on the glass substrate. Another possible reason is due to the lower ignition power supplied for the ignition, which causes a long ignition delay. An optimum ignition power can be found to reduce the ignition energy. This will be discussed in detail in Chapter 5.

Figure 4.12 is a time-based extended plot of the combustion region shown in Figure 4.11. The combustion and thrust production processes can be seen in Fig-

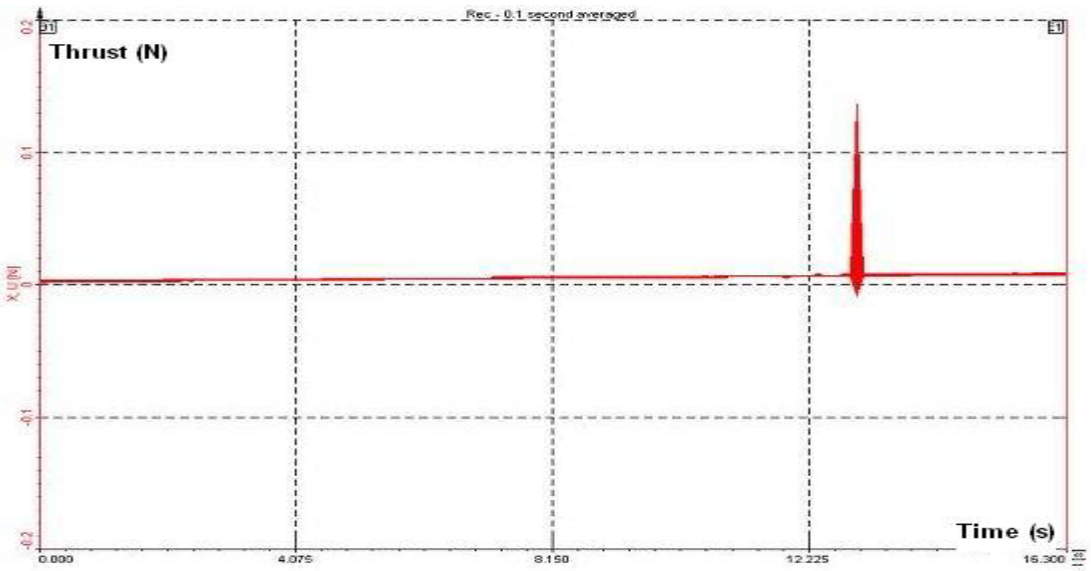

Figure 4.11. Original signal of the microthruster testing.

ure 4.12. The combustion duration is about 0.66 ms and the peak value of thrust is around 0.13 N. At t = 0 ms, the Au/Ti igniter is energized and the propellant combustion is triggered, generating the thrust and impulse. The thrust increases rapidly and achieves its peak value at t = 0.25 ms. The high value of thrust lasts for about 0.05 ms and decreases gradually. By t = 0.66 ms, the propellant combustion is complete, and the impulse has been delivered. Total impulse, defined as the integration of thrust over combustion time, is an important factor to describe the propulsion performance [Sutton and Biblarz 2001]. For this single microthruster, total impulse is $3.52 \times 10^{-5}\ N \cdot s$. The total impulse of our microthruster is similar to that reported by David [Lewis et al 2000], even though the design and propellant are different.

4.3.4 Microthruster Performance Variation with Exit-to-Throat Area Ratio

The nozzle exit-to-throat area ratio (A_e/A_t) is a major driver of the microthruster performance. If A_e/A_t is too small, the gas expansion is incomplete. The nozzle

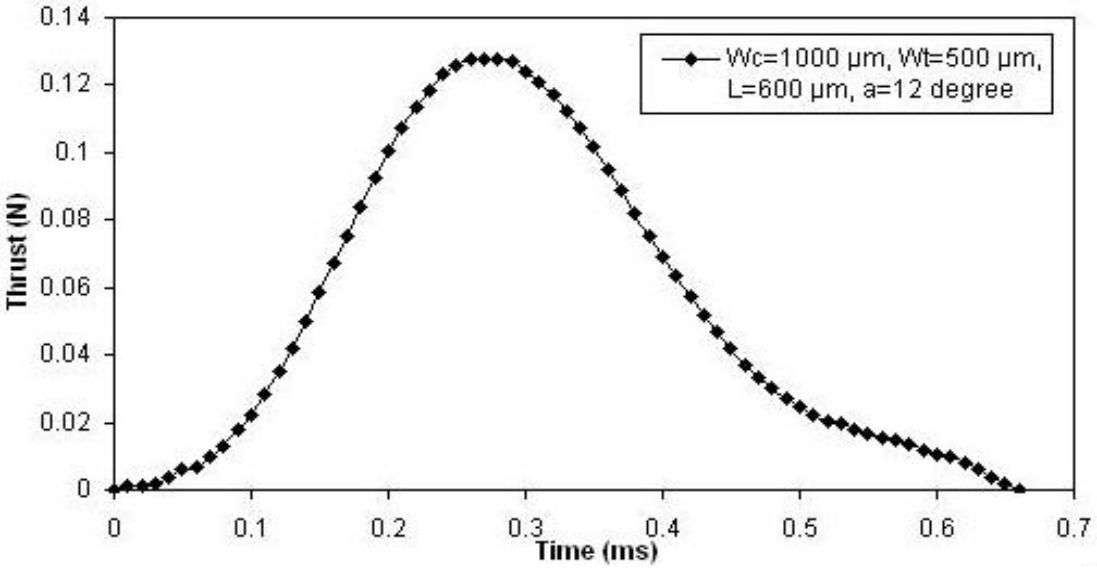

Figure 4.12. Variation of the thrust with the combustion time.

exit pressure is higher than the ambient pressure. The nozzle is underexpanded. However, if A_e/A_t is too large, nozzle exit pressure is lower than the ambient pressure. The nozzle is overexpanded. Both the overexpansion and underexpansion affect the nozzle performance. Optimum expansion is achieved when the gas exits at ambient pressure. Figure 4.13 shows the thrust and total impulse variations with A_e/A_t in vacuum. The single microthrusters have a similar chamber width of 1000 μm, a similar divergence length of 600 μm, and a similar half divergence angle of 12 degree. The peak thrust increases from 0.13 N to 0.60 N and the total impulse is changed from $3.25 \times 10^{-5}\ N \cdot s$ to $2.22 \times 10^{-4}\ N \cdot s$ when A_e/A_t increases from 1.47 to 1.78. Therefore, this is one of possible ways to vary the thrust and total impulse to satisfy different requirements by adjusting the microthruster exit-to-throat area ratio. The thrust curve trends in Figure. 4.13 are somewhat different, especially for $A_e/A_t = 1.63$. This is mainly caused by differing contact areas between the propellant and the igniter, non-uniformities in the propellant grain. The specific impulse is another important metric for evaluating the solid propellant microthruster performance. According to experimental results, specific impulses of 4.48 to 28.29 s are generated in vacuum, which are much less than those of traditional solid rockets. This is mainly caused by the relatively low specific

impulse of the gunpowder-based propellant, the small size of the microthruster, and possible incomplete combustion of the propellant.

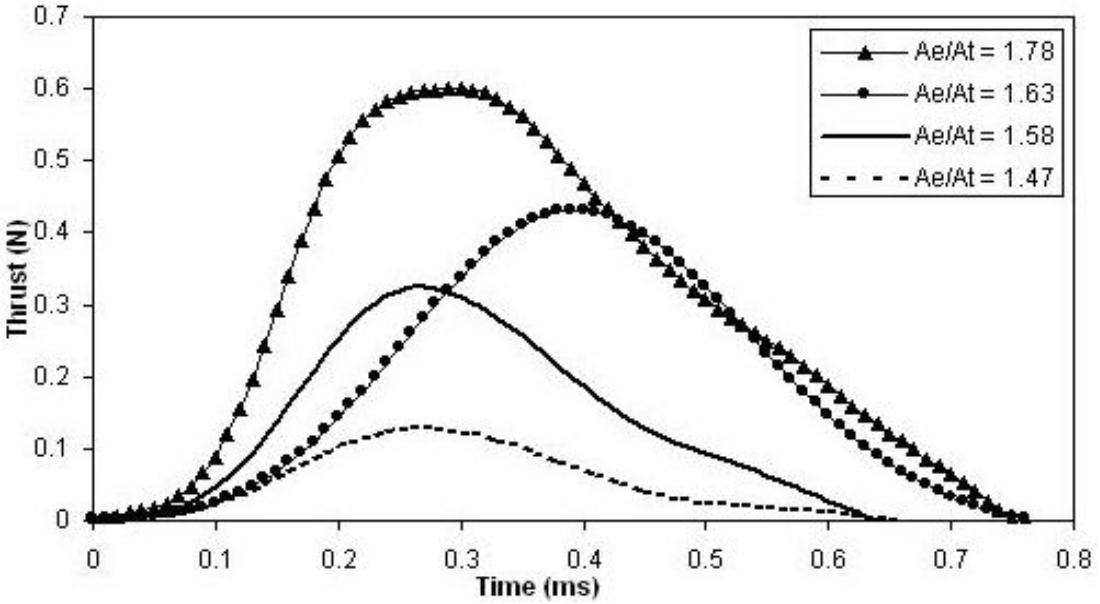

Figure 4.13. Thrust and total impulse variations with A_e/A_t in vacuum.

4.3.5 Microthruster Performance Variation with Chamber-to-Throat Area Ratio

The propellant burning rate is dependent on the propellant composition and the chamber pressure. The chamber pressure, however, is determined by the equilibrium that exists between the combustion gas generation rate and the nozzle exhaust flow rate. Thus, the stable pressure level that can be attained is determined by the propellant composition and the ratio between the propellant burning area A_c and the nozzle throat area A_t. Consequently, the chamber-to-throat area ratio (A_c/A_t) is an important factor that impacts the microthruster performance. Figure 4.14 shows the thrust and total impulse variations with A_c/A_t at sea level. The single microthrusters have a similar chamber width of 1000 μm, a similar divergence length of 600 μm, and a similar half divergence angle of 12 degree. The

peak thrust increases from 0.05 N to 0.34 N and the total impulse is changed from $2.11\times10^{-5}\ N\cdot s$ to $1.15\times10^{-4}\ N\cdot s$ when Ac/At increases from 2.00 to 3.85. Specific impulses of 2.68 to 14.65 s are produced at sea level, which are similar to Teasdale's results (10∼15 s) using HTPB/AP as the solid propellant [Teasdale et al 2001].

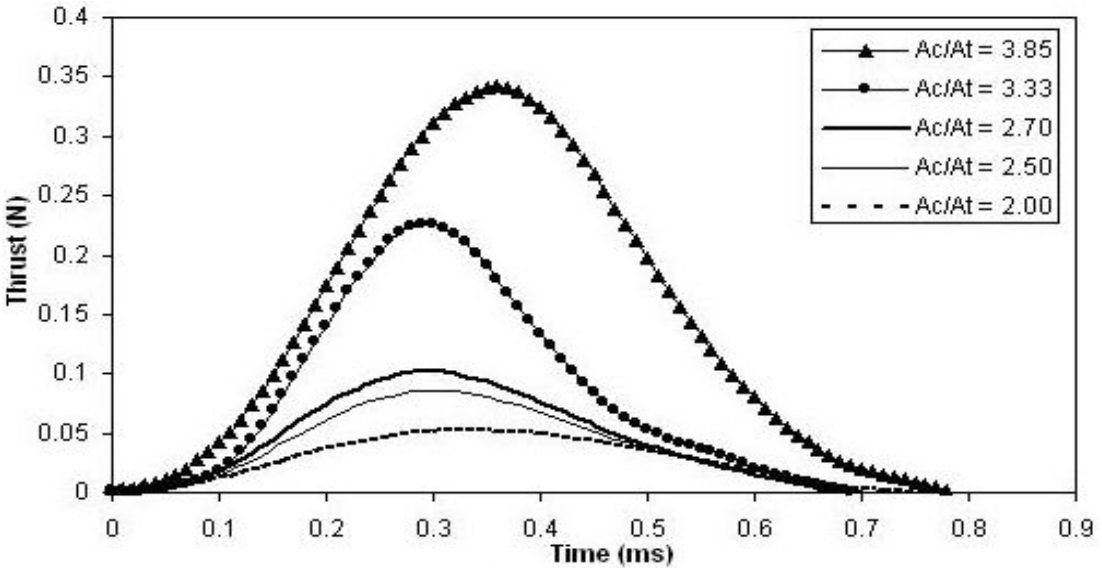

Figure 4.14. Thrust and total impulse variations with A_c/A_t at sea level.

4.3.6 Microthruster Performance Comparison at Sea Level and in Vacuum

The microthruster testing is performed both at sea level and in vacuum. Figure 4.15 shows the performance comparison at sea level and in vacuum for the microthrusters with a similar divergence length of 600 μm and a similar half divergence angle of 12 degree, whereas the A_c/A_t is different. When A_c/A_t is 2.5, the thrust peak value is increased from 0.08 N to 0.32 N, the total impulse is changed from $2.81\times10^{-5}\ N\cdot s$ to $9.16\times10^{-5}\ N\cdot s$, and the specific impulse is increased from 3.58 s to 11.67 s while the back pressure is changed from sea level to vacuum. When A_c/A_t is 2.7, the peak thrust changes from 0.10 N to 0.43 N, the total impulse increases from $3.28\times10^{-5}\ N\cdot s$ to $1.44\times10^{-4}\ N\cdot s$, and specific impulse increases

from 4.18 s to 18.35 s when the back pressure changes from sea level to vacuum. The microthruster performance is considerably improved in vacuum. One reason for the improvement is the increase of the exit-ambient pressure difference in vacuum. The other reason is the difference in the flow pattern of the microthruster jet. At sea level, the jet flow is subsonic because of the high back pressure. Whereas in vacuum, the jet flow is supersonic due to the low back pressure. The supersonic jet produces higher thrust and impulse than the subsonic jet.

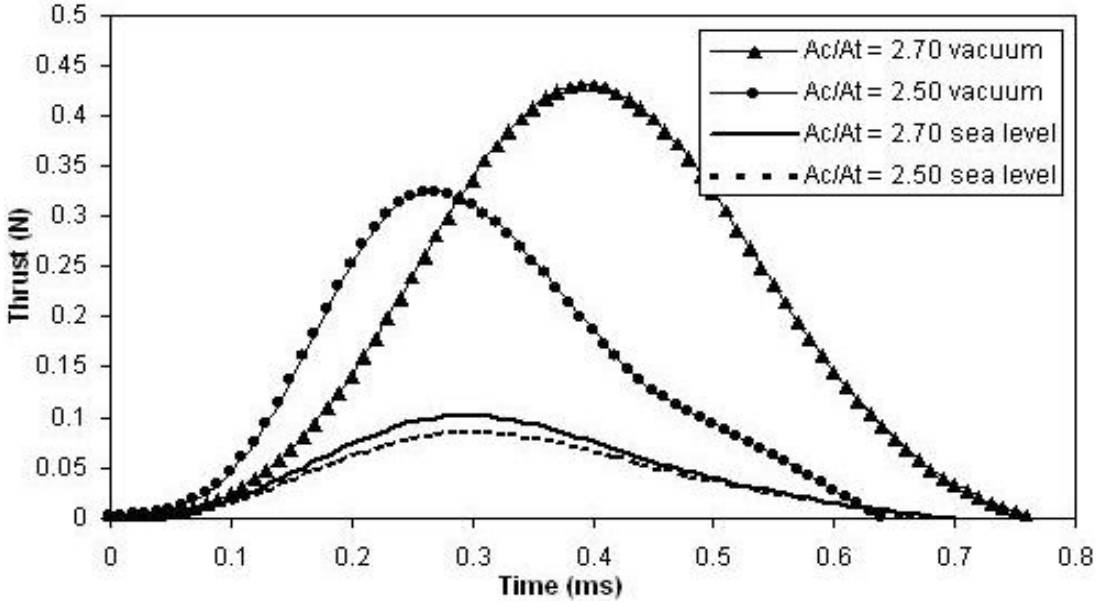

Figure 4.15. Microthruster performance comparison at sea level and in vacuum.

4.3.7 Comparison between Microthrusters with Au/Ti Igniter and Wire Igniter

A solid propellant microthruster with wire igniter is developed in Chapters 2 and 3, which has a similar design as the solid propellant microthruster with Au/Ti igniter. Figure 4.16 shows the performance comparison between the microthruster with the Au/Ti igniter and the microthruster with the wire igniter at sea level. These microthrusters have a similar chamber width of 1000 μm, a similar divergence length

of 600 μm, and a similar half divergence angle of 12 degree. The propellants employed for experiment are almost identical except that the potassium perchlorate in Chapter 3 is replaced by ammonium perchlorate here. Nevertheless, the mass fractions of potassium perchlorate and ammonium perchlorate are very small (6%). The thrusts and total impulses produced by the microthrusters with Au/Ti igniter and wire igniter are similar for same A_c/A_t. This is because of the identical geometries and similar propellant employed. However, specific impulses produced by the microthruster with the Au/Ti igniter are higher than those generated by the microthruster with the wire igniter (14.65 s vs. 11.32 s for Ac/At = 3.85; 7.57 s vs. 6.68 s for Ac/At =3.33). This is because of the lower propellant mass (Table 4.1) of the microthruster with Au/Ti igniter compared with that of the microthruster with wire igniter.

A oscillatory drop can be observed from the thrust curves of the microthruster with the wire igniter. This is probably caused by the combustion instability of the solid propellant in the microthruster as stated in Chapter 3. The wire igniter and ignition slot in the microthruster are supposed to be the possible causes of the combustion instability due to the flow disturbance. The instability is harmful to the microthruster performance and the hardware. However, the combustion instability is absent for the microthruster with the Au/Ti igniter. This is because the wire igniter is replaced by the thin film Au/Ti igniter deposited on the glass layer of the microthruster. Therefore, the igniter does not disturb the gas flow.

4.3.8 Repeatability of the Measurements

The last section presents the repeatability of the testing results. Figure 4.17 shows the thrust measurement results for the same single microthruster with a chamber width of 1000 μm, a throat width of 260 μm, a divergence length of 600 μm, and a half divergence angle of 12 degree at sea level. The total impulses for the three

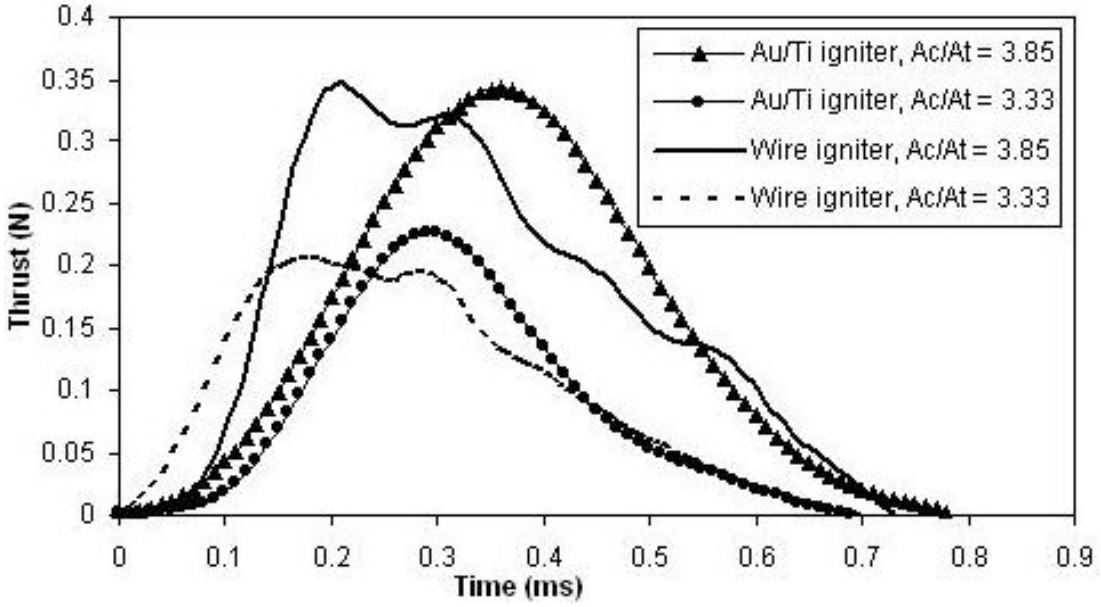

Figure 4.16. Performance comparison between microthrusters with Au/Ti igniter and wire igniter.

samples are $1.15 \times 10^{-4}\ N \cdot s$, $1.17 \times 10^{-4}\ N \cdot s$, and $1.14 \times 10^{-4}\ N \cdot s$, respectively. The results are within experimental uncertainties and establish the repeatability of the measurements. The small difference is mainly caused by the non-uniformities in the propellant grain.

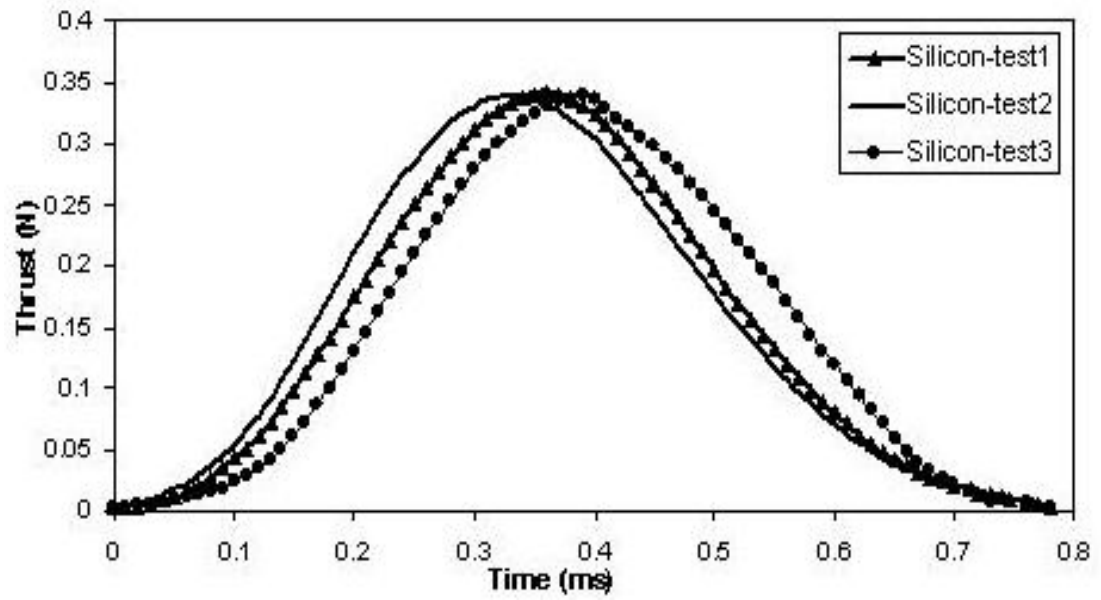

Figure 4.17. Repeatability of the thrust measurement.

4.4 Chapter Summary

A MEMS-based solid propellant microthruster with Au/Ti igniter has been successfully developed for meeting the propulsion requirements of the microspacecraft. The new design is suitable for batch fabrication and a high degree of miniaturization. It has a high fabrication efficiency, a large design flexibility, and a good anodic bonding quality. The new design is validated by microcombustion experiment, thrust, and impulse measurements. Propellant combustion in the microchamber is visually observed through the transparent glass layer of the microthruster. The tests employing gunpowder-based solid propellant, have produced 0.05 N to 0.34 N of thrust peak value and $2.11 \times 10^{-5}\ N \cdot s$ to $1.15 \times 10^{-4}\ N \cdot s$ of total impulse at sea level, and 0.13 N to 0.60 N of thrust peak value and $3.52 \times 10^{-5}\ N \cdot s$ to $2.22 \times 10^{-4}\ N \cdot s$ of total impulse in vacuum. The solid propellant microthruster with the Au/Ti igniter presents a similar total impulse, but a higher specific impulse than that of the solid propellant microthruster with the wire igniter.

Chapter 5

Electro-thermal Modeling of the Solid Propellant Microthruster with Au/Ti Igniter

5.1 Introduction

Microsystem technology allows engineers to combine electrical circuitry and other microdevices for "ambient intelligence" applications. Many of these microdevices are powered by electrical current, so that they can sense their environment and, depending on circumstances, even produce corresponding actions. An important part of the design process is to take into account inevitable electro-thermal effects, which very often play a parasitic role through Joule heating. Electro-thermal modeling therefore has become an essential design task in microsystem technology. The solid propellant microthruster investigated here is somewhat unusual for the electro-thermal community, as a primary design goal for the device is to reach a critical high temperature (ignition temperature) rather than to escape it. The operating principle of the solid propellant microthruster is as follows. The microheater (resistor) is powered electrically. Through the Joule effect, its temperature rises enabling the temperature of the propellant in contact with the resistor to

rise until its ignition temperature is reached. The propellant's auto-combustion is triggered, the combustion occurs and propagates in the rest of the propellant. The hot gases produced by the combustion exhaust through the nozzle exit, producing the desired thrust and impulse. However, in the other hand, the need to avoid thermal cross-talk between adjacent single microthrusters in a microthruster array is exactly the same as the usual case.

In this chapter, a finite-element based electro-thermal modeling is performed for the solid propellant microthruster with Au/Ti igniter to predict and optimize the transient propellant ignition process. Propellant temperature variations with time, space, and voltage are calculated and ignition power, ignition delay, and ignition energy are derived from the modeling. Thin film Au/Ti property difference from bulk Au/Ti and heat transfer in microthruster are highlighted in the model. The necessity of the thermal oxidation process in the microthruster fabrication is also evaluated.

5.2 Overview of Electro-thermal Process and Finite-element Modeling

The Au/Ti igniter is ohmically heated and can be viewed as a nonlinear resistor. Heating of the igniter occurs when current-conducting electrons are energized by the applied power and collide with the lattice. The resulting increased lattice-vibration energy corresponds to a higher igniter temperature. As the igniter temperature increases, collisions of electrons with vibrating lattice atoms are more likely, so the electrical resistance increases while the thermal conductivity decreases. At higher power, these changes lead to increased lattice heating both because more heat is being generated and because the generated heat cannot flow away as easily. The solid radiates electromagnetic radiation at all temperatures, but the effect of radiative energy flow is significant only at higher temperatures.

The electro-thermal process can be described by the following equation,

$$\nabla \cdot (\kappa \nabla T) + Q_{ohmic} - Q_{conduction} - Q_{convection} - Q_{radiation} - \rho C_p \frac{\partial T}{\partial t} = 0 \quad (5.1)$$

where Q_{ohmic} is the heat generated by ohmic heating; $Q_{conduction}$, $Q_{convection}$, and $Q_{radiation}$ are the heat lost by conduction, convection, and radiation, respectively; T is the temperature distribution that is to be determined over space and time.

For the transient multi-physics electro-thermal process, finite-element modeling using commercial software is the most feasible way to model the temperature distribution of the three-dimensional structure. In this project, ANSYS 7.0 from ANSYS Inc. is employed because of its excellent capacity to solve multi-physics problems in microscale [Ansys 2004].

In finite-element modeling, a structure is divided into smaller parts called finite elements. The finite elements are typically triangular or rectangular prisms for three-dimensional objects. The corners (and possibly the centers of faces of three-dimensional objects) of the elements are called nodes. Boundary conditions are applied to the structure. Different regions can be modeled as different materials to accurately replicate the physical situation. The differential equations (e.g. equation 5.1) that govern the behavior of the physical quantities of interest are applied to each element. Approximate solutions to the differential equations are found for each element that agree at the coincident nodes from each element. Rather than exactly matching the true solution, these approximate solutions assume that the output variable varies linearly, quadratically, or as some higher-order polynomial from node to node within the element. By dividing the structure into sufficiently fine elements and/or using a sufficiently high-order approximation inside each element, it is possible to achieve a solution with negligible error.

In finite-element analysis, several steps must be taken: drawing the geometry, meshing this geometry, establishing boundary conditions and related parameters, and entering physical data. In this section we discuss the details of finite-element analysis and how our model is set up. Modeling results both for the Au/Ti micro-

heater and the microthruster with Au/Ti igniter are presented. The comparison between modeling and experiment is discussed in Chapter 7.

5.3 Material Properties

The electrical resistivity, thermal conductivity, specific heat, and radiative emissivity as functions of temperature of the materials, can be used as parameters in the ANSYS finite-element analysis in several ways. In one method, a polynomial curve fit is entered for each of these quantities. This method is simple, but has the disadvantage of not being able to follow sudden changes in the true curve accurately. Another method is to enter a table of data and have ANSYS make an interpolation between the data points given. This latter method is used for most of our simulations because of the ease of data entry.

The modeling requires knowledge of the electrical resistivity, thermal conductivity, specific heat, and density of thin film Au, thin film Ti, thin film silicon dioxide, Pyrex-7740 glass, silicon, and solid propellant. The properties of bulk Pyrex-7740 glass, silicon, and propellant are from the suppliers, respectively. The variation of these bulk materials' physical parameters with temperature is ignored. The properties of thin film Au, Ti, and silicon dioxide are the key properties for the modeling and they are different from those of the bulk materials. Moreover, the fabrication conditions also affect the thin film material properties. Therefore, the properties of the thin film materials must be measured directly or decided carefully.

5.3.1 Electrical Resistivity of Thin Film Titanium

The resistivity of Ti as a function of temperature can be found in Ref. [Vladislav 1998]. However, these data for bulk Ti cannot be used for thin film Ti because of the different microstructures. The resistivity of a metal can be divided into temperature dependent and temperature independent portions. The temperature dependent portion is due to the electron scattering by vibrating lattice atoms. Higher tem-

perature results in more electron scattering, and thus a higher resistivity. The temperature independent portion relies on the metal crystal lattice, the impurities, and the microstructure. Impurity atoms and vacancies in the crystal lattice cause deviations from the highly ordered structure. The disordered lattice interacts more heavily with the electrons comprising an electrical current, and brings about a higher resistivity. The term "microstructure" refers to material parameters such as grain size, dislocation density, and stacking-fault density. Smaller grain size and greater imperfection densities cause increased electron scattering and thus higher resistivity. The thin film Ti used in this project has a higher resistivity than the bulk Ti tested in Ref. [Lide 1998] at room temperature. This higher resistivity is caused by the low deposition temperature (room temperature for E-beam evaporation) not allowing for diffusion of individual Ti atoms during deposition to form a lattice with a lower defect density as compared to the bulk Ti.

The measured thin film Ti resistivity at room temperature (300 K) combined with the temperature-variation data from Ref. [Lide 1998] is employed to estimate the thin film Ti resistivity using Matthiessen's Rule [Kittel 1996]. Matthiessen's Rule states that the resistivity of a metal is made up by two components. One is the "residual" resistivity, ρ_0, which is independent of temperature and would be observed at a temperature of absolute zero. The other is the lattice resistivity $\rho_l(T)$, due to the vibrating lattice. Experiments justify that the two resistivities can be separated and it is expected that $\rho_l(T)$ would be the same for the bulk and thin film metals, but that ρ_0 would be different. As a result, the bulk Ti resistivity $\rho_{bulk}(T)$ and thin film Ti resistivity $\rho_{thin-film}(T)$ can be written in the following equations,

$$\rho_{bulk}(T) = \rho_{0,bulk} + \rho_l(T) \tag{5.2}$$

$$\rho_{thin-film}(T) = \rho_{0,thin-film} + \rho_l(T) \tag{5.3}$$

Therefore, the resistivity difference between thin film Ti and bulk Ti is

$$\Delta\rho = \rho_{thin-film}(T) - \rho_{bulk}(T) = \rho_{0,thin-film} - \rho_{0,bulk} = \rho_{thin-film}(300) - \rho_{bulk}(300) \tag{5.4}$$

Consequently, the value from the table of bulk Ti resistivity versus temperature in the CRC Handbook can be adjusted for the thin film Ti by adding $\Delta\rho$

$$\rho_{thin-film}(T) = \rho_{bulk}(T) + \Delta\rho \tag{5.5}$$

The thin film Ti resistivity at 300 K ($\rho_{thin-film}(300)$) is measured using a Veeco FPP-5000 4-Point Probe. A Ti layer with the thickness of about 200 nm is deposited using E-beam on a 4-inch silicon wafer with silicon dioxide insulation layer. The deposition conditions are similar to those employed for fabricating the Au/Ti igniter of the microthruster. Then the sheet resistivity of Ti at 300 K is measured by the 4-Point Probe. The thin film Ti resistivity is obtained through multiplying the sheet resistivity by Ti layer thickness. The resistivity of thin film Ti at 300 K is $156.35 \times 10^{-8}\Omega \cdot m$, which is much higher than $51.1 \times 10^{-8}\Omega \cdot m$, the bulk Ti resistivity from Ref. [Lide 1998]. The estimated resistivity variation with temperature of thin film Ti using equation (5.5) is shown in Figure 5.1.

It is seen that the curve is fairly linear. A first-order regression fit of the data gives

$$\rho(T) = 2 \times 10^{-9}T + 1 \times 10^{-6} \tag{5.6}$$

with R^2 of 0.9938. R^2 is the proportion of total variation that is "explained" by the curve fit. R^2 is between 0 and 1. For a perfect fit $R^2 = 1$; lower values indicate a less good fit. The second-order fit is,

$$\rho(T) = -8 \times 10^{-13}T^2 + 3 \times 10^{-9}T + 8 \times 10^{-7} \tag{5.7}$$

R^2 is 0.9994. The third-order fit gives,

$$\rho(T) = -1 \times 10^{-15}T^3 + 2 \times 10^{-12}T^2 + 1 \times 10^{-9}T + 1 \times 10^{-6} \tag{5.8}$$

with a R^2 of 0.9999. Consequently, the third-order fit is chosen for $\rho(T)$.

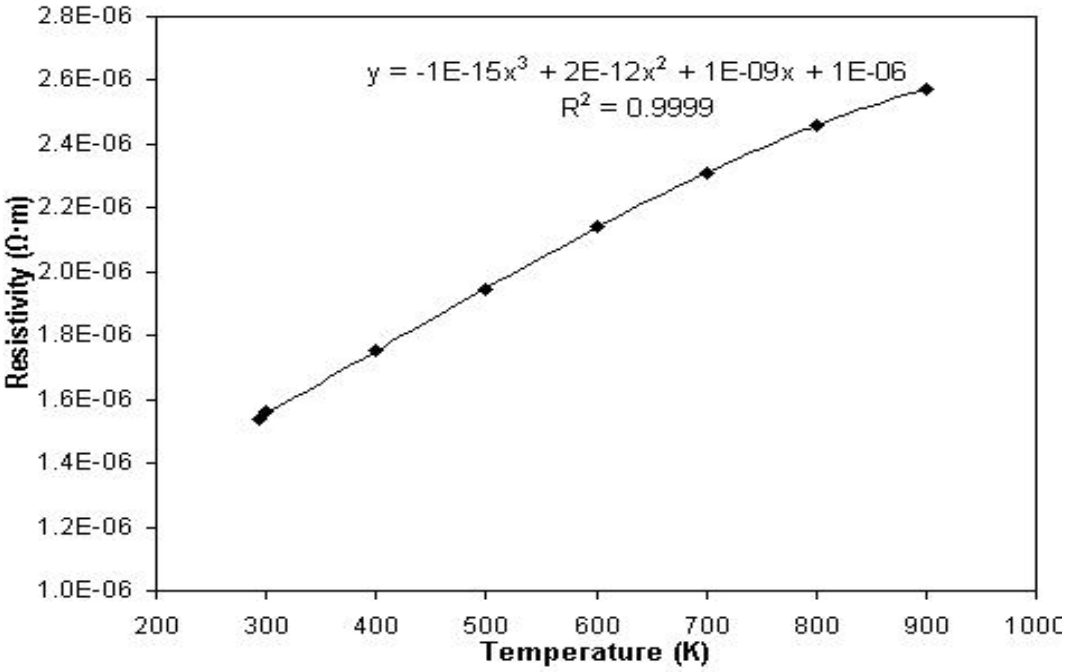

Figure 5.1. Estimated electrical resistivity and curve fit for thin film Ti.

5.3.2 Thermal Conductivity of Thin Film Titanium

The thermal conductivity of bulk Ti as a function of temperature can be found in Ref. [Lide 1998]. These data must be adjusted for thin film Ti because of the different microstructures of bulk and thin film Ti. Heat is transported in metal both by lattice vibrations (phonons) and electrons. In pure metals, the component of heat transport due to electrons dominates and the phonon effects can be neglected [Kittel 1996]. Both heat and electrical transport involve the free electrons in metal. The thermal conductivity κ increases with the average particle velocity since that increases the forward transport of energy. However, the electrical conductivity $\sigma(\sigma = 1/\rho)$ decreases with particle velocity increase because the collisions divert the electrons from forward transport of charge. This means that the ratio of thermal to electrical conductivity depends upon the average velocity squared, which is proportional to the kinetic temperature. The ratio of the thermal conductivity to the electrical conductivity illustrates the Wiedemann-Franz Law [Kittel 1996].

$$\kappa/\sigma = \kappa\rho = LT \tag{5.9}$$

where L, called the Lorentz number, is theoretically equal to $2.45 \times 10^{-8} W \cdot \Omega / K^2$. Measurements show this value to be the correct order of magnitude for most metals, although it is found to vary slowly with temperature. The value for Ti used here, based on several temperatures and references [Lide 1998, Kittel 1996, Vladislav 1998], is estimated as $3.09 \times 10^{-8} W \cdot \Omega / K^2$. No measurement of the thin film Ti thermal conductivity at room temperature is made. Instead, the Wiedemann-Franz Law is employed to obtain a value for κ (300 K) of 5.93 W/mK.

The thin film Ti thermal conductivity as a function of temperature is estimated as follows. The inverse of the thermal conductivity ($1/\kappa$, called thermal resistivity) is assumed to have two components. One is due to lattice defects ($1/\kappa_0$) and the other is due to thermal vibrations ($1/\kappa_l(T)$) in analogy to the electrical resistivity.

$$1/\kappa(T) = 1/\kappa_0 + 1/\kappa_l(T) \tag{5.10}$$

The thermal resistivity difference $\Delta(1/\kappa)$ between thin film and bulk Ti is written as

$$\begin{aligned} \Delta(1/\kappa) = 1/\kappa_{thin-film}(T) - 1/\kappa_{bulk}(T) &= 1/\kappa_{0,thin-film}(T) - 1/\kappa_{0,bulk}(T) \\ &= 1/\kappa_{thin-film}(300) - 1/\kappa_{bulk}(300) \end{aligned} \tag{5.11}$$

Therefore,

$$\kappa_{thin-film}(T) = (1/\kappa_{bulk}(T) + \Delta(1/\kappa))^{-1} \tag{5.12}$$

The thermal conductivity variation with temperature of thin film Ti using equation (5.12) is shown in Figure 5.2.

The third-order curve fit gives,

$$\kappa(T) = -2 \times 10^{-9} T^3 + 5 \times 10^{-6} T^2 + 0.0037T + 6.6715 \tag{5.13}$$

with a R^2 of 0.9997. Equation (5.13) will be used for thermal conductivity of thin film Ti in the modeling.

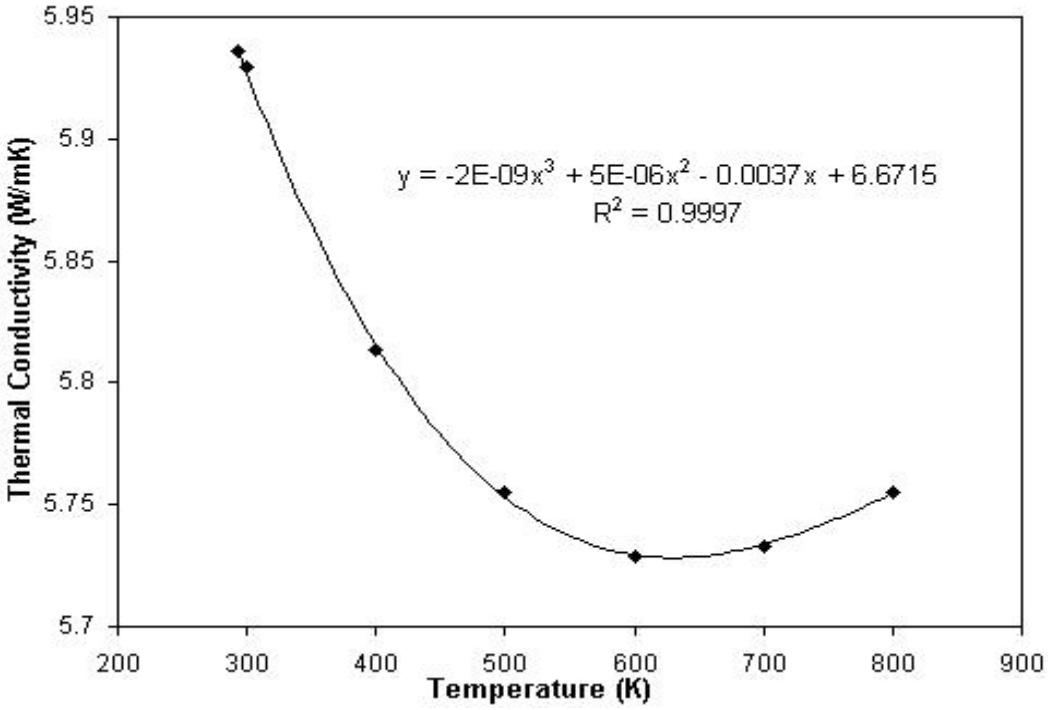

Figure 5.2. Estimated thermal conductivity and curve fit for thin film Ti.

5.3.3 Total Emissivity of Thin Film Titanium

The total emissivity ε is a surface radiative property defined as the ratio of the radiation emitted by the surface to the radiation emitted by a black body at the same temperature. The total emissivity of titanium as a function of temperature has been studied in Ref. [Weast 1984]. These values assume a smooth surface. Because the titanium used in this project is deposited in thin film onto a very smooth glass surface, it is indeed smooth and the emissivity values from Ref. [Weast 1984] do not need to be adapted for use here.

The fourth-order curve fit for the data from Figure 5.3 gives

$$\varepsilon(T) = 9 \times 10^{-13} T^4 - 2 \times 10^{-9} T^3 + 2 \times 10^{-6} T^2 - 0.0009T + 0.4426 \qquad (5.14)$$

which has a R^2 of 0.9988.

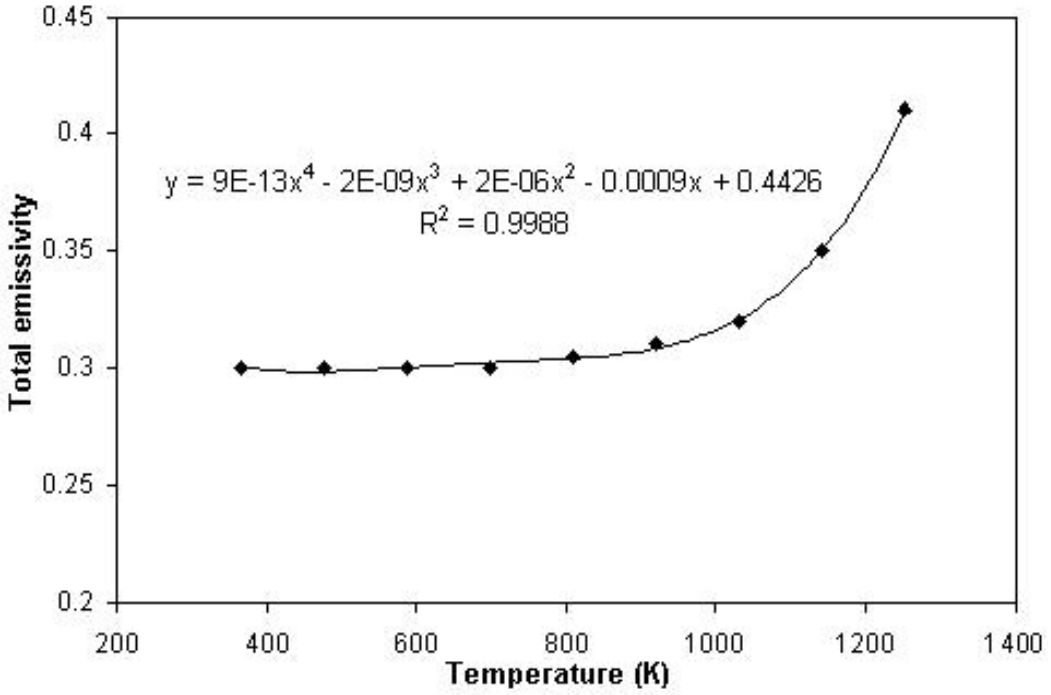

Figure 5.3. Emissivity of thin film Ti and curve fit.

5.3.4 Electrical Resistivity, Thermal Conductivity, and Total Emissivity of Thin Film Gold

The electrical resistivity and thermal conductivity of thin film Au are obtained in similar ways as those of thin film Ti. A layer of Au with a thickness of 77 nm is deposited on a 4-inch silicon wafer with silicon dioxide insulation layer using E-beam. The thin film Au resistivity at room temperature (300 K) is measured using a Veeco FPP-5000 4-Point Probe. The thin film Au resistivity variation with temperature is calculated with the Matthiessen's Rule and bulk Au resistivity data from Ref. [Lide 1998]. The thermal conductivity of thin film Au as a function of temperature is achieved by Wiedemann-Franz Law and bulk Au thermal conductivity data from Ref. [Lide 1998]. The electrical resistivity and thermal conductivity of thin film Au are shown in Figures 5.4 and 5.5, respectively.

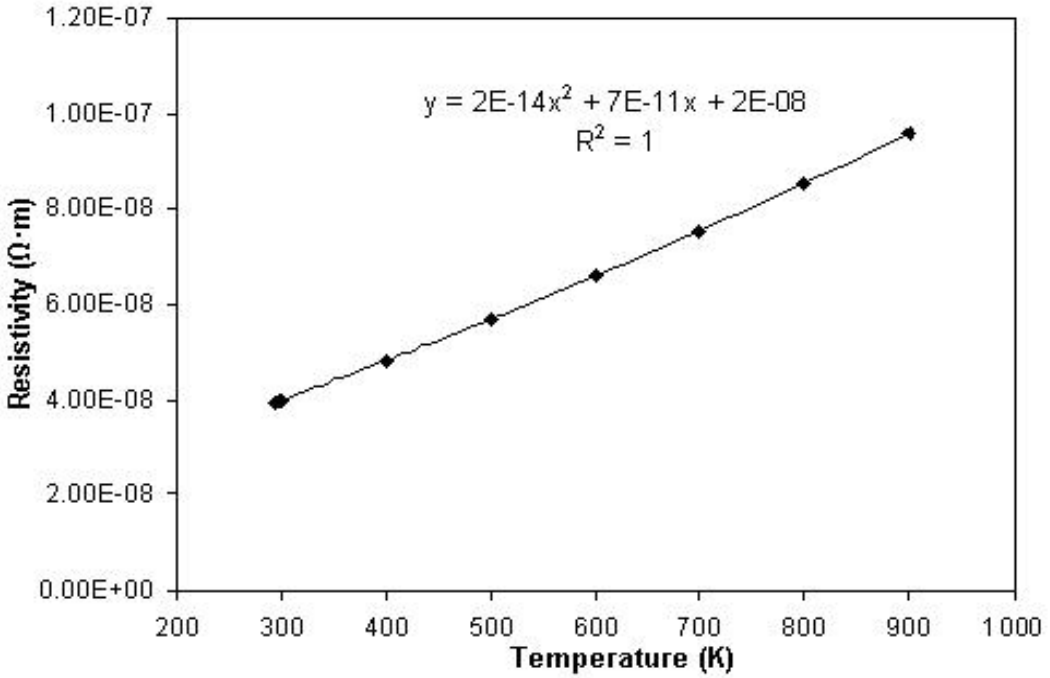

Figure 5.4. Estimated electrical resistivity and curve fit for thin film Au.

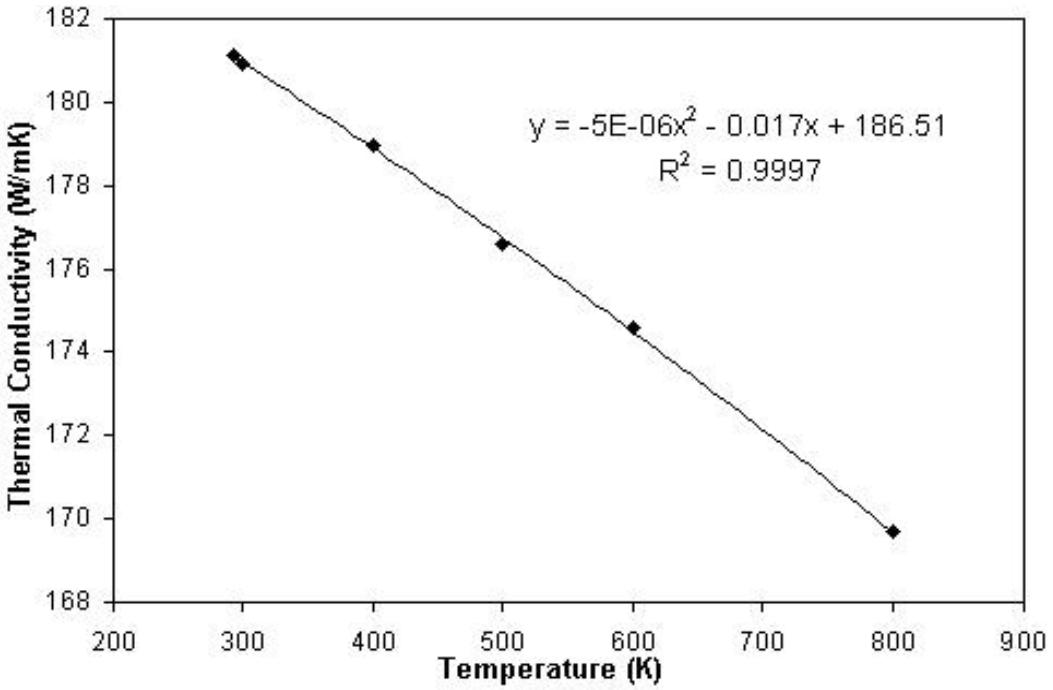

Figure 5.5. Estimated thermal conductivity and curve fit for thin film Au.

The curve fit for electrical resistivity gives

$$\rho(T) = 2 \times 10^{-14} T^2 + 7 \times 10^{-11} T + 2 \times 10^{-8} \tag{5.15}$$

R^2 is 1. The curve fit for thermal conductivity gives

$$\kappa(T) = -5 \times 10^{-6}T^2 - 0.017T + 186.51 \tag{5.16}$$

which has a R^2 of 0.9997.

The total emissivity of Au is obtained from Ref. [Wood et al 1969]. There are only two data available (ε = 0.02 at T = 373 K; ε = 0.03 at T = 873 K). The variation of Au total emissivity with temperature is assumed to be linear and curve fit gives

$$\varepsilon(T) = 3 \times 10^{-5}T + 0.0082 \tag{5.17}$$

5.3.5 Thermal Conductivity of Thin Film Silicon Dioxide

The silicon dioxide is a wet grown thermal oxide with a thickness of 246 nm. Its thermal conductivity as a function of temperature is obtained from Ref. [Shackelford 1994] as shown in Figure 5.6 together with the curve fit.

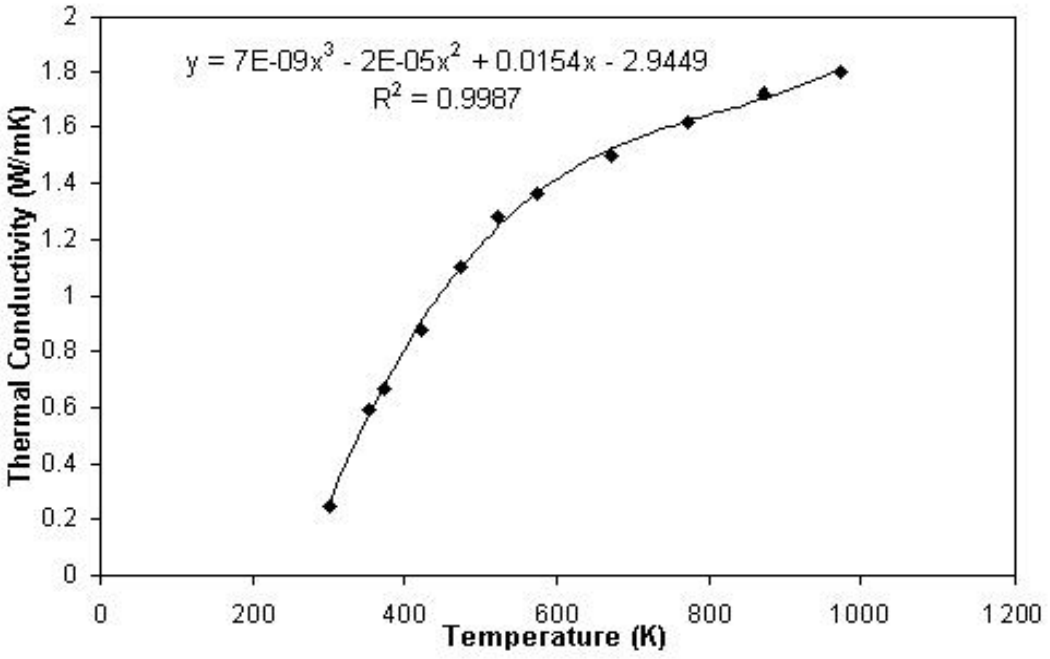

Figure 5.6. Estimated thermal conductivity and curve fit for thin film SiO_2.

5.3.6 Specific Heat of Thin Film Titanium, Gold, and Silicon Dioxide

The specific heats of thin film Ti, Au, and SiO_2 are supposed to be similar to those of bulk Ti, Au, and SiO_2. These data are from Ref. [Lide 1998] as shown in Figure 5.7 together with the curve fits. A summary of the materials' properties is listed in Table 5.1.

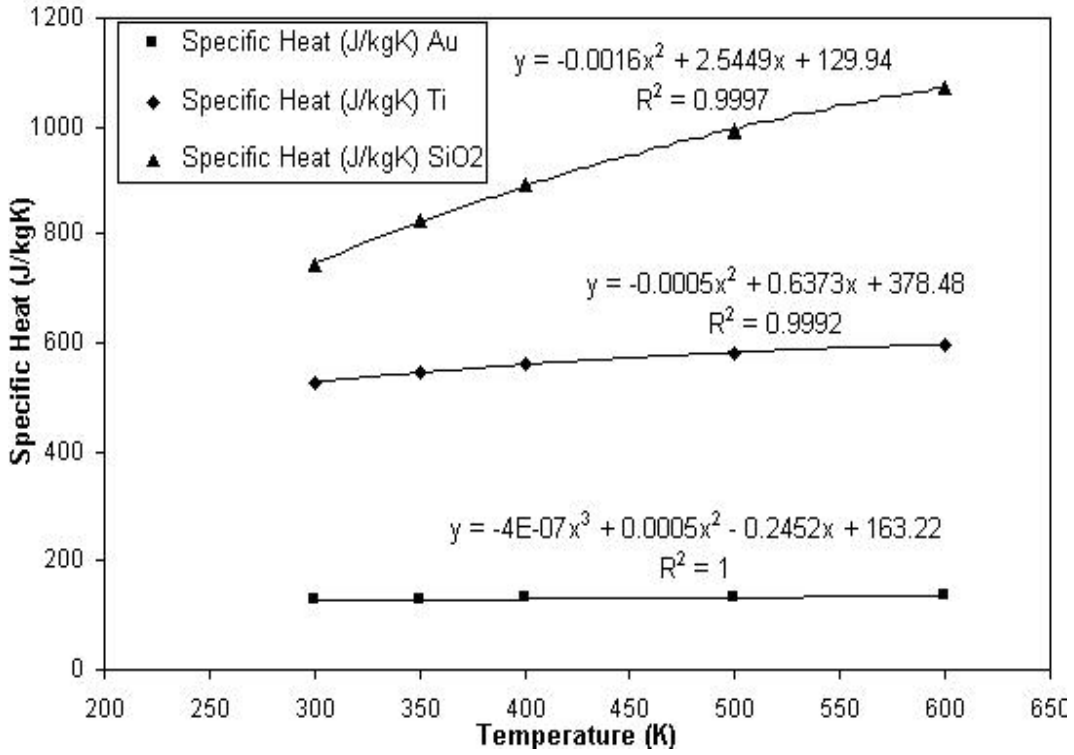

Figure 5.7. Estimated specific heats and curve fits for thin film Ti, Au and SiO_2.

5.4 Finite-element Modeling of the Thin Film Au/Ti Micro-heater

The Au/Ti igniter is a key part of the solid propellant microthruster for igniting the propellant. However, the Au/Ti igniter itself, as a kind of micro-heater, has many

Table 5.1. Material properties

	Thin film Ti	Thin film Au	Thin film SiO_2	Silicon	Pyrex 7740	Propellant
Electrical resistivity $(\Omega \cdot m)$	$\rho(T)$	$\rho(T)$	1×10^{16}	1	1.26×10^6	∞
Thermal conductivity (W/mK)	$\kappa(T)$	$\kappa(T)$	$\kappa(T)$	141.2	1.18	0.65
Density (Kg/m^3)	4507	19320	2200	2330	2230	1870
Specific heat (J/KgK)	$C_p(T)$	$C_p(T)$	$C_p(T)$	713.5	753.12	1790
Emissivity	$\varepsilon(T)$	$\varepsilon(T)$				

other potential applications such as pressure measurement [Herwaarden and Sarro 1988], thermal regulation [Oh et al 1992], and gas detection [Gajda and Ahmed 1995]. Moreover, because there is no propellant covered on the Au/Ti micro-heater, it is more convenient to characterize the micro-heater temperature distribution experimentally. Consequently, it is easier to validate the finite-element modeling by experiments. Therefore, it is necessary to perform the modeling for the Au/Ti micro-heater itself firstly.

5.4.1 Geometry and Meshing

The dimensions of the simulated Au/Ti micro-heater are exactly the same as the Au/Ti micro-heater fabricated in Chapter 4 (see Figures 4.3 and 4.4). The geometry of the simulated Au/Ti micro-heater is shown in Figure 5.8. The thin film Au/Ti micro-heater is fabricated on a piece of Pyrex-7740 glass by e-beam deposi-

tion. The thickness of Ti, Au, and Pyrex-7740 glass are 0.206 μm, 0.077 μm, and 550 μm, respectively.

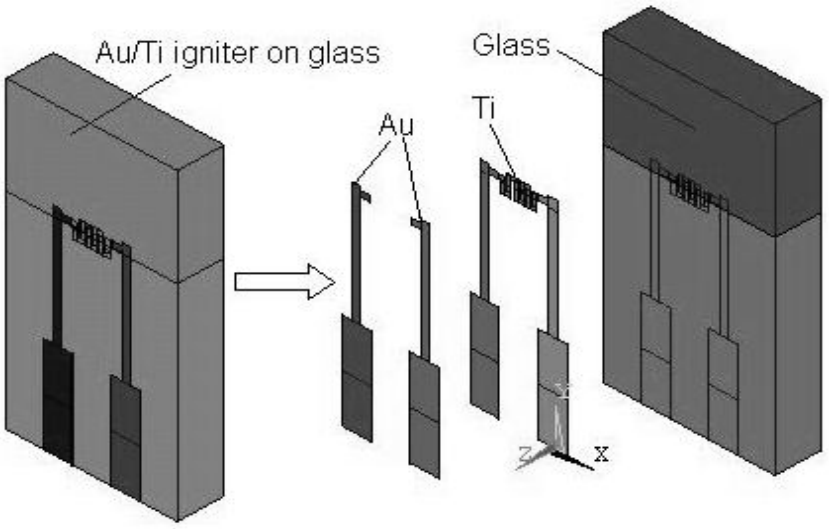

Figure 5.8. Geometry of the simulated Au/Ti micro-heater.

The nonlinear thermal-electric coupled-field problem is solved using coupled-field element (SOLID98) in ANSYS. SOLID98 is a 10-node tetrahedral element. The element has a quadratic displacement behavior and is well suited to model irregular meshes. When used in structural and piezoelectric analyses, SOLID98 has large deflection and stress stiffening capabilities. The coupled-field problem is solved using the direct method. The direct method performs the coupled-field analysis in one step using coupled-field elements. A model that is meshed (divided into elements) too coarsely will yield incorrect results. However, a model that is meshed more finely than required for correct results will greatly slow the simulation speed. Therefore, appropriately fine mesh for the Au/Ti micro-heater must be found. For ease of meshing, it is advantageous to break up regions of a given material into high- and low-density-mesh regions. The thin film Au conductor and thin film Ti resistor have the finest mesh to simulate the electro-thermal process more accurately as shown in Figures 5.9 and 5.10 (not to same scale), respectively. Nodes are located at the intersections of the lines. For the glass layer, the region

near the Ti resistor is meshed finely to match the Ti layer mesh and to capture the conductive heat transfer; the mesh becomes coarser away from this region as shown in Figure 5.11.

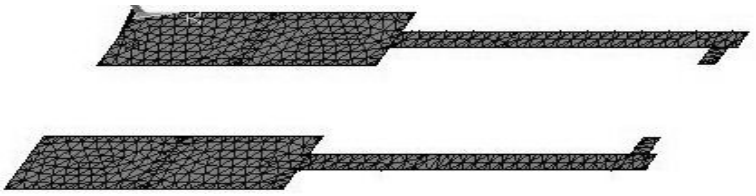

Figure 5.9. Meshed thin film Au layer.

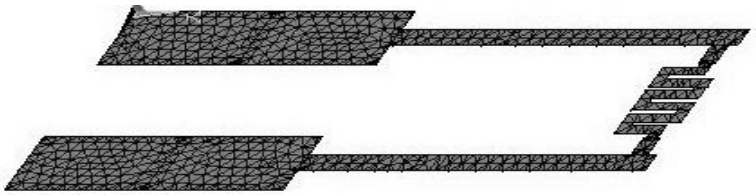

Figure 5.10. Meshed thin film Ti layer.

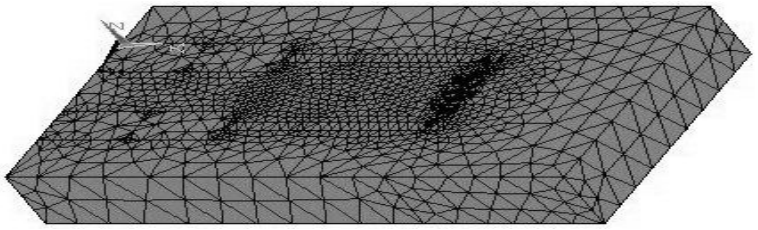

Figure 5.11. Meshed glass layer.

The computational grids used for the simulations are determined by performing grid-independent study to minimize the modeling error. When the change in the solution between subsequent stages of grid refinement is considered to be negligible, the lower, but still sufficient, grid resolution is kept. The micro-heater maximum

temperature that is crucial to the application, is compared among different stages of grid refinement as shown in Figure 5.12. The results are obtained at 1 ms with a voltage of 10 V. Finally, the model is meshed using 38320 nodes.

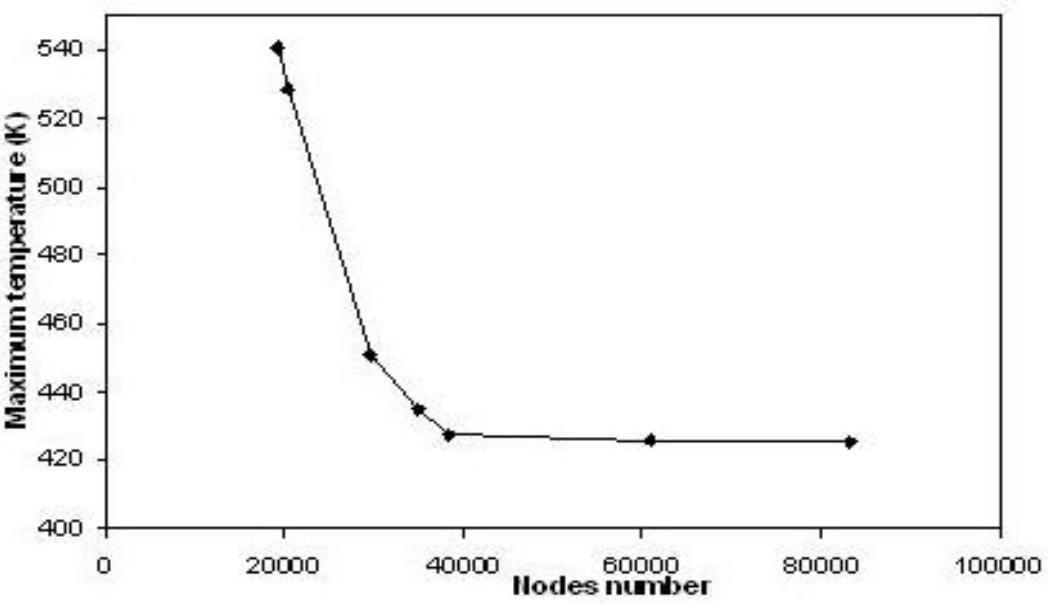

Figure 5.12. Grid-independent study.

5.4.2 Boundary Conditions and Initial Condition

The next step in setting up this finite-element model is entering the boundary conditions. The boundary conditions are as follows: the temperature of the ambient is 300 K; heat convection on all the surfaces of the structure in contact with ambient air; the ohmic heating in the element volumes; and radiation power from the element surfaces. The ohmic heating and radiation are both functions of the temperature of each element. To model the radiation power flow to and from each element, making a single node in "space" and fixing its temperature at the ambient temperature is required. Radiation power flows away from the hot micro-heater to the ambient and also from the ambient to the micro-heater. For this transient modeling, the initial temperature of the entire structure is set to be

300 K. The heat convection coefficient value of 100 W/m^2K estimated by Infra-red (IR) method in Ref. [Rossi et al 1997] is used here because the polysilicon micro-heater in Ref. [Rossi et al 1997] has similar structure and conditions as the Au/Ti micro-heater in this research. Due to the small size of the heated structures, the heat convection losses are supposed to be negligible at median-low temperatures for micro-heater. To study the effect of heat convection on the Au/Ti micro-heater temperature, simulation is performed for the micro-heater with different convection coefficient values of 100 W/m^2K and 10 W/m^2K, respectively. Figure 5.13 is the micro-heater maximum temperature comparison with a voltage of 8 V. When the micro-heater maximum temperature is below 673.15 K, the temperature difference is within 1 % even if the convection coefficient increases from 10 W/m^2K to 100 W/m^2K. When the maximum temperature is below 773.15 K, the difference is within 7 %. Because the work temperature of the Au/Ti micro-heater is below 773.15 K, the effect of convection coefficient can be neglected. Therefore, 100 W/m^2K is safely employed for the following simulations.

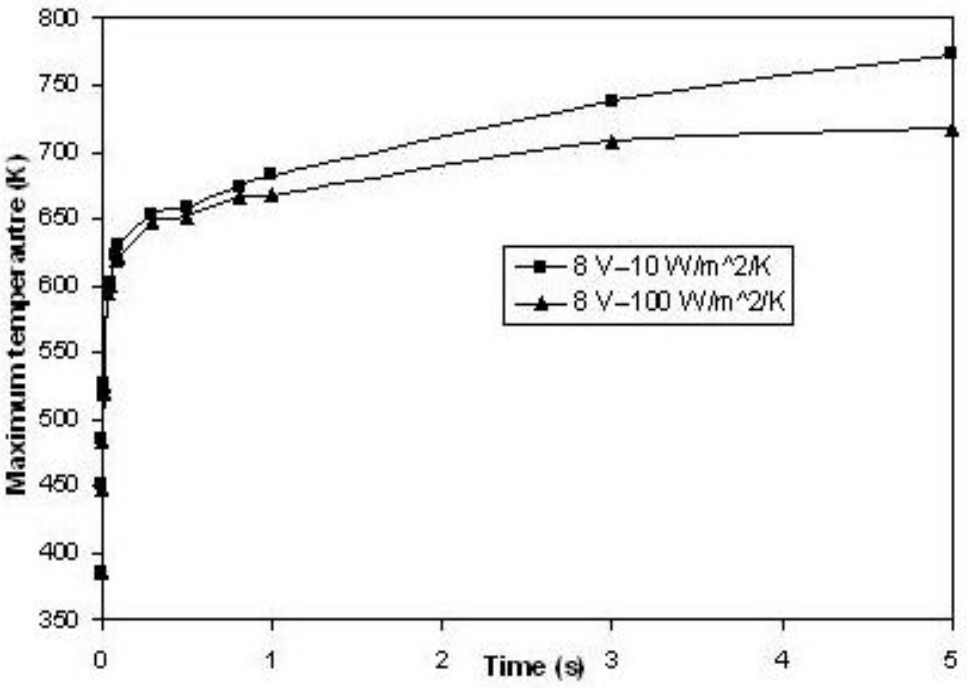

Figure 5.13. Effect of heat convection coefficient.

5.4.3 Simulation Results

Initial Comparison between Experiment and Modeling

A simple experiment is performed to visually verify the finite-element model. A Au/Ti micro-heater is connected to a voltage power source for long time so that part of the Ti is damaged because of long time exposure to high temperature. A photo is taken for the zigzag Ti part of the Au/Ti micro-heater using a microscope as shown in Figure 5.14 (a). The temperature profile of the Ti resistor when connecting to a voltage source can be indicated by Figure 5.14 (a). Then finite-element modeling is performed for the Au/Ti micro-heater. The simulated temperature profile of the Ti resistor is shown in Figure 5.14 (b). The temperature profiles from the experiment and modeling match very well. A more precise temperature comparison between experiment and modeling is presented in Section 7.4.3, Chapter 7.

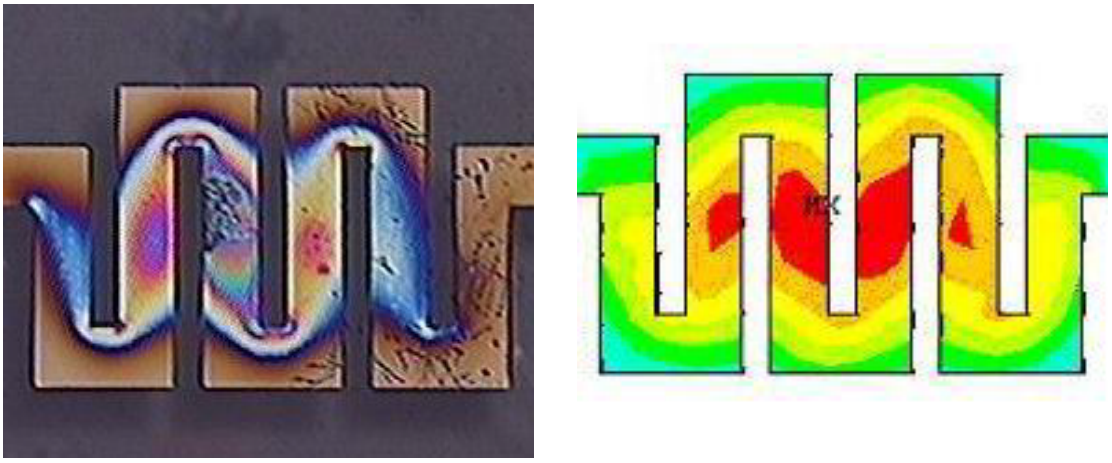

(a) (b)

Figure 5.14. (a) Micro-heater temperature profile from experiment. (b) Micro-heater temperature profile from modeling.

Micro-heater Temperature Variation with Time and Space

The micro-heater temperature variation with time and space is very useful for understanding the thin film heater performance and for better device themal management. Figures 5.15 to 5.18 show the micro-heater temperature (K) variation from 1 ms to 10 s with a voltage input of 10 V. For a thin film heater, minimizing thermal heat loss is the key to gain better thermal yield (maximum temperature over the electrical power consumption). One way to reduce considerably the thermal loss is to have a good heat confinement. It can be seen from these figures that a good heat confinement is achieved for the Au/Ti micro-heater. The temperature at the designed part (Ti resistor part) increases rapidly, whereas the temperature does not change very much at other parts. This is mainly caused by the zigzag micro-heater design and the better thermal insulation property of Pyrex 7740 glass substrate compared to silicon substrate.

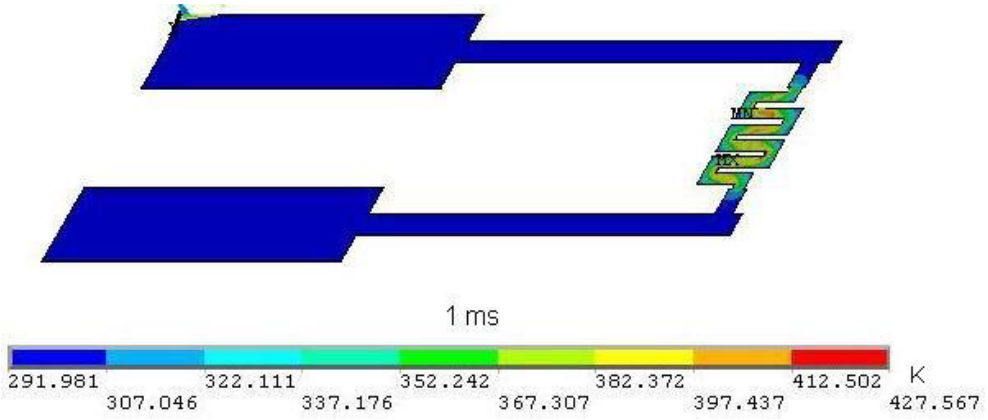

Figure 5.15. Ti resistor temperature profile at 1 ms.

Thermal Radiation Effect on Micro-heater Maximum Temperature

Thermal radiation is an important way of heat loss, especially for high temperature objects. Because the micro-heater is supposed to operate in high temperature range, the radiation heat loss of the micro-heater should be addressed. Figure 5.19

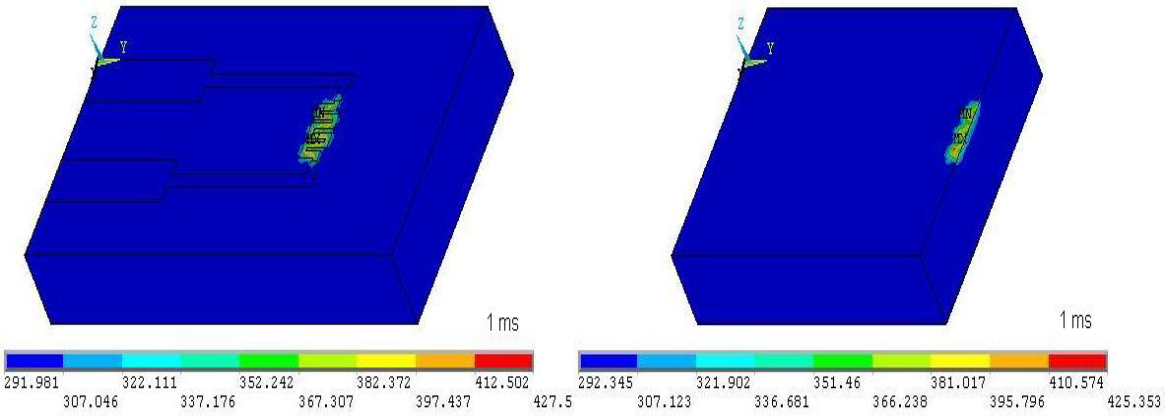

(a) (b)

Figure 5.16. (a) Temperature profile at 1 ms. (b) Temperature profile at 1 ms.

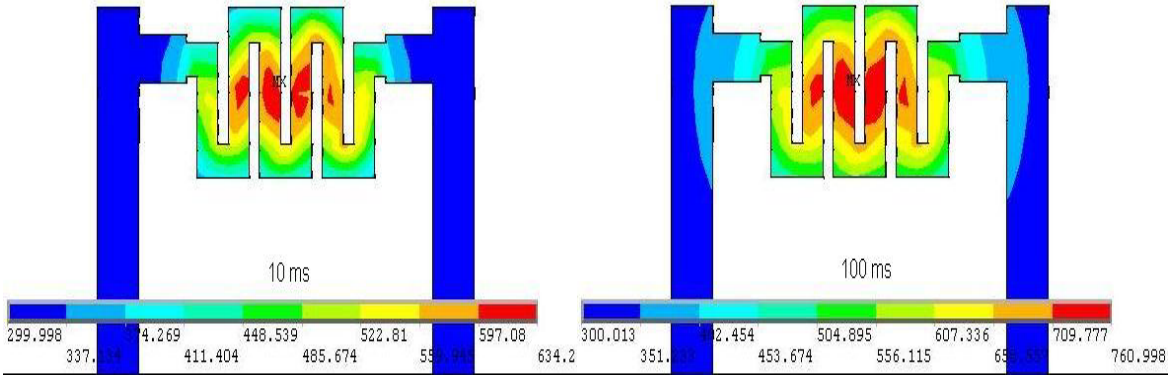

(a) (b)

Figure 5.17. (a) Ti temperature at 10 ms. (b) Ti temperature at 100 ms.

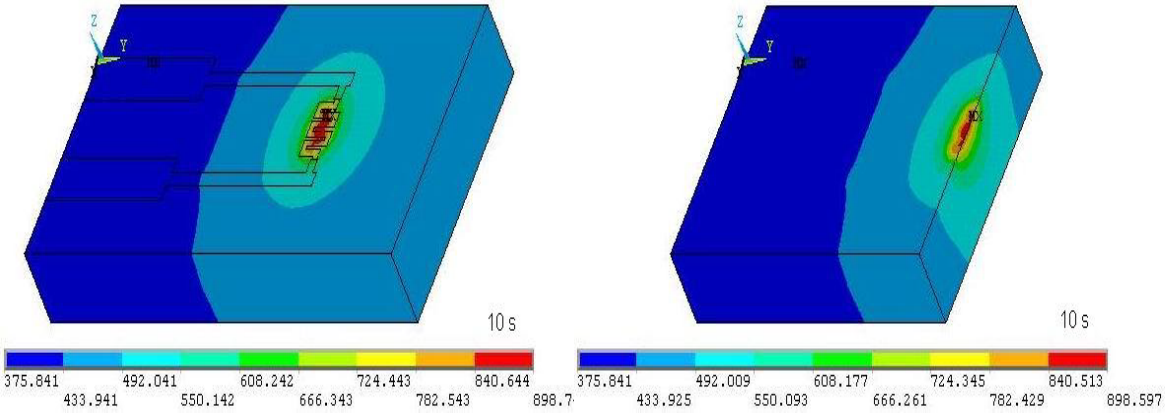

(a) (b)

Figure 5.18. (a) Temperature profile at 10 s. (b) Temperature profile at 10 s.

shows the effect of radiation heat loss on the micro-heater maximum temperature wit a voltage input of 10 V. The micro-heater maximum temperature changes only

2.43 % because of radiation loss even if the micro-heater maximum temperature increases to 898.74 K. Consequently, the radiation heat loss is neglected in the following simulations.

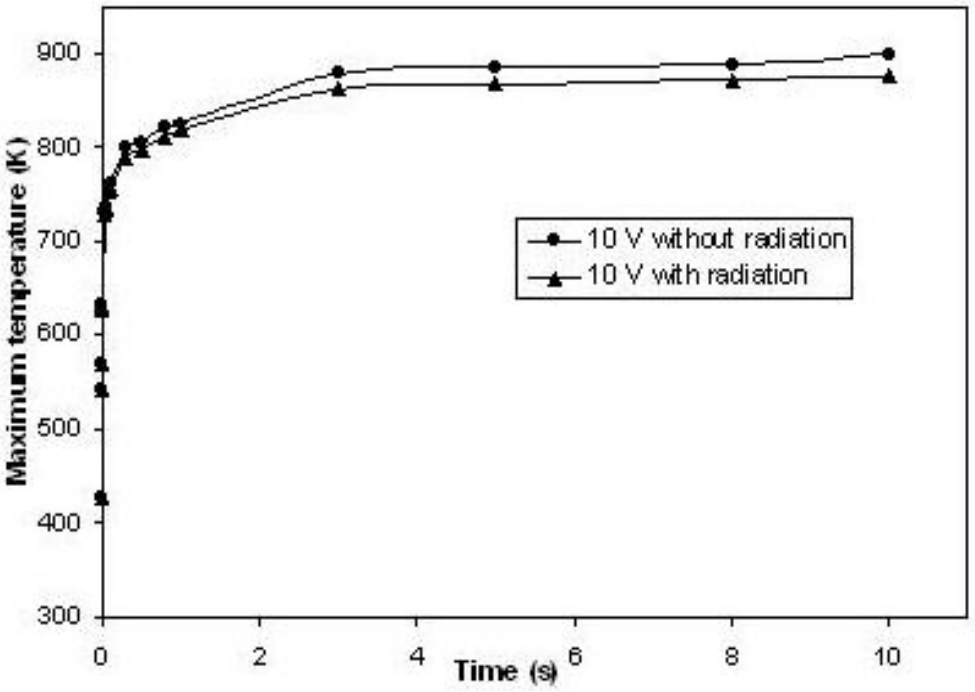

Figure 5.19. Effect of thermal radiation heat loss.

Micro-heater Maximum Temperature Variation with Voltage

The micro-heater maximum temperature is a key parameter of the thin film heater, especially for ignition purpose. Figure 5.20 shows the micro-heater maximum temperature variation as a function of voltage. The curves indicate that the maximum temperature increases quickly at the early stage of voltage (power) supply but increases slowly after around 4 s. This is because of the equilibrium between heat generation by Joule effect and heat loss by convection and conduction. The micro-heater maximum temperature can be controlled by adjusting the power supply.

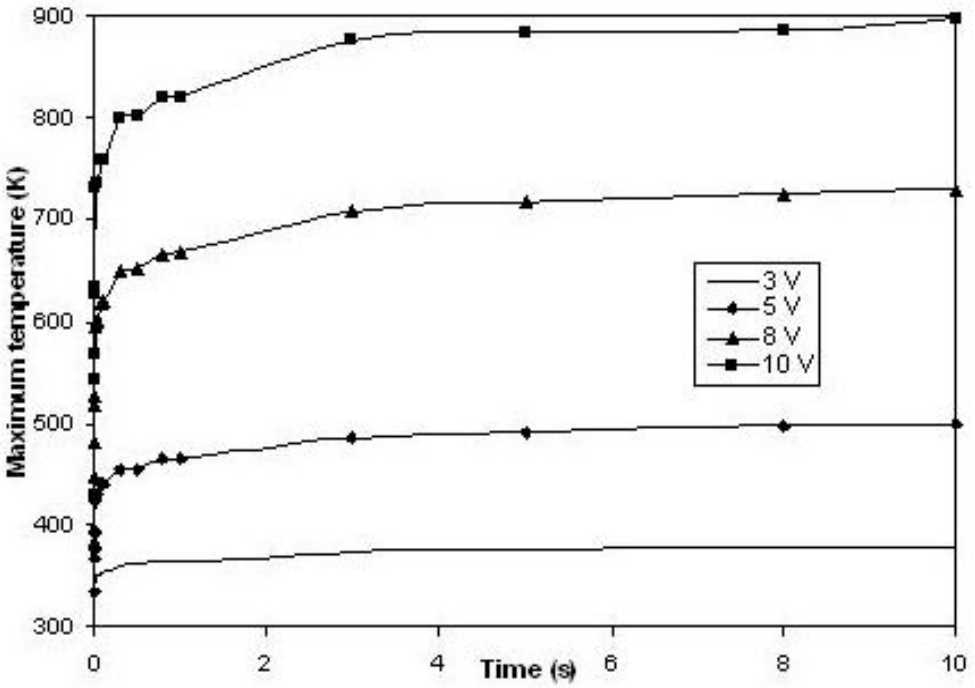

Figure 5.20. Maximum temperature variation with voltage.

5.5 Finite-element Modeling of the Solid Propellant Microthruster with Au/Ti Igniter

In this section, we present the finite-element modeling for the ignition process of the solid propellant microthruster with Au/Ti igniter. As discussed in Section 4.3.3, an optimum ignition process is needed to improve the ignition efficiency. The finite-element modeling can simulate the transient ignition process so as to minimize the ignition energy that is defined as the product of ignition power and ignition delay.

5.5.1 Geometry and Meshing

The dimensions of the simulated microthruster with Au/Ti igniter are exactly the same as the microthruster with Au/Ti igniter fabricated in Chapter 4 (see Figures 4.3, 4.5, and 4.7). The geometry of the simulated microthruster with Au/Ti igniter is shown in Figure 5.21. Figure 5.22 illustrates all the components with different material properties in the model.

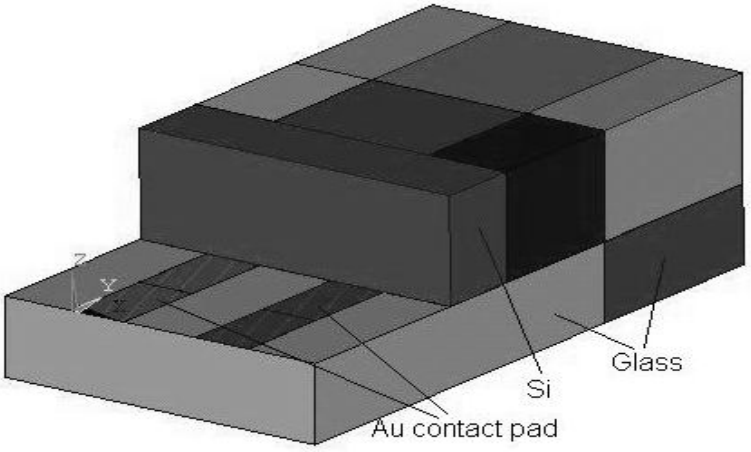

Figure 5.21. Geometry of the simulated microthruster with Au/Ti igniter.

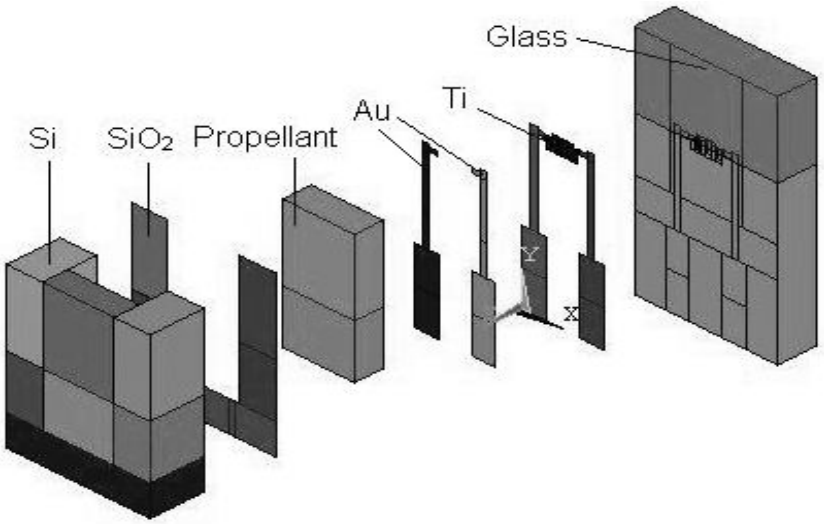

Figure 5.22. Components of the simulated microthruster.

The meshing strategy for the microthruster is similar to that for the Au/Ti micro-heater in Section 5.4. The mesh for the three-dimensional microthruster structure is shown in Figure 5.23. The meshes for Au layer, Ti layer, and glass layer are similar to those in Section 5.4 shown in Figures 5.9 - 5.11, respectively. For the solid propellant, the region near the Ti resistor is meshed finely to match the Ti layer mesh and to capture the conductive heat transfer; the mesh becomes coarser

away from this region as shown in Figure 5.24. The maximum temperature of the propellant is selected for the grid-independent study. Finally, the microthruster model is meshed using 40805 nodes.

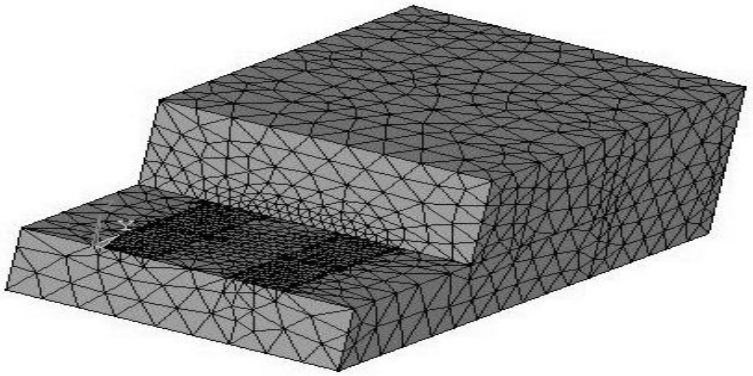

Figure 5.23. Meshed microthruster with Au/Ti igniter.

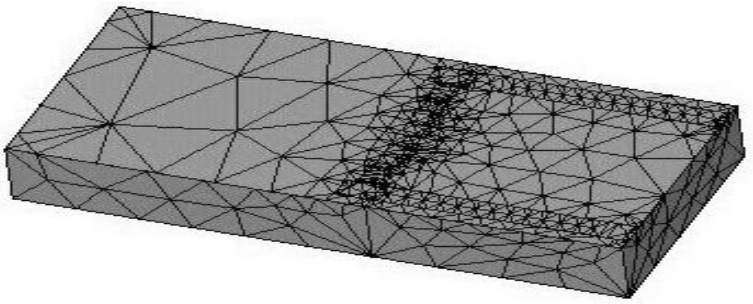

Figure 5.24. Meshed solid propellant layer.

5.5.2 Boundary Conditions and Initial Condition

The initial condition and boundary conditions are similar to those in Section 5.4.2 except that radiation is not considered because the high temperature part of the Au/Ti igniter is covered by the propellant and silicon layer.

5.5.3 Simulation Results

Propellant Temperature Variation with Time and Space

The propellant temperature variation with time and space is very important for understanding the ignition process. Figures 5.25 - 5.27 show the propellant temperature variation from 1 ms to 10 s with a voltage input of 10 V. The cross-section views of the propellant temperature profile are also shown in these figures.

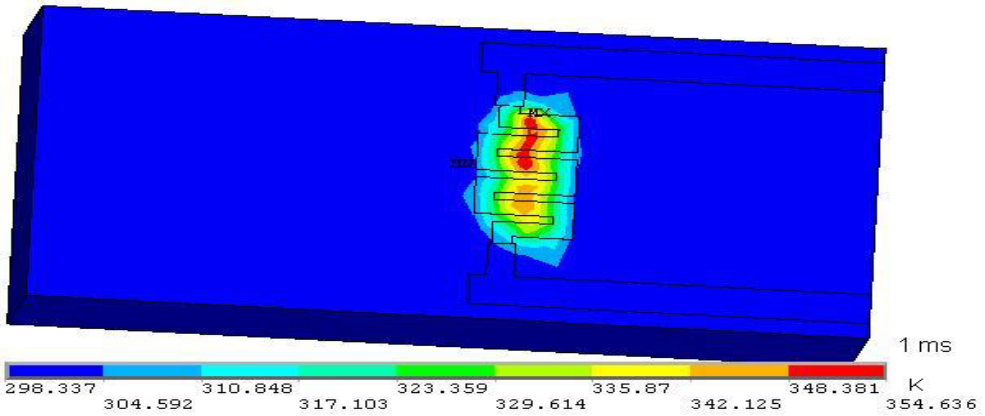

Figure 5.25. Propellant temperature profile at 1 ms.

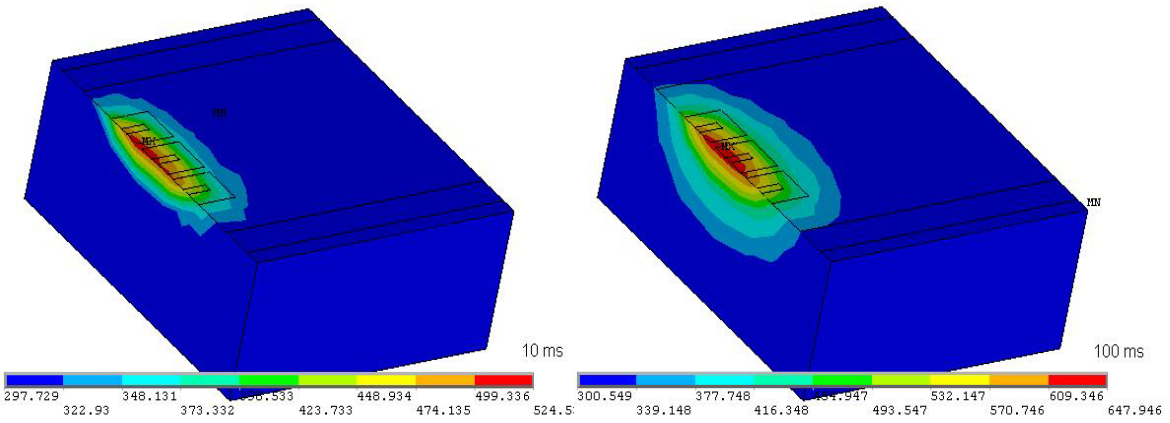

(a) (b)

Figure 5.26. (a) Propellant temperature at 10 ms. (b) Temperature at 100 ms.

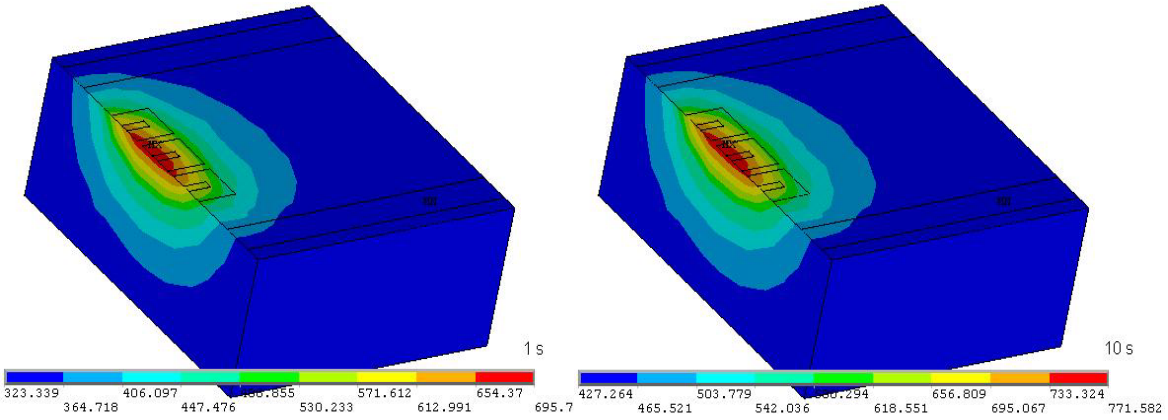

(a) (b)

Figure 5.27. (a) Propellant temperature at 1 s. (b) Temperature at 10 s.

Propellant Maximum Temperature Variation with Voltage

The propellant maximum temperature is a key parameter for the ignition. Figure 5.28 shows the propellant maximum temperature variation as a function of voltage. The curves indicate that the maximum temperature increases quickly at the early stage of voltage (power) supply but increases slowly after around 1 s. This is because of the equilibrium between heat generation by Joule effect and heat loss by conduction. The propellant maximum temperature and thus the ignition process can be controlled by adjusting the voltage supply. The simulation results show that below a certain voltage close to 8 V, the ignition fails even if the application time is infinite. In fact, if the voltage is lower than 8 V, the propellant temperature reaches its steady state characterized by a constant maximum temperature lower than the ignition temperature (613.15 K). When the voltage is higher than 8 V, the ignition delay decreases with the increase of voltage supply.

Ignition Power, Ignition Delay, Ignition Energy, and Ignition Efficiency

One main purpose of the electro-thermal modeling is to find an optimum voltage (power) supply so as to minimize ignition energy and to improve ignition efficiency. Figure 5.29 shows ignition power and ignition delay variations as a function of volt-

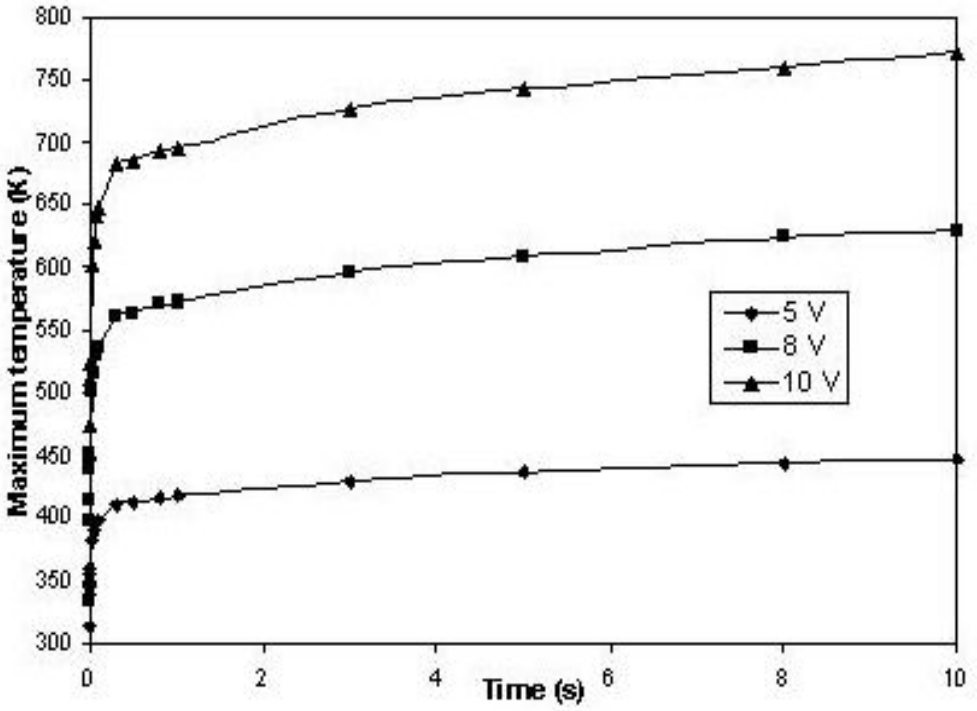

Figure 5.28. Propellant maximum temperature variation with voltage.

age. Ignition power increases and ignition delay decreases when the voltage supply is increased. Ignition delay changes more drastically with the voltage compared to ignition power. Therefore, ignition delay is the main factor that affects ignition energy, and thus, ignition efficiency.

Figure 5.30 is the ignition energy variation as a function of voltage. Ignition energy decreases rapidly with voltage when voltage is below 15 V. When voltage is over 15 V, ignition energy decreases slowly and reaches the lowest value at 22 V. When voltage is higher than 22 V, ignition energy increases slowly with voltage. The trend is similar to that of thin film polysilicon igniter studied in Ref. [Rossi et al 1998b]. According to the modeling, 22 V is the optimum voltage input for highest ignition efficiency. Besides ignition efficiency, the capability of voltage source power supply also needs to be considered in actual applications, especially for a wireless circuitry with battery as the power supply.

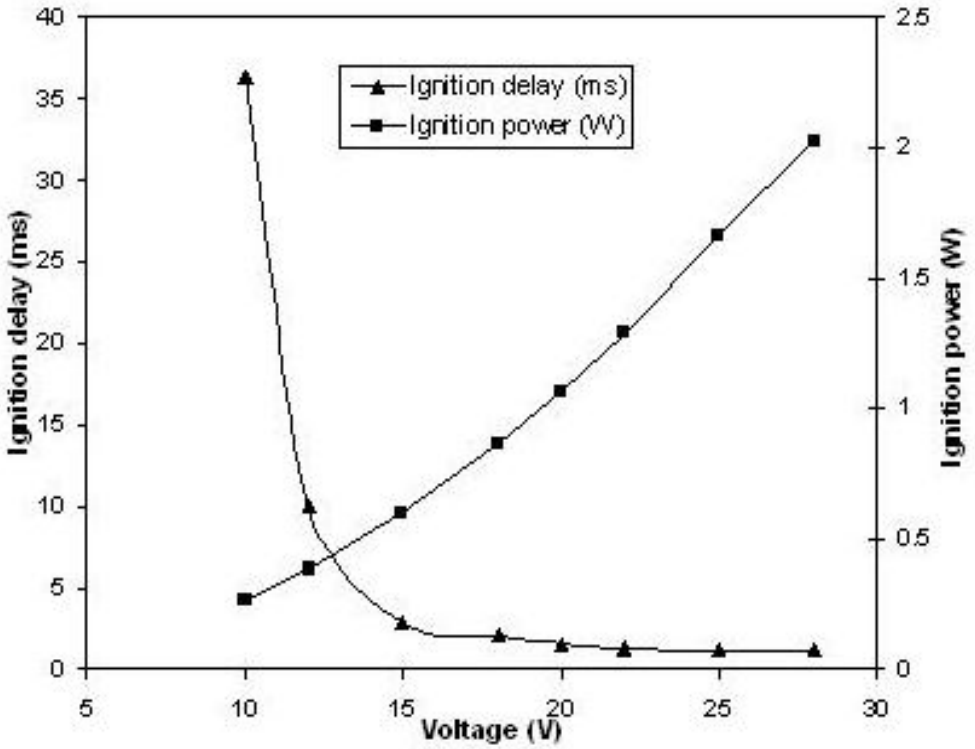

Figure 5.29. Ignition power and ignition delay variations with voltage.

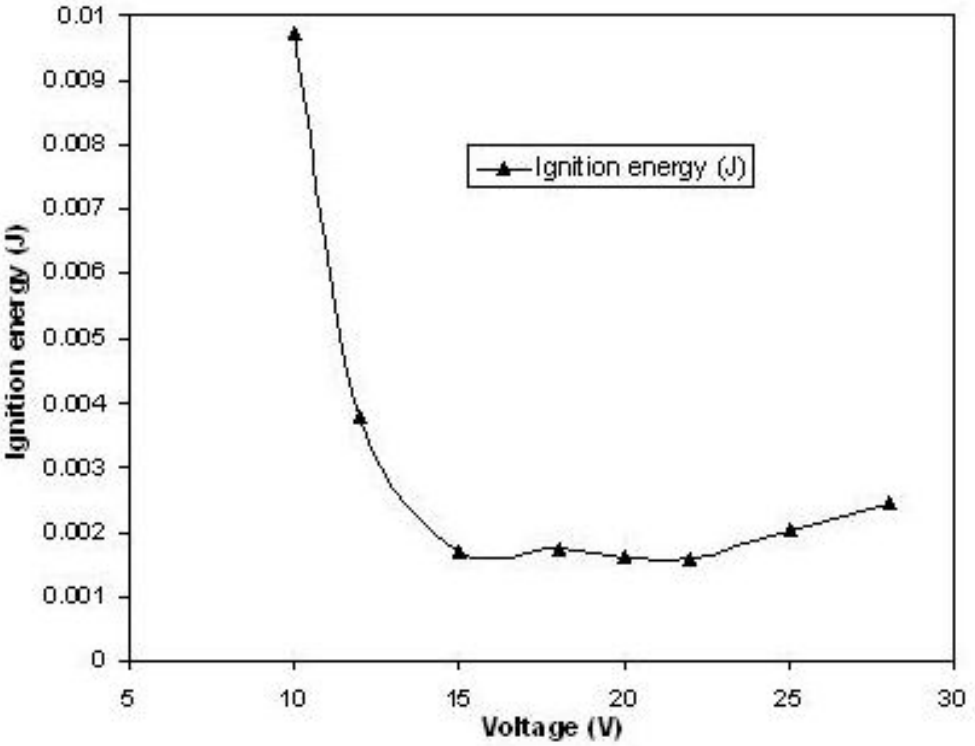

Figure 5.30. Ignition energy variation as a function of voltage.

Figure 5.31 shows the entire structure temperature profile at the time of ignition with a voltage input of 10 V. Although the glass substrate has a better thermal resistance than silicon (thermal conductivity: Pyrex-7740 glass, 1.18 W/mK; silicon, 141.2 W/mK), it is still possible to have a large heat loss because the thin film heater is directly deposited onto the glass substrate.

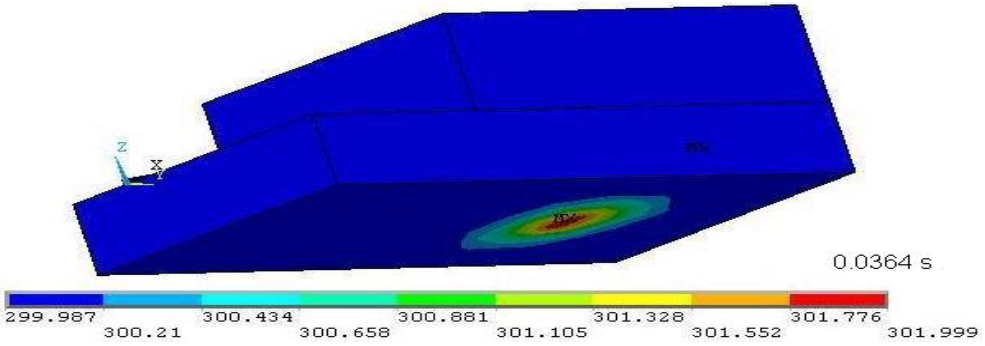

Figure 5.31. The entire structure temperature profile at the time of ignition.

To document heat loss through the glass substrate and to address the ignition efficiency, simulation is performed with the assumption of adiabatic glass substrate. Figure 5.32 shows the propellant maximum temperature comparison between the condition of adiabatic substrate and that of non-adiabatic substrate with a voltage input of 10 V. The maximum temperature becomes much higher if the substrate is assumed to be adiabatic. The ignition energy for adiabatic substrate is 0.00157 J, which is much lower than that (0.00974 J) for non-adiabatic substrate. Therefore, a better way is expected to reduce the heat loss through the substrate and to improve the ignition efficiency.

Effect of Silicon Dioxide on Ignition Efficiency

As stated in Section 4.2, Chapter 4, a thermal oxidation process is performed for the silicon part of the microthruster. After thermal oxidation, the entire silicon

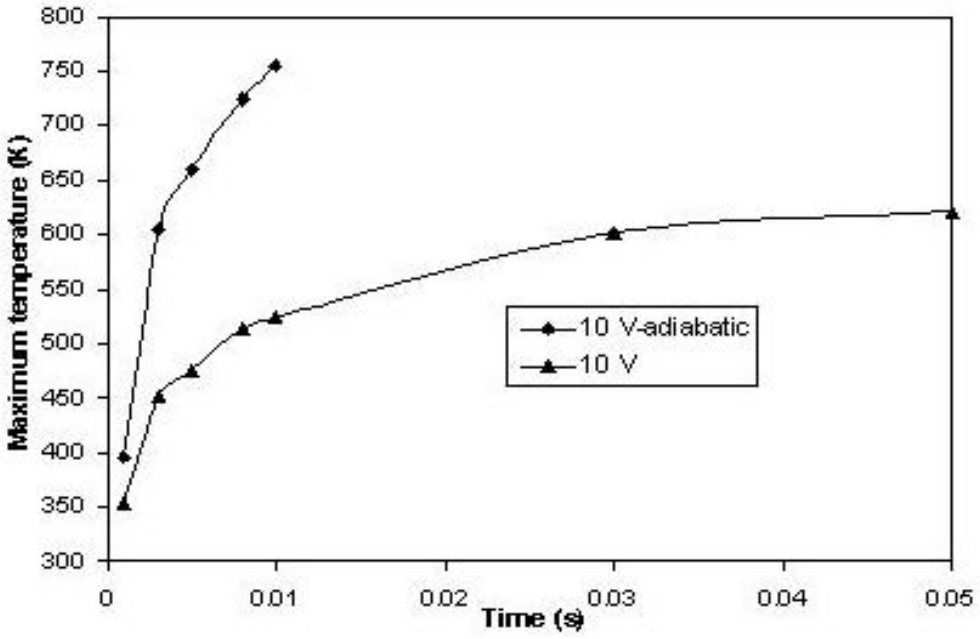

Figure 5.32. Effect of heat loss through glass substrate.

part is covered by the silicon dioxide with a thickness of 246 nm. The insulation performance of the silicon is improved by the thermal oxidation process. Consequently, the ignition efficiency is expected to increase because of the decrease of the possible current leakage. Figure 5.33 shows the propellant maximum temperature variation as a function of time with and without SiO_2 layer. With a same voltage input of 10 V, the propellant maximum temperature with SiO_2 layer is higher than that without SiO_2 layer. Moreover, the ignition energy (0.00974 J) with SiO_2 layer is much lower than that (0.03465 J) without SiO_2 layer. Therefore, the thermal oxidation process in the fabrication is a valuable choice for improving the ignition efficiency although the anodic bonding requires higher power for its formation due to the existence of this SiO_2 layer.

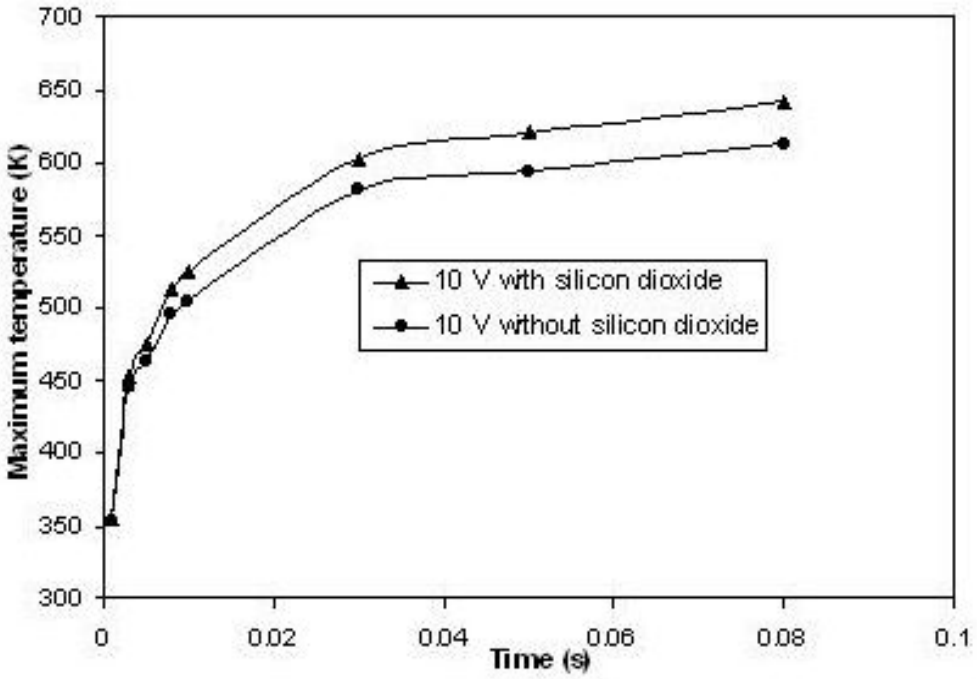

Figure 5.33. Effect of SiO_2 layer on ignition efficiency.

5.5.4 Comparison between Experimental Measurement and Electro-thermal Modeling

The comparison between the experimental testing and electro-thermal modeling for the solid propellant microthruster with Au/Ti igniter is presented in Section 7.5.3, Chapter 7.

5.6 Chapter Summary

Thin film Au/Ti characteristics are very much different from those of bulk Au/Ti. A method is presented to estimate the temperature variation of resistivity and thermal conductivity for our thin film Au/Ti that is based on a room-temperature measurement of resistivity and trends of the variations reported in the literature. Finite-element modeling is introduced and used to simulate the entire three-dimensional device structure both for the Au/Ti micro-heater and the solid propellant microthruster with Au/Ti igniter. Initial comparison between experiment and modeling is performed for the Au/Ti micro-heater. The temperature profiles from

the experiment and modeling match very well. Because of the small size of the heated structures, the heat convection losses are negligible at median-low temperatures for micro-heater. Propellant temperature variations with time, space, and voltage are obtained from the modeling for the solid propellant microthruster with Au/Ti igniter. Ignition power, ignition delay, and ignition energy are derived from the modeling. Although Pyrex-7740 glass has a better thermal resistance than silicon, the ignition efficiency is still very low because the thin film Au/Ti igniter is deposited directly onto the glass substrate. The thermal oxidation process in the fabriation can improve the ignition efficiency greatly by reducing the current leakage.

Chapter 6

Development of the Low Temperature Co-fired Ceramic Solid Propellant Microthruster

Main Publication:

K. L. Zhang, S. K. Chou, and S. S. Ang, "Development of a Low Temperature Co-fired Ceramic Solid Propellant Microthruster", Journal of Micromechanics and Microengineering, Vol. 15, No. 5, pp. 944-952, 2005.

6.1 Introduction

MEMS have shown steady growth, pushing the frontiers of new materials and processes for many interesting applications as described in Chapter 1. MEMS technologies take advantage of all previous microelectronics developments and present new challenges in packaging, media interfacing, and interfacing with microscale devices and three-dimensional structures implementation. However, despite their technical and commercial successes, the planar manufacturing processes have some fundamental limitations that have slowed the adoption and growth of MEMS-based systems:

- The two-dimensional MEMS processes today provide limited capability to achieve a true three-dimensional functionality. The structures created by these processes are inherently limited to two-dimensional or to 2.5-dimensional structures that can be erected from two-dimensional structures. True three-dimensional mechatronics implemented this way requires, often tricky, assembly of multiple two-dimensional MEMS components.

- The cost of packaging these components is high. Integration of planar MEMS with other components (optical, chemical, etc) and housing often represents 80 % of the manufacturing cost of a microsystem. In addition, there is a lack of microsystem packaging standards. As a result, custom tooling and significant process development is required to assemble integrated microsystems employing MEMS.

- The non-recurring engineering costs, including mask generation, are high on a multi-layer process, thus making it difficult for emerging companies with comparatively small volumes to deploy the technology.

- The batch nature of the process, while efficient from a production efficiency standpoint, introduces significant time and tooling investment to achieve functioning product.

It would be desirable to have a technology that can partially mitigate the limitations of MEMS and act as an alternative for MEMS. Low Temperature Co-fired Ceramic (LTCC) technology is an interesting alternative. LTCC is a ceramic substrate system that has advantages of both High Temperature Co-fired Ceramic (HTCC) and thick film technologies. The process, though is similar to HTCC, has an advantage of being able to use low resistivity conductors like silver, gold, copper, and alloys with palladium and platinum because the firing temperature of LTCC is below 900 ^{o}C which is close to the melting point of Au and Ag. LTCC slurry is a mixture of recrystallized glass and ceramic powder in binders and organic solvents.

On the other hand HTCC is an aluminum oxide substrate. The firing temperature of alumina (Al_2O_3) is at 1600 ^{o}C, which only allows co-firing of conductors like tungsten and molybdenum.

The LTCC technology can also be defined as a way to produce multilayer circuits with the help of single green-tapes, which are to be used to apply conductive, dielectric and/or resistive pastes on. These single sheets are laminated together and fired in a single step. This saves time, money and reduces circuits' dimensions. Another great advantage is that every single layer can be inspected, (and in the case of inaccuracy or damage) replaced before firing; this prevents the need of manufacturing an entire new circuit. Some advantages of LTCC are listed below:

- Low temperature coefficient of expansion (TCE)
- Low tolerance in dielectric constant
- Easy fabrication for multi-layer circuits
- R, L, C elements can be integrated between layers
- Good hermeticity of the substrate
- Good electrical conductivity of metal paste buried in LTCC
- Would cost cheaper for mass production
- Tapes of different compositions can be formulated to obtain desired layer properties, for instance, thermo-physical properties of single layers
- Possibility of auto-packaged devices fabrication
- High numbers of signal layers

LTCC manufacturing process starts with slitting of the green-tape. The green-tape is generally available in rolls, which are cut into the required dimensions. The transverse direction has to be recorded as soon as the tape is unrolled and

cut. This is very important as the LTCC has different shrinkage rates in machined and transverse directions. This is followed by pre-conditioning of the tape, which means that the green-tapes are to be cured for 1-1/2 hour at 120 ^{o}C (depends on the manufacturer).

The next step is to create vias in the required layers using a punching machine or a laser followed by inspection of each layer to make sure that no pieces of Mylar backing tape are blocking the punched vias. This is followed by filling of the vias with conductor pastes. This is performed by either a conventional thick film screen printer or an extrusion via filler. In the former process the tape is placed on a stainless steel stencil resting on a porous plate, a vacuum pump holds the tape onto its place and it is used as an aid for via filling. The latter uses a special extrusion via filler that works with under pressures. However, both processes require a mask.

In the next step, the screen printer is used to print the conductor pastes and also the resisitor pastes onto the green-tape. This is followed by stacking of all the layers in the required order onto a tooling plate and is laminated under pressure and heat. The lamination can be either uniaxial or isostatic. In uniaxial lamination, the LTCC stack is pressed between two parallel plates, whereas in the isostatic process, water heated up to 80 ^{o}C is used as a medium to distribute the force of lamination. In case of substrate having cavities, the latter process is preferred to former, as it will lead to deformation of cavities due to fact that a strong pressure exerts onto the edges. This is followed by sintering of the substrate. A specific temperature time profile, depending on the type of glass-ceramic mixture, is followed for the firing process. The fired LTCC substrate is now ready for further processing which can either be dicing of the substrates into different modules or further printing of conductors or resistors which is also called post-firing or assembly process like wire bonding, SMD technology, etc. It is, however, not necessary that the same order is to be followed. Depending on the design and device to be fabricated the order of the above processes can be changed.

LTCC technology has many applications in diverse fields, such as sensor applications, microfluidic devices, actuator applications, and biomedical applications including drug delivery, gas or liquid chromatographs, and biological parameter monitoring [Palmer and Newton 1993, Rubio et al 2001, Pavio et al 2002]. One possible application of LTCC technology is in the aerospace field. LTCC technology is employed in this chapter to develop a novel solid propellant microthruster system. The LTCC solid propellant microthruster system has many interesting advantages over the silicon-based solid propellant microthruster systems.

6.2 Design of the Low Temperature Co-fired Ceramic Solid Propellant Microthruster

The designed LTCC solid propellant microthruster configuration has no pumps, fuel lines, and valves. Therefore, there are no moving parts and the leakage possibility of the propellant is very low. The microthruster is fabricated by lamination of 10 individual layers of green-tapes; each of which is individually processed. The design of each layer is decided by the structure of the microthruster. The microthruster has a cavity (combustion chamber), a convergent-divergent nozzle, and a resistor embedded inside the cavity. The resistor is connected to the catch pads, on the top of the thruster, through electrical vias.

Cross-sectional and isometric views of the LTCC microthruster are shown in Figures 6.1 (a) and 6.1 (b), respectively. Since the device has a large cavity, a blank layer (Layer 1) is added at the base to prevent collapse of the layers. The next double-layer (Layer 2-3) has the resistor along with its termination pads and the via catch pads for connection along the z-axis direction. The microcavity layer (Layer 4-8) is formed by a total of five layers of green-tape to yield a thickness of 400 μm. The top layer (Layer 9-10) provides the catch pads for the resistors.

The cavity is then loaded with the solid propellant. The propellant ignition

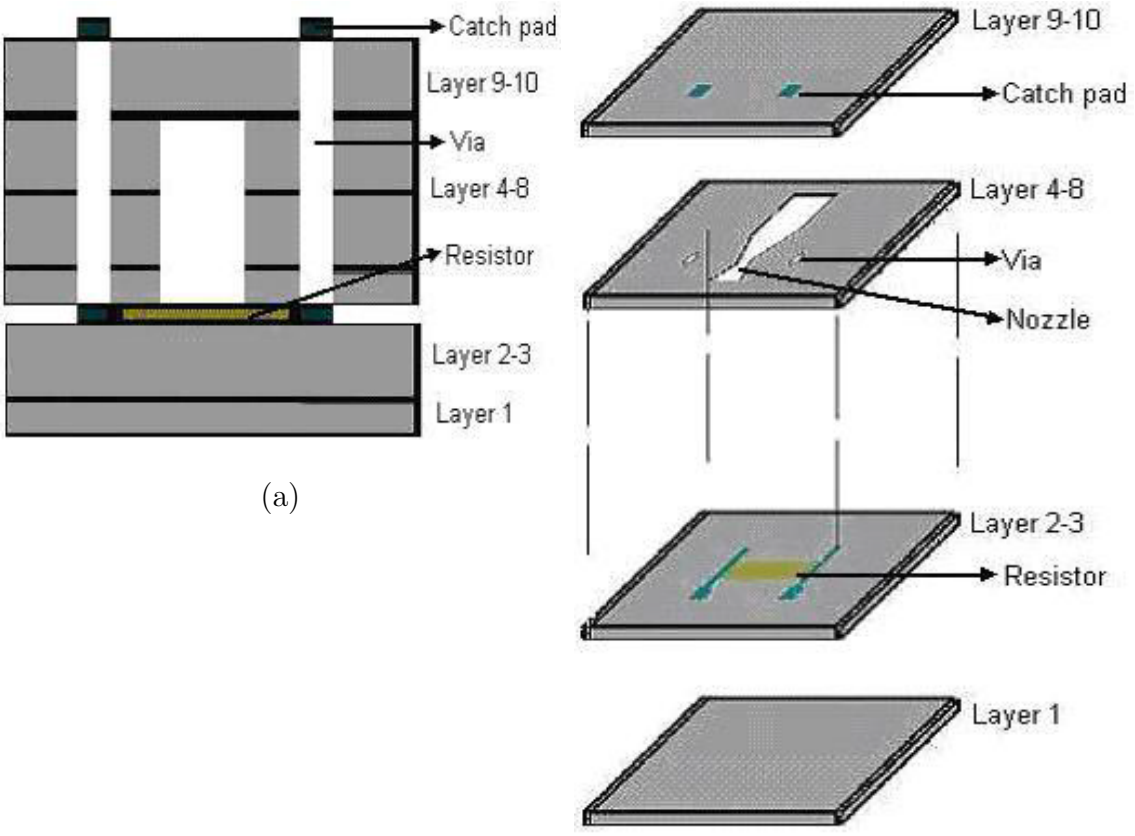

Figure 6.1. Cross-sectional and isometric views of LTCC microthruster.

process is triggered by electrical power delivered to the resistor through the catch pads and interconnections. When the propellant is ignited at any point of its surface, the combustion occurs and propagates to all the surface and then progresses perpendicular to the combustion surface. The resultant gas expands through the convergent-divergent nozzle as its velocity increases drastically, thus producing the desired thrust and impulse. The LTCC solid propellant microthruster is installed into a special micro-connector to interconnect the motherboard which contains the power source, addressing electronics, and communication ports.

To punch a LTCC green-tape, the punching machine needs a punching file, which specifies the co-ordinates where it has to be punched to form a cavity or a via. However it would be difficult to specify all the co-ordinates where the punching machine has to punch. A better way to do is to draw the complete design in a drawing software, then convert the drawing file into punch file using a

conversion software. AutoCAD is used as a drawing software and E-CAM 8.0 (from Circuit CAD Corporation) is employed to convert from drawing format (.dxf) to punch format. Similarly for the conductor and resistor printing, AutoCAD is used to design and it is converted into Gerber format using CAM 350. The Gerber files are used to generate the photo plot, which is then transferred onto a stencil used to print on the green-tape. Single, 2-array and 3-array microthruster of six different dimensions are designed on the green-tape. Dicing marks are also added to the design so as to make it easier for dicing. Also while making the design, the shrinkage property of the LTCC is taken into consideration. The shrinkage factor assumed is 14 %. As such, the dimensions of all the devices are scaled up by 14 %, so that after firing the devices will have the correct dimensions.

The LTCC solid propellant microthruster design inherits all the important advantages of the solid propellant microthrusters developed in Chapters 3 and 4, such as a more design freedom of nozzle and chamber, a more effective and efficient fabrication process, better bonding quality, and a more freedom of igniter position selection. Moreover, it has some other advantages over the former solid propellant microthruster designs. First, the new design employs the embedded igniter instead of wire igniter, which is more suitable for batch fabrication and the ignition efficiency and reliability are improved. Second, adding addressing capability is one key part of developing the microthruster array. The new design makes the realization of addressing capability easier by employing the special micro-connector. In addition, a higher level of integration can be possibly achieved. Third, the fabrication is relatively simple, inexpensive, and environmentally friendly as compared to that of the silicon-based microthrusters. True three-dimensional solid propellant microthruster can be easily realized by co-firing required tape layers together. Fourth, the thermal properties of the LTCC tape can be tailored by clever formulation. Microstructure designer possesses a great deal of latitude in the selection of a ceramic formulation to match either the thermal expansion coefficient or the thermal conductivity of most interested materials for hybrid integration. For in-

stance, the ceramic LTCC tape has a better thermal insulation characteristic than silicon. Consequently, the combustion thermal loss through the wall is lower, thus producing a higher thrust. The better thermal insulation characteristic is also desired to avoid the possible presence of thermal cross-talk that could cause the fuel in neighboring cavities to ignite. Fifth, although the in-plane fabrication approach for solid propellant microthruster provides a more design freedom compared to out-of-plane fabrication, the microthruster dimensions are still limited by DRIE and wafer thickness. However, for LTCC fabrication, the microthruster dimensions are almost unlimited due to high layer count capacity. Finally, LTCC microthruster array can be easily fabricated so as to partially mitigate the lack of restart ability, to produce the controlled, vectored thrust and impulse according to the applications. A schematic of the way to address and ignite single LTCC microthrusters individually in the LTCC microthruster array is shown in Figure 6.2.

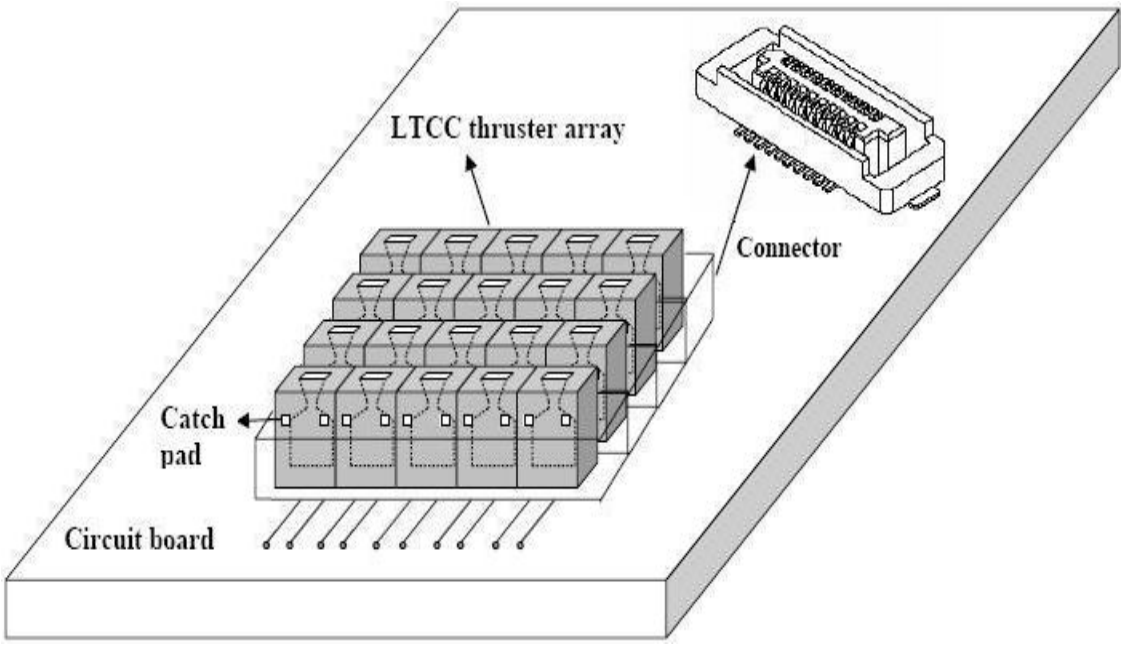

Figure 6.2. Schematic of addressing single LTCC microthrusters in an array.

6.3 Fabrication of the Low Temperature Co-fired Ceramic Solid Propellant Microthruster

The microthruster is designed using LTCC, as it is easily to fabricate three dimensional structures such as vias, cavities, channels, and embedded capacitors, resistors and inductors. In the green state, the tapes are processed to form the desired shape. The individual tapes are then stacked and laminated under heat and pressure to yield the desired structure.

Dupont 951 AT green-tape is used as the substrate. The tape packed as a roll is slit into $5'' \times 5''$ tapes. The green-tapes are then pre-conditioned in a box furnace for 30 minutes at 120 ^{o}C. The thickness of the Dupont 951 AT green-tape is 4.5 mils (1 inch = 1000 mil). If only a single layer of green-tape is used it will be somewhat difficult to handle. Therefore two layers of green-tape are pre-laminated using an Isostatic Laminator system at 800 psi and 70 ^{o}C for 10 minutes.

Five layers (Layer 4-8, see Figure 6.1) are punched, using an automatic punching machine. The green-tape is mounted onto the punch-tooling plate and is held tightly by vacuum as the punching machine punches at the co-ordinates specified by the punch file. Punches with diameters of 4, 6, 10 and 20 mils are used for punching of the cavities and vias. For registration holes, a 94-mil punch is used. Registration and alignment holes are also punched on every layer for alignment purposes. All the layers are inspected individually to make sure that no pieces of Mylar backing block the punched vias. Mylar backing is attached to the rolled ceramic tape to aid in handling of the tape. This backing is left on during the punch phases as to prevent rupture of the tape. Also the top layer, which is a double layer, is punched for vias. A via catch-pad is also printed on it. This is performed using a screen printer and Dupont 6142 Ag paste is used to print the catch-pad. The photo-plot, which is generated from Gerber format, is used to print the via-catch pads. Registration holes/alignment marks are used to correctly position the tape using a magnifying camera. A porous stone vacuum system holds the ceramic tape

in place. As the tape is held tightly by vacuum a doctor blade squeezes the paste through the stencil to print the required design onto the tape. This is followed by printing of Layer 2-3. Dupont CF021 resistor paste is used for the embedded resistors and Dupont 6142 Ag paste is used for the termination pad and the contact pads. A similar procedure is followed for this layer, however, the printing process is repeated twice, once for resistor paste and then for the conductor paste.

After processing of all the layers is completed, they are all stacked in a laminating fixture plate that has tooling posts into which the registration holes of all the layers fit. The stack is then inspected under a microscope and aligned in such a way that all the alignment vias are aligned. The laminating fixture plate is then sealed in a vacuum bag and placed in an Isostatic Laminator system at 800 psi and 70 ^{o}C for 10 minutes.

This is followed by sintering of the stack in a programmable forced-draft furnace. The furnace is programmed to follow the temperature-time profile for the firing process. The stack is placed on a quartz tray and heated according to the programmed temperature profile. The firing profile is shown in Figure 6.3.

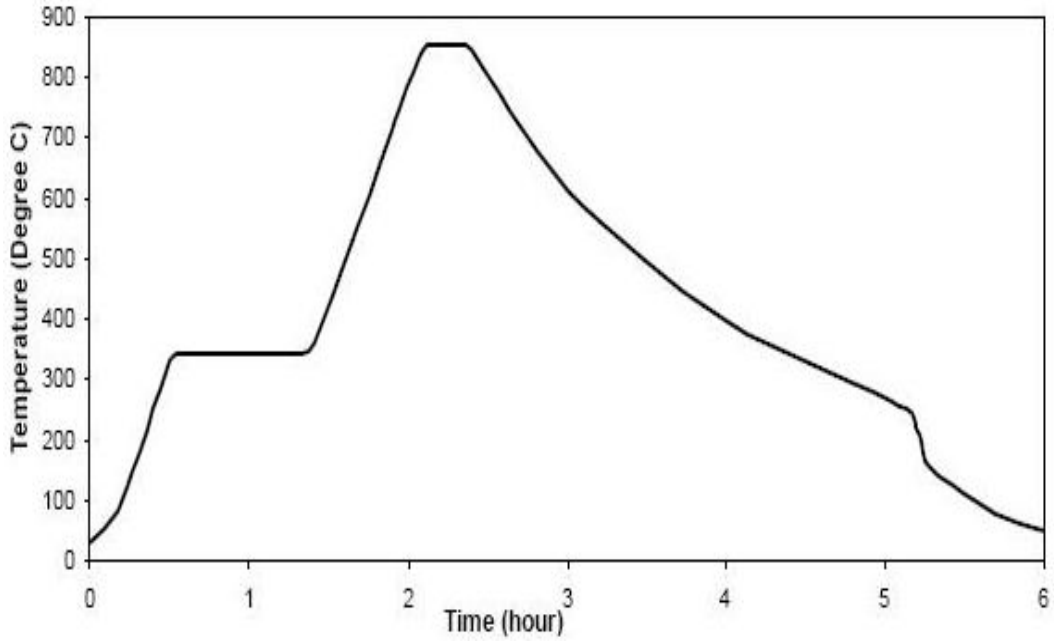

Figure 6.3. Firing profile of 951 Dupont green-tape.

Filling of the vias follows the firing. The vias are filled with a Dupont 6141 Ag paste using Pacific Trinetics PTC VF-1000 via filler to form the interconnections in the Z-axis direction. A doctor blade squeezes the paste through the stencil, developed from the photo plot designed, into the vias, while a vacuum pump below the porous nest helps to fill the via with the ink. After the fabrication of the complete design, a dicing saw is used to dice the substrate into required dimensions using the dicing marks. Closed circuit TV with split image optics is used to align the blade to the dicing marks on the substrate, which is held tightly onto the vacuum chuck. The substrate is cut into required dimensions. Figure 6.4 shows the fabricated three-dimensional LTCC solid propellant microthruster arrays. The catch pads and nozzle exits can be clearly seen from Figure 6.4. The LTCC microthruster cross-section view is shown in Figure 6.5. Part of the embedded resistor (black color) appears in one broken LTCC microthruster chip. Figure 6.6 shows the SEMs of a LTCC microthruster chip and the nozzle exit. The nozzle divergent part can be clearly seen from the SEMs.

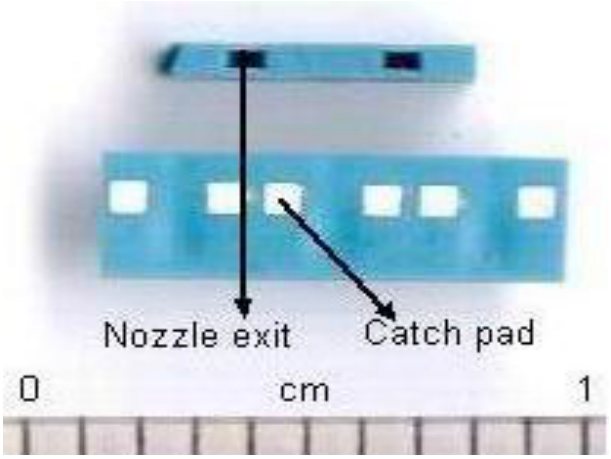

Figure 6.4. Three-dimensional LTCC solid propellant microthruster.

The LTCC solid propellant microthruster is installed into a special micro-connector to realize the connection with the motherboard which contains the power source,

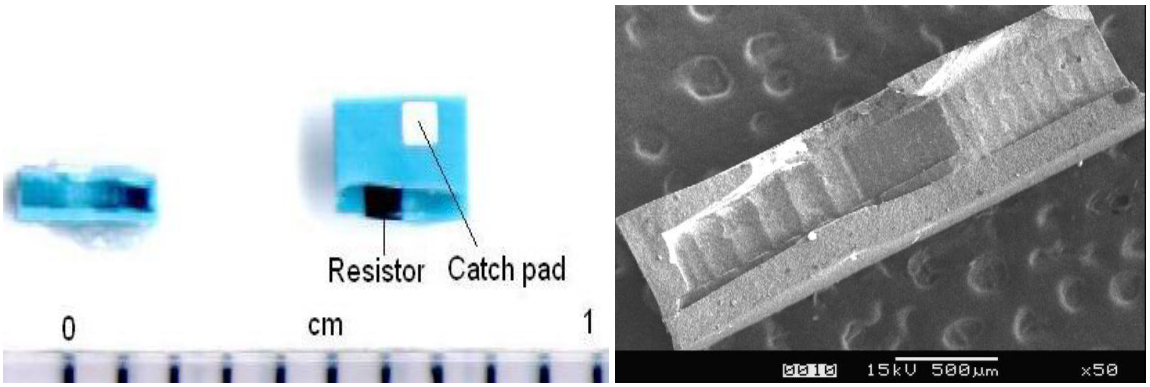

(a) (b)

Figure 6.5. Cross-sectional views of LTCC microthruster.

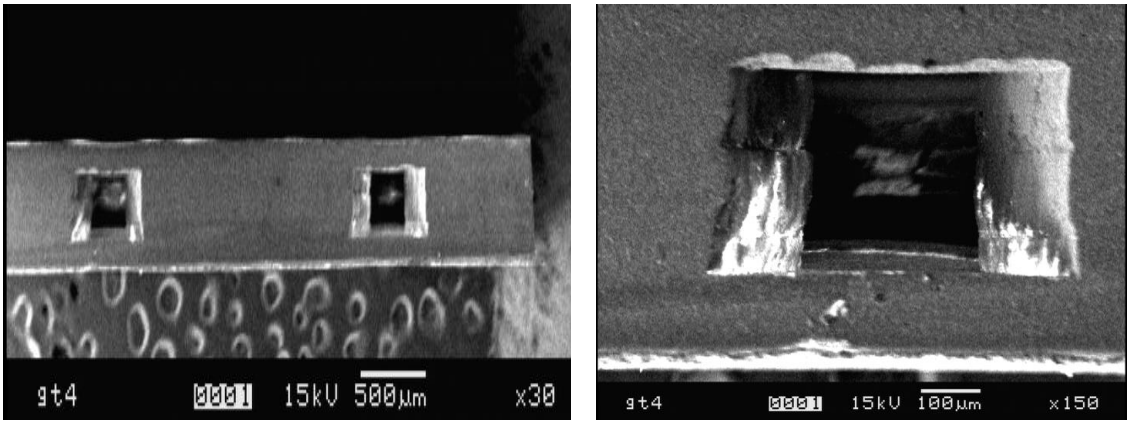

(a) (b)

Figure 6.6. (a) SEM of LTCC microthruster chip. (b) SEM of the nozzle exit.

addressing electronics, and communication ports. The microthruster and micro-connector have the matched pitches. The catch pads on top of the LTCC microthruster are held tightly with a plated gold contact area of the micro-connector to achieve a good ohmic contact. Figure 6.7 shows one LTCC microthruster layer installed inside a micro-connector.

6.4 Experimental Testing

The specially designed experimental setup developed in Chapter 3 as shown in Figure 3.5 (see also Figure 3.6) is used to address the viability of the new design

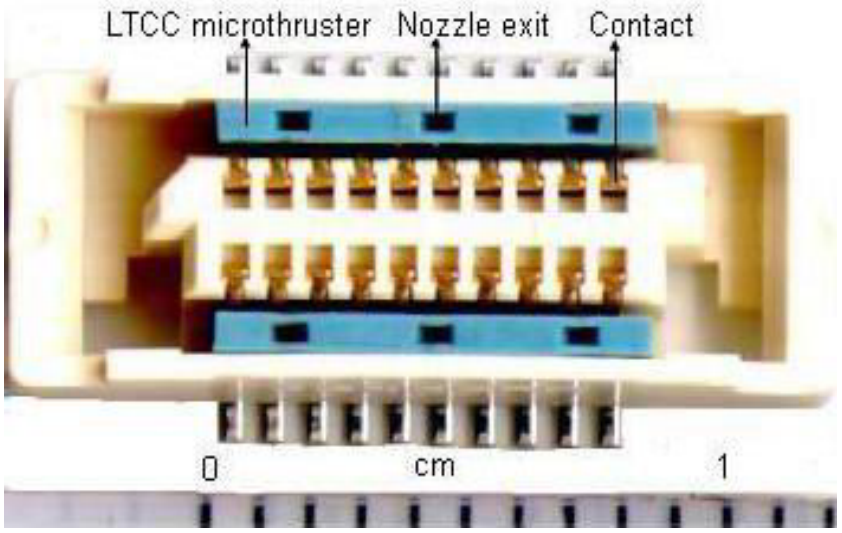

Figure 6.7. The LTCC microthruster with connector.

and acquire the characteristics of the LTCC solid propellant microthruster both at sea level and in vacuum.

6.4.1 Propellant Description and Microthruster Geometry

Gunpowder-based solid propellant is employed here for the experiment because of its lower ignition temperature compared to HTPB/AP/Al-based solid propellant. The mass fractions of the solid propellant are as follows: 90 % gunpowder (75 % potassium nitrate, 15 % charcoal, and 10 % sulfur); 6 % ammonium perchlorate; 3 % aluminum; and 1 % Fe_2O_3. Ammonium perchlorate is used to lower the ignition temperature and to improve the specific impulse of the propellant. Adding aluminum is to increase the burning rate, flame temperature, and specific impulse. Fe_2O_3 is utilized as the combustion catalyst. The single LTCC microthruster is tested to yield thrust measurements to optimize the microthruster geometry. The dimensions of the LTCC single microthruster for the testing are similar to those in Figure 2.2. The LTCC microthruster has different nozzle divergence lengths (L), half divergence angles (a), combustion chamber widths (W_c), microthruster throat widths (W_t), and microthruster exit widths (W_e). Thus different chamber-to-throat section ratios (A_c/A_t) and exit-throat section ratios (A_e/A_t) are available

Table 6.1. Masses of the LTCC microthruster and gunpowder-based propellant

LTCC single microthruster	Empty vehicle mass (mg)	Loaded mass (mg)	Propellant mass (mg)	Propellant mass fraction (%)
$W_c = 1000\ \mu m$	12.1	12.8	0.7	5.47
$W_c = 1500\ \mu m$	11.7	12.6	0.9	7.14

for evaluation. Since the chamber and nozzle have the same depth of 400 μm, A_c/A_t equals W_c/W_t and A_e/A_t equals W_e/W_t.

The loaded propellant mass affects the LTCC microthruster performance in terms of specific impulse that is defined as the ratio of total impulse to propellant weight. Consequently, the propellant mass should be controlled and measured carefully before the testing. Table 6.1 shows the masses of the LTCC microthruster and propellant. The empty vehicle mass is the LTCC microthruster mass before loading, the loaded mass is the microthruster mass with the propellant loaded, and the propellant mass fraction is equal to the ratio of the propellant mass to the mass of the loaded microthruster before firing.

6.4.2 Microcombustion Experiment

Microcombustion experiment is performed to prove the feasibility of the LTCC microthruster design. The increased surface-area-to-volume ratio that comes with the small size of the microthruster may cause chemical and thermal quenching. Quenching has been shown to stop microcombustion [Lee and Kwon 2002]. Although the ceramic-based LTCC solid propellant microthruster has a better thermal resistance than the silicon-based solid propellant microthruster (thermal conductivity: LTCC green-tape, 3.0 W/mK; silicon, 141.2 W/mK), the quenching problem for the microscale LTCC thruster still needs to be addressed. Continuous combustion is observed after igniting the gunpowder-based solid propellant with the embedded Dupont CF021 resistor. The combustion time for a typical LTCC

single microthruster is about 0.7 ms. A series of frames from a high-speed digital video camera of the microcombustion are shown in Figure 6.8. The images are acquired at 10,000 frames/s. The LTCC microthruster is installed inside a micro-connector for microcombustion testing as shown in Figure 6.7. The ejected plume from the convergent-divergent nozzle exit can be visually observed from Figure 6.8.

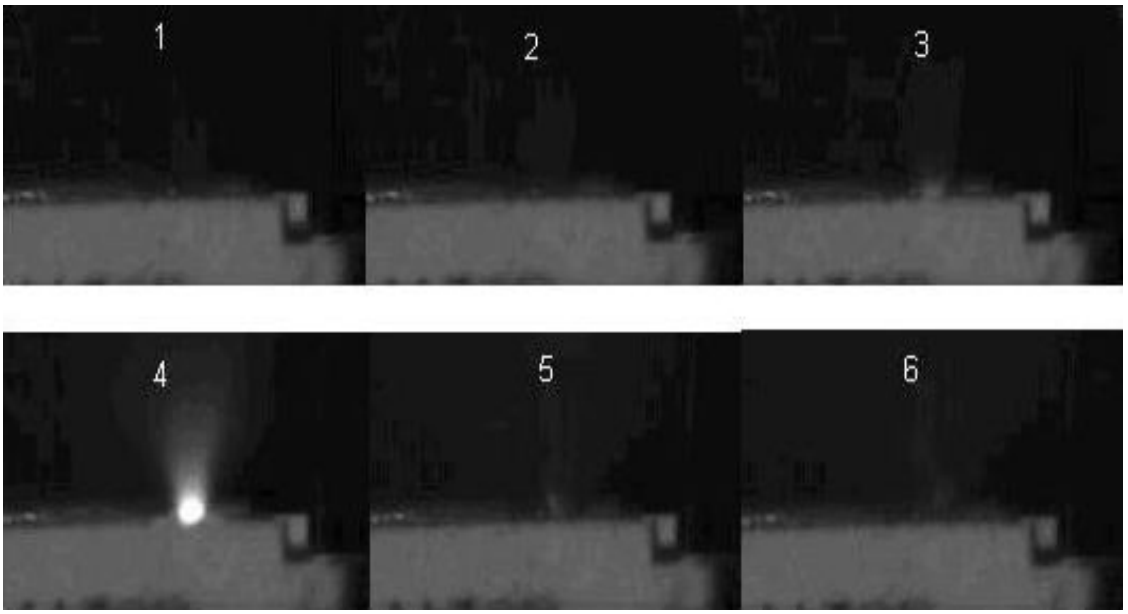

Figure 6.8. LTCC solid propellant microthruster firing (Images are acquired at 10,000 frames/s).

6.4.3 Thrust and Impulse Testing

Thrust and impulse tests are performed both at sea level with the surrounding temperature of approximately 300 K and in vacuum at a pressure of about 80 Pa. To more efficiently capture the thrust and impulse signals, the dynamic acquisition rate of the acquisition system is selected as 100,000 samples per second.

Figure 6.9 shows a typical test signal at sea level for the LTCC microthruster with W_c = 1500 μm, W_t = 370 μm, L = 600 μm, and a half divergence angle a = 16 degree. It can be seen that the peak value of the thrust produced is about

0.38 N. A vibration wave can be found after the peak value, which is caused by the vibration of the platform as a result of thrust impact. Although the range of the wave is negligible compared with the thrust, a damping system is recommended to reduce the vibration and improve the accuracy. Ignition occurs with an input voltage of 37 V. Although current is not measured directly, a current output of 36 mA is observed on the DC power supply at the time of ignition. The ignition power is then estimated to be 1.332 W. The power supply and the data acquisition are sychronized to start at the same time. Consequently, the ignition delay can be acquired through the testing signal as shown in Figure 6.9. The ignition delay is 1.211 s with the ignition energy estimated to be 1.613 J.

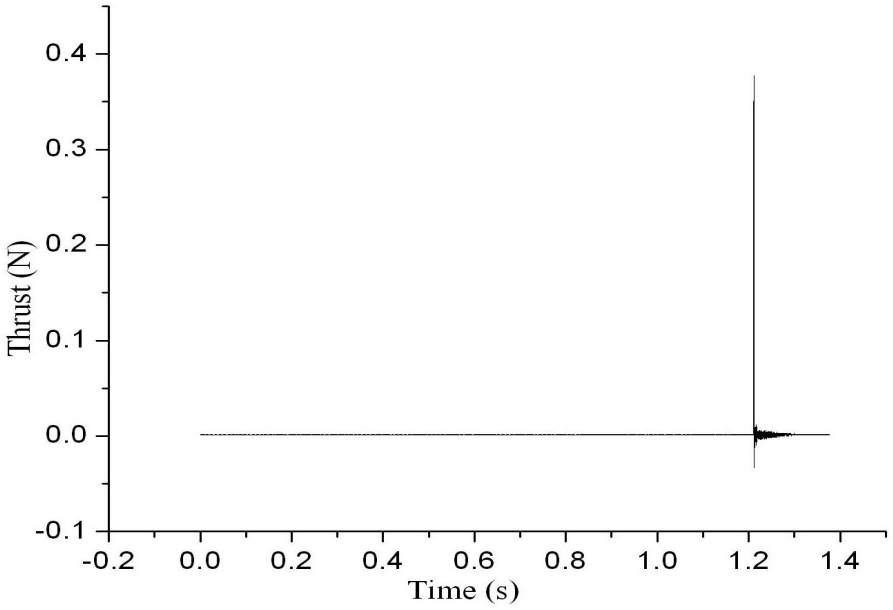

Figure 6.9. Original signal of the LTCC microthruster testing.

Figure 6.10 is an enlarged plot of the combustion region shown in Figure 6.9. It can be seen that the duration of combustion and thrust produced are about 0.70 ms and the peak value of thrust is about 0.38 N. At $t = 0$ ms, the embedded Dupont CF021 resistor is energized and the propellant combustion begins, producing the thrust. The thrust increases fast and reaches its peak value at $t =$

0.35 ms. The high value of thrust lasts for about 0.07 ms and decreases gradually. By $t = 0.70$ ms, the propellant combustion is complete, and the impulse of thrust has been delivered. Total impulse is an important parameter to describe the propulsion performance [Sutton and Biblarz 2001]. For this LTCC microthruster, total impulse is $1.27 \times 10^{-4}\ N \cdot s$. When the gunpowder-based propellant is ignited, its combustion is extremely quick. Therefore, the chemical energy of the propellant is released within a very short time, producing a high peak value of thrust. David et al [Lewis et al 2000] showed some results for their digital microthruster, which have the same magnitude on the total impulse as those of the LTCC microthruster although the design and propellant are different. According to Teasdale's results [Teasdale et al 2001], the thrust of their solid propellant microrocket can sustain for several seconds using HTPB/AP as the solid propellant, but the magnitude of the thrust is in mN.

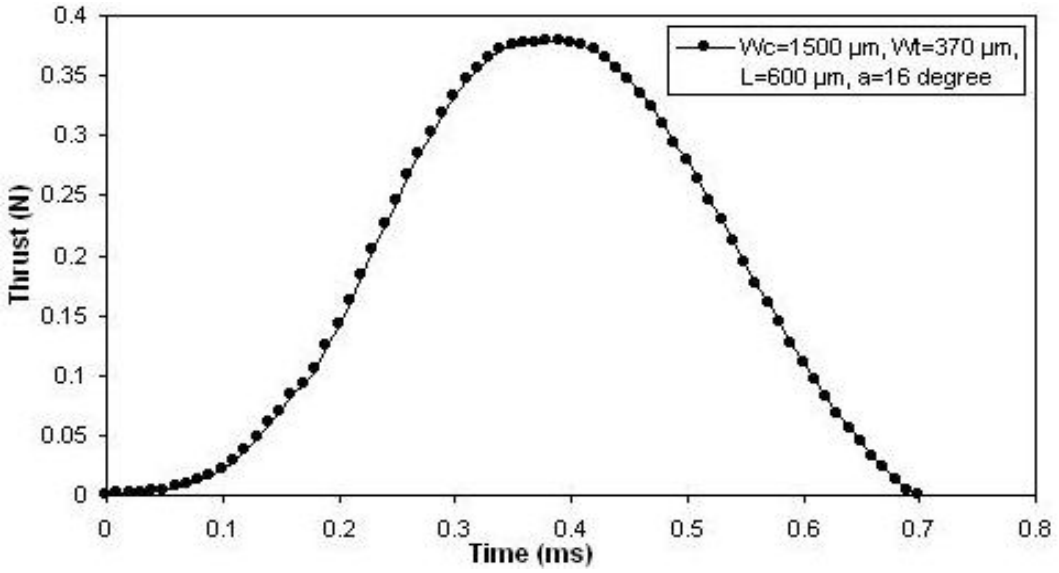

Figure 6.10. Variation of the thrust with the combustion time.

6.4.4 Effect of Chamber-to-Throat Area Ratio on LTCC Microthruster Performance

The propellant burning rate is dependent on the propellant composition and the chamber pressure. The chamber pressure, however, is determined by the equilibrium that exists between the combustion gas generation rate and the nozzle exhaust flow rate. Thus, the stable pressure level that can be achieved is determined by the propellant composition and the ratio between the propellant burning area A_c and the nozzle throat area A_t. Therefore, A_c/A_t ratio is an important parameter that impacts the LTCC microthruster performance. By increasing A_c/A_t, the chamber pressure is greatly increased and the combustion gas can be accelerated to a higher velocity, thus resulting in a greater thrust level. Figures 6.11 and 6.12 show the thrust and total impulse variations with A_c/A_t at sea level and in vacuum, respectively. The tested single LTCC microthrusters have a similar divergence length of 600 μm and a similar half divergence angle of 16 degree. At sea level (Figure 6.11), the total impulse is changed from $3.81 \times 10^{-5}\ N \cdot s$ to $1.27 \times 10^{-4}\ N \cdot s$ and the specific impulse increases from 5.55 s to 14.41 s when A_c/A_t increases from 2.70 to 4.05. In vacuum (Figure 6.12), the total impulse changes from $1.31 \times 10^{-4}\ N \cdot s$ to $2.79 \times 10^{-4}\ N \cdot s$ and the specific impulse increases from 19.05 s to 31.55 s when A_c/A_t varies from 2.70 to 4.05. Therefore, this is one of possible ways to vary the thrust and total impulse to satisfy different applications and requirements by adjusting the LTCC microthruster A_c/A_t ratio.

The specific impulse is an important metric for evaluating the solid propellant microthruster performance. According to the testing results, specific impulses of 5.55 s to 14.41 s are produced at sea level (similar to Teasdale's results using HTPB/AP as the solid propellant: 10 s to 15 s [Teasdale et al 2001]), and specific impulses of 19.05 s to 31.55 s are generated in vacuum, which are much less than those of traditional solid rockets. This is mainly caused by the relatively low specific impulse of the gunpowder-based propellant, the small size of the LTCC

microthruster, and possible incomplete combustion of the propellant.

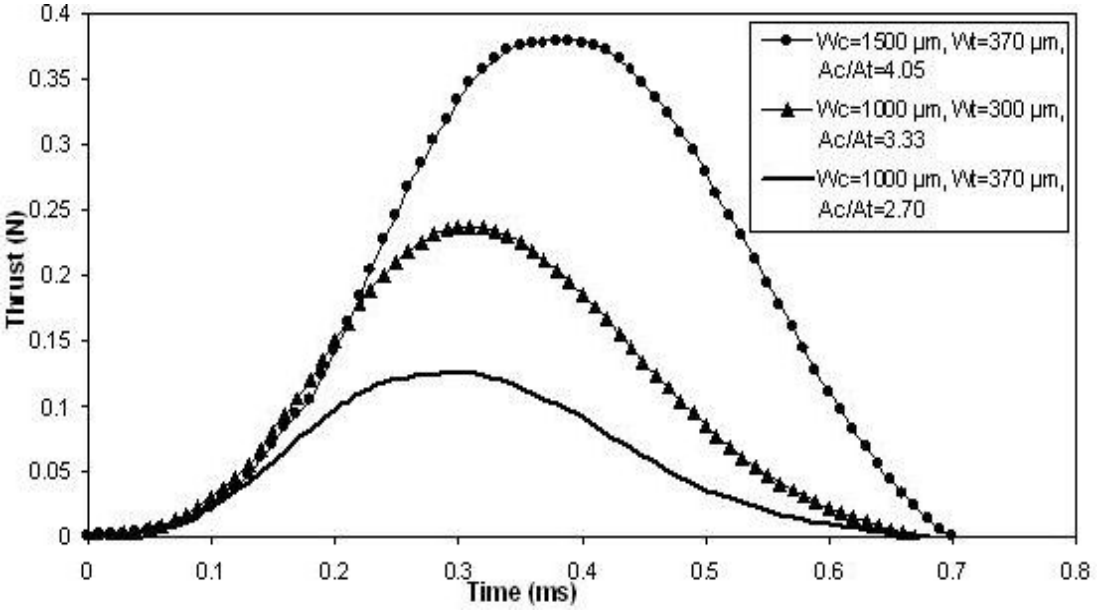

Figure 6.11. Thrust and total impulse variations with A_c/A_t at sea level.

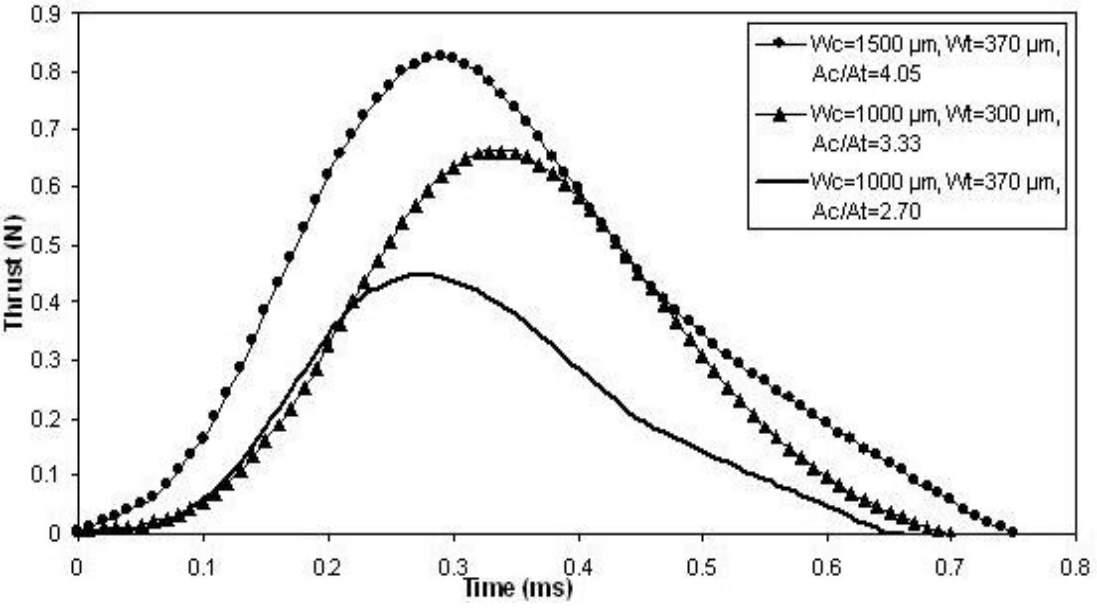

Figure 6.12. Thrust and total impulse variations with A_c/A_t in vacuum.

6.4.5 LTCC Microthruster Performance Comparison at Sea Level and in Vacuum

The LTCC microthruster performance is tested both at sea level and in vacuum. Figure 6.13 shows the performance comparison at sea level and in vacuum for the LTCC microthrusters with a similar divergence length of 600 μm and a similar half divergence angle of 16 degree, whereas the A_c/A_t ratios are different. For $A_c/A_t = 2.7$, the specific impulse increases from 5.55 s to 19.05 s and the total impulse is changed from 3.81×10^{-5} $N \cdot s$ to 1.31×10^{-4} $N \cdot s$ when the back pressure is changed from sea level to vacuum. For $A_c/A_t = 3.3$, the specific impulse increases from 10.28 s to 29.24 s and the total impulse increases from 7.06×10^{-5} $N \cdot s$ to 2.01×10^{-4} $N \cdot s$ when the back pressure is changed from sea level to vacuum. As can be seen, the LTCC microthruster performance is greatly improved in vacuum. One cause for the improvement is the increase of the exit-ambient pressure difference in vacuum. The other possible reason is the flow pattern difference of the LTCC microthruster jet. At sea level, the jet flow is subsonic caused by the high back pressure. Whereas in vacuum, the jet flow is supersonic due to the low back pressure. The supersonic jet produces higher thrust and impulse than the subsonic jet.

6.4.6 Performance Comparison between LTCC Microthruster and Silicon-based Microthruster with Wire Igniter

A silicon-based microthruster with a wire igniter is developed in Chapters 2 and 3, which has the similar design as the LTCC microthruster. Figure 6.14 shows the performance comparison between the LTCC microthruster and the silicon microthruster using the same propellant at sea level. The LTCC microthruster and the silicon microthruster have a similar divergence length of 600 μm and a similar half divergence angle of 16 degree. The thrusts produced by the LTCC microthrusters

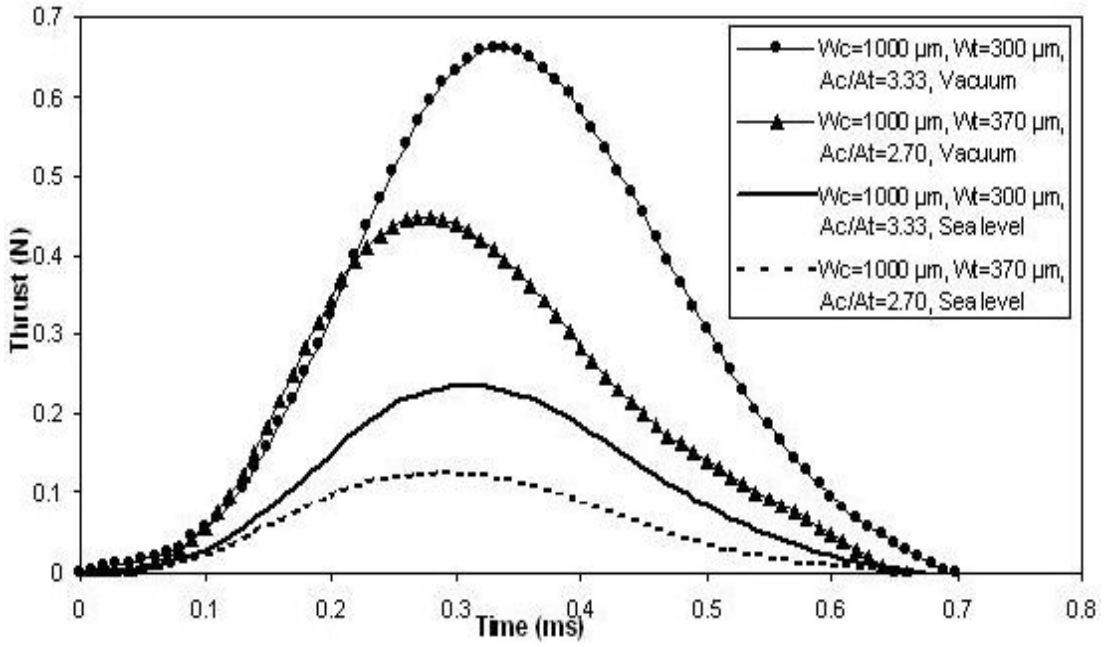

Figure 6.13. LTCC microthruster performance comparison (sea level vs. vacuum).

are higher than those produced by the silicon microthrusters. This is caused by higher thermal resistance of the ceramic LTCC tape compared to that of silicon. Consequently, the thermal loss through the wall is lower, thus producing a higher thrust. Specific impulses produced by the LTCC microthrusters are also higher than those generated by the silicon microthrusters (14.41 s vs. 10.74 s; 10.28 s vs. 6.56 s), which is caused by the higher thermal resistance of the LTCC tape and the higher mass fractions (Table 6.1) of LTCC microthrusters compared with those of the silicon microthrusters with wire igniter (Table 3.1).

The oscillatory decrease can be seen from the thrust curves of the silicon-based microthruster with wire igniter. The main cause is the combustion instability of the propellant in the microthruster as stated in Chapter 3. The dynamic response of the combustion to a flow disturbance is one of the reasons for combustion instability, which is due to the wire igniter and ignition slot in the silicon-based microthruster. The instability is harmful to the microthruster performance and the hardware. However, the combustion instability does not occur for the LTCC microthruster. The wire igniter is replaced by the embedded thin film igniter deposited on the

LTCC microthruster bottom layer. Thus it does not disturb the gas flow.

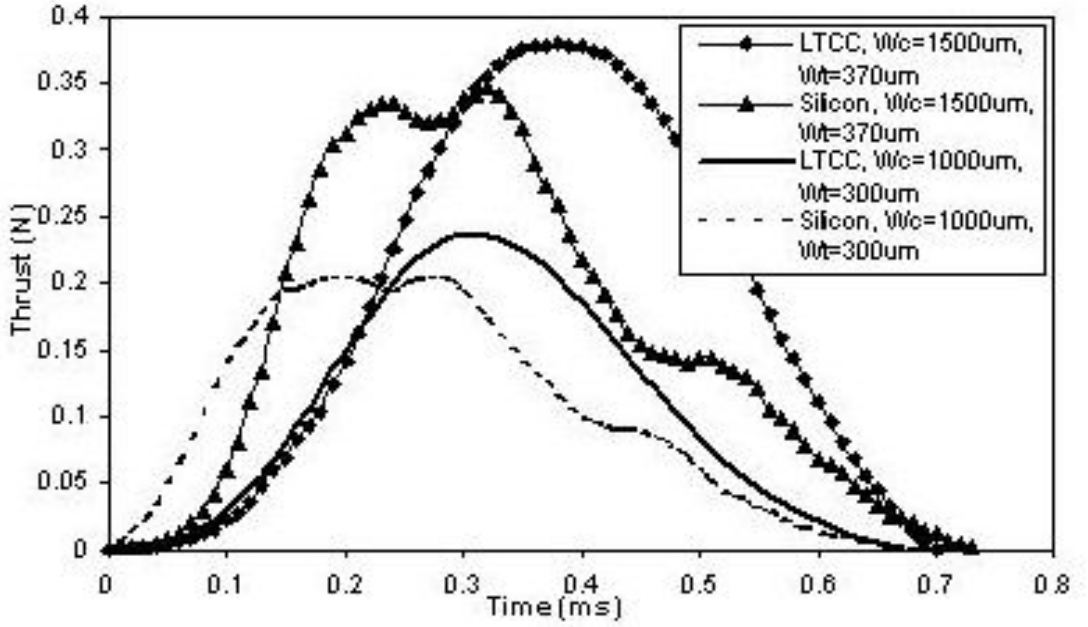

Figure 6.14. Performance comparison between LTCC microthruster and silicon-based microthruster with wire igniter.

6.4.7 Performance Comparison between LTCC Microthruster and Silicon-based Microthruster with Au/Ti Igniter

A silicon-based microthruster with Au/Ti igniter is developed in Chapter 4, which has the similar design as the LTCC microthruster. Figure 6.15 shows the performance comparison between the LTCC microthruster and the silicon microthruster in vacuum. The two types of microthrusters have a similar divergence length of 600 μm and a similar half divergence angle of 16 degree. The thrusts produced by the LTCC microthrusters are higher than those produced by the silicon microthrusters. This is caused by the higher thermal resistance of the ceramic LTCC tape compared to that of silicon. Consequently, the heat loss through the wall is lower, thus producing a higher thrust. Specific impulses produced by the LTCC microthrusters are also higher than those generated by the silicon microthrusters (14.41 s vs. 11.32

s; 10.28 s vs. 6.68 s). This is due to the higher thermal resistance of the LTCC tape and the higher mass fractions (Table 6.1) of LTCC microthrusters compared with those of the silicon microthrusters (Table 4.1).

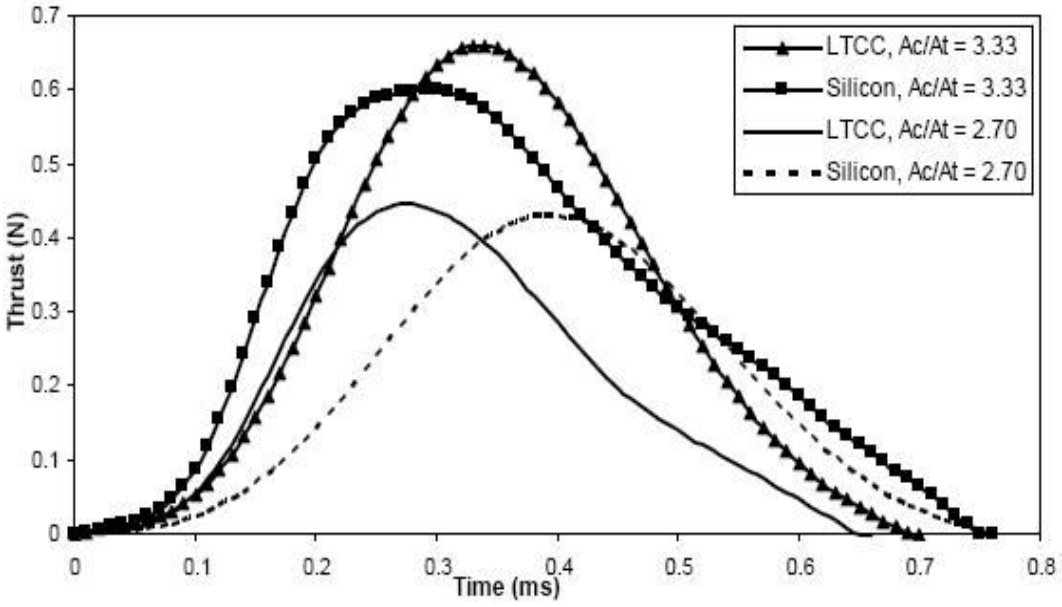

Figure 6.15. Performance comparison between LTCC microthruster and silicon-based microthruster with Au/Ti igniter.

6.4.8 Repeatability of the Measurements

Figure 6.16 shows the thrust measurement results for the LTCC microthrusters with a similar chamber width of 1500 μm, a similar throat width of 370 μm, a similar divergence length of 600 μm, and a similar half divergence angle of 16 degree at sea level. The total impulses for the three samples are $1.31 \times 10^{-4}\ N \cdot s$, $1.26 \times 10^{-4}\ N \cdot s$, and $1.27 \times 10^{-4}\ N \cdot s$, respectively. The results are within the experimental uncertainty and establish the repeatability of the measurements. The input voltages are set to be a same value of 37 V for the three samples. The current outputs are 35 mA, 36 mA, and 38 mA, respectively. Consequently, the ignition powers are estimated to be 1.295 W, 1.332 W, and 1.406 W, respectively. However,

the ignition delays are 2.076 s, 1.211 s, and 0.628 s, respectively. It is unclear why such a wide range of ignition delays are observed. Possible explanations include differing contact areas between the propellant and the igniter, non-uniformities in the propellant grain, or varied properties of the heaters due to process variations.

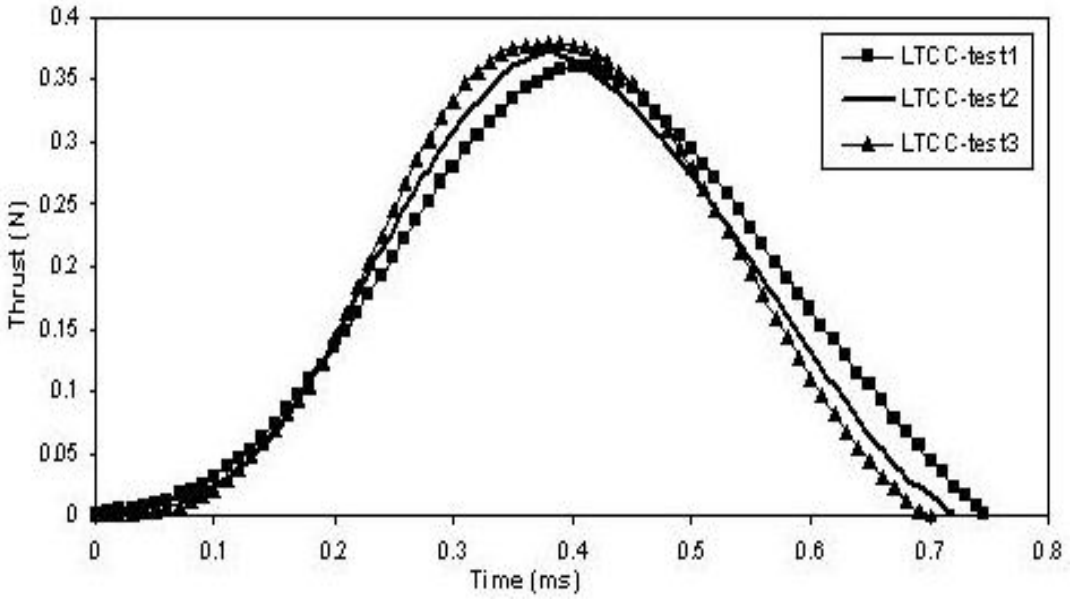

Figure 6.16. Repeatability of the thrust measurements.

6.5 Chapter Summary

This chapter describes the design, fabrication, and testing of the LTCC solid propellant microthruster. LTCC technology is first successfully utilized to design and fabricate a workable solid propellant microthruster. The LTCC solid propellant microthruster has many interesting advantages over former silicon-based solid propellant microthrusters, such as more suitability for batch fabrication, a high level of integration, a better ignition efficiency and reliability, adjustable thermal characteristics, and a more design freedom. The feasibility of the novel LTCC solid propellant microthruster is validated by microcombustion experiment, thrust, and impulse measurements both at sea level and in vacuum. Measurements using

gunpowder-based solid propellant, have produced 0.125 N to 0.379 N of thrust peak value and $3.81 \times 10^{-5}\ N \cdot s$ to $1.27 \times 10^{-4}\ N \cdot s$ of total impulse at sea level, and 0.446 N to 0.826 N of thrust peak value and $1.31 \times 10^{-4}\ N \cdot s$ to $2.79 \times 10^{-4}\ N \cdot s$ of total impulse in vacuum. The LTCC solid propellant microthrusters perform better than the silicon-based solid propellant microthruster with wire igniter developed in Chapter 3 and the silicon-based solid propellant microthruster with Au/Ti igniter developed in Chapter 4.

Chapter 7

Development of the Prototype Wireless Addressing Circuitry for Solid Propellant Microthrusters

7.1 Introduction

The main application of solid propellant microthrusters is micropropulsion. The microthrusters can also have terrestrial, security, and biomedical applications. For instance, they can be used as potential microscale explosive boiling devices. Explosive boiling of a liquid at high degrees of superheat can generate large forces. Such explosive boiling devices have many applications in biology, medicine, and microelectronic cooling. Microthruster-based drug delivery system is an application example of microthrusters in biomedical area [Vidal et al 2003]. Fluid actuator and thermoelectric microgenerator are some emerging applications of microthruster [Hong et al 2003, Rossi et al 2004]. For all the applications, the key points are as follows:

- The realization of addressing ability of the microthruster system.
- The optimization of the ignition process in terms of ignition energy.

- The robustness and reliability of the microthruster system.

The electronic circuitry is indispensable for the microthruster system to realize addressing for microthruser array, to trigger and control the ignition process. There are several basic requirements for the electronic circuitry:

- The electronic circuitry has to contribute to the optimization of the ignition process in order to reduce the response time and minimize the power consumption, especially if the system employs battery as the power source.
- The wireless communication system is necessary for the state-of-the-art microthruster system, especially for the applications in space.
- The electronic circuitry must be compatible with the microthruster system design, fabrication, and assembly so as to achieve a high level of integration.

7.2 Design of the Wireless Addressing Circuitry

The main functions of the designed circuitry are as follows: to realize addressing of the microthruster array; to measure the transient temperature variation of the igniter so as to control the ignition process; and to control the microthruster system both via RS232 and RF wireless communications. The addressing is achieved by multiplexing. The experimental temperature is obtained by measuring the electrical resistance change of the igniter. The electrical resistance change is caused by the heating process when a voltage is applied. The experimental calibration law between the igniter electrical resistance and temperature is needed to extract the actual temperature of the igniter. A programmable voltage source is designed in the circuitry to analyze wide range of voltage values. The schematic of the circuitry is shown in Figure 7.1. The principle of acquiring the igniter temperature is shown in Figure 7.2.

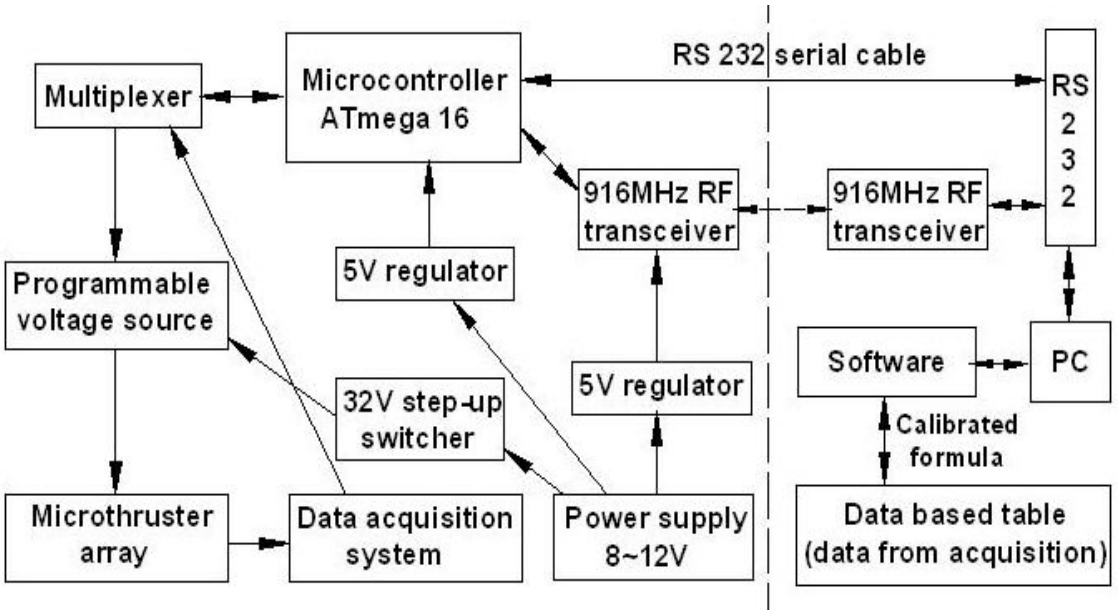

Figure 7.1. Schematic of the wireless addressing circuitry.

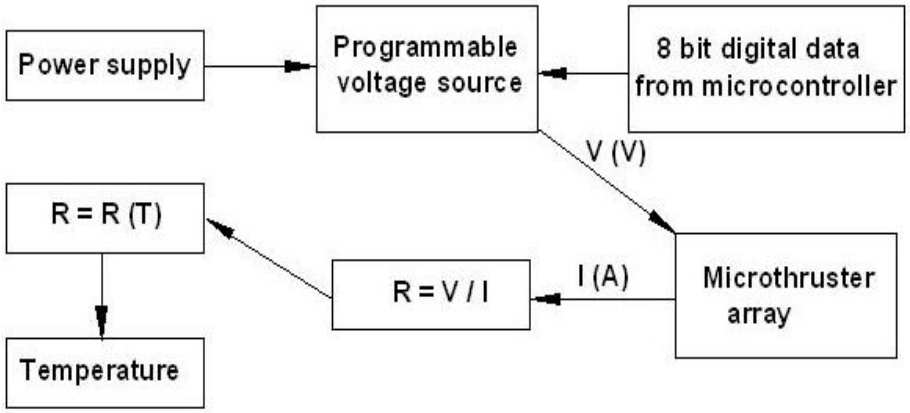

Figure 7.2. Principle of acquiring the igniter temperature.

Power supply is designed to accept 8-12 V DC (battery or adaptor). One part of the power supply is regulated to 5 V by a positive voltage regulator (LM7805) for the operation of microcontroller and other ICs. The other part is boosted to a maximum of 31.2 V by a boost switching converter (LM2577), supplying the collector of transistors and operational amplifier (Op-Amp) (LM124). Signals from serial RS232 are leveled to standard TTL 5V by a multi-channel RS232 driver/receiver (MAX232) for the microcontroller. Communication of this signal is at TX/RX of

4800 bps.

The Atmel ATmega 16 microcontroller operates using the internal 1 MHz RC clock. Port A is used by analog to digital converter (ADC), port B is for the output to digital to analog converter (DAC), port C is used for multiplexing of DAC chips, and port D is used for some control lines, such as Wrt (write enable), Xfer (transfer enable), latch enable, TX/RX of serial, and wireless control. Each port has 8 pins, thus 1 byte. 8 bit data received from the PC are fed to all DAC chips at the same time, whereas selecting the correct respective chip to enable the conversion is done via port C. When the data are converted into analog voltages, typically 0-2.2 V, Op-Amp and NPN transistor are employed to boost the voltage output so as to obtain sufficient power to drive the igniter. The power amplification principle is shown in Figure 7.3.

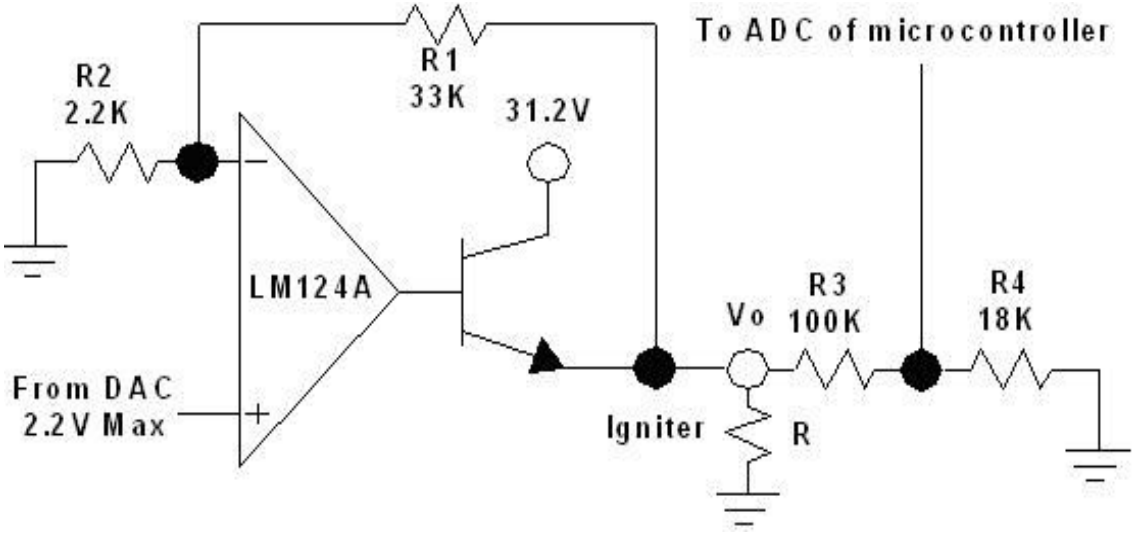

Figure 7.3. Principle of power amplification.

ATmega 16 microcontroller comes with 8 channel 10 bits ADC. Voltage is measured across a 0.5 ohm 1 % tolerance resistor in series with the igniter and is converted into digital data by ADC. It is used to calculate the current flow through the igniter. The current data information is sent back to PC for further manipulation. The change in the igniter resistance is calculated using $R = V/I$. The transient

temperature of the igniter is then obtained using the formula derived from the calibration law. Resistor voltage divider is used to limit the input to ADC. All ICs are decoupled by capacitors to maintain good level of VCC supply, in order to operate well.

LINX SC-S 916 MHz transceivers are employed both on the circuit board and PC for wireless communication. They provide a transparent wireless serial data communication between two equipments up to 33.6 kbps. The system works on half duplex mode with wireless communication at current design. Therefore, there are some limitations for wireless communication, especially for applications required for full duplex mode. Full duplex wireless communication is expected to be implemented to have data sent at interval, swap the TX/RX mode, and vice versa. In this way, data are communicated slower with half of the bandwidth. The detailed design of the circuitry is shown in Figures 7.4 and 7.5.

7.3 Fabrication of the Wireless Addressing Circuitry

A double-side printed circuit board (PCB) for the circuitry is designed and drawn using Eagles cadsoft software. The gerber RS274x files are generated from Eagles cadsoft and are viewed to confirm under Linkcad ver 5 software. The gerber files are then sent to a factory for PCB fabrication. The two-layer PCB drawing is shown in Figure 7.6. When the PCB is ready, the electronic components including microcontroller, DAC chips, power supply connector, battery, RS232 ports, Op-Amp chips, step-up switcher, voltage regulators, RF transceiver chips, antennas, and microthruster arrays are soldered manually onto the PCB. The fabricated electronic circuitry is shown in Figure 7.7.

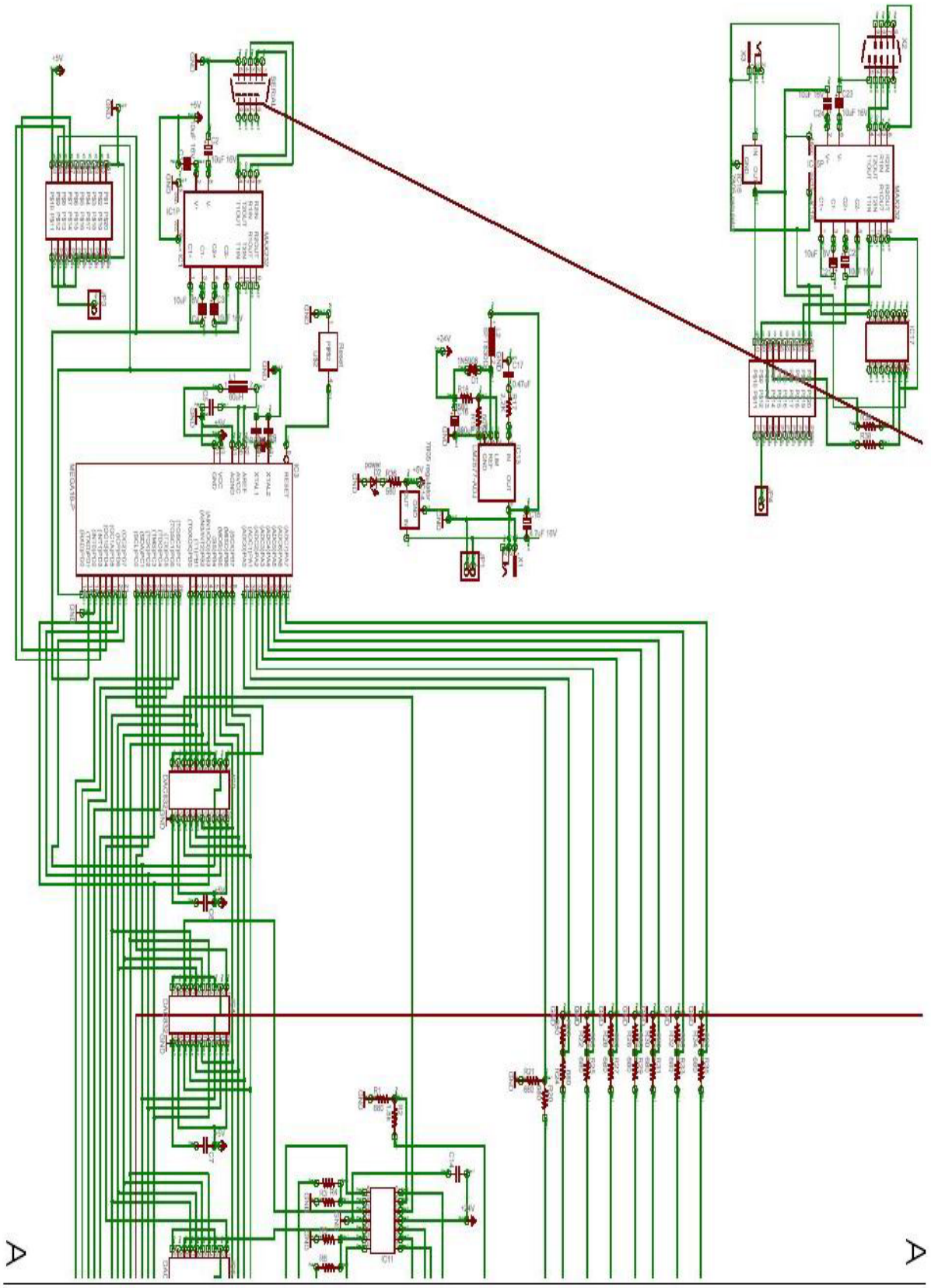

Figure 7.4. Design of the wireless addressing circuitry.

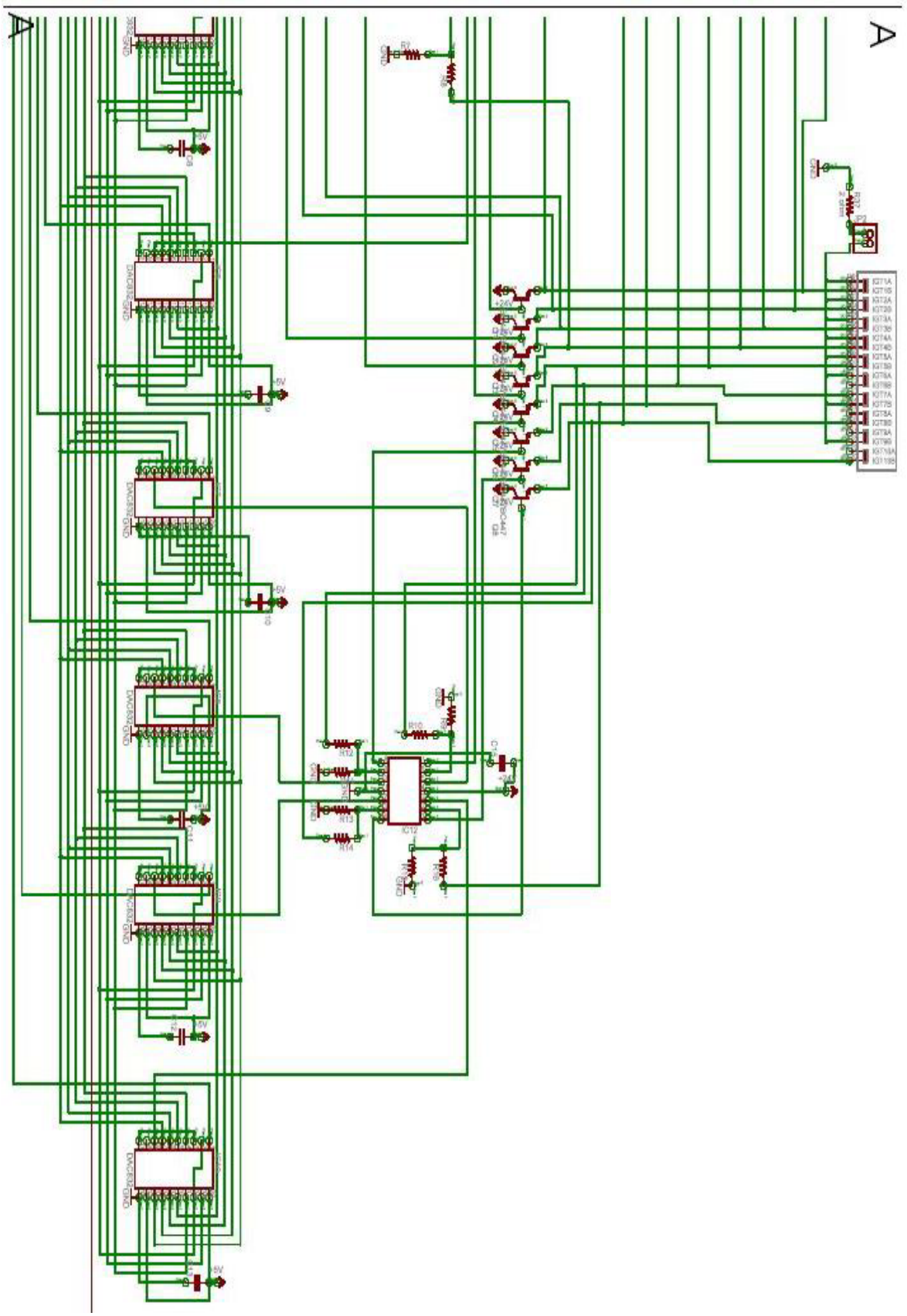

Figure 7.5. Design of the wireless addressing circuitry (continued).

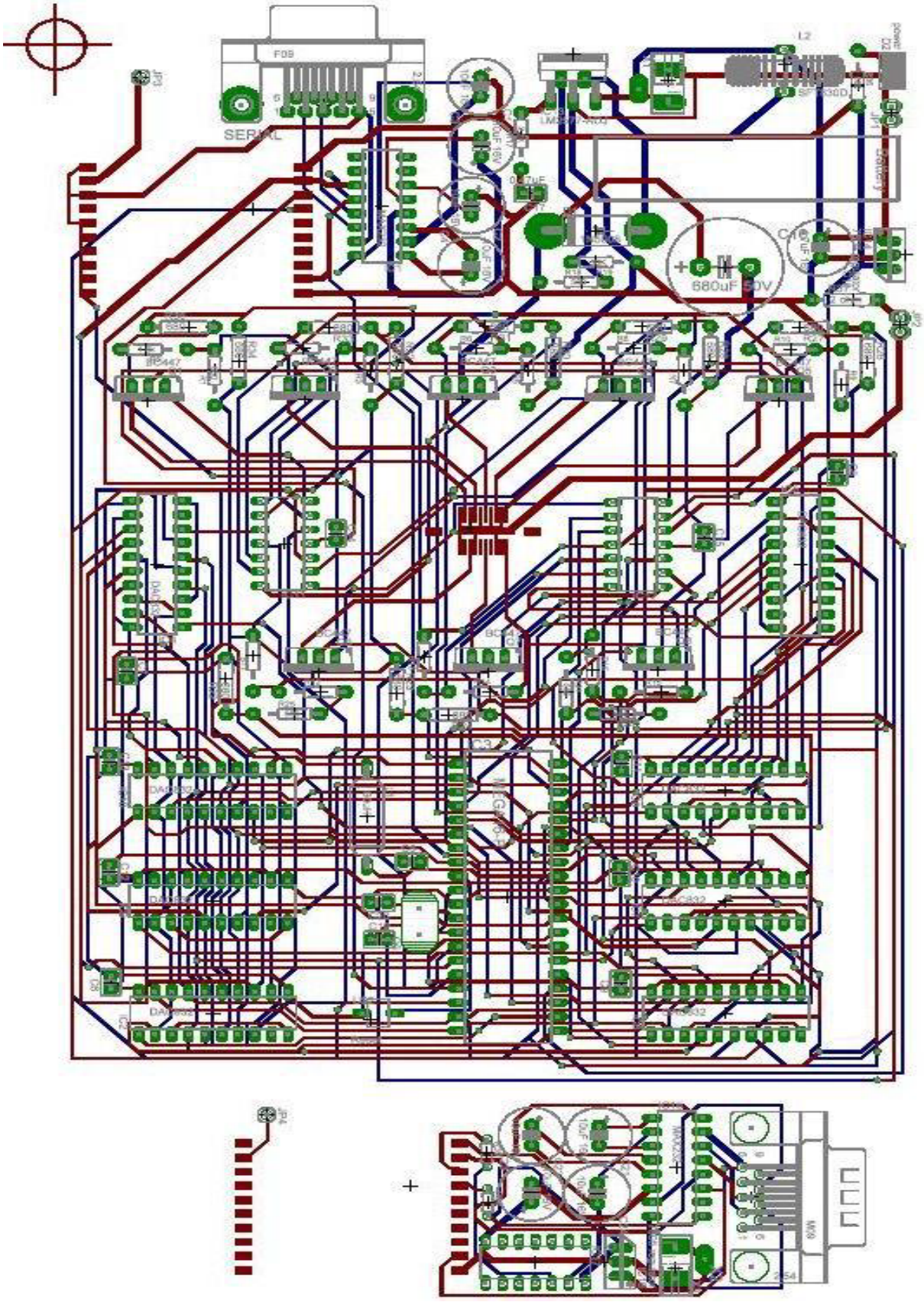

Figure 7.6. Drawing of the two-layer PCB.

Figure 7.8 shows the silicon and LTCC microthruster arrays installed a micro-connector onto the circuitry.

The program source code of firmware for microcontroller and RF transceiver is developed using C language and the communication and user interface are realized by Visual Basic. The C and Visual Basic source codes are included in Appendix B and Appendix C, respectively. The designed friendly user interface is shown in Figure 7.9.

7.4 Experimental Testing for Thin Film Au/Ti Micro-heater

The developed circuitry is utilized to measure the transient temperature of the thin film Au/Ti micro-heater fabricated in Chapter 4 (see Figures 4.3 and 4.4).

7.4.1 Resistance versus Temperature Calibration

A key issue for achieving meaningful temperature measurements is careful resistance vs. temperature calibration of the Au/Ti micro-heater. Because conventional printed circuit boards are not suitable for high temperature application, a silicon chip with a silicon dioxide insulation layer and Au contact pads is selected to hold the glass substrate with Au/Ti micro-heater. The small Au contact pads of the micro-heater are connected to the Au contact pads in the silicon layer using a thin Au wire by ultrasonic wire bonding. Then the Au contact pads in the silicon layer are attached to flexible wires using a high-temperature solder. The micro-heater installed on the silicon chip is placed into a Carbolite 1200 burn-off furnace.

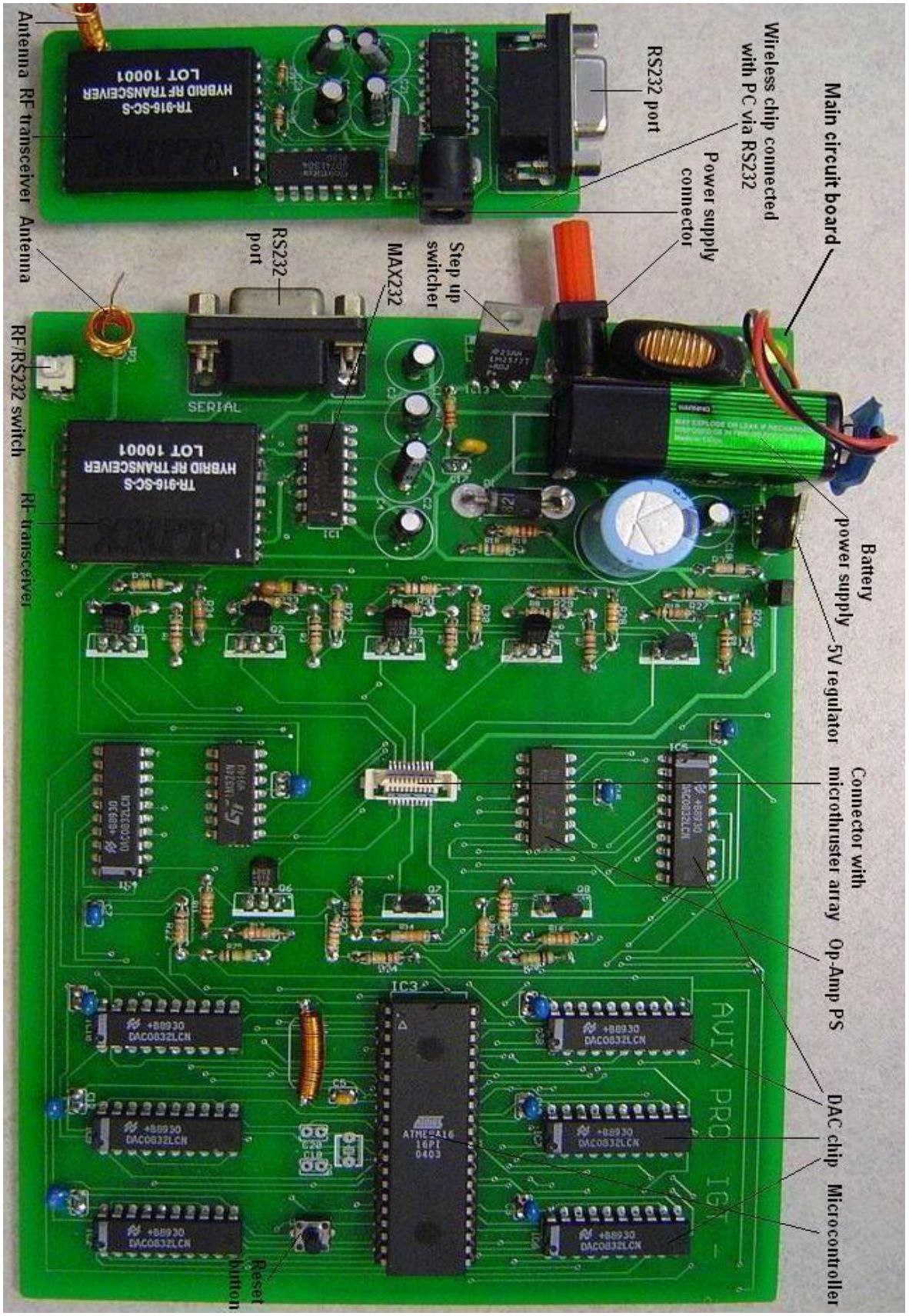

Figure 7.7. Fabricated wireless addressing circuitry.

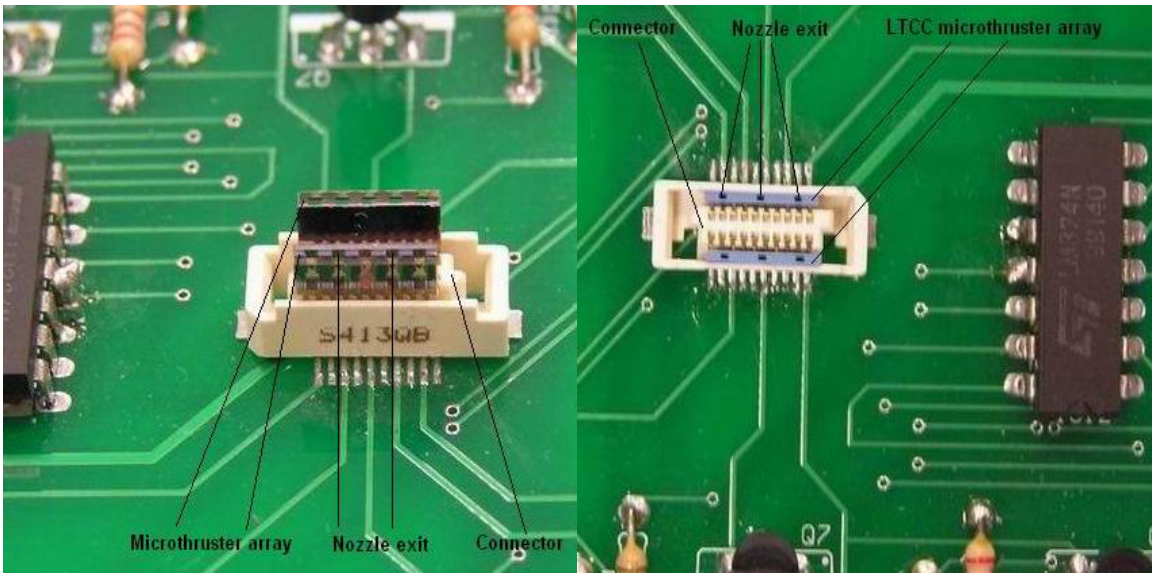

(a) (b)

Figure 7.8. (a) Silicon microthruster array on the circuitry. (b) LTCC microthruster array on the circuitry.

The furnace temperature and the micro-heater resistance are simultaneously measured using an Agilent 34970A data acquisition unit. The furnace temperature is gradually increased and measured by taking the average readings of two type-K thermocouples mounted very close to the micro-heater. The thermocouples are calibrated using a Pegasus^{PLUS} 1200 portable calibration furnace that is suitable for the high temperature calibration of thermocouples. The temperature difference between the two thermocouples never exceeds 0.5 ^{o}C. The resistance of the micro-heater is measured using a four-wire technique to improve resistance measurement accuracy. The offset-compensated four-wire measurement is employed because offset compensation removes the effects of any dc voltages in the circuit being measured, thus giving a more accurate measurement. The furnace temperature is increased in small steps and held at a constant level after each step until the temperature of the furnace and the resistance of the micro-heater are stabilized. The micro-heater resistance vs. temperature curve is shown in Figure 7.10.

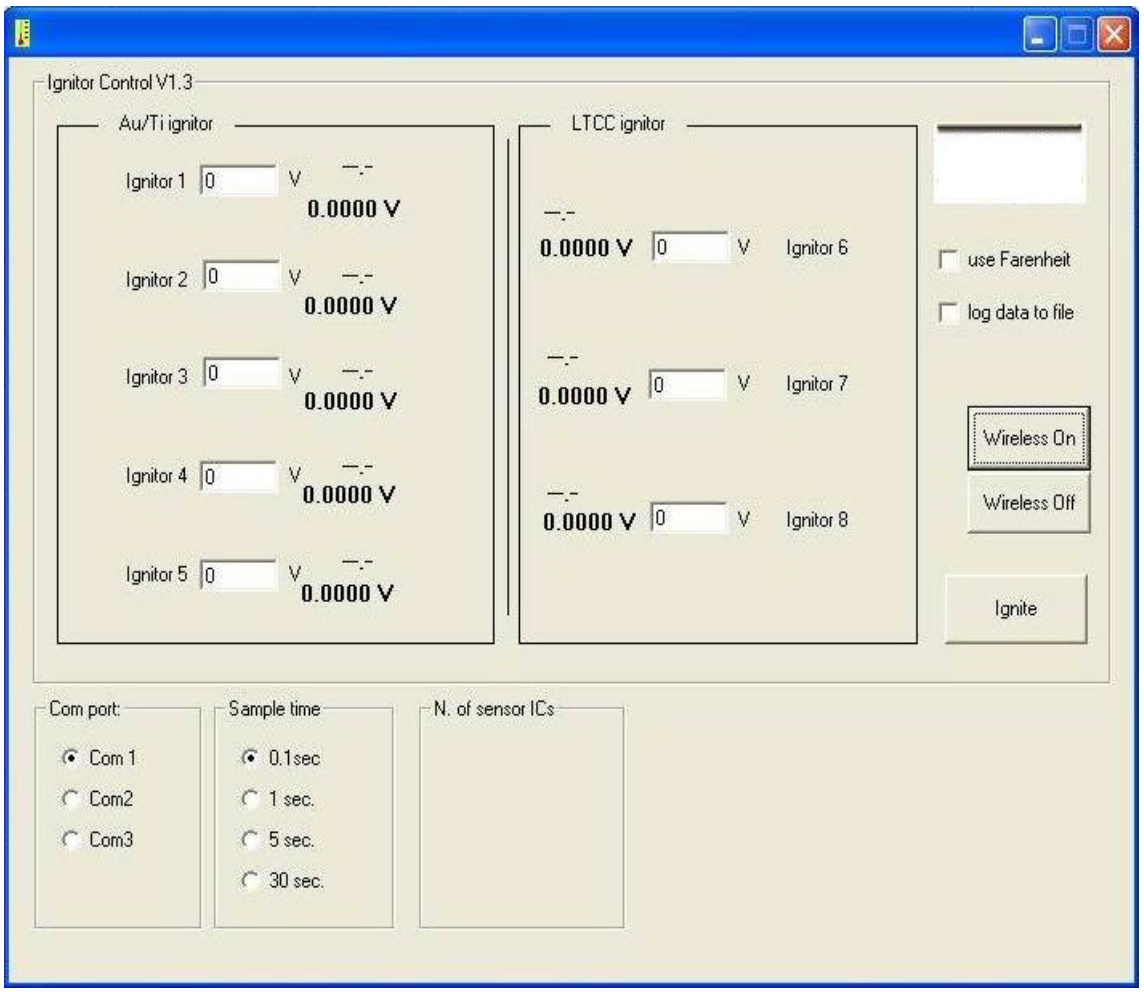

Figure 7.9. Designed user interface to implement the addressing and ignition.

The final calibration law deduced from the experiment is given by,

$$R = 0.3522T + 249.13 \tag{7.1}$$

where T is the micro-heater temperature (K) and R is the resistance of the micro-heater (ohm). A clear positive temperature coefficient of resistance (TCR) behavior can be concluded from the observed increase of the micro-heater resistance with temperature over the entire temperature range as investigated. The mechanism that is accounted for the positive TCR is mainly because the electrical conduction of the thin film micro-heater is controlled by electron mean free path that varies with the amplitude of thermal-agitated lattice vibrations.

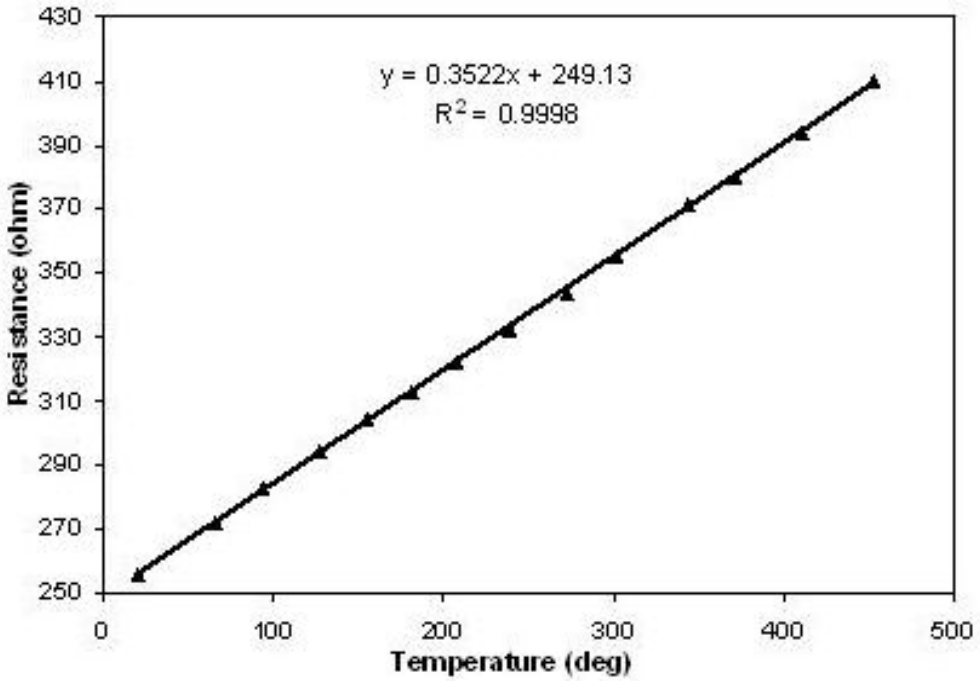

Figure 7.10. Au/Ti micro-heater resistance vs. temperature calibration curve.

7.4.2 Micro-heater Temperature Variation with Time

For more accurate measurement and higher data acquisition rate, an Agilent 34970A data acquisition unit with a 34901A plug-in module is connected to the circuitry to measue the small current change with a scan rate of 3 ms. Because the internal resistance of the amperemeter in 34901A is very small (0.5 ohm) compared to the resistance of the thin film Au/Ti micro-heater (in the range of 300 ohm), the current measurement error caused by the series resistance can be neglected. Figure 7.11 shows the measured current change with a voltage input of 8 V. It can be seen that the current change is very small. That is why a well-calibrated amperemeter is needed for accurate measurement. The calculated micro-heater resistance change is also shown in Figure 7.11.

Consequently, the micro-heater average temperature variation with a voltage input of 8 V is deduced from the calibration law and is shown in Figure 7.12. The average temperature increases quickly at the early stage of voltage supply but increases slowly after around 4 s. This is because of the equilibrium between heat

generation by Joule effect and heat loss by convection and conduction. As can be seen, the variation in temperature follows a logarithmic trend. Using Excel, a logarithmic curve of $T = 15.183Ln(t) + 237.29$ can be used to fit the plot with a R^2 value of 0.9866.

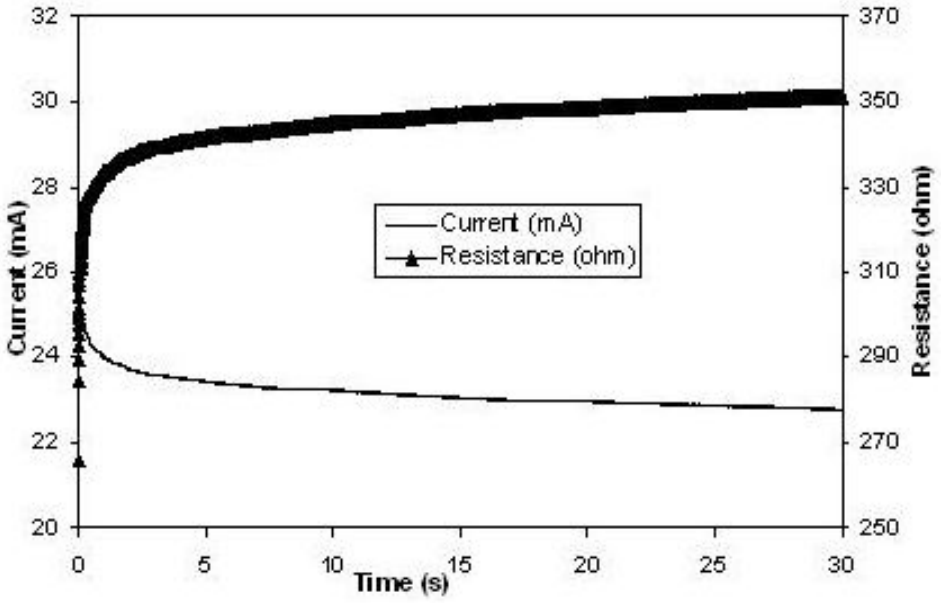

Figure 7.11. Current and resistance variations with time.

7.4.3 Comparison between Experimental Measurements and Electro-thermal Modeling

Figure 7.13 is the electrical field of the Au/Ti micro-heater with a voltage input of 8 V obtained from the electro-thermal modeling described in Section 5.4, Chapter 5. Almost all the voltage drop occurs in the zigzag part of the Ti resistor, which is expected because thin film Au has a much lower electrical resistivity than that of thin film Ti. This means the Au contact pad and Au conductor resistance can be neglected. Therefore, the calibration law of resistance vs. temperature of the micro-heater can be considered as the calibration law of the Ti zigzag part.

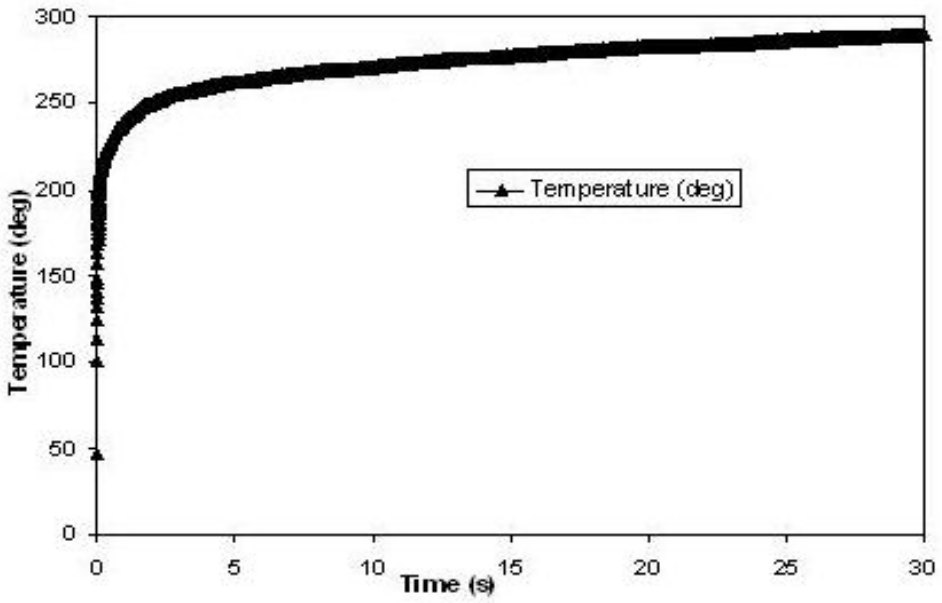

Figure 7.12. Thin film Au/Ti micro-heater temperature variation with time.

Consequently, the average temperature of the Ti zigzag part is derived from the electro-thermal modeling for comparison with the experimental measurements.

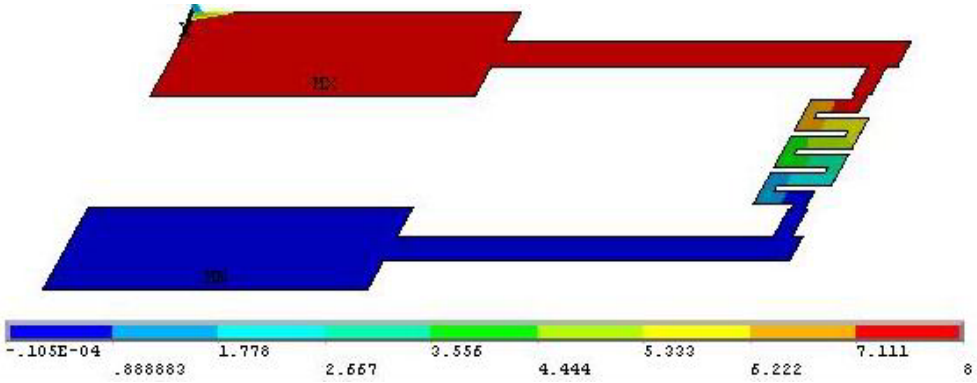

Figure 7.13. Electrical field of the Au/Ti micro-heater.

Figure 7.14 shows the micro-heater temperature comparison among electro-thermal modeling, experimental measurements using the circuitry and a type-K thermocouple with voltage inputs of 3 V and 5 V. The thermocouple is attached tightly to the Ti resistor zigzag part of the micro-heater. Temperature is acquired using an Agilent 34970A data acquisition unit with a scan rate of 1 ms. Temperatures obtained from the type-K thermocouple measurements are much lower than

those from modeling and circuitry measurements. This is mainly caused by thermocouple heat conduction as well as the presence of a thermal resistance between the thermocouple and micro-heater. As such, direct thermocouple measurement is not very practical for microscale heater. The temperature difference between electro-thermal modeling and experimental measurement using circuitry is small. The difference is mainly caused by the variation between actual thin film Au/Ti material characteristics and those calculated in the modeling, the uncertainty in resistance vs. temperature calibration, and the series resistance in current measurement. However, the temperature difference becomes somewhat big for voltage inputs of 8 V and 10 V as shown in Figure 7.15. The main possible causes are the oxidation of Ti and the degradation of Au/Ti due to agglomeration at high temperatures as stated in Refs. [Firebaugh et al 1998, Puigcorbe et al 2003].

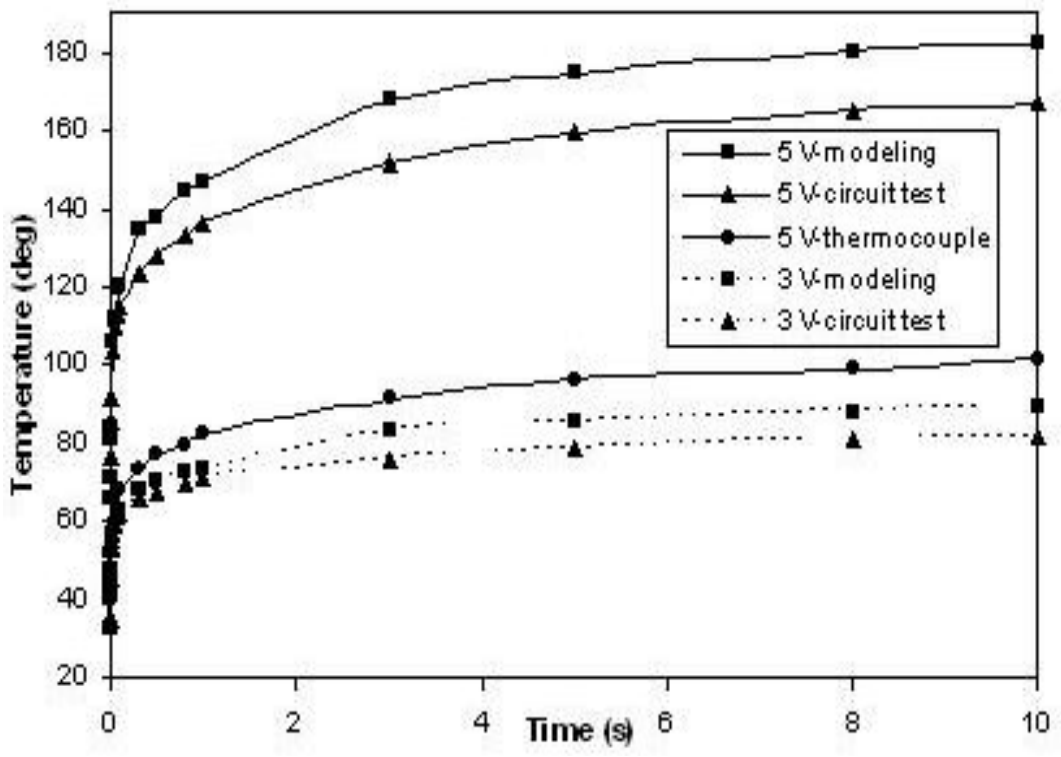

Figure 7.14. Comparison between measurements and electro-thermal modeling.

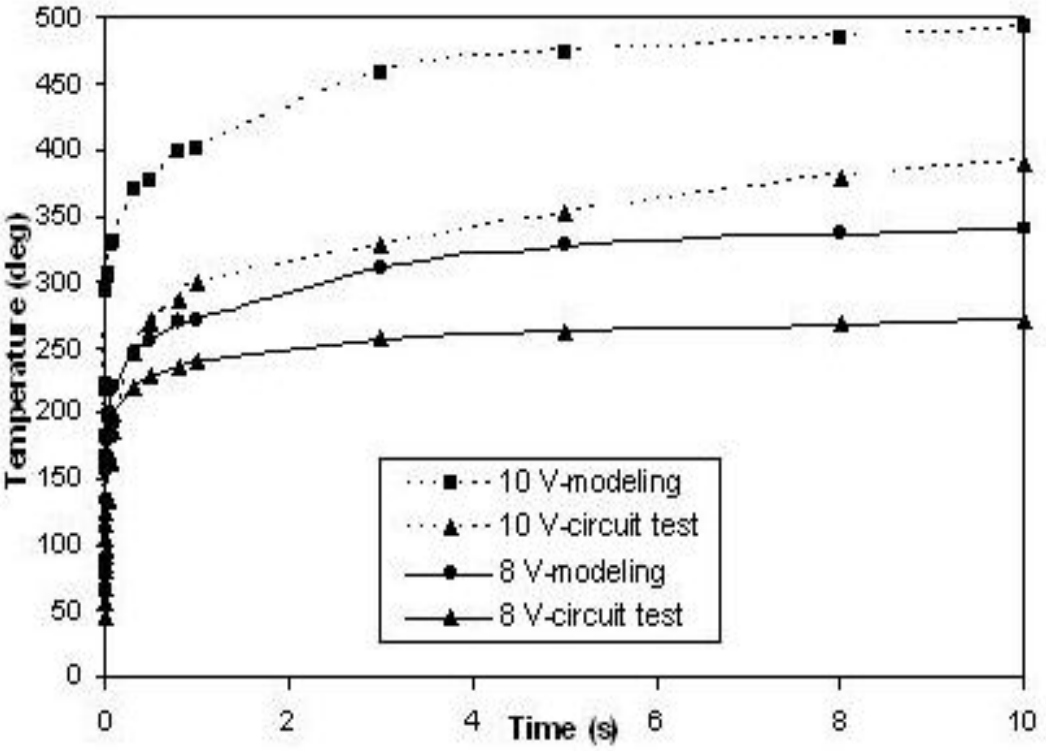

Figure 7.15. Comparison between measurements and electro-thermal modeling.

7.5 Experimental Testing for Solid Propellant Microthruster with Au/Ti Igniter

Using the wireless addressing circuitry, the transient temperature of the Au/Ti igniter of the solid propellant microthruser is measured experimentally.

7.5.1 Resistance versus Temperature Calibration

The resistance vs. temperature calibration of the solid propellant microthruser Au/Ti igniter is performed using the similar method as described in Section 7.4.1. The resistance vs. temperature curve is shown in Figure 7.16.

The final calibration law deduced from the experiment is given by,

$$R = -0.0001T^2 + 0.1614T + 346.32 \tag{7.2}$$

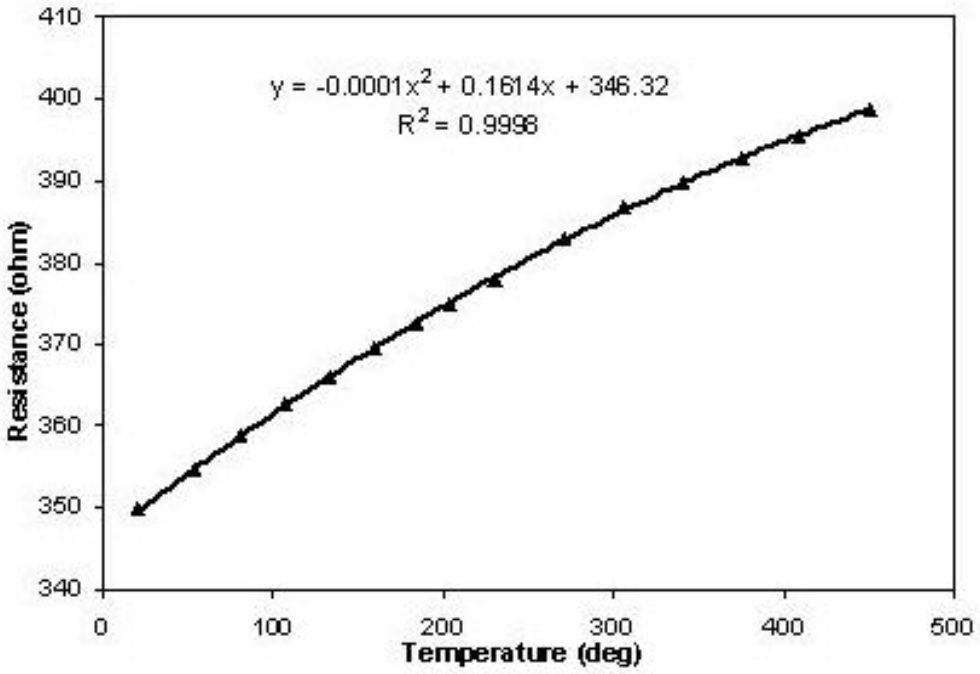

Figure 7.16. Au/Ti igniter resistance vs. temperature calibration curve.

A positive TCR behavior can be seen from the observed increase of the igniter resistance with temperature. Nevertheless, the resistance increase is not linear as would be expected for pure Au and Ti. This is probably caused by the formation of Au-Si eutectic at the interface between the igniter and silicon cover during the thermal cycle of the anodic bonding.

7.5.2 Igniter Temperature Variation with Time

Using the similar method described in Section 7.4.2, the igniter temperature variation with time is acquired using the circuitry. The measurement is performed only for low voltage values and ammonium perchlorate is not added into the propellant to increase the ignition temperature. The current change with a voltage input of 8 V is measured for the microthruster with Au/Ti igniter as shown in Figure 7.17. The calculated igniter resistance change is also shown in Figure 7.17.

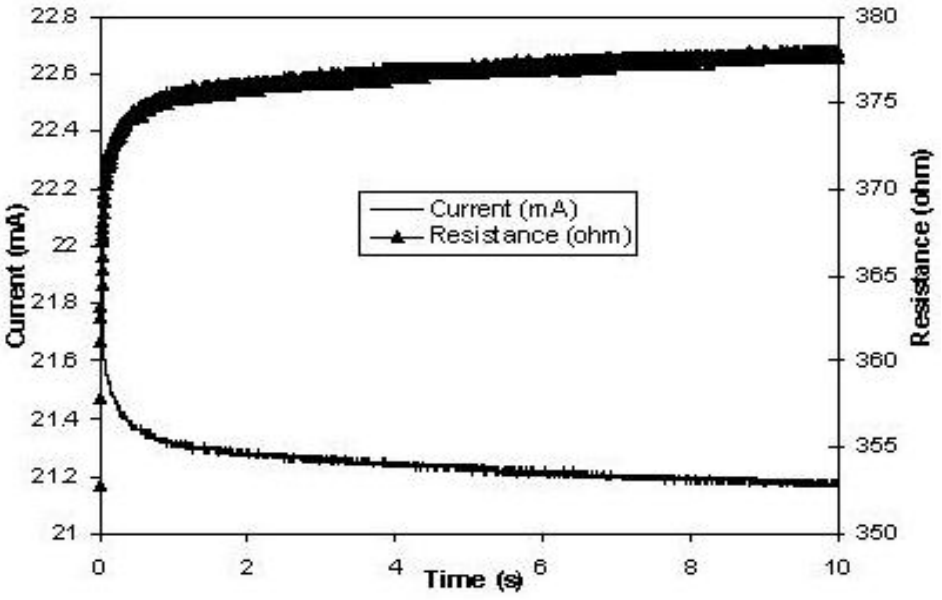

Figure 7.17. Current and resistance variations with time.

Accordingly, the igniter average temperature variation with a voltage input of 8 V is deduced from the calibration law and is shown in Figure 7.18. The curve indicates that the average temperature increases quickly at the early stage of voltage supply but increases slowly after around 1 s. This is because of the equilibrium between heat generation by Joule effect and heat loss by conduction.

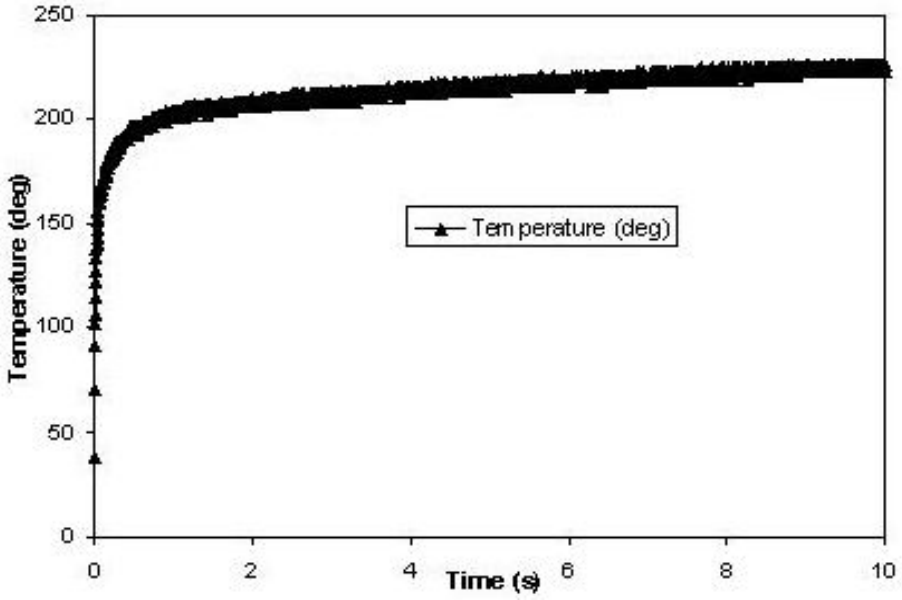

Figure 7.18. Au/Ti igniter temperature variation with time.

7.5.3 Comparison between Experimental Measurement and Electro-thermal Modeling

Employing the similar method stated in Section 7.4.3, the igniter temperature comparison between experimental measurement using the circuitry and electro-thermal modeling described in Chapter 5 is performed and shown in Figure 7.19. For a voltage input of 5 V, the temperature difference between experiment and modeling is small. The main causes for the difference are similar to those explained in Section 7.4.3, such as the thin film Au/Ti characteristics difference, the calibration uncertainty, and the series resistance. However, for a voltage input of 8 V, the difference becomes somewhat big. This is mainly caused by the oxidation of Ti and the degradation of Au/Ti due to agglomeration at high temperatures.

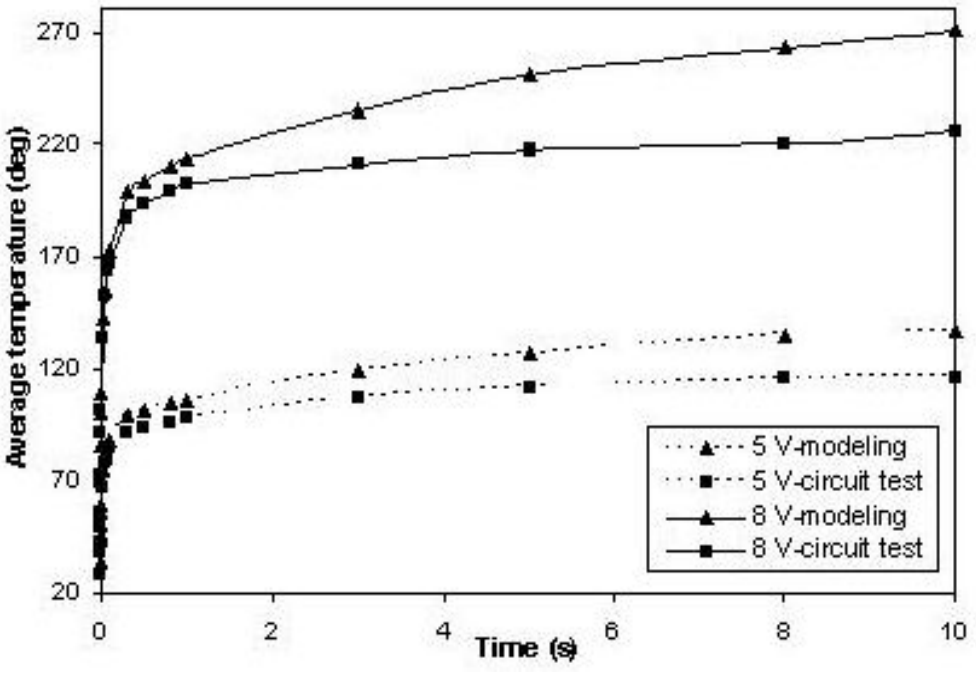

Figure 7.19. Comparison between measurements and electro-thermal modeling.

Figure 7.20 shows the testing signal of the microthruster with Au/Ti igniter with a voltage input of 10 V. The test is performed using the setup developed in Chapter 3 as shown in Figure 3.5. A current output of 27 mA is observed on the power supply at the time of ignition. The ignition power is estimated to be 0.27 W. The power supply and the data acquisition are set to start synchronously. Consequently, the ignition delay can be acquired through the testing signal as shown in Figure 7.20. The ignition delay is 0.0412 s with the ignition energy estimated to be 0.0111 J. From the electro-thermal modeling in Chapter 5, for a voltage input of 10 V, the ignition delay and ignition energy are 0.0364 s and 0.0097 J, respectively. The ignition delay and ignition energy differences between testing and electro-thermal modeling are 11.650 % and 12.415 %, respectively. The differences are mainly caused by differing contact areas between the propellant and the igniter, non-uniformities in the propellant grain, or the variation between actual thin film Au/Ti material characteristics and those calculated in the modeling.

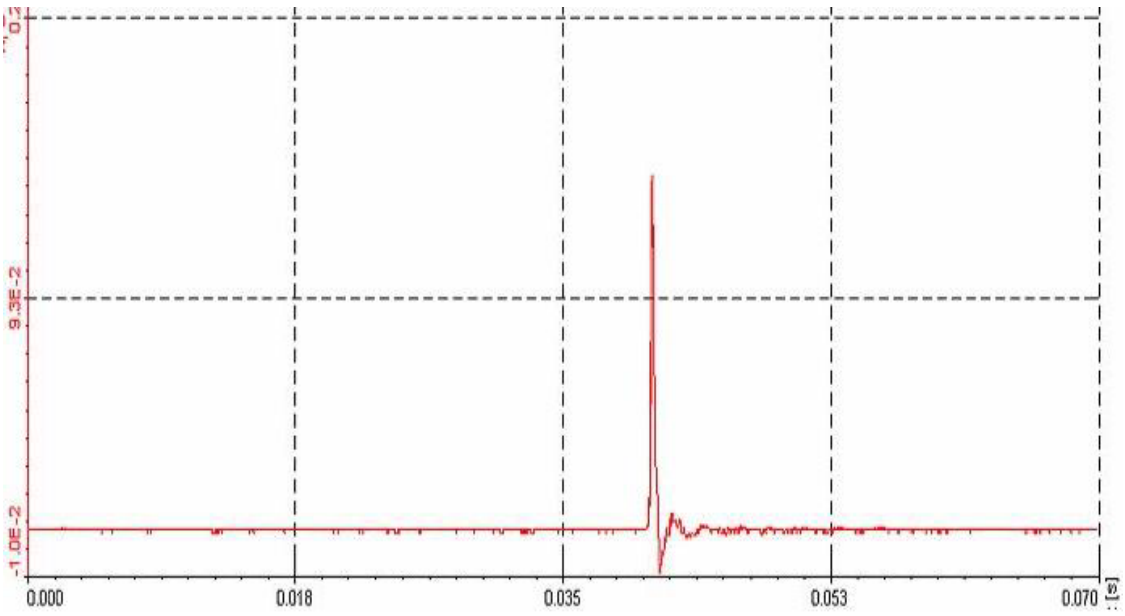

Figure 7.20. Testing signal with a voltage input of 10 V.

7.6 Chapter Summary

A prototype wireless addressing circuitry is designed and fabricated to realize the addressing of individual microthrusters in the microthruster array by multiplexing system, to measure the igniter temperature variation with time by measuring the igniter resistance change, and to achieve automatic control by RS232 and RF wireless communications. Using the programmable voltage source in the circuitry, the igniter temperature can be accurately controlled by 8 bit voltage levels (256 different levels). The RF wireless communication and 9 V battery power supply enable the circuitry to be very suitable for mobility. The 10 bit ADC feedback loop circuitry can monitor real-time status of each igniter in the microthruster array and allows each igniter to be functionally controlled. Utilizing the circuitry, the temperature variations with time of the thin film Au/Ti micro-heater and the solid propellant microthruster Au/Ti igniter are measured experimentally. The transient temperatures measured by the circuitry are compared with those from the FEM electro-thermal modeling described in Chapter 5. The electro-thermal modeling is validated by the experimental measurements.

Chapter 8

Conclusions

8.1 Summary of the Research

Three types of solid propellant microthrusters are developed.

- CFD modeling is performed to establish a benchmark for the experimental microthrusters. The micro nozzle jet flow is discussed in detail. The simulation indicates that wall heat loss effect is important for the viability of microthruster. Slip wall boundary layer effect is significant because rarefaction effects play an important role in microthruster.

- A MEMS-based microthruster with wire igniter has been designed, fabricated, and packaged. The feasibility of the new microthruster is proven by microcombustion experiment, thrust and impulse measurements both employing HTPB/AP/Al-based propellant and gunpowder-based propellant.

- A MEMS-based microthruster with Au/Ti igniter has been developed. The new design is suitable for batch fabrication and a high degree of miniaturization. It has a high fabrication efficiency, a large design flexibility, and a good anodic bonding quality. The feasibility of the new design is proven by microcombustion experiment along with thrust and impulse measurements.

- FEM modeling is used to simulate the microthruster with Au/Ti igniter.

The temperature profiles of the Au/Ti micro-heater from the experiment and modeling match very well. Ignition power, ignition delay, and ignition energy are derived from the modeling.

- LTCC technology has been used to develop a microthruster. The LTCC microthruster has many advantages over the silicon-based microthrusters, such as a better ignition efficiency, an adjustable thermal characteristics, and a more design freedom.

- An electronic circuitry has been developed to realize the addressing of the microthruster array, to measure the igniter temperature, and to achieve automatic control by RS232 and RF wireless communications.

8.2 Contributions of the Work

The contributions of this thesis can be summarized as follows:

1. A new silicon-based solid propellant microthruster with wire igniter is developed. It has a higher fabrication efficiency, much more design flexibility, and a better anodic bonding quality over former solid propellant microthrusters.

2. A new silicon-based solid propellant microthruster with Au/Ti igniter is developed. It not only inherits the advantages of microthruster with wire igniter, but also is more suitable for integration and batch fabrication.

3. A new ceramic-based solid propellant microthruster is developed. It has many advantages over the silicon-based solid propellant microthrusters, such as more suitability for a high level of integration, a better ignition efficiency and reliability, an adjustable thermal characteristics, and a more design freedom.

4. CFD modeling for the new designed solid propellant microthrusters is performed. In the modeling, some interesting phenomena appearing in mi-

crothrusters are emphasized such as the viability of microthruster due to wall heat loss and the slip wall boundary layer effects.

5. Modeling of the electro-thermal transient ignition for the three-dimensional solid propellant microthruster is carried out. The ignition power, ignition delay, and ignition energy are derived from the modeling.

6. The wireless addressing circuitry for the new designed solid propellant microthrusters is developed.

8.3 Recommendations for Future Work

Additional research is suggested in the following areas:

- For the CFD modeling in Chapter 2, basically, the model can simulate the thrust variation with combustion time. However, the thrust peak at the early stage of combustion can not be simulated. One improvement is to include the detailed combustion process of the propellant in the model.

- For the Au/Ti igniter in Chapter 4, the igniter can be improved for increased efficiency by employing other resistor materials, such as tungsten and nichrome, and improving the structural design.

- The addressing circuitry developed in Chapter 7 is far from optimization at its current stage. Future improvement on the circuitry is expected to improve the integration and minimization level of the microthruster arrays.

- Besides micropropulsion applications, the microthrusters developed in this thesis together with their microigniters can also have other applications such as drug delivery, microscale explosive boiling, sensors, actuators, and thermoelectric microgenerator applications. More investigations on these applications are expected to be performed in the future.

Bibliography

[Ansys 2004] http://www.ansys.com/, Feb. 2004.

[Archer and Saarlas 1996] R. Douglas Archer and Maido Saarlas, Introduction to Aerospace Propulsion, Upper Saddle River, N.J.: Prentice Hall, 1996.

[Arkilic 1997] E. B. Arkilic, "Measurement of the Mass Flow and Tangential Momentum Accommodation Coefficient in Silicon Micromachined Channels", Ph.D. Dissertation, Massachusetts Institute of Technology, 1997.

[Bayt 1999] Bayt, R.L., "Analysis, Fabrication, and Testing of a MEMS-based Micropropulsion System", Ph.D. Dissertation, Massachusetts Institute of Technology, 1999.

[Bayt and Breuer 2001] R. Bayt and K. Breuer, "Systems Design and Performance of Hot and Cold Supersonic Microjets", 39th AIAA Aerospace Sciences Meeting and Exhibit, AIAA Paper 2001-0721, 2001.

[Beckwith et al 1995] Beckwith T. G., Marangoni R. D., and Lienhard J. H., "Mechanical Measurements", 5th Edition, Addison-Wesley Publishing Company, June 1995.

[Bejan and Kraus 2003] Adrian Bejan and Allan D. Kraus, Heat Transfer Handbook, New York: J. Wiley, pp. 560-562, 2003.

[Chang and Sze 1996] C. Y. Chang and S. M. Sze, ULSI Technology, McGraw Hill, 1996.

[Choueiri 1999] E. Y. Choueiri, "Overview of U. S. Academic Programs in Electric Propulsion", in 35th AIAA Joint Propulsion Conference, AIAA Paper 99-2163, 1999.

[Collins et al l996] Collins D. Kukkonen K. and Venneri S. "Miniature, Low-cost, Highly Autonomous Spacecraft-A Focus for the New Millennium", In 46th International Astronautical Congress, IAF-96-U.2.06, 1996.

[Dewe 2002] DEWESoft User Manual, Software Version 5.4, October 30, 2002.

[Fluent 2003] Fluent Inc. Computational Fluid Dynamics Software, "FLUENT", Release 6.1, 2003, http://www.fluent.com.

[Firebaugh et al 1998] S. L. Firebaugh, K. F. Jensen, and M. A. Schmidt, "Investigation of High Temperature Degradation of Platinum Thin Films with an In-situ Resistance Measurement Apparatus", Journal of Microelectromechanical Systems, Vol. 7, No. 1, pp. 128-135, 1998.

[Gajda and Ahmed 1995] M. A. Gajda and H. Ahmed, "Applications of Thermal Silicon Sensors on Membranes", Sensors and Actuators A, Vol. 49, No. 1-2, pp. 1-9, 1995.

[Gatsonis et al 2000] Gatsonis, N.A., Nanson, R.A., and Le Beau, G.J., "Simulations of Cold-Gas Nozzle and Plume Flows and Flight Data Comparisons", Journal of Spacecraft and Rockets, Vol. 37, No. 1, pp. 39-48, 2000.

[Goldsmith et al 1961] Alexander Goldsmith, Thomas E. Waterman, and Harry J. Hirschhorn, Handbook of Thermophysical Properties of Solid Materials, Vol. III–Ceramics, Pergamon Press, Oxford, pp. 895, 1961.

[Gombosi 1994] Tamas I. Gombosi, Gaskinetic Theory, Cambridge University Press: 1994.

[Herwaarden and Sarro 1988] A. W. Van Herwaarden and P. M. Sarro, "Floating Membrane Thermal Vacuum Sensor", Sensors and Actuators A, Vol. 14, pp. 259-268, 1988.

[Hong et al 2003] Chien-Chong Hong, Suresh Murugesan, Sanghyo Kim, Gregory Beaucage, Jin-Woo Choi, and Chong H. Ahn, "A Functional On-chip Pressure Generator Using Solid Chemical Propellant for Disposable Lab-on-a-chip", Lab on a Chip, Vol. 3, No. 4, pp. 281-286, 2003.

[Hoskins et al 1999] Hoskins, WA, Wilson MJ, Willey MJ, Campbell, M and Chung S, "PPT Development Efforts at Primex Aerospace Company", AIAA Paper 99-2291, 35th Joint Propulsion Conference, Los Angeles, CA, June, 1999.

[Janson and Helavijian 1996] Janson, S. and Helavijian, H., "Batch-Fabricated Microthrusters: Initial Results", 32nd SISS/ ASME/SAE/ASEE Joint Propulsion Conference, Lake Buena Vista, FL, 1996.

[Janson et al 1999] Janson, S.W., Helvajian, H., Hansen, W., Lodmell, and Lt. J., "Microthrusters for Nanosatellites", Proc. MicroNanotechnology for Space Applications, Vol. 1, 1999.

[Kail and Mahr 1999] Dipl.-lng. R. Kail and Dipl.-lng. W. Mahr, "Piezoelectric Measuring Instruments and their Applications", Kistler Reprint 20. 116e, 1999.

[Kakamia et al 2004] Akira Kakamia, Hiroyuki Koizumib, Kimiya Komurasakib, and Yoshihiro Arakawa, "Design and Performance of Liquid Propellant Pulsed Plasma Thruster", Vacuum, Vol. 73, No. 3-4, pp. 419-425, 2004.

[Kang et al 2002] Tae Goo Kang, Sang Wook Kim, and Young-Ho Cho, "High-impulse, Low-power, Digital Microthrusters Using Low Boiling Temperature Liquid Propellant with High Viscosity Fluid Plug", Sensors and Actuators A, Vol. 97-98, pp. 659-664, 2002.

[Karniadakis and Beskok 2002] George Em Karniadakis and Ali Beskok, Micro Flows: Fundamentals and Simulation, Springer, 2002.

[Kittel 1996] Charles Kittel, Introduction to Solid State Physics, 7th Edition, New York; Singapore: John Wiley and Sons, pp. 159-162, 166-168, 1996.

[Koeneman et al 1997] Paul B. Koeneman, Ilene J. Busch-Vishniac, and Kristin L. Wood, "Feasibility of Micro Power Supplies for MEMS", Journal of Microelectromechanical Systems, Vol. 6, No. 4, pp. 355-362, 1997.

[Kohler et al 2002] Johan Kohler, Johan Bejhed, Henrik Kratz, Fredrik Bruhn, Ulf Lindberg, Klas Hjort, and Lars Stenmark, "A Hybrid Cold Gas Microthruster System for Spacecraft", Sensors and Actuators A, Vol. 97-98, pp. 587-598, 2002.

[Lamedica et al 2002] G. Lamedica, M. Balucani, A. Ferrari, P.D. Tromboni, and M. Marchetti, "Microthruster in Silicon for Aerospace Application", IEEE AESS Systems Magazine, pp. 22-77, September 2002.

[Lee and Kwon 2002] Dae Hoon Lee and Sejin Kwon, "Heat Transfer and Quenching Analysis of Combustion in a Micro Combustion Vessel", Journal of Micromechanics and Microengineering, Vol. 12, No. 5, pp. 670-676, 2002.

[Lewis et al 2000] David H. Lewis Jr., Siegfried W. Janson, Ronald B. Cohen, and Erik K. Antonsson, "Digital Micropropulsion", Sensors and Actuators A, Vol. 80, No. 2, pp. 143-154, 2000.

[Lide 1998] David R. Lide, Editor-in-chief, CRC Handbook of Chemistry and Physics, 79th Edition, Boca Raton: CRC Press, 1998-1999.

[Liu 1995] Jianqiang Liu, "Integrated Micro Devices for Small Scale Gaseous Flow Study", Ph.D. Dissertation, California Institute of Technology, 1995.

[London et al 2001] A. P. London, A. H. Epstein, and J. L. Kerrebrock, "High-Pressure Bipropellant Microrocket Engine", Journal of Propulsion and Power, Vol. 17, No. 4, pp. 780-787, 2001.

[McCreary 2000] Terry W. McCreary, Experimental Composite Propellant: Murray, KY: T.W. McCreary, 2000.

[Mcgrath 1995] Mcgrath, D., "The History of Thiokol STAR^{TM} Motor Missions", AIAA Paper 95-3129, San Diego, CA, July 1995.

[Mehra 2000] Amitav Mehra, "Development of a High Power Density Combustion System for a Silicon Micro Gas Turbine Engine", Ph.D. Dissertation, Massachusetts Institute of Technology, 2000.

[Menz et al 2001] W. Menz, J. Mohr, O. Paul, Microsystem Technology, Wiley-Vch, pp. 242-245, 2001

[Mirels 1999] H. Mirels, "Effect of Wall on Impulse of Solid Propellant Driven Millimeter-Scale Thrusters", AIAA Journal, Vol. 37, No. 12, pp. 1617-1624, 1999.

[Mueller 1997] J. Mueller, "Thruster Options for Microspacecraft: A Review and Evaluation of Existing Hardware and Emerging Technologies", in 33rd AIAA/ASME/SAE/ASEE Joint Propulsion Conf and Exhibit, AIAA Paper 97-3058, 1997.

[Mukerjee et al 2000] E. V. Mukerjee, A. P. Wallace, K. Y. Yan, D. W. Howard, R. L. Smith, and S. D. Collins, "Vaporizing Liquid Microthruster", Sensors and Actuators A, Vol. 83, No. 1-3, pp. 231-236, 2000.

[Oh et al 1992] S. Oh, W. Chu, and S. Cahill, "Thin Film Heater on a Thermally Isolated Microstructure", Mater. Res. Soc. Symp. Proc., Vol. 276, pp. 277-282, 1992.

[Orieux et al 2002] S. Orieux, C. Rossi, and D. Esteve, "Compact Model Based on a Lumped Parameter Approach for the Prediction of Solid Propellant Microrocket Performance", Sensors and Actuators A, Vol. 101, No. 3, pp. 383-391, 2002.

[Palmer and Newton 1993] E. G. Palmer and C. M. Newton, "3-D Packaging Using Low Temperature Cofired Ceramic (LTCC)", International Journal of Microcircuits and Electronic Packaging, Vol. 16, No. 4, pp. 279-284, 1993.

[Pavio et al 2002] Jeanne Pavio, Joseph Bostaph, Allison Fisher, Jerry Hallmark, Billy-Joe Mylan, and Chenggang Xie, "LTCC Fuel Cell System for Portable Wireless Electronics", Advancing Microelectronics, Vol. 29, No. 5, pp. 8-11, 2002.

[Pham et al 2003] P. Q. Pham, D. Briand, C. Rossi, and N. F. De Rooij, "Downscaling of Solid Propellant Pyrotechnical Microsystems", Tech. Digest Transducers'03, Boston, USA, pp. 1423-1426, June 8-12, 2003.

[Plumer et al 2000] J. D. Plummer, M. D Deal, and P. B Griffin, Silicon VLSI Technology, Prentice Hall, 2000.

[Puigcorbe et al 2003] J Puigcorbe, D Vogel, B Michel, A Vila, I Gracia, C Cane, and J R Morante, "Thermal and Mechanical Analysis of Micromachined Gas Sensors", Journal of Micromechanics and Microengineering, Vol. 13, No. 5, pp. 548-556, 2003.

[Purrington 1999] Gary W. Purrington, Plastic Resin Bonded High Energy Rocket Fuel Systems. Volume III, Basic Ingredient Study and Small Motor Production: Pocatello, Idaho: Firefox Enterprises Inc., 1998-2001.

[Raju et al 2002] Reni Raju, B. P. Pandey, and Subrata Roy, "Finite Element Model of Fluid Flow Inside a Micro-Thruster", AIAA paper 2002-5733, 2002.

[Reichbach 2001] Jeffrey Reichbach, Micropropulsion System Selection for Precision Formation Flying Satellites, Master Thesis, Massachusetts Institute of Technology, 2001.

[Rossi et al 1997] C. Rossi, E. Scheid, and D. Esteve, "Theoretical and Experimental Study of Silicon Micromachined Microheater with Dielectric Stacked Membranes", Sensors and Actuators A, Vol. 63, No. 3, pp. 183-189, 1997.

[Rossi et al 1998a] C. Rossi, P. Temple-Boyer, and D. Esteve, "Realization and Performance of Thin SiO_2/SiN_x Membrane for Microheater Applications", Sensors and Actuators A, Vol. 64, No. 3, pp. 241-245, 1998.

[Rossi et al 1998b] C. Rossi, D. Esteve, P. Temple-Boyer, and G. Delannoy, "Realization, Characterization of Micro Pyrotechnic Actuators and FEM Modelling of the Combustion Ignition", Sensors and Actuators A, Vol. 70, No. 1-2, pp. 141-147, 1998.

[Rossi et al 1999] C. Rossi, D. Esteve, and C. Mingues, "Pyrotechnic Actuator: a New Generation of Si Integrated Actuator", Sensors and Actuators A, Vol. 74, No. 1-3, pp. 211-215, 1999.

[Rossi et al 2000] C. Rossi, M. D. Rouhani, and D. Esteve, "Prediction of the Performance of a Si-micromachined Microthruster by Computing the Subsonic Gas Flow inside the Thruster", Sensors and Actuators A, Vol. 87, No. 1-2, pp. 96-104, 2000.

[Rossi et al 2001] C. Rossi, T. Do Conto, D. Esteve, and B. Larangot, "Design, Fabrication and Modeling of MEMS-based Microthrusters for Space Application", Smart Materials and Structures, Vol. 10, No. 6, pp. 1156-1162, 2001.

[Rossi et al 2002] C. Rossi, S. Orieux, B. Larangot, T. Do Conto, and D. Esteve, "Design, Fabrication and Modeling of Solid Propellant Microrocket-

Application to Micropropulsion", Sensors and Actuators A, Vol. 99, No. 1-2, pp. 125-133, 2002.

[Rossi et al 2004] C. Rossi, A. Chaalane, D. Esteve, and H. Granier, "Main Direction of Solid Propellant Microthruster Activity at LAAS", in Proceedings of the CANEUS Micro-Nano-Technologies for Aerospace Applications, Monterey, CA, USA, 1-5 November, 2004.

[Rubio et al 2001] M. R. Gongora-Rubio, P. Espinoza-Vallejos, L. Sola-Laguna, and J. J. Santiago-Aviles, "Overview of Low Temperature Co-fired Ceramics Tape Technology for Meso-system Technology (MsST)", Sensors and Actuators A, Vol. 89, No. 3, pp. 222-241, 2001.

[Senturia 2001] Stephen D. Senturia, Microsystem Design, Kluwer Academic Publishers: 2001.

[Shackelford 1994] Shackelford, James F., CRC Materials Science & Engineering Handbook, 2ed Edition, Boca Raton, Florida, CRC Press, pp. 289, 566, 568, 1994.

[Straker 1992] David Straker, C Style: Standards and Guidelines: Defining Programming Standards for Professional C Programmers, New York: Prentice Hall, 1992.

[Sutton and Biblarz 2001] George P. Sutton and Oscar Biblarz, Rocket Propulsion Elements, New York: John Wiley & Sons, pp. 59, 63, 428, 479, 730, 2001.

[Takahashi et al 2002] K. Takahashi, H. Ebisuzaki, H. Kajiwara, T. Achiwa, and K. Nagayama, "Design and Testing of Mega-bit Microthruster Arrays", Proceedings of the AIAA Nanotech 02 conference, Houston, USA, September 9-11, 2002.

[Tanaka et al 2003] Shuji Tanaka, Ryuichiro Hosokawa, Shin-ichiro Tokudome, Keiichi Hori, Hirobumi Saito, Masashi Watanabe, and Masayoshi Esashi,

"MEMS-based Solid Propellant Rocket Array Thruster with Electrical Feedthroughs", Transactions of the Japan Society for Aeronautical and Space Science, Vol. 46, No. 151, pp. 47-51, 2003.

[Teasdale et al 2001] Dana Teasdale, Veljko Milanovic, Paul Chang, and Kristofer S J Pister, "Microrockets for Smart Dust", Smart Materials and Structures, Vol. 10, No. 6, pp. 1145-1155, 2001.

[Vidal et al 2003] M. Puig-Vidal, J. Lopez, P. Miribel, J. Samitier-Marti, C. Rossi, and A. Berthold, "Smart Drug Delivery System Based on Pyrotechnical Actuation", LAAS Report 03119, 2003.

[Vladislav 1998] Vladislav E. Zinov'ev, Handbook of Thermophysical Properties of Metals at High Temperatures, New York: Nova Science Publishers, Inc., pp. 257, 1998.

[Weast 1984] Robert C. Weast, Editor-in-chief, CRC Handbook of Chemistry and Physics, Boca Raton, Florida: CRC Press, pp. E-380, 1984-1985.

[Williams 1997] Kirt Reed Williams, "Micromachined Hot-Filament Vacuum Devices", Ph.D. Dissertation, University of California, Berkeley, pp. 11-13, 1997.

[Wood et al 1969] W.D. Wood, H.W. Deem and C.F. Lucks, "The Emittance of Titanium and Titanium Alloys", Columbus, Ohio: Defense Metals Information Center, Battelle Memorial Institute, pp. 4, 1969.

[Ye et al 2001] X. Y. Ye, F. Tang, H. Q. Ding, and Z. Y. Zhou, "Study of a Vaporizing Water Micro-thruster", Sensors and Actuators A, Vol. 89, No. 1-2, pp. 159-165, 2001.

[Youngner et al 2000] Daniel W. Youngner, Son Thai Lu, Edgar Choueiri, Jamie B. Neidert, Rober E. Black III, Kenneth J. Graham, Dave Fahery, Rodney Lucus, and Xiaoyang Zhu, "MEMS Mega-pixel Micro-thruster Arrays for Small Satellite Stationkeeping", in 14th Annual

AIAA/USU Conference on Small Satellites, AIAA Paper SSC00-X-2, 2000. http://alfven.princeton.edu/papers/MMMAabs.htm.

[Zhang et al 2003a] K. L. Zhang, S. K. Chou, Simon S. Ang, X. S. Tang, and J. S. Phang, "Investigation of Solid Propellant Microthrusters", International Journal of Computational Engineering Science, Vol. 4, No. 3, pp. 517-520, 2003.

[Zhang et al 2003b] K. L. Zhang, S. K. Chou, and Simon S. Ang, "Design, Fabrication and Testing of a Solid Propellant Microthruster", in Proceeding of PowerMEMS 2003, Makuhari, Japan, December 4-5, pp. 61-64, 2003.

[Zhang et al 2004a] K. L. Zhang, S. K. Chou, and Simon S. Ang, "MEMS-based Solid Propellant Microthruster Design, Simulation, Fabrication and Testing", IEEE/ASME Journal of Microelectromechanical Systems, Vol. 13, No. 2, pp. 165-175, 2004.

[Zhang et al 2004b] K. L. Zhang, S. K. Chou, and Simon S. Ang, "Development of a Solid Propellant Microthruster with Chamber and Nozzle Etched on a Wafer Surface", Journal of Micromechanics and Microengineering, Vol. 14, No. 6, pp. 785-792, 2004.

[Zhang et al 2004c] K. L. Zhang, S. K. Chou, and S. S. Ang, "A Solid Propellant Microthruster with Metal Igniter", in Proceeding of PowerMEMS 2004, Kyoto, Japan, November 28-30, pp. 129-132, 2004.

[Zhang et al 2005a] K. L. Zhang, S. K. Chou, and S. S. Ang, "Development of a Low Temperature Co-fired Ceramic Solid Propellant Microthruster", Journal of Micromechanics and Microengineering, Vol. 15, No. 5, pp. 944-952, 2005.

[Zhang et al 2005b] K. L. Zhang, S. K. Chou, and S. S. Ang, "A Low Temperature Co-fired Ceramic Solid Propellant Microthruster for Micropropulsion Applications", in Proceeding of the 13th International Conference on Solid State

Sensors, Actuators and Microsystems (IEEE Transducers'05), Seoul, Korea, June 5-9, pp. 672-675, 2005.

[Zhang et al 2005c] K. L. Zhang, S. K. Chou, S. S. Ang, and X. S. Tang, "A MEMS-based Solid Propellant Microthruster with Au/Ti Igniter", Sensors and Actuators A: Physical, Vol. 122, No. 1, pp. 113-123, 2005.

[Zhang et al 2005d] K. L. Zhang, S. K. Chou, and S. S. Ang, "A Wireless Addressing Circuitry for Microthruster Array", in Proceeding of PowerMEMS 2005, Tokyo, Japan, November 28-30, pp. 105-108, 2005.

[Zhang et al 2006a] K. L. Zhang, S. K. Chou, and S. S. Ang, "Performance Prediction of a Novel Solid-Propellant Microthruster", AIAA Journal of Propulsion and Power. (Accepted for publication, will appear in Vol. 22, No. 1, 2006)

[Zhang et al 2006b] K.L. Zhang, S.K. Chou, and S.S. Ang, "Fabrication, Modeling and Testing of a Thin Film Au/Ti Microheater", Journal of Micromechanics and Microengineering. (Accepted for publication)

[Zhang et al 2006c] K.L. Zhang, S.K. Chou, and S.S. Ang, "Investigation on the Ignition of a MEMS Solid Propellant Microthruster", Sensors and Actuators A: Physical. (Submitted)

Appendix A

Uncertainty Analysis

This appendix quantifies the uncertainty in the measurements presented in this thesis. It first presents the uncertainty associated with the independent measurements, and then presents the predicted uncertainty in the derived quantities.

The uncertainty in the independent measurements will be based on the accuracy of the instruments. The uncertainty in the derived quantities will be propagated using:

$$u_y = \sqrt{\sum_{i=1}^{n} (\frac{\partial y}{\partial x_i} \cdot u_i)^2} \tag{A.1}$$

where y is a function of n independent variables $x_1, x_2, ..., x_n$, u_i is the uncertainty (systematic/random uncertainty) in each of the variables [Beckwith et al 1995].

A.1 Uncertainty in the Independent Measurements

A.1.1 Temperature Measurements

All the type-K thermocouples are calibrated against the standard liquid-in-glass thermometer that has an accuracy of $\pm$ 0.05 ^oC by immersing them in a constant temperature water bath for temperatures below 100 ^oC. For temperatures between 100 ^oC and 500 ^oC, the thermocouples are calibrated using a Pegasus^{PLUS} 1200 portable calibration furnace that has an accuracy of $\pm$ 0.5 ^oC. Consequently, the

Table A.1. Equations of calibration curves of the thermocouples (y = actual temperature, ^oC; x = measured temperature, ^oC).

Thermocouples	Type	Equation of calibration curve
T_1	K	$y = 0.9919x - 0.0327$
T_2	K	$y = 0.9875x + 0.0270$
T_3	K	$y = 0.9859x - 0.0239$

uncertainty in the temperature measurements using thermocouple is estimated as $\pm$ 0.5 ^oC. The equations of the calibration curves for the thermocouples are given in Table A.1.

A.1.2 Resistance Measurements

The resistance for the Au/Ti resistance vs. temperature calibration is measured using an Agilent 34970A data acquisition unit with a 34902A plug-in module. The offset-compensated four-wire measurement is employed to remove the effects of any dc voltages in the circuit being measured. The uncertainty is $\pm$ 0.01 % of the range. For the range of 1000 ohm, the uncertainty is $\pm$ 0.1 ohm.

A.1.3 DC Current Measurements

The current is measured using an Agilent 34970A data acquisition unit with a 34901A plug-in module. The uncertainty is $\pm$ 0.05 % of the range. For the range of 100 mA, the uncertainty is $\pm$ 0.05 mA.

A.1.4 Uncertainty in the Feature Geometry

The uncertainties in the feature geometry, while having no effect on the accuracy of the thrust, directly affect the derived quantities of thrust. The nozzle throat is a critical point in the geometry because it sets the mass flow rate in the choked

condition. The nozzle is measured using an optical microscope with a calibrated stage. By translating the stage in x and y, a distance between two points can be determined. This method is used to measure the width and length of nozzle to an accuracy of 1 μm. There is a 0.5 % uncertainty in the throat width for the smallest nozzle tested. The depth of the nozzles is measured by the observation of fringes from an interferometer on the focal plane. These fringes are focused on the top surface, and through a calibrated adjustment of the focal plane they are focused on the bottom surface. This is accurate to ± 2 μm, although the uncertainty is a smaller precentage of the feature size (0.6 %).

A.2 Uncertainty in the Derived Quantities

A.2.1 Temperature of the Au/Ti Micro-heater

The Au/Ti micro-heater temperature is tested by the circuitry using the following equation:

$$T = 1/0.3522(R - 249.13) \tag{A.2}$$

where R is the resistance of the micro-heater. The uncertainty in the micro-heater temperature is expressed by:

$$u_T = \sqrt{((dT/dR) \cdot u_R)^2} \tag{A.3}$$

where, u_R is the uncertainty in the resistance measurement. The resistance R is obtained from the voltage source output value and the measured current value.

$$R = U/I \tag{A.4}$$

Therefore,

$$u_R = \sqrt{(\frac{\partial R}{\partial U} \cdot u_U)^2 + (\frac{\partial R}{\partial I} \cdot u_I)^2} \tag{A.5}$$

where u_U is the uncertainty in voltage supply and u_I is the uncertainty in current measurement (± 0.05 mA). The voltage source output uncertainty is ± 0.025 %

of the range. For the range of 20 V, the uncertainty is ± 0.005 V. By solving equation (A.5), u_R is obtained with a value of ± 0.676 ohm. Substituting u_R into equation (A.3), the uncertainty in the Au/Ti micro-heater temperature measurement is estimated as ± 1.918 ^oC.

A.2.2 Temperature of the Solid Propellant Microthruster Igniter

The solid propellant microthruster igniter temperature is tested by the circuitry using equation (A.6):

$$T = 0.0638R^2 - 39.197R + 5926.1 \tag{A.6}$$

Employing the similar procedure in Section A.2.1, the uncertainty in the igniter temperature measurement is ± 4.263 ^oC.

A.2.3 Thrust

The force sensor is calibrated by Kistler Instrument Corp. with a sensitivity of -118.8 pC/N and an uncertainty of 0.5 mN for the measuring range of 10 N. The charge amplifier is calibrated by Kistler Instrument Corp. with an uncertainty of ± 0.05 % full scale. The charge amplifier error is thus negligible in its effect on the calibration of the entire measuring chain. The percentage drift of the measuring signal per second is calculated from:

$$Drift[\%/sec] = 0.03pC \cdot 1sec \cdot 100\%/E \cdot F \tag{A.7}$$

where E is the sensitivity of the sensor, F is the force to be measured. For a measuring range of 10 N, there is a measuring drift error of 0.0025 % per second. Therefore, the drift error is negligible. The uncertainty in thrust measurement is then estimated as ± 0.5 mN.

Appendix B

C Code for Microcontroller and RF Transceiver

```
// Using the UART in C
// Routines for interrupt controlled UART
// Last modified: 02-06-2005
// Modified by: Zhang Kaili

/* Includes */
#include <io.h>
#include <ina90.h>
#include <inttypes.h>
#include <avr/signal.h>

/* Constants-transmiting start code "00ff00*/
#define    trans_head1   0x00
#define    trans_head2   0xFF
#define    trans_head3   0x00

/* Global variable */
unsigned char currentChannel = 0;
unsigned char PCC0 =1;
unsigned char PCC1 =1;
unsigned char PCC2 =1;
unsigned char PCC3 =1;
unsigned char PCC4 =1;
unsigned char PCC5 =1;
unsigned char PCC6 =1;
unsigned char PCC7 =1;
```

```
/* Prototypes */
void InitUART( unsigned int baudrate );
void InitADC(void);
void Initval_zero(void);
//void SPI_MasterInit(void);
void TransmitByte( unsigned char data );
//void SPI_MasterTransmit(char cData);

unsigned char i;
unsigned char adc_rus[8][2]; // adc reading, 8 sets of adc x 2 high/low byte
unsigned char dac_val[8]; //dac value obtain from PC
unsigned char b, s; // vairable for adc_rus

/* Main - a simple test program*/
void main( void )
{
      unsigned char button;
      DDRB = 0xFF; // set port B, C and D as output
      DDRC = 0xFF;
      DDRD = 0xFB;
      button = PIND; // read portD
      button &= 0x04;   // mask the rest, except PD2
                  /* Enable interrupts => enable Gobal interrupts */
      InitUART( 12 ); /*Set the bitrate to 4800 bps using a 1MHz crystal */
      if (button == 4) // check for wireless
            InitADC();
      //SPI_MasterInit();
      _SEI();
      Initval_zero(); // initialise all DAC value zeros, zeros at output
      PORTD = (1<<PD4)|(0<<PD3); //set wireless Linx SCs916 to receive mode

      // temperorily assignment of ADC data
      /* */
      //adc_rus[0][0] = 0xfe; adc_rus[0][1] = 0x6e;
      //adc_rus[1][0] = 0x55; adc_rus[1][1] = 0x6e;
      //adc_rus[2][0] = 0x54; adc_rus[2][1] = 0x6e;
      //adc_rus[3][0] = 0x65; adc_rus[3][1] = 0x6e;
      //adc_rus[4][0] = 0x73; adc_rus[4][1] = 0x6e;
      //adc_rus[5][0] = 0x74; adc_rus[5][1] = 0x6e;
      //adc_rus[6][0] = 0x31; adc_rus[6][1] = 0x6e;
      //adc_rus[7][0] = 0x32; adc_rus[7][1] = 0x6e;

      for( ; ; )        /* Forever */
      {
            //SPI_MasterTransmit(0xc3);
            //SPI_MasterTransmit(0xc3);

            //RTC = (0<<PC7)|(1<<PC6)|(0<<PC5);
            //PORTD = (0<<PD7)|(1<<PD6)|(1<<PD5);
            button = PIND; // read portD
            button &= 0x04;   // mask the rest, except PD2
            if (button == 4) //  dont do ADC if wireless is activated
            {
                  /* ADC in process for all 8 channel */
                  for (currentChannel=0;currentChannel<8;currentChannel++)
                  {
                        ADMUX = currentChannel;
```

```
ADCSRA |= (1<<ADSC);
                                    //Start conversion in Free-running mode
                                          //Now the conversions are running
                        while(!(ADCSRA & 0x10));
                             // check for ADIF flag to set for ADC complete
                        adc_rus[currentChannel][1] = ADCL;
                        adc_rus[currentChannel][0] = ADCH;

                  //PORTB = ADCL;
                  //PORTC = ADCH;
                  }
            // transmit the first 3 code for PC to recognize the start byte
                  TransmitByte (trans_head1);
                  TransmitByte (trans_head2);
                  TransmitByte (trans_head3);
            /* sending the data over to PC via RS232   */
                  for (s=0;s<8;s++)
                  {
                        for (b=0;b<2;b++)
                        {
                              TransmitByte(adc_rus[s][b]);
                                 /* Echo the received character */
                              _NOP();
                              _NOP();
                              _NOP();
                        }
                  }
            }
            else
            {
            }
      }
}

/* Initialize UART */
void InitUART( unsigned int baudrate )
{
      UBRRH = (baudrate>>8);
      UBRRL = baudrate;
      /* Enable UART receiver and transmitter, and receive interrupt */
      UCSRB = ( (1<<RXCIE)|(1<<RXEN) | (1<<TXEN) );
}
void InitADC(void)
{
      //Enable the ADC
      //Use prescale factor 8 -> ADC clock is 250kHz
      ADCSRA = (1<<ADEN) | (1<<ADPS1) | (1<<ADPS0);
}
void Initval_zero(void)
{
      //set all output to zeros
      unsigned char ct;
      for (ct =0;ct<8;ct++)
      {
            PORTB = 0xFF;
            switch (ct)
            {
```

```
case 0:
                  PCC4 = 0;
                  break;
            case 1:
                  PCC2 = 0;
                  break;
            case 2:
                  PCC3 = 0;
                  break;
            case 3:
                  PCC1 = 0;
                  break;
            case 4:
                  PCC0 = 0;
                  break;
            case 5:
                  PCC5 = 0;
                  break;
            case 6:
                  PCC7 = 0;
                  break;
            case 7:
                  PCC6 = 0;
                  break;

            }

            PORTC =
(PCC7<<PC7)|(PCC6<<PC6)|(PCC5<<PC5)|(PCC4<<PC4)|(PCC3<<PC3)|(PCC2<<PC2)|(PCC1<<PC1)
(PCC0<<PC0);
            PORTD = (0<<PD7)|(1<<PD6)|(0<<PD5);//enable ILE,then WRT to DAC
            _NOP();
            _NOP();
            PCC0 = 1;
            PCC1 = 1;
            PCC2 = 1;
            PCC3 = 1;
            PCC4 = 1;
            PCC5 = 1;
            PCC6 = 1;
            PCC7 = 1;
            PORTC = 0xFF; // unselect DAC

      }
}
void SPI_MasterInit(void)
{
      /* Set MOSI and SCK output, all others input */
      DDRB = (1<<DDB5)|(1<<DDB7);
      /* Enable SPI, Master, set clock rate fck/16 */
      SPCR = (1<<SPE)|(1<<MSTR)|(0<<CPOL)|(1<<CPHA)|(0<<SPI2X)|(0<<SPR1)|(1<<SPR0);
}

void SPI_MasterTransmit(char cData)
{
      /* Start transmission */
```

```
SPDR = cData;
      /* Wait for transmission complete */
      while(!(SPSR & (1<<SPIF)))
      ;
}

/* Interrupt Uart recieve handler */

SIGNAL (SIG_UART_RECV)
{
      unsigned char count;

      /* Read the received data */
      /* Calculate buffer index */
      /* Wait for data to be received */

      /* Get and return received data from buffer */
      for (count =0;count<8;count++)
      {
            while ( !(UCSRA & (1<<RXC)) )
            ;
            dac_val[count] = UDR;
            PORTB = dac_val[count];
            switch (count)
            {
            case 0:
                  PCC4 = 0;
                  if (dac_val[count] <= 25)
                              // this limits the output, val25 -> 20V max
                        PORTB = 0x19;
                  break;
            case 1:
                  PCC2 = 0;
                  if (dac_val[count] <= 25)
                        PORTB = 0x19;
                  break;
            case 2:
                  PCC3 = 0;
                  if (dac_val[count] <= 25)
                        PORTB = 0x19;
                  break;
            case 3:
                  PCC1 = 0;
                  if (dac_val[count] <= 25)
                        PORTB = 0x19;
                  break;
            case 4:
                  PCC0 = 0;
                  if (dac_val[count] <= 25)
                        PORTB = 0x19;
                  break;
            case 5:
                  PCC5 = 0;
                  if (dac_val[count] <= 117)
                              // limits to 15V, val 117 is NOT of (9.2*15V)
                        PORTB = 0x75;
                  break;
```

```
case 6:
                  PCC7 = 0;
                  if (dac_val[count] <= 117)
                        PORTB = 0x75;
                  break;
            case 7:
                  PCC6 = 0;
                  if (dac_val[count] <= 117)
                        PORTB = 0x75;
                  break;

            }
             // Chip select the correct DAC
             // PC0 to PC7 are the chipselect of the DAC chip

             // PD7 -> WRT active low , write to chip
             // PD6 -> ILE active high, latch enable
             // PD5 -> XFER active low, transfer from latch to output.

             // PD4 -> is connect to Linx SCs 916, RXenable , active high
             // PD3 -> is connect to Linx SCs 916, TXenable , active high
             // PD2 -> unused, gounded
             // PD1 -> TXD
             // PD0 -> RXD
             //selecting the correct chip
            PORTC =
(PCC7<<PC7)|(PCC6<<PC6)|(PCC5<<PC5)|(PCC4<<PC4)|(PCC3<<PC3)|(PCC2<<PC2)|(PC
C1<<PC1)|(PCC0<<PC0);
            PORTD = (0<<PD7)|(1<<PD6)|(0<<PD5);//enable ILE,then WRT to DAC
            _NOP();
            _NOP();
            PCC0 = 1;
            PCC1 = 1;
            PCC2 = 1;
            PCC3 = 1;
            PCC4 = 1;
            PCC5 = 1;
            PCC6 = 1;
            PCC7 = 1;
            PORTC = 0xFF; // unselect DAC

      }

      //SPI_MasterTransmit(dac_val[0]);
      //SPI_MasterTransmit(dac_val[0]);

}

/* write functions */
void TransmitByte( unsigned char data )
{
      while ( !(UCSRA & (1<<UDRE)) )
            ;                                   /* Wait for empty transmit
buffer */
      UDR = data;                              /* Start transmittion */
}
```

Appendix C

VB Source Code for Circuitry

```
// VB Source code
// Last modified: 02-06-2005
// Modified by: Zhang Kaili


Option Explicit

Public Const ERROR_TEMPERATURE_NOT_READ = 1000
Public Const ERROR_OPENING_PORT = 1
Public Const NO_ERROR = 0
Public adc(1 To 10) As Long
Public dac(1 To 8) As Long
Public Arr() As Byte
Public avg_resist(1 To 20) As Double
Public avg_count(1 To 20) As Integer


Option Explicit

Private Sub Command1_Click()
MSComm1.DTREnable = True
End Sub

Private Sub Command2_Click()
MSComm1.DTREnable = False
End Sub

Private Sub Command3_Click()
MSComm1.RTSEnable = True
End Sub

Private Sub Command4_Click()
MSComm1.RTSEnable = False
End Sub
```

```
Private Sub Form_Load()
    'ReadIni
    update_com_port
    update_sample_rate
End Sub

Private Sub Form_Unload(Cancel As Integer)
    close_iic_bus
    'SaveIni
End Sub

Private Sub Ignite_Click()
    Dim count As Integer
    Dim tedac As Double

    For count = 1 To 8
        tedac = Val(Text1(count - 1).Text) '+ 1
        'Text1(count - 1).Text = dac(count)
        If tedac < 0 Or tedac > 30 Then
            MsgBox ("The range of this value is between 0V and 30V only.")
            dac(count) = 0
            Text1(count - 1).Text = "0"
        End If
        If tedac = 0 Then
            Text1(count - 1).Text = "0"
        End If
        If count < 6 Then
           dac(count) = tedac * 11.53
        Else
            dac(count) = tedac * 9.2
        End If
        'dac(count) = tedac

        dac(count) = Not (CByte(dac(count))) 'inverse the code to
                                             'replace hardware invertor
        ''MsgBox (dac(count))

    Next count

    IIC_tx_byte

End Sub

Private Sub option_200_ms_Click()
    update_sample_rate
End Sub

Private Sub option_200_ms_KeyPress(KeyAscii As Integer)
    update_sample_rate
End Sub

Private Sub option_1_sec_Click()
    update_sample_rate
End Sub

Private Sub option_1_sec_KeyPress(KeyAscii As Integer)
    update sample rate
```

```
End Sub

Private Sub option_30_sec_Click()
    update_sample_rate
End Sub

Private Sub option_30_sec_KeyPress(KeyAscii As Integer)
    update_sample_rate
End Sub

Private Sub option_5_sec_Click()
    update_sample_rate
End Sub

Private Sub option_5_sec_KeyPress(KeyAscii As Integer)
    update_sample_rate
End Sub

Private Sub option_com1_Click()
    update_com_port
End Sub

Private Sub option_com1_KeyPress(KeyAscii As Integer)
    update_com_port
End Sub

Private Sub option_com2_Click()
    update_com_port
End Sub

Private Sub option_com2_KeyPress(KeyAscii As Integer)
    update_com_port
End Sub

Private Sub option_com3_Click()
    update_com_port
End Sub

Private Sub option_com3_KeyPress(KeyAscii As Integer)
    update_com_port
End Sub

Private Sub Timer1_Timer()
    Dim t As Double
    Dim unit As String
    Dim i As Integer
    Dim resis As Double
    Dim temp_v As Double

    If check_farenheit Then
        unit = "°F"
    Else
        unit = "°C"
    End If

    't = temperature(0)
    open iic bus MSComm1.object
```

```
    IIC_rx_byte
    If t = ERROR_TEMPERATURE_NOT_READ Then
        MsgBox "Unable to read internal temperature", vbOKOnly, "Error"
        Timer1.Enabled = False
        voltage(0).Caption = "--.-" + unit
    Else

        For i = 1 To 8
           t = (5 / 1024) *adc(i) '5V max ,10 bit resolution (2 to power 10
           If i < 4 Then
            t = t * 6.63
           Else
            t = t * 3.1556
           End If

           If check_farenheit Then
                t = farenheit(t)
           End If
           voltage(i - 1).Caption = Format(t, "#0.0000" + " V")

           ' writing the resistance changes
           temp_v = dac(i)
           temp_v = Not (CByte(temp_v))
           temp_v = temp_v / 8.5
           'temp_v = temp_v / 8273.5
           'resis = (969.55 * temp_v)
           'resis = (1020 * temp_v)
           If adc(i) = 0 Or temp_v = 0 Then
                 resis = 0
           Else
                 resis = (resis - t) / temp_v
                 'resis = t / 2.2
                 'resis = temp_v / resis
                 resis = resis - 969.55
           End If

           'If avg_count(i) = 4 Then

              '      avg_resist(i) = avg_resist(i) / 5
               '     res_templ(i - 1).Caption = Format(avg_resist(i),
"#0.000" + unit)
                '    avg_count(i) = 0
                 '   avg_resist(i) = 0
           'Else
            'avg_count(i) = avg_count(i) + 1
            'avg_resist(i) = avg_resist(i) + resis
           'End If

        Next i
   End If

   'log_to_file

End Sub

Private Function temperature(address As Integer) As Double
    Dim temperature int As Long
```

```
Dim temperature_frac As Long

    address = address * 2
    On Error GoTo errors
    open_iic_bus MSComm1.object

    '/*resettiamo bene il chip*/

    '/**/
    'temperature_frac = IIC_rx_byte
    temperature = (temperature_int * 256 + temperature_frac) / 128 * 5 / 10
    If temperature_int >= 128 Then
        temperature = temperature - 256
    End If
    'IIC_stop
    Exit Function
errors:
    temperature = ERROR_TEMPERATURE_NOT_READ
End Function

Private Function update_sample_rate()
    If option_1_sec Then
        Timer1.Interval = 1000
    ElseIf option_5_sec Then
        Timer1.Interval = 5000
    ElseIf option_30_sec Then
        Timer1.Interval = 30000
    ElseIf option_200_ms Then
        Timer1.Interval = 250
    Else
        Timer1.Interval = 1000
    End If
End Function
Private Function update_com_port()
    If MSComm1.PortOpen Then
        MSComm1.PortOpen = False
    End If

    If option_com1 Then
        MSComm1.CommPort = 1
        Timer1.Enabled = True
    ElseIf option_com2 Then
        MSComm1.CommPort = 2
        Timer1.Enabled = True
    ElseIf option_com3 Then
        MSComm1.CommPort = 3
        Timer1.Enabled = True
    Else
        MSComm1.CommPort = 1
        Timer1.Enabled = False
    End If
    MSComm1.Settings = "4800,N,8,1"
    MSComm1.InputMode = comInputModeBinary

End Function

Private Function farenheit(t As Double)
```

```
farenheit = 32 + 9 / 5 * t
End Function

'Private Function log_to_file()
    'If check_log_to_file Then
       ' Open "pc_thermometer.txt" For Append As #1
       ' Print #1, Date$, Time$, label_temperature_outside.Caption,
label_temperature_indoor.Caption
      '  Close #1
    'End If
'End Function



Option Explicit
Dim MSComm1 As Object

Public Function open_iic_bus(serial_port As Object) As Integer
    Set MSComm1 = serial_port
    MSComm1.Settings = "4800,N,8,1"
    MSComm1.InputMode = comInputModeBinary
     If Not MSComm1.PortOpen Then
        MSComm1.PortOpen = True
    End If
    open_iic_bus = NO_ERROR
    Exit Function
End Function

Public Sub close_iic_bus()
    If MSComm1.PortOpen Then
        MSComm1.PortOpen = False
    End If
End Sub

Public Sub IIC_tx_byte()

    'Private Sub Text1_KeyPress(KeyAscii As Integer)
    Dim Buffer As Variant
    Dim d As Integer
    Dim temp As Long

    For d = 1 To 8

        Buffer = Buffer + Chr$(dac(d))
    Next d

        MSComm1.Output = Buffer

End Sub

Public Sub IIC_rx_byte()
    Dim Buffer As Variant
    Dim a As Long
    Dim b As Long
    Dim i, j As Integer
    Dim counter As Byte
    a = 256
```

```
    counter = 1
    ' Set InputMode to read binary data

    ' Assign to byte array for processing
    Arr = MSComm1.Input
    ' Arr now contains all the info received from the port
    On Error GoTo errors2

    For i = 100 To 158
        If (Arr(i) = 0) And (Arr(i + 1) = 255) And (Arr(i + 2) = 0) Then
'check for start code
          For j = 1 To 16 Step 2   ' read 2 byte at a time
            adc(counter) = (Arr(j + i + 2) * a) + (Arr(j + i + 3)) 'store
high/low byte
            counter = counter + 1
          Next j
        Exit For ' the reading is taken, save time for loop
    End If
    Next i

errors2:

End Sub

Private Sub iic_wait()
'void , insert here wait code for very fast systems
'actual measured speed is 1,5 kbps on a P90...
End Sub



Option Explicit

Const IniFileName = "\pc_thermometer.INI"
Private IniFileDirectory As String

Declare Function GetPrivateProfileStringA% Lib "Kernel32" (ByVal
ApplicationName$, ByVal KeyName$, ByVal Default$, ByVal ReturndString$,
ByVal Size%, ByVal FileName$)
Declare Function WritePrivateProfileStringA% Lib "Kernel32" (ByVal
ApplicationName$, ByVal KeyName$, ByVal StringToWrite$, ByVal FileName$)

Public Sub WriteIniString(ByVal key As String, ByVal Value As String)
    If WritePrivateProfileStringA("ARB", key, Value, IniFileDirectory +
IniFileName) <> True Then
    End If
End Sub

Public Function ReadIniString(key As String, Default As String)
Dim ReturnedString As String
    ReturnedString = Space$(128)
    If Not GetPrivateProfileStringA%("ARB", key, Default, ReturnedString,
128, IniFileDirectory + IniFileName) <> True Then
        MsgBox "INI file is invalid or does not exist."
    End If
    ReadIniString = Trim(ReturnedString)
End Function
```

```
Public Sub ReadIni()
    Dim i As Integer
    Dim C As Control
    'useful when developing...
    IniFileDirectory = CurDir$
    If IniFileDirectory = "C:\Programmi\DevStudio\VB" Then
        IniFileDirectory = "C:\Alberto\DS1621"
    End If
    'check for INI file
    If Left$(ReadIniString("FileId", "None"), 5) <> "therm" Then
        MsgBox "Unable to find Startup file" + Chr$(13) + IniFileDirectory
+ "\" + IniFileName + Chr$(13) + Chr$(13) + "Using defaults", , "Error"

    Else
        On Error Resume Next
        For Each C In frm_thermometer.Controls
            C.Caption = ReadIniString("frm_thermometer." + C.Name +
".caption", C.Caption)
            C.Value = Val(ReadIniString("frm_thermometer." + C.Name +
".value", C.Value))
        Next
        On Error GoTo 0
    End If
End Sub

Public Sub SaveIni()
    Dim i As Integer
    Dim C As Control
    WriteIniString "FileId", "therm"
    On Error Resume Next
    For Each C In frm_thermometer.Controls
        WriteIniString "frm_thermometer." + C.Name + ".caption", C.Caption
        If TypeOf C Is CheckBox Or TypeOf C Is OptionButton Then
            If C.Value Then
                WriteIniString "frm_thermometer." + C.Name + ".value", 1
            Else
                WriteIniString "frm_thermometer." + C.Name + ".value", 0
            End If
        Else
            WriteIniString "frm_thermometer." + C.Name + ".value", C.Value
        End If
    Next
    On Error GoTo 0
End Sub
```